Developing Clinically Orientated Diffusion-Weighted Magnetic Resonance Imaging of the Brachial Plexus in Adults

Submitted in accordance with the requirements for the degree of Doctorate in Philosophy

School of Medicine

University of Leeds

Ryckie George Wade

2022

The candidate confirms that the work submitted is his/her own and that appropriate credit has been given where reference has been made to the work of others.

Publications

Derivations of this work have been published in the following citations:

1. **Wade RG**, Takwoingi Y, Wormald JCR, Ridgway JP, Tanner S, Rankine JJ, Bourke G. Magnetic Resonance Imaging for Detecting Root Avulsions in Traumatic Adult Brachial Plexus Injuries: Protocol for a Systematic Review of Diagnostic Accuracy. **Systematic Reviews**; https://doi.org/10.1186/s13643-018-0737-2

   This work features in Chapter 11 and Appendix 1. The contributions to this work are as follows: The candidate (RGW) conceived the review and participated in the review design, registration, data collection, analysis and write-up. As a biostatistician with expertise in studies of diagnostic test accuracy and reviews thereof, YT supervised the methodological aspects of review design, data collection, analysis and write-up. JCRW participated in the review design, data collection, analysis and write-up. JPR participated in the design of the review and provided expert clinical context as a MRI physicist for the write-up. ST participated in the design of the review and provided expert context as a MRI Physicist for the write-up. JJR participated in the design of the review and provided expert clinical context as a musculoskeletal radiologist for the write up. GB supervised the design of the review, analysis and write-up providing expert input as a nerve surgeon; she will also act as guarantor of the review.

2. **Wade RG**, Takwoingi Y, Wormald JCR, Ridgway JP, Tanner S, Rankine JJ, Bourke G. MRI for Detecting Root Avulsions in Traumatic Adult Brachial Plexus Injuries: A Systematic Review of Diagnostic Accuracy. **Radiology**; https://doi.org/10.1148/radiol.2019190218

   This work is featured in Chapter 11 and Appendix 2. The contributions to this work are as follows: The candidate (RGW) and GB are guarantors of

the integrity of the entire study. All authors partook in the study conceptualisation. RGW performed the literature searches. RGW and JCRW extracted data and performed the methodological appraisals. RGW and YT performed the statistical analyses. All authors were involved in the manuscript drafting, revision and approval of final version.

3. **Wade RG**, Teh I, Tanner S, Ridgway JR, Rankine JJ, Chaka B, Shelley B, Bourke G. Diffusion Tensor Imaging for Diagnosing Brachial Plexus Injuries: A Proof-of-Concept Study. Frontiers in Surgery. https://doi.org/10.3389/fsurg.2020.00019

This work features in Chapter 12 and Appendix 3. The contributions to this work are as follows: The candidate (RGW), MW, and GB conceived the study. RGW, GB, MW, JJR, JPR, and ST designed the study. Data were collected and MRIs performed by RGW, ST, IT, JPR, DS, and BC. Aspects of image analyses were performed by RGW, ST, IT, GA, JPR, and JJR. RGW led the statistical analyses and prepared the manuscript. All authors edited and approved the manuscript.

4. **RG Wade**, E Bligh, K Nar, RS Stone, DJ Roberts, I Teh, G Bourke. The Geometry of the Roots of the Brachial Plexus. **Journal of Anatomy**, https://doi.org/10.1111/joa.13270

This work features in Chapter 13 and Appendix 4. The contributions to this work are as follows: The candidate (RGW) conceived the study. RGW and GB designed the study. EB and RGW performed the dissections. RGW acquired the medical images, performed the statistical analyses and drafted the manuscript. KN and RSS designed the scripts for medical image analysis. DJR supervised the dissection of specimens. IT provided engineering supporting. GB was the primary supervisor and provided clinical oversight.

5. **RG Wade**, A Whittam, G Andersson, F Yeh, M Wiberg, Bourke G. Diffusion Tensor Imaging of the Roots of the Brachial Plexus: A Systematic

Review and Meta-Analysis of Normative Values. **Clinical and Translational Imaging**, https://doi.org/10.1007/s40336-020-00393

This work features in Chapter 14 and Appendix 5. The contributions to this work are as follows: The candidate (RGW) conceived and designed the study, registered the protocol, extracted and analysed data, performed risk of bias assessments and co-authored the manuscript. AW extracted data, performed risk of bias assessments and co-authored the manuscript. IT, GA, FY and MW supervised the analysis of data analysis, interpretation and co-authored the manuscript. GB had oversight of the entire project, supervising the design, analysis and interpretations, and co- authored the manuscript.

6. **RG Wade**, I Teh, G Andersson, Y Fang-Cheng, M Wiberg, G Bourke. Fractional Anisotropy Thresholding for Deterministic Tractography of the Roots of the Brachial Plexus. **Scientific Reports**, https://doi.org/10.1038/s41598-020-79840-8

This work features in Chapter 15 and Appendix 6. The contributions to this work are as follows: The project was conceived and designed by the candidate (RGW), IT and GB. Data were collected by RGW and IT. Data analysis was performed by RGW, IT, GA and FY. The interpretation of results and manuscript preparation by performed by all authors (RGW, IT, GA, FY, MW, GB).

Presentations

Derivations of this work have been disseminated through oral and poster presentations at numerous international conferences, including:

1. **American Society for Peripheral Nerve (ASPN) Scientific Meeting** 14-16th January 2021; Virtual

"Diffusion Tensor Imaging of the Roots of the Brachial Plexus: A Systematic Review and Meta-Analysis of Normative Values"
Wade RG, Whittam A, Andersson G, Yeh FC, Teh I, Bourke G

"Safety and Outcomes of Different Surgical Techniques for Cubital Tunnel Decompression: A Systematic Review and Network Meta-Analysis"
Wade RG, Griffiths TG, Flather R, Burr N, Teo M, Bourke G

"Diffusion Tensor Imaging for Diagnosing Brachial Plexus Injuries: A Proof of Concept Study"
Wade RG, Teh I, Tanner S, Ridgway JR, Rankine JJ, Chaka B, Shelley B, Bourke G

"The Geometry of the Roots of the Brachial Plexus"
RG Wade, <u>E Bligh</u>, K Nar, RS Stone, DJ Roberts, I Teh, G Bourke

2. **British Association of Plastic, Reconstructive and Aesthetic Surgeons (BAPRAS) Summer Scientific Meeting.** 27th June 2019; Bournemouth, UK

   Wade RG, Takwoingi Y, Tanner S, Ridgway JR, Rankine JJ, Bourke G
   "MRI for diagnosing root avulsions in traumatic brachial plexus injuries: A Diagnostic Test Accuracy Review and Meta-analysis" and "Diffusion Tensor Imaging for Diagnosing Brachial Plexus Injuries: A Proof of Concept Study"

3. **NARAKAS.** 18th May 2019; Leiden, Netherlands

   Wade RG, Takwoingi Y, Tanner S, Ridgway JR, Rankine JJ, Bourke G
   "MRI for diagnosing root avulsions in traumatic brachial plexus injuries: A Diagnostic Test Accuracy Review and Meta-analysis" and "Diffusion Tensor Imaging for Diagnosing Brachial Plexus Injuries: A Proof of Concept Study"

4. **The International Society for Magnetic Resonance in Medicine Symposium.** 14th May 2019; Montreal, Canada

Wade RG, Teh I, Tanner S, Ridgway JR, Rankine JJ, Chaka B, Shelley B, Bourke G. "Diffusion Tensor Imaging for Diagnosing Brachial Plexus Injuries: A Proof of Concept Study"

5. **Royal College of Surgeons of Edinburgh Triennial Surgical Innovation Congress.** 22nd March 2018; Edinburgh, UK

Wade RG, Teh I, Tanner S, Ridgway JR, Rankine JJ, Chaka B, Shelley B, Bourke G. "Novel MRI to avoid exploratory surgery in traumatic brachial plexus injuries"

Prizes Awarded

The following prizes have been awarded to Ryckie George Wade for data presented within this thesis:

1. **Royal College of Surgeons of Edinburgh Triennial Surgical Innovation Congress: 2nd place (2018)**

   "Novel MRI to avoid exploratory surgery in traumatic brachial plexus injuries"

2. **The International Society of Magnetic Resonance in Medicine Clinical Stipend (2019)**

   "Diffusion Tensor Imaging for Diagnosing Brachial Plexus Injuries: A Proof-of-Concept Study"

3. **York Medical Society Founders Prize – 1st place   (2019)**

   "Diffusion Tensor Imaging for Diagnosing Brachial Plexus Injuries: A Proof-of-Concept Study"

<u>Dedication</u>

I dedicate this work to my fabulous wife Emily, and our wonderful children Harrison and Charlotte. This journey would have been impossible without your love, support, understanding and encouragement.

<u>Acknowledgements</u>

I wish to thank the following people for their invaluable support:

- **Associate Professor Grainne Bourke** for more than can be summarised here. Since 2015, when I began my NIHR ACF post, she has been my academic supervisor, clinical trainer and role model. She is eternally optimistic and encouraging. Her energy and support enabled me to develop personally and professionally. It is impossible to list the myriad things she has selflessly done to further my development and this project, or the wider academic plastic surgery program in Leeds and beyond. I will be eternally grateful and forever thankful.

- **Dr Irvin Teh** for your boundless patience and stewardship. Thank you for the education and assurances; for your reliability and enthusiasm in creating and further developing these sequences. For your sincere and patient help in reconstructing and interpreting the data fundamental to this thesis. You are the cornerstone of the physics aspect of this work.

- **Professor Sven Plein** for your faith, support, and guidance. Without your generous invitation to transfer our work to the AIC in 2017, and the wider support you provided over the years, this programme of research would have been impossible.

- **Mr David Shelley** for enduring me as your trainee radiographer and the considerable teachings you have shared. As a trainee surgeon, I thought it absurd that I might safely operate the scanner. Your stewardship enabled me to achieve more than I could have imagined.

- **Dr Hamied Haroon** for your happiness and help. It was a pleasure to be taught by you and a privilege to co-design our pre-processing pipeline. I will be always grateful for the wisdom and guidance you have imparted on my dMRI adventure.

- **Dr Frank Yeh** for so frequently and happily updating DSI Studio to optimise its compatibility, accept non-brain diffusion MRI datasets and

- **Ms Kathryn Richards** for overseeing the organisation and day-to-day running of the Advanced Imaging Centre, arranging scan slots, vouchers and training
- **Dr David Broadbent** for your frequent support at the console, the MRI safety training, hardware certification and sign-off of patients with implants in the Advanced Imaging Centre.
- To all the **friends, family and colleagues** who kindly volunteered to be scanned for both our sequence development work or as healthy controls in particular studies, I am immensely grateful for your patience and generosity.

Competing Interests

None

Funding

Abstract

Introduction: The nerves of the brachial plexus control movement and feeling in the upper limb. The most common form of traumatic brachial plexus injury (BPI) is root avulsion. Morphological magnetic resonance imaging (MRI) is used clinically to diagnose root avulsion, but its accuracy remains unclear. Diffusion MRI (dMRI) techniques characterise tissue microstructure and generate proxy measures of nerve 'health' which are sensitive to myelination, axon diameter, fibre density and organisation.

Chapter 11 describes a meta-analysis of the diagnostic accuracy of MRI for identifying root avulsions in adults with traumatic BPI in 11 studies. It shows that that conventional (morphological) MRI has modest diagnostic accuracy (mean sensitivity 93% and specificity of 72%), meaning that MRI fails to identify 7 in 100 avulsed nerves and incorrectly classifies 28 in 100 nerves as avulsed when they are in continuity.

Chapter 12 shows a clinically viable dMRI sequence which is sensitive to established traumatic root avulsion in adults. Equally, this work highlights uncertainties in the acquisition, preprocessing and postprocessing of DTI data in the brachial plexus which warrant investigation before the technique is applied clinically.

Chapter 13 is concerned with modelling the microscopic geometry of the brachial plexus in fixed cadavers, to inform the step angle used for deterministic tractography. We suggest that when generating deterministic streamlines of the brachial plexus from DTI at a resolution typically performed clinically, a step angle of 70° is likely to propagate 99% of streamline bundles which truly represent root.

Chapter 14 is a meta-analysis of 9 studies which defines the normal fractional anisotropy and mean diffusivity values in healthy adult the brachial plexus. We show that roots of the brachial plexus in adults appear to have a pooled mean fractional anisotropy of 0.36 (95% CI 0.34, 0.38) and pooled mean diffusivity of 1.51 x10^{-3} mm^2/s (95% CI 1.45, 1.56). Equally, we show how these parameters are dependent on experimental conditions and vary slightly from C5 to T1.

Chapter 15 explores the effect of fractional anisotropy thresholding on deterministic tractography in the brachial plexus, identifying areas of uncertainty in the intrathecal and intraforminal areas. We shows that the FA threshold required to consistently generate valid streamlines (~0.06) was lower than that which is conventionally used in the brain (~0.1). This may be due to crossing fibres in the region or partial voluming from CSF, which warrants more complex acquisitions and models.

Chapter 16 shows that two most common pre-processing pipelines worldwide (FSL and DSI Studio) generate important differences in dMRI parameters and tractograms. When FSL was used, estimates of the anisotropy and diffusivity, both at the voxel-level and within streamlines, were a mean 2% and 7% lower (up to 10% and 17%), respectively. Equally, streamlines differed in their spatial location by a median of 2 voxels (5.56 mm). Such discrepancies must be factored into the interpretation of studies which use different preprocessing pipelines.

Chapter 17 we develop and deploy high b-value multishell dMRI to show that up to 44% of the brachial plexus contains multiple (crossing) fibre orientations which means that, perhaps, DTI is insufficient to describe the microstructure of these peripheral nerves.

Table of Contents

Figures

Tables

Equations

Appendices

Abbreviations

AD axial diffusivity

ADC apparent diffusion coefficient

AP anterio-posterior

BP brachial plexus

BPI brachial plexus injury

CISS constructive interference in steady state

CSD constrained spherical deconvolution

CSF cerebrospinal fluid

CT computed tomography

dODF diffusion orientation distribution function

DSI diffusion spectrum imaging

DTA diagnostic test accuracy

DTI diffusion tensor imaging

DW diffusion weighted

DWI diffusion weighted image

FA fractional anisotropy

fODF fibre orientation distribution function

EPI echo planar imaging

FID free induction decay

FN false negative

FOD fibre orientation distribution

FOV field of view

FP false positive

GQI generalised q-space imaging

GRAPPA GeneRalized Autocalibrating Partial Parallel Acquisition

HARDI high angular resolution diffusion-weighted imaging

ICC intraclass correlation coefficient

IQR interquartile range

IVIM intravoxel incoherent motion

MD mean diffusivity

MIP maximum intensity projection

MRI Magnetic Resonance Imaging

NODDI neurite orientation dispersion and density imaging

NPV negative predictive value

ODF orientation dispersion function

ODI orientation dispersion index

PCA principal component analysis

PGSE pulsed-gradient spin echo

PPV positive predictive value

PSIR phase-sensitive inversion recovery

QUADAS Quality Assessment of Diagnostic Accuracy Studies

RD radial diffusivity

RF radiofrequency

ROI region of interest

rsEPI readout segment echo-planar imaging

SH spherical harmonics

SROC summary receiver operating characteristic

ssEPI single-shot echo-planar imaging

SSFP steady-state free precession

STARD STAndards for the Reporting of Diagnostic accuracy studies)

STIR short tau inversion recovery

TN true negative

TP true positive

TR repetition time

TSE turbo spin echo

Part 1. Introduction

Chapter 1. The Peripheral Nervous System

The peripheral nervous system is designed to receive information from the environment (e.g., sensation from the skin) and relay such information to the central nervous system. More specifically, peripheral nerves conduct information between tissues and organs, in the form of electrical impulses and molecular transport, and the central nervous system.

1.1.1 Overall structure

Nerves which carry information towards the brain are termed afferent (Figure 1). Once information is processed in the brain, the peripheral nerve system communicates changes to end-organs and tissues through outflow via the somatic (controlled), autonomic (automatic) nervous systems. Nerves which carry information away from the brain are known as efferent. Together, these nerves and end-organs form a neural circuit which constantly relays information.
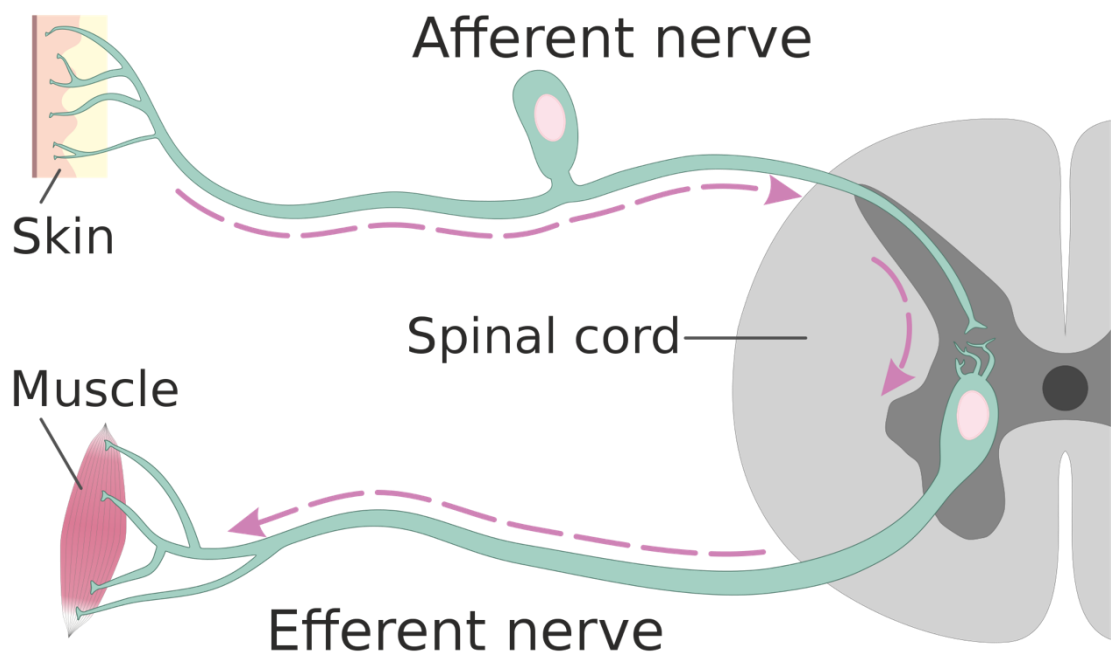
Figure 1. The arrangement of afferent and efferent nerves, in relation to the central nervous system. Reproduced from Helixitta (2019)[1].

1.1.2 Cellular composition of peripheral nerves

Peripheral nerves contain a variety of different cells designed to conduct electrical impulses, cells which provide supporting roles and microanatomical structures which provide a stable framework. The typical arrangement of cells and structures within peripheral nerves is shown in Figure 2
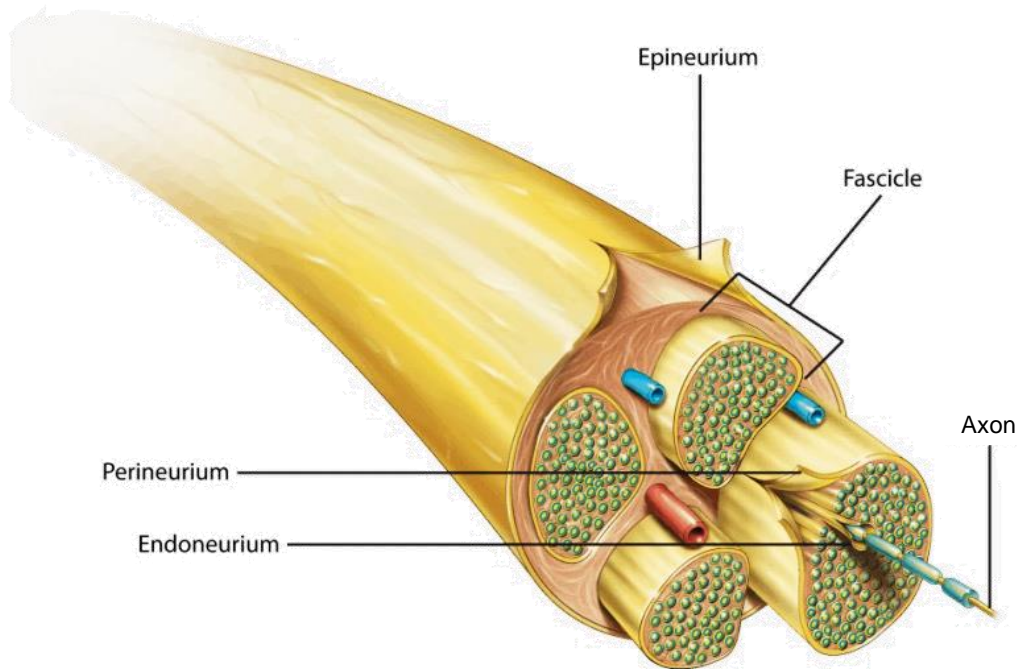
Figure 2. A peripheral nerve in cross section. Reproduced under the Creative Commons License, author unknown.

1.1.2.1 Neurons

Neurons (also known as nerve cells) are electrically excitable cells which communicate with receive and relay information (communicate) between other nerves, tissues and organs. This communication is done via specialised connections known as synapses. Neurons are typically described as having three distinct sections:

1. **Cell body**: The cell body (soma) which contains the cell nucleus and organelle (such as the rough endoplasmic reticulum [Nissl bodies] which synthesises neurotransmitters)
2. **Dendrites**: the short and numerous protoplasmic extensions from the cell body (which typically extend a few hundred micrometres) are known as dendrites. Dendrites synapse with neighbouring cells to receive and then propagate stimuli.

3. **A single axon**: arising from the axon hillock, axons (also known as nerve fibres) are long cytoplasmic projections of the neuron which are responsible for propagating information (received by dendrites, via the cell body) to the endplate at the synaptic terminal. These synapses communicate information to cells or organs. Axons can be short (millimetres) and up to tens or hundreds of centimetres long.

4. **Synaptic terminals**: Also known as terminal buttons and endplates, the terminals of the axon are the region of the neuron which is furthest from the cell body and where it synapses with other cells. At the synaptic terminal, neurotransmitters are released which stimulate the next cell in the circuit.
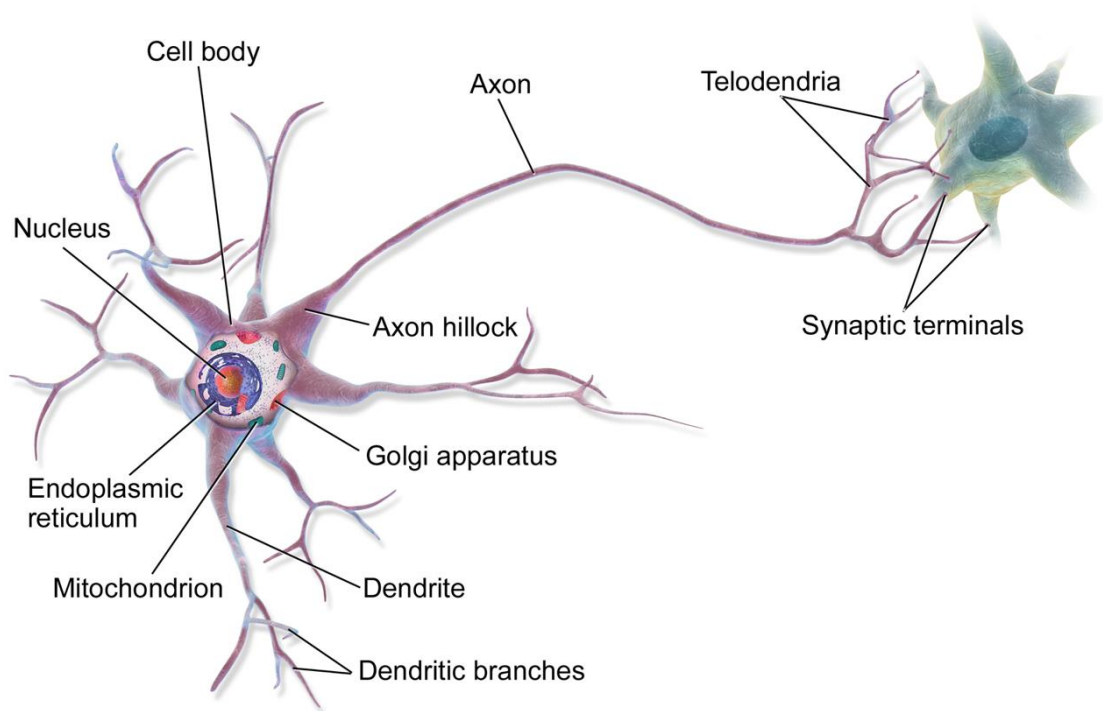
Figure 3. The general structure of a multipolar neuron (relative sizes are not to scale) and how it synapses with other cells. Reproduced from Blausen Medical 2014[2].

1.1.2.2 Myelin sheath

The axons of peripheral nerves may be myelinated or unmyelinated. Typically, axons which must conduct information fast (such as those involve in the withdrawal reflex or those involved in proprioception) are myelinated, whilst fibres carrying information which is less time critical (such as those dilating blood vessels) are unmyelinated.

The myelin sheath is derived from Schwann cells which are the glial cells of the peripheral nervous. Schwann cells synthesise a specialist multi-layered membrane which wraps around axons, forming an insulating sheath (Figure 4). The myelin sheath resembles the insulation of an electrical wire and performs a similar role.
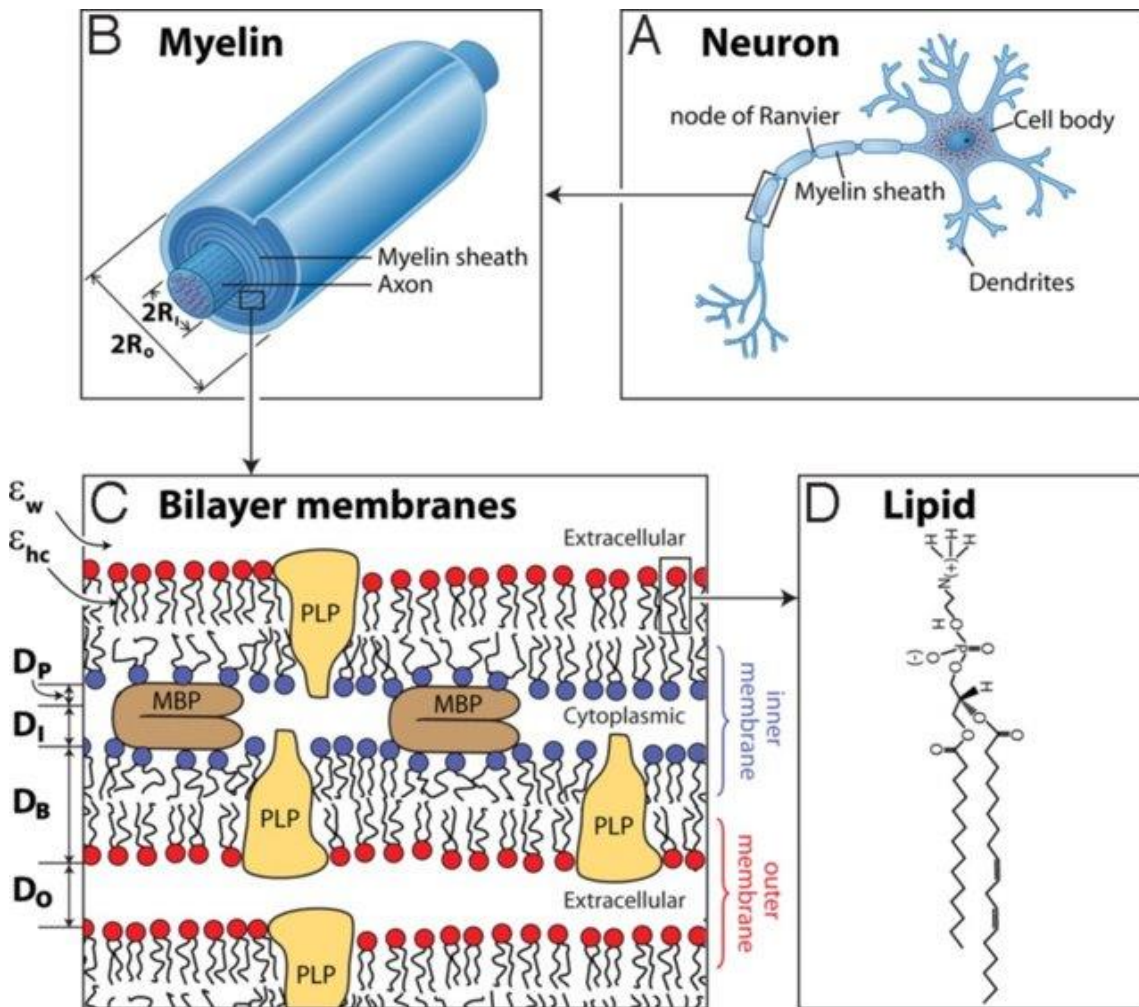
Figure 4. The myelin sheath and its structure. Panel A shows a neuron. Panel B shows an axon enveloped by a myelin sheath. Panel C shows the arrangement of the myelin sheath, which is formed by multi-layered, polar membranes composed chiefly of phosphatidylethanolamine (Panel D) which are bound together by myelin basic protein (MBP). The red and blue circles within Panel C represent differences in charge (hydrophilic and hydrophobic) between the membranes. Reproduced from Min et al (2009)[3].

1.1.2.3 Connective tissue

There is an abundance of connective tissue in peripheral nerves, which provides insulation, tensile strength, and structure (Figure 2). Each axon (whether it is enveloped in myelin or not) is encased in a delicate sheath known as endoneurium. Bundles of these nerve fibres (myelinated and unmyelinated axons, wrapped in endoneurium) together form a fascicle.

Fascicles are themselves enveloped in a sheath and a continuous matrix of connective tissue, known as perineurium. This space between fascicles, the perineurium, is a lamellar structure formed from flattened cells derived from fibroblasts. Perineural cells are linked together by tight junctions and desmosomes. The surrounding extra-cellular matrix is rich in collagen and glycosaminoglycans. Embedded within the perineurium are blood vessels and lymphocytes.

The outermost layer of a peripheral nerve is the epineurium, which is principally made of collagen.

1.1.2.4 Axon diameter and myelination

Axons have been classified in many different ways but the most widely accepted is that of Erlanger and Gasser (1930)[4] shown in Table 1. In this system, nerves are broadly categorised into myelinated (type A and B) and non-myelinated (type C). However, the radius of myelinated nerves determines conduction velocity[5] and therefore what functions it may serve, so group A was later subcategorised based on axon diameter. More recently, sensory nerves classifications have been introduced (Figure 5).
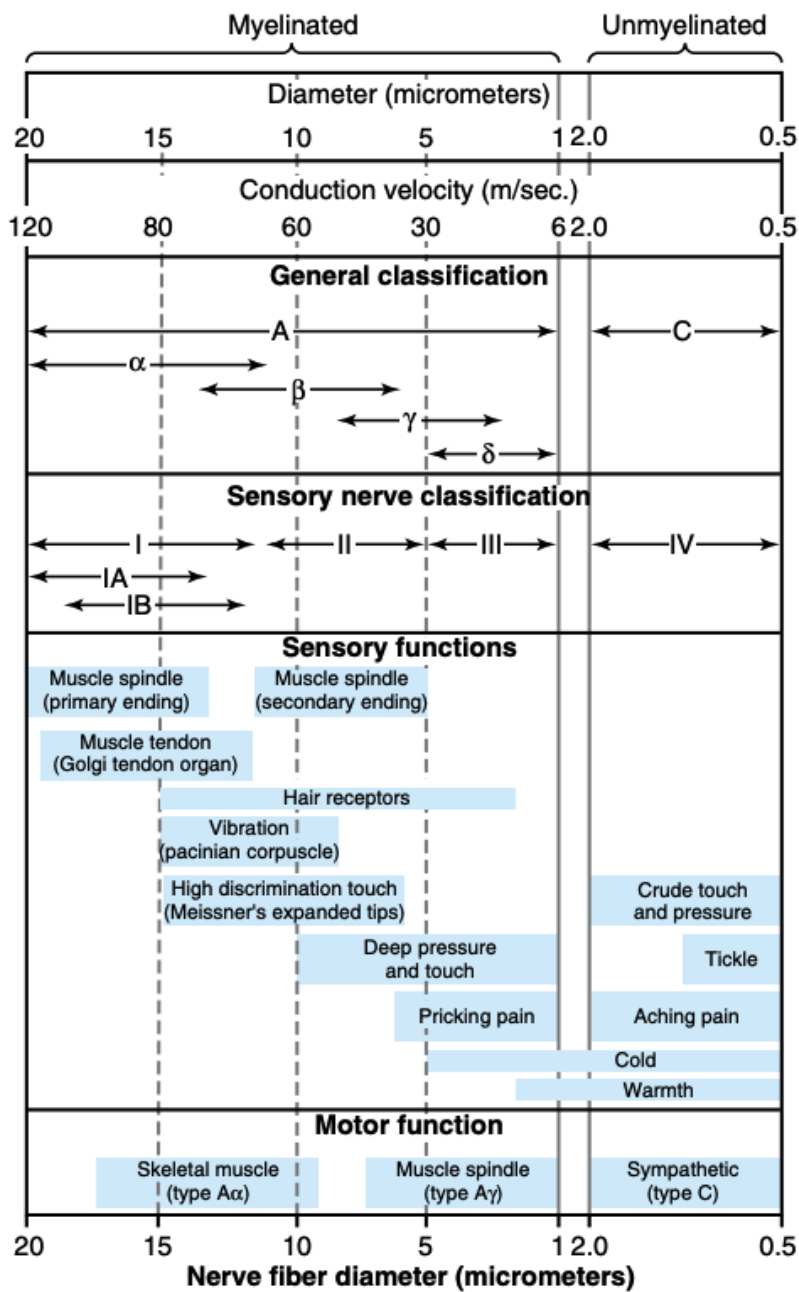
Figure 5. Classification systems for peripheral nerves.
Reproduced from Guyton & Hall (2010)[6].

Group	Subgroup	Diameter (µm)	Conduction velocity (m/s)	Myelinated	Sensory function	Motor function
A	α	13-20	80-120	Yes	Proprioception via Golgi tendon apparatus and muscle spindle fibres	Extrafusal skeletal muscle
	ß	6-12	80-120	Yes	Proprioception via muscle spindle fibres All cutaneous mechanoreception Some nociception	None
	γ	5-8	4-24	Yes	None	Intrafusal skeletal muscle
	δ	1-5		Yes	Light touch and pain (free nerve endings), temperature and nociception	None
B		3	3-15	Yes	Preganglionic autonomic	Preganglionic autonomic
C		0.2-1.5	0.3-1.6	No	All nociception derived from the spinothalamic tract (chemical, mechanical or thermal)	Pilomotor, sudomotor and vasomotor

Table 1. Erlanger-Gasser classification of peripheral nerve fibres

1.1.3 Axonal transport

In neurons, the cytoplasm is termed axoplasm. Longitudinally oriented cylindrical neurofibrils (microtubules) connect the cell body to the synaptic terminals to enable more efficient transport of axoplasm containing molecules and organelles, between the cell body and the synaptic terminals (Figure 6).
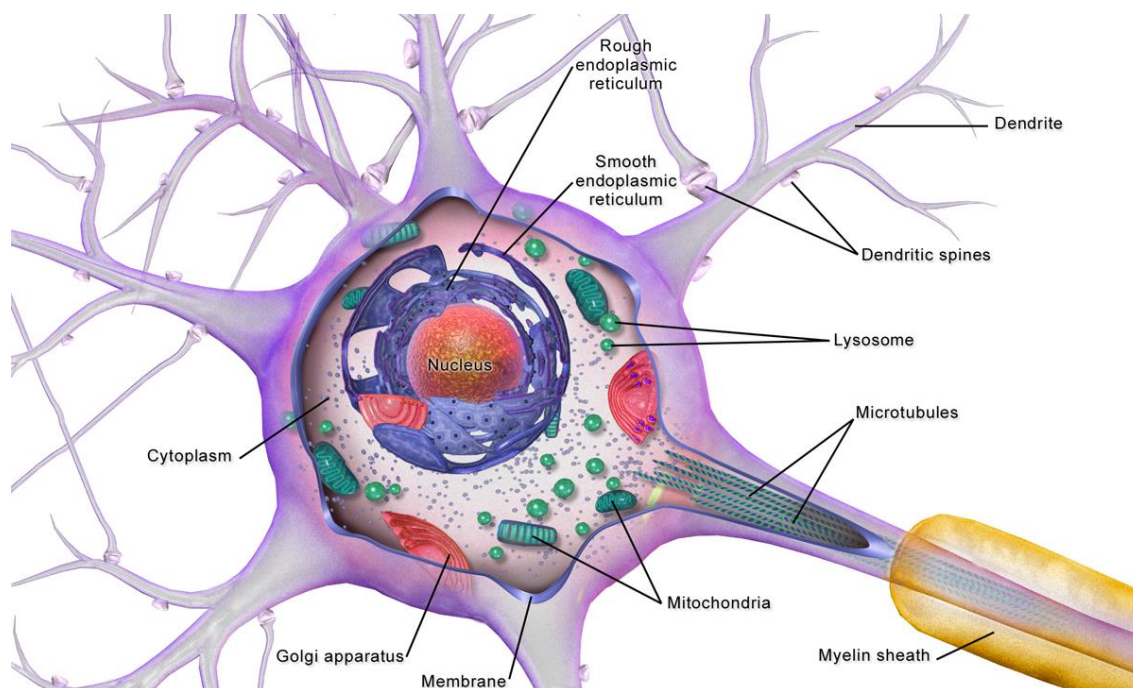
Figure 6. The microtubules arising at the axon hillock, extending into the axon. Reproduced from Blausen Medical 2014[2].

Anterograde transport moves proteins, mitochondria and membrane proteins from the cell body down the axon. Retrograde transport carries cell waste from the axon back towards the cell body.

1.1.4 Conduction

Neurons carry information in the form of an action potential. These are discrete electrical impulses which travel from the cell body, down an axon and into the terminal synapse. When the impulse reaches the synaptic endplate, it stimulates the release of neurotransmitters which effect the next cell in the circuit.

1.1.4.1 Resting Membrane potential

The membrane potential is the electrical difference across a plasma membrane, between the inside and outside of a neuron. At rest, the membrane potential across an axon is approximately -70mV in humans. This is maintained by active Na^+/K^+ pumps (Figure 7). This channel pumps $3Na^+$ out of the cell, whilst pumping $2K^+$ inside. The Na^+ ions are accompanied by Cl- ions outside the cell, whilst the K^+ ions are balanced by various organic anions within the cell. The difference in ion concentrations generates the resting membrane potential.
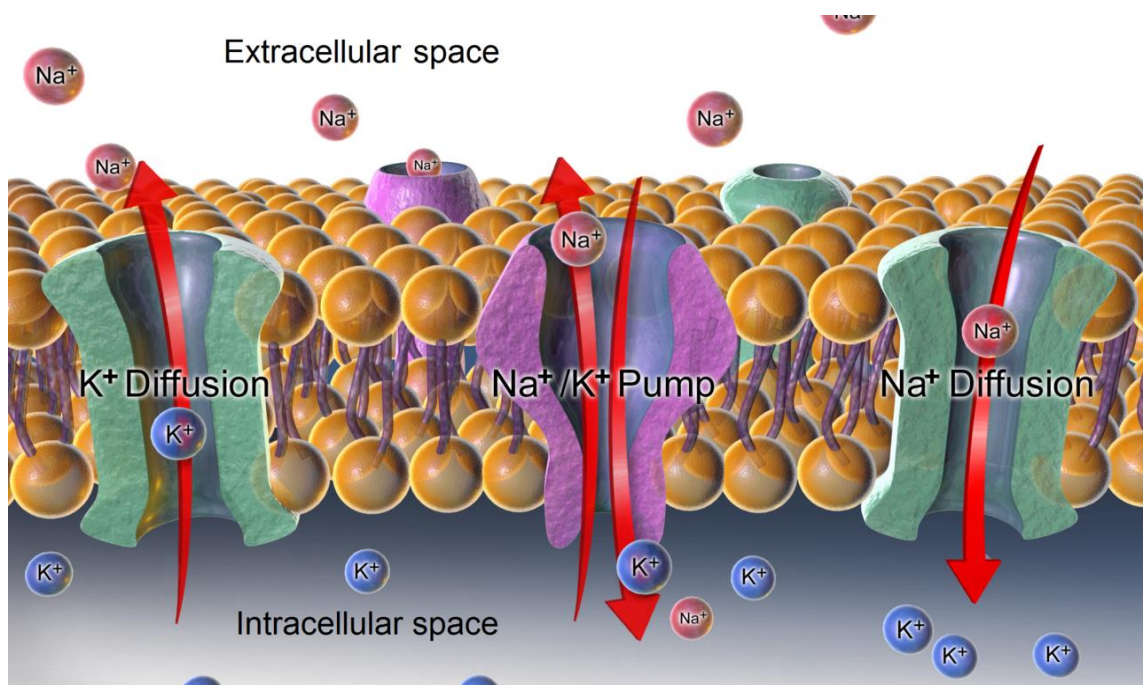
Figure 7. The resting membrane potential maintained by Na+/K+ ATPase pumps. Reproduced from Blausen Medical 2014[2].

1.1.4.2 Action potential

The conduction of an electrical impulse along a nerve is called an action potential, which is a brief reversal of the resting membrane potential. When neurotransmitters bind to receptors on the dendrites of the cell, some voltage-gated Na^+ channels open (Figure 8, box 1). Once the threshold potential is reached (approximately -55mV), all voltage-gated Na^+ channels open and the entire axon depolarises (Figure 8, box 2). At peak depolarisation (~30mV, Figure 8, box 1), Na^+ channels close and K^+ channels open, which together with the Na^+/K^+ cotransporters causes membrane repolarisation – there is an overshoot in repolarisation known as hyperpolarisation which protects the nerve from tetanic

stimulus (Figure 8, box 4). Ultimately, the resting membrane potential is restored (Figure 8, box 5) to allow another stimulus.
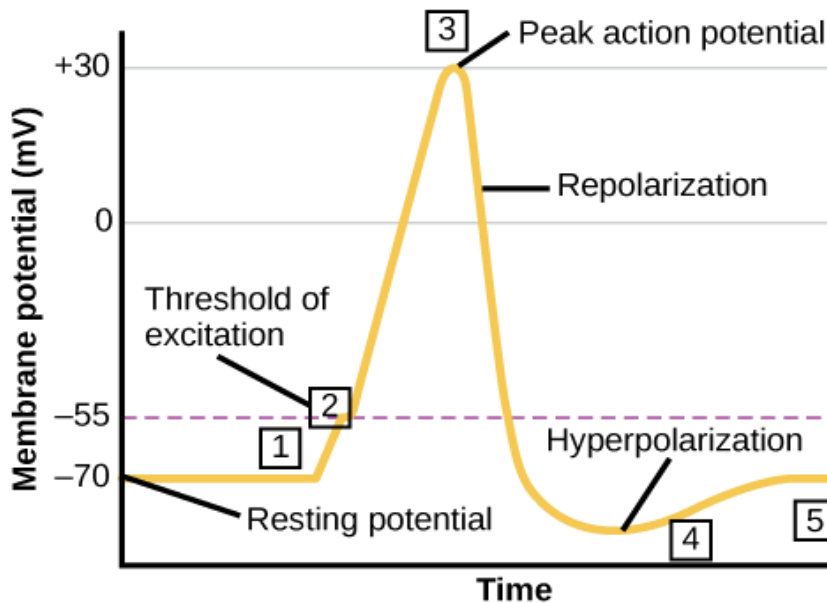
Figure 8. The action potential. Reproduced from Blausen Medical 2014[2].

1.1.4.3 Nodes of Ranvier

The gaps between myelin (Schwann cells) are known as the nodes of Ranvier (Figure 9). They are short unmyelinated sections of the axon, where the diameter is also reduced, which contain voltage-gated K^+ and Na^+ channels. The nodes of Ranvier enable saltatory conduction, which is the phenomenon by which electrical current at each node is conducted (with little attenuation) to the next node. The net effect is that action potentials 'jump' from node to node, making the overall conduction speed substantially greater.
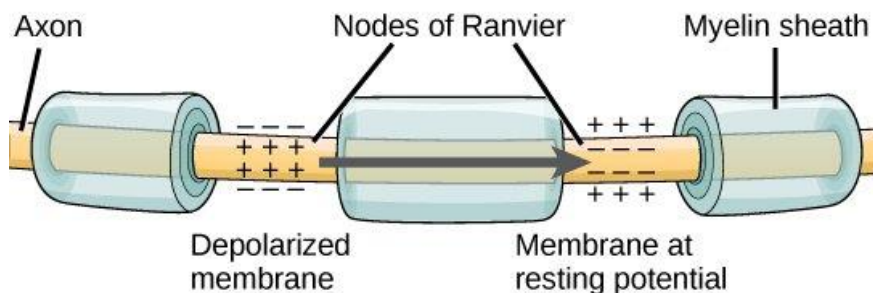
Figure 9. The Nodes of Ranvier. Reproduced from OpenStax.org under the Creative Commons License.

1.1.5 Traumatic nerve injury

After peripheral nerve injury, there is a coordinated response to remove damaged tissue and initiate regeneration. The goal of regeneration is to reconnect the nerve to an end organ.

Seconds-to-minutes after being disrupted, the proximal nerve stump retracts due to the elastic endoneurium, calcium influx cause the segregation and proliferation of cellular organelles and depolymerisation of microtubules. Division of the vasa nervorum causes haemorrhage from both stumps and thus, acute inflammation in the general zone. Within minutes-hours, axons undergo acute degeneration in the distal stump which results in complete fragment.

Within 24-36 hours, Wallerian degeneration[7] begins (Figure 10). This is an active process whereby the nerve seeks to generate an environment distal to the site of injury which is receptive to axonal regrowth, while the proximal stump alters its phenotype to promote axon regeneration.

Schwann cells are active in Wallerian degeneration, as they promote the recruitment of macrophages (via Monocyte chemoattractant protein, MCP-1) to phagocytose myelin and secrete neurotrophic factors (nerve growth factor, NGF and ciliary neurotrophic factor, CNTF), which promote and guide axon regeneration. In the distal stump Schwann cells extrude their myelin sheath, downregulate myelin genes, dedifferentiate and proliferate. The new Schwann cells align via Bünger bands to provide a guide for regenerating axons.
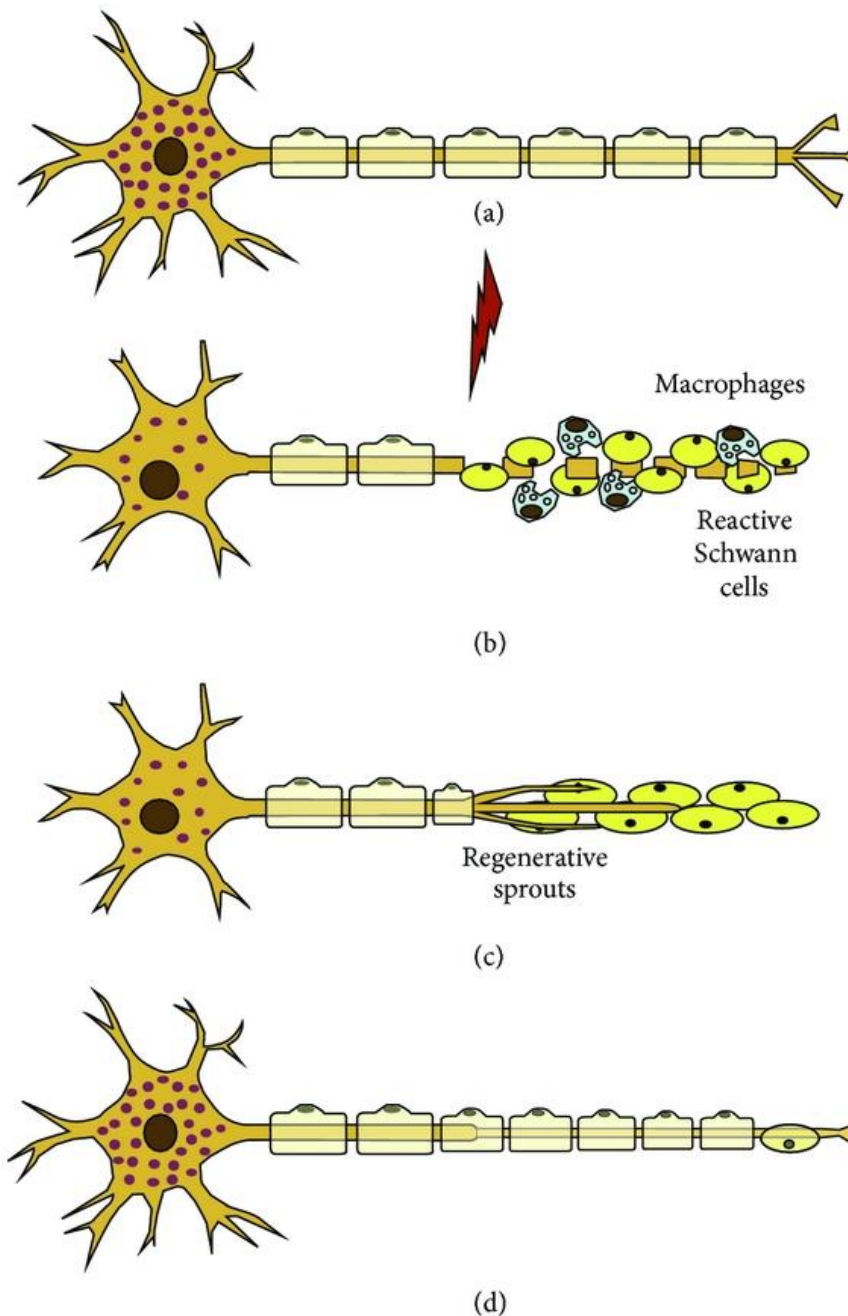
Figure 10. Wallerian degeneration. Reproduced from Allodi et al (2012)[8].

Approximately 3-4 days after injury, axons begin sprouting from the proximal stump and advance, attracted by the growth factors secreted by Schwan cells, into the new tubes they have formed. Axons within such tubes grow at ~ 1mm per day. There are several factors which slow and speed up axon regeneration, although the exact mechanisms have yet to be fully and clearly elucidated.

Within the zone of injury fibroblasts proliferate and generate immature scar tissue which encases the injured zone.

<u>1.1.5.1 Classification of nerve injury</u>

Many classification systems have been proposed over time, although those of Seddon (1942)[9] (Figure 11) and Sunderland (1951)[10] are the most popular. Their similarities and differences are shown in Table 2.
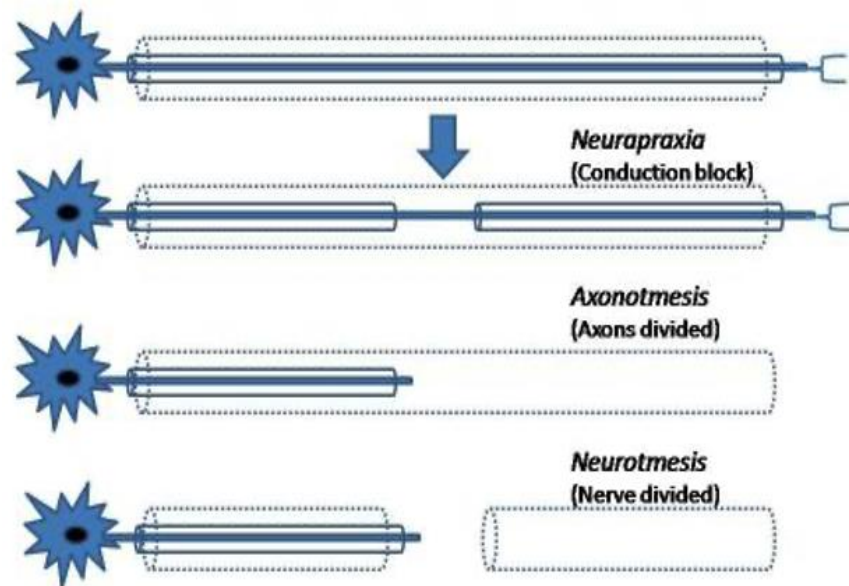
Figure 11. Graphical depictions of nerve injury patterns according to Seddon (1942)[9]. Adapted from Hems (2016)[11].

Seddon	Sunderland	Axons injured	Endoneurium injured	Perineurium injured	Myelin injured	Recovery	Nerve conduction	Electromyography
Neurapraxia	1	✗	✗	✗	✓ (focal)	Spontaneous, within weeks	Partial/complete conduction block	Normal
Axonotmesis	2	✓	✗	✗	✗	Spontaneous, within months		Abnormal
Axonotmesis	3	✓	✓	✗	✗	Potentially		
Axonotmesis	4	✓	✓	✓	✗	Potentially		
Neurotmesis	5	✓	✓	✓	✓	Potentially	Complete conduction block	

Table 2. Classification systems for peripheral nerve injury

Chapter 2. The Brachial Plexus

The brachial plexus is specialised section of the peripheral nervous system which controls movement and feeling in the shoulder, arm, forearm and hand.

1.2.1 Anatomy of the brachial plexus

The brachial plexus is a network of motor, sensory and autonomic fibres within the neck and shoulder region (Figure 12).
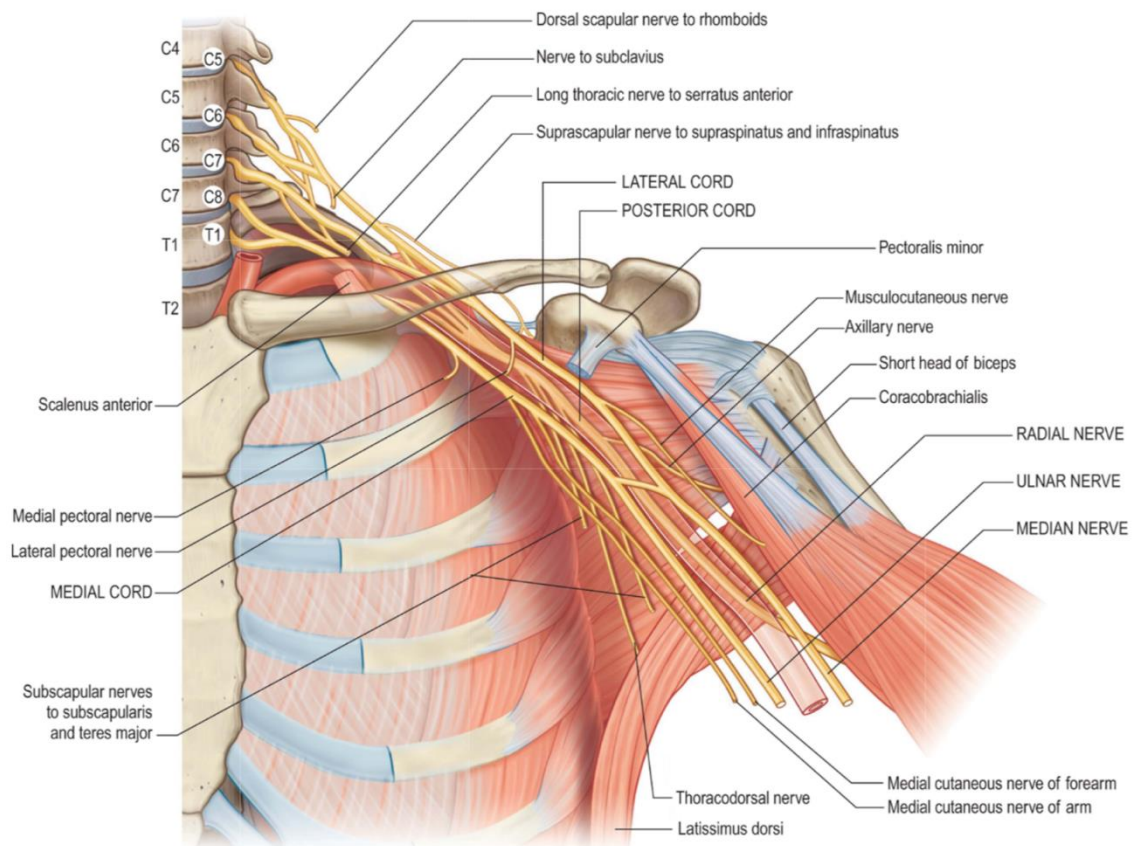
Figure 12. The brachial plexus. Reproduced from Gray's Anatomy
70th Edition, Elsevier at https://studentconsult.inkling.com/

1.2.1.1 The spinal roots of the brachial plexus

The spinal nerve roots (Figure 13) are formed by the ventral rami of the lower four cervical spinal nerves and the majority of the ventral ramus of the 1st thoracic spinal root.
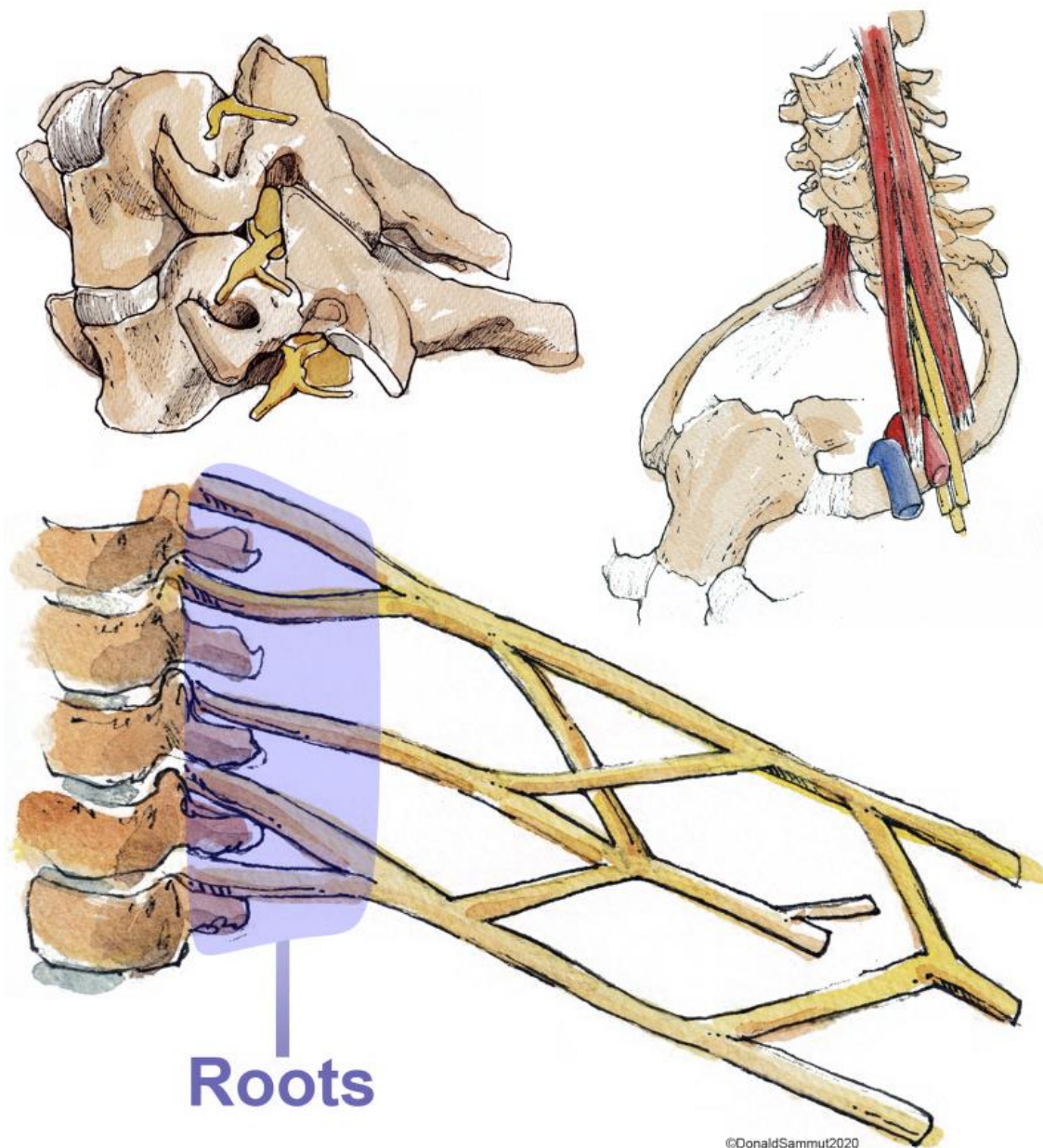
Figure 13. A schematic of the roots of the brachial plexus (lower image, highlighted in purple) emerging from the intervertebral foramina (upper left) and their relationship to the scalene muscles and vasculature of the upper limb (upper right). Reproduced with permission from Mr Donald Sammut.

The cephalad roots (C5/6) unite to form the upper trunk whilst the caudal roots (C8/T1) unit as the lower trunk. Both trunks and the 7th cervical root give anterior and posterior divisions which unite as cords and further divide into five (principal) terminal branches, amongst numerous other smaller branches.

1.2.1.2 Anatomical variation

There is considerable variation in the contribution of the 4th cervical and 2nd thoracic spinal roots, and autonomics to the brachial plexus. A systematic review by Pellerin et al (2010)[12] summarised the observed variations into a) prefixed and b) postfixed as depicted in the artwork from Sakellariou et al (2014)[13] in Figure 14. The prevalence of a prefixed plexus was 10-63% and postfixed 0-59%. The variability is largely due to heterogeneous definitions; for example, a single intradural fascicule and the entire C4 ventral root anastomosing to the C5 were both defined as prefixed although the clinical meaningfulness is debatable.
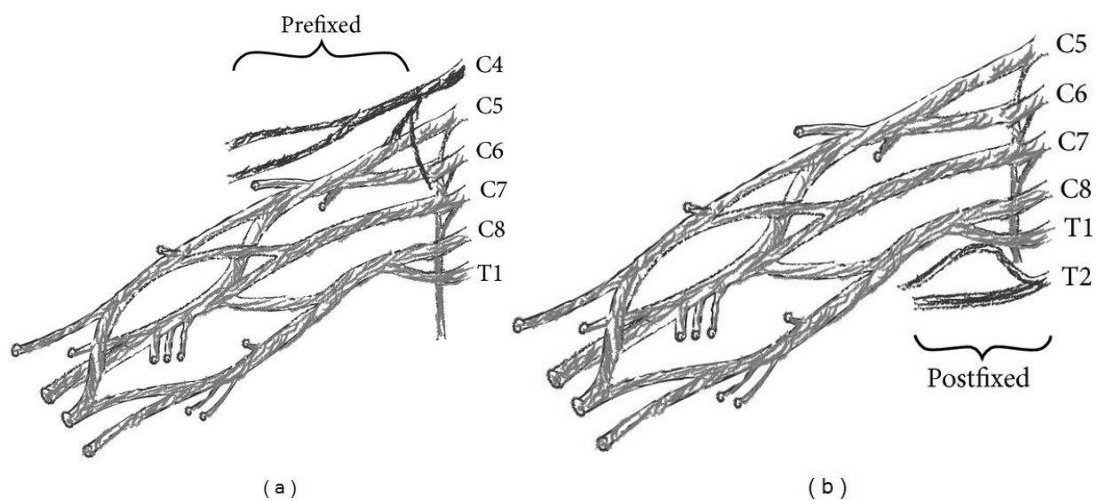
Figure 14. Schematics of the (a) prefixed and (b) postfixed roots of the brachial plexus. Reproduced from Sakellariou et al (2014)[13]

1.2.1.3 Microscopic topography of the brachial plexus

The roots of the brachial plexus are mixed motor (efferent) and sensory (afferent) fibres. These nerves are housed within distinct tracts in the spinal cord but merge via the dorsal and ventral rootlets to form the spinal nerve roots.

The microscopy topography of the brachial plexus has been studied extensively but there is still disagreement about the exact extent of axonal or fascicular exchange at various levels (Figure 15).
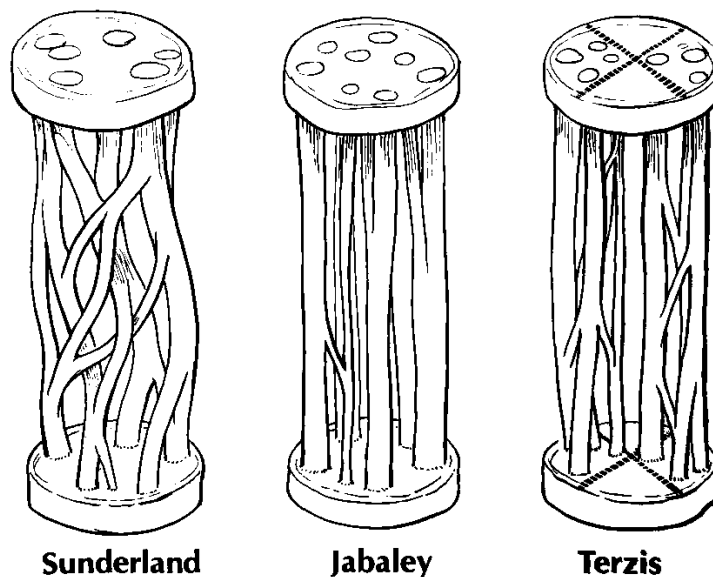
Figure 15. Theories of the fascicular arrangement within peripheral nerves. The Terzis model is the closest to in-vivo research findings

The original proposals of Sunderland (that fascicular arrangement is entirely unpredictable and as such, fascicular dissection is impossible) have been largely disproven because fascicles are readily dissected over (at least) several centimetres in vivo, for the purposes of nerve transfers. Jabley proposed that there was minimal fascicular branching at discrete identifiable locations with no overall topography whilst Terzis hypothesised that whilst interchanges did occur, there was an appreciable and constant topography that can be both identified and traced, proximally and distally.

Slingluff, Terzis and Edgerton histologically examined the brachial plexus at 0.5mm intervals[14] in 1987. Their work demonstrated that the spinal nerve roots (as well as the divisions of the upper trunk and origins of the suprascapular and musculocutaneous nerves) exhibited little or no meaningful fascicular exchange (i.e., they are monofascicular) for up to 2.5cm of their length. subsequent microanatomical dissection studies have demonstrated consistent fascicular topography in the spinal roots
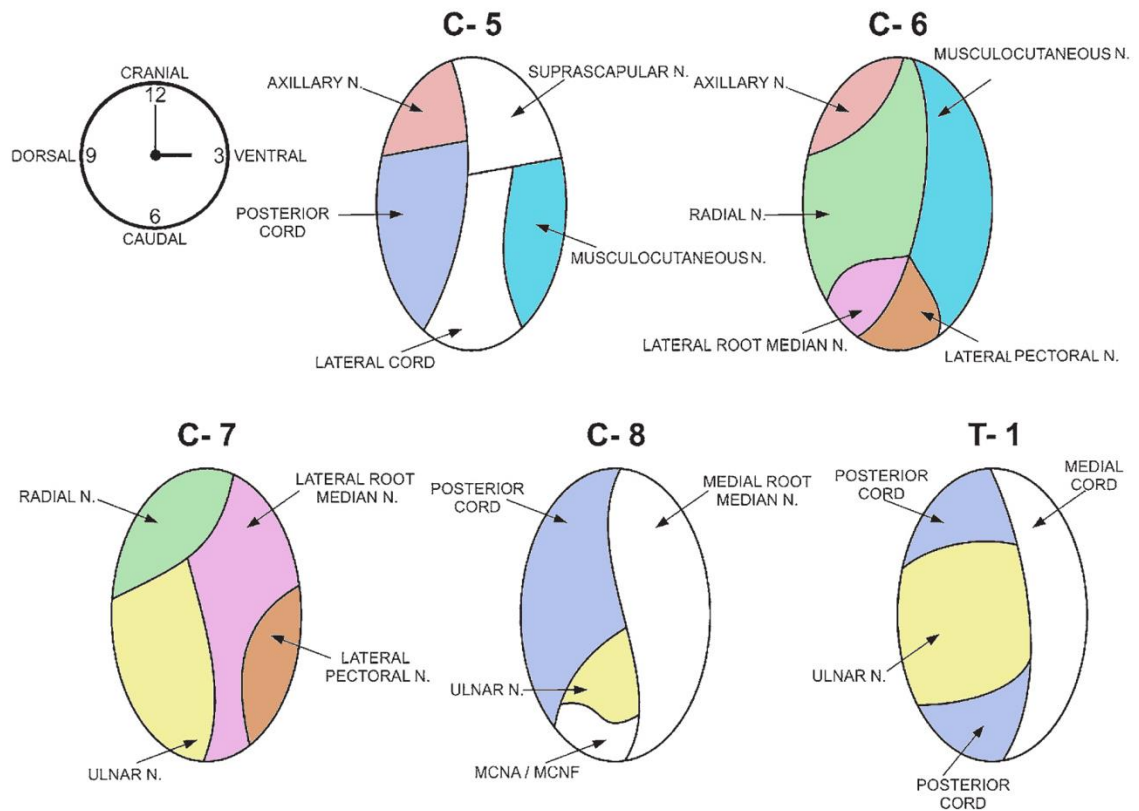
Figure 16. The topography of fascicular groups in the spinal nerve roots of the brachial plexus. Adapted from Sinha et al (2016)[15].

However, within all other regions of the brachial plexus, which is the majority of its course, there is considerable axonal and fascicular branching akin to the model proposed by Terzis. As such, axons and fascicles branches on average every 5mm to join neighbouring fascicles.

1.2.1.4 The cellular composition of the roots of the brachial plexus

The majority (57-85%) of the cross-sectional area of the spinal roots are connective tissue[14]. The remainder are a mixture of motor, sensory and autonomic nerves. Gesselbauer et al (2017)[16]. The roots of the brachial plexus on both sides of the neck house approximately 700,000 axons, although these are distributed unevenly across the spinal roots (Table 3), with the majority of axons (94%) being sensory.

Root	Mean Total Axon Count (SD)	Mean % Motor (SD)
C5	38,210 (9388)	12 (1.6)
C6	75,861 (9856)	6 (0.7)
C7	84,008 (10,578)	6 (0.9)
C8	90,376 (12,533)	6 (1.0)
T1	61,421 (22,815)	4 (0.8)
Total	**349,876 (43,226)**	**6 (0.4)**

Table 3. Axon composition & counts in the roots of the brachial plexus. Derived from Gesselbauer et al (2017)[16].

1.2.2 Brachial plexus injury in adults

Traumatic brachial plexus injuries (BPI) affect 1% of patients involved in major trauma[17] and occur in polytraumatised patients. BPIs are typically caused by traction forces on the upper limb and/or forces which separate the head from limb (Figure 17). The most serious form of BPI is avulsion of the roots (Figure 17, red arrow).
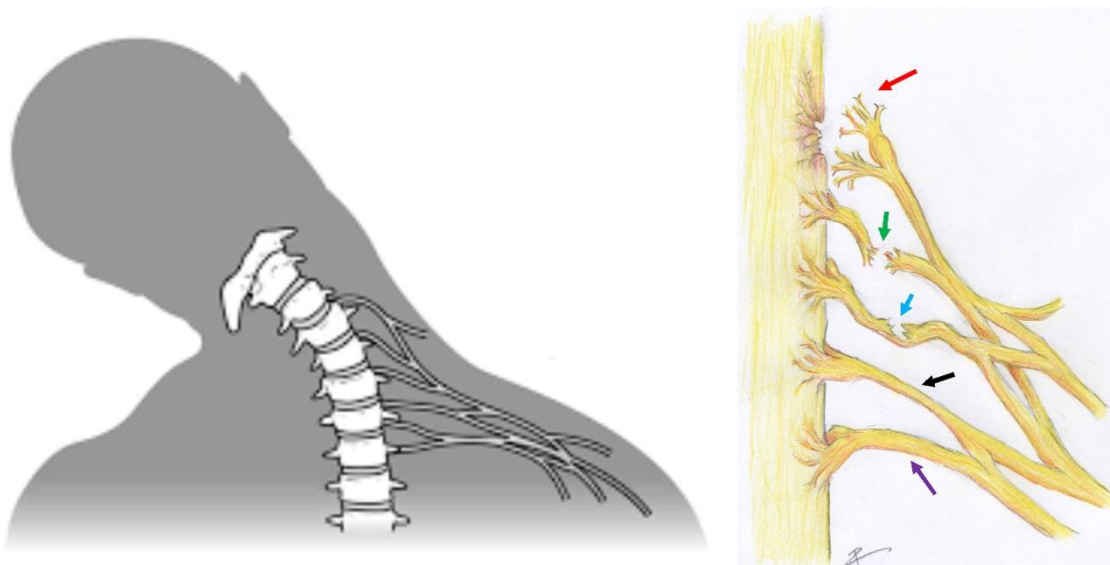
Figure 17. Forceful lateral flexion on the neck (as occurs when a helmet-wearing motorcyclist collides with a solid object) may cause traction injuries (black arrow), partial rupture (blue arrow), complete rupture (green arrow) and/or root avulsion (red arrow).

BPIs are serious given that they may cause permanent disability[18–22], pain[23–25], psychological morbidity[26,27] and reduced quality of life[18,20,28].

1.2.2.1 Clinical features of root avulsion

Adults with traumatic BPIs typically have deficient movement and feeling in the upper limb, alongside substantial neuropathic pain. The various patterns of deficits depend on the part of the plexus which is injured and beyond the scope of this report. Suffice-to-say, root avulsion results in flaccid paralysis, paraesthesia and intractable neuropathic pain in the elements of the limb supplied by that root.

1.2.2.2 Diagnosing root avulsion

Internationally, practice is heterogenous with respect to the diagnosis of root avulsion. At one of end of the spectrum, clinicians keep patients under surveillance for months-years, intervening surgically if there no sign of recovery. Conversely, some clinicians deploy medical tests, such as imaging and neurophysiological studies and undertake operative exploration, to reach the diagnosis faster and therefore, also delivery treatment more quickly.

MRI is the best non-invasive test for brachial plexus injuries[29]. MRI is superior to nerve and muscle electrophysiology studies[30], ultrasonography[31–34] and intraoperative somatosensory-evoked potentials[35]. To identify patients with roots avulsion who need urgent reconstructive nerve surgery, most surgeons use pre-operative MRI although it is currently unable to reliably diagnose root avulsion (or differentiate them from other nerve injuries outside the intervertebral exit foramen) alone.

Ultimately, the most reliable test to-date is surgical exploration of the brachial plexus (Figure 18), although this carries considerable risk of morbidity and cost for both patients and the health service.
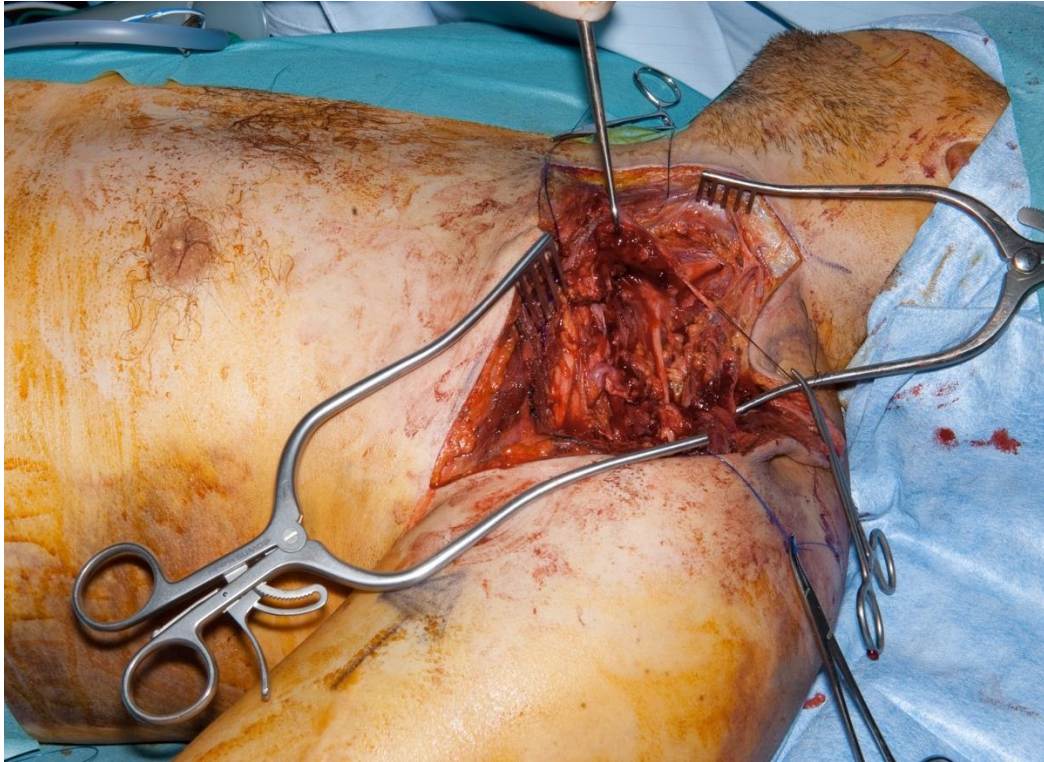
Figure 18. Intraoperative photograph of a male undergoing left brachial exploration with clavicular osteotomy.

Early diagnosis is of critical importance because this enables early reconstruction which is associated with better functional recovery[18,19,28,36–38], improved quality of life[20] and might mitigate chronic neuropathic pain[39] which is experienced by 95% of patients with BPIs[40].

1.2.2.3 Reconstruction for root avulsion

In patients who eventually undergo surgical exploration for traumatic BPI, root avulsions are the most prevalent type of injury[41]. These are typically high-force injuries which affect all neural elements including the anterior horn cells[42] and fibres in the transitional zone of the spinal cord, the free rootlets branching from the spinal cord and distally into the brachial plexus itself. The large zone of trauma to spinal cord and peripheral nerve precludes re-implantation[43] or interposition nerve grafting because prior work has shown this to yield no meaningful recovery. In the context of root avulsions, neurotisation of the end-organs can only be reliably achieved by distal nerve transfer (neurotisation).

Nerve transfers are relatively minor cost-effective procedures[44], which have a low morbidity[45–48] but significantly improve function and quality of life[44,45,49]. An

example of neurotisation of the biceps brachii muscle, to restore elbow flexion, using a fascicle from the ulnar nerve is shown in Figure 19.
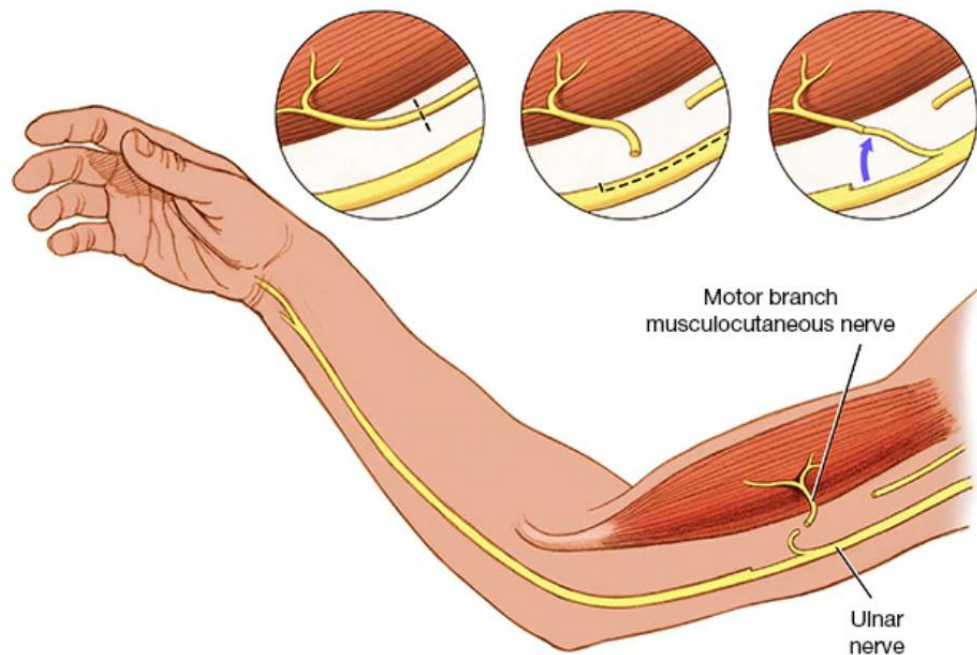
Figure 19. A 'spare' fascicle from the ulnar nerve is transferred to the biceps muscle to reinnervate the muscle and thus, restoring elbow flexion. Reproduced from www.mayoclinic.org

In the same way that early diagnosis is beneficial to patients, recent work in patients with pan-plexus injuries (which are typically root avulsions) also shows that early neurotisation is beneficial. Specifically, the delay from injury to neurotisation is important because every month of delay reduces the probability of meaningful recovery by 7%[50]. Therefore, the early identification of patients with root avulsion(s) who require early nerve transfer is of paramount importance and improved imaging may help.

Chapter 3. Magnetic Resonance Imaging

This chapter provides an overview of the basic concepts of magnetic resonance imaging (MRI) from the origin of signal to image formation.

1.3.1 History

Isidor Isaac Rabi was awarded the 1944 Nobel Prize in Physics for describing the concept of nuclear magnetic resonance (NMR), using a molecular beam in a vaccum[51]. In 1946, Bloch and Purcell independently described the NMR phenomenon[52,53] in matter for which they jointly received the Nobel Prize for Physics in 1952. However, cross-sectional images were only made possible in 1973 when Lauterbur and Mansfield described methods for spatially localising the NMR signal[54,55]. Once spatially localised, the term magnetic resonance imaging (MRI) is commonplace. MRI is appealing for both clinical and research purposes given that it is non-invasive and does not involve ionising radiation.

1.3.2 Bulk magnetisation

The majority of medical MRI is based upon hydrogen atoms (^1H). This is the most abundant atom in the human body (~63%) and largely found in water and lipids (fat).

The hydrogen nucleus has a single (positively charged) proton. According to quantum theory, nearly all elementary particles (such as protons) possess a property known as the 'spin'. Spin describes the rotation of a particle about its axis, like a spinning top. Spin is a result of intrinsic angular momentum of the charged particle, which generates a magnetic moment (Figure 20). The magnetic moment is effectively a magnetic dipole and akin to a bar magnet.

Hydrogen atom (^{1}H)
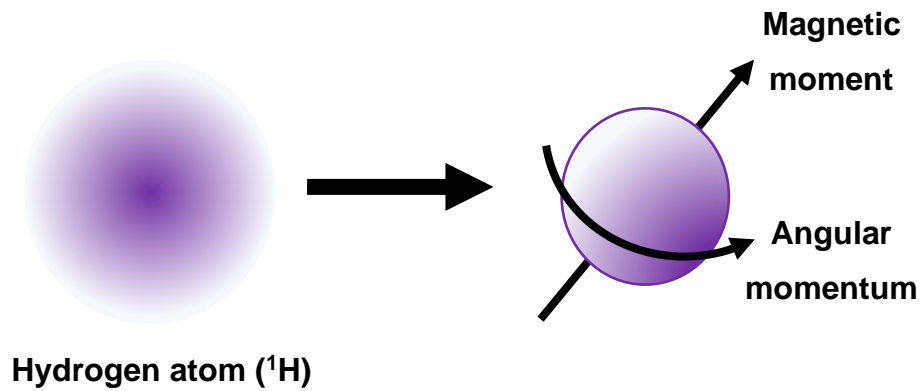
Figure 20. Angular momentum of the ^{1}H proton generates a magnetic field (magnetic moment).

The manipulation and measurement of spins is central to image generation in MRI. Whilst there are nuclei with non-zero spins (e.g., ^{23}Na and ^{31}P) their concentrations in human tissue are much lower. Therefore, the rest of this chapter refers to ^{1}H in living human tissues.

1.3.2.1 Precession

Once at equilibrium within B_0 spins exhibit precession, whereby the magnetic moments of individual protons rotate around B_0. When the net magnetisation (M) reaches a stable state, longitudinal magnetisation is established (M_z). For an individual proton experiencing B_0, the phenomenon of precession is shown in Figure 21.
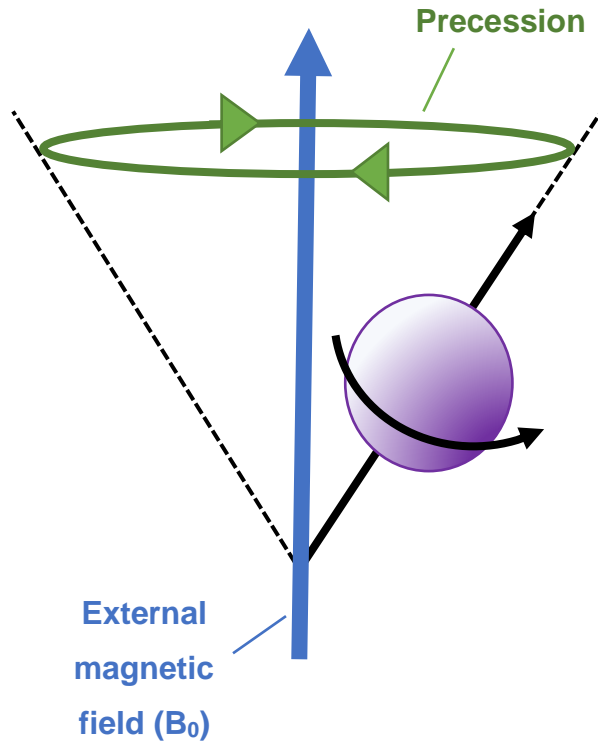
Figure 21. When exposed to B_0, protons undergo precession

The speed of the precession (angular frequency) is known as the Larmor frequency (ω) and it is proportion to the strength of B_0 as well as the gyromagnetic ratio (γ, which is a constant specific to a particular nucleus, 42.58MHz/T in the case of ^1H protons).

The relationship between B_0 and γ is given by the Larmor equation (Equation 1). The Larmor frequency is the resonant frequency of the system, whereby energy exchange (absorption and emission) can occur.

$$\omega = \gamma B$$

Equation 1. The Larmor equation

In practice, we cannot affect or measure individual spins, but rather MRI is based on the manipulation and measurement of bulk magnetisation, derived from many discrete protons. Stronger magnetic fields force more protons to align with B_0, meaning that more protons can be manipulated. In practice, the number of spins from which we can generate signal is very small e.g., 5 per million at 1.5T.

1.3.2.2 The rotating frame of reference

To simply the complex motion of the vector of net magnetisation, the frame of reference is important. Consider a Merry-Go-Round (Figure 22), if we take a photograph from a static location whilst the ride is spinning, the motion of the horses (up and down) it would be blurred – this position is known as the laboratory frame of reference. If we are interested in the motion of the net magnetisation vector (the horses in this example) then we must rotate around at the same speed whilst taking the photograph. In this way, the motion of the vectors (horses) would be clear and simple – this is known as the rotating frame of reference.

Figure 22. The same Merry-Go-Round viewed from the laboratory frame (left) and rotating frame (right). Reproduced from Questions and Answers in MRI (https://mriquestions.com/rotating-frame.html).

Henceforth, diagrams in this thesis are created and explained in terms of the rotating frame of reference. In NMR, the frame of reference rotates at the Larmor frequency.

1.3.3 Signal generation and decay

Within the bore of an MRI scanner, net magnetisation aligns with B_0 to produce longitudinal magnetisation (M_z).

1.3.3.1 Excitation

Energy can be introduced into the system using a radiofrequency (RF) pulse, at the Larmor frequency (Figure 23). The process of applying energy to the system (B1) and its absorption is known as excitation of spins. The application of an RF

pulse causes the net magnetisation vector to rotate about the axis of the applied B1 field. The stronger the RF pulse, the more the net magnetisation vector is rotated.

In the below example, the RF pulse is designed to flip the magnetisation 90° into the transverse (M_{xy}) plane. Transverse magnetization precesses about the z-axis which, according to Faradays law, induces an alternating voltage in the receiver coil(s) – this MR signal is captured and processed to generate an image.
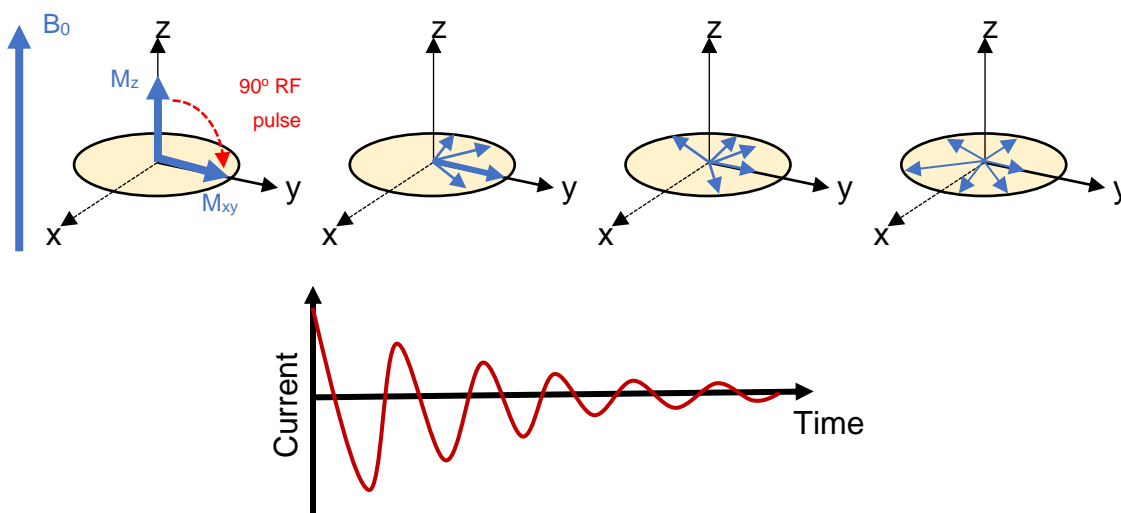
Figure 23. Longitudinal magnetisation is flipped from the M_z plane into the transverse (M_{xy}) plane, by an RF pulse at the resonant frequency. This induces an alternating voltage in the receiver coil(s). Adapted from Ridgway et al (2010)[57].

As soon as the MR signal is generated (transverse magnetisation) it also begins a free induction decay (FID). This occurs due to two distinct processes known as T1 and T2 relaxation.

1.3.3.2 T1 relaxation

This describes the recovery of net magnetisation to the equilibrium (M_0) i.e., net magnetisation returns to the z-axis (M_z,). For T1 relaxation to occur, energy must leave the system and be transferred to neighbouring spins and the wider environment. This energy transfer is principally thermal, hence the alternative name of thermal relaxation.
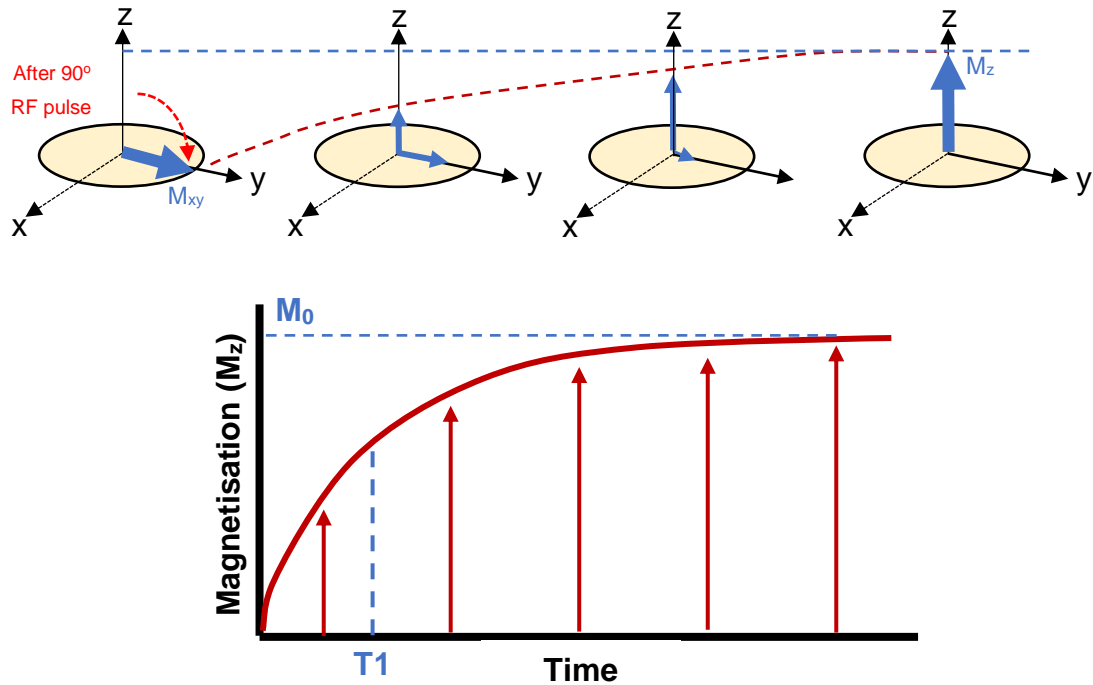
Figure 24. The longitudinal relaxation phenomenon (T1) modelling the recovery of M_z, as exponential function ($1 – e^{-t/T1}$). Adapted from Ridgway et al (2010)[57].

T1 follows a first order exponential function and describes the time required for the M_z to reach ~63% of its maximum (Figure 24). The original NMR experiments which described the T1 phenomenon were based upon crystalline lattices which is why the process was (historically) termed "spin-lattice relaxation".

Many physiological factors affect the T1 of living tissues, including temperature, viscosity, state (solid, liquid or gas), ionic content and diffusion. In practice, the T1 is used to guide the repetition time (TR). For example, after approximately 5 T1s (e.g., if T1 for the tissue of interest was 1 second, then this would be 5 seconds) 99.5% of M_z would have recovered and thus be available for excitation.

1.3.3.3 T2/T2* relaxation

Also known as spin-spin relaxation, T2 relaxation describes the progressive dephasing of spins and thus, decay of transverse magnetisation (M_{xy}). T2 is a time constant for M_{xy} to decay to 1/e of its original magnitude.

T2 relaxation depends on spin-spin interactions. Free water (e.g., cerebrospinal fluid) contains numerous water molecules which interact frequently, so more energy is exchanged and the time constant T2 is long (3-4 seconds), similar to T1. Spins of macromolecules and water bound to such larger molecules interact less, so dephase more rapidly and therefore a M_{xy} decays faster. This means that spins of larger molecules (e.g., lipids) have a shorter T2. When tissues have an increased free water content (as occurs with inflammation), then the T2 typically lengthens. The effect of spin-spin interactions on M_{xy} are shown in Figure 25.
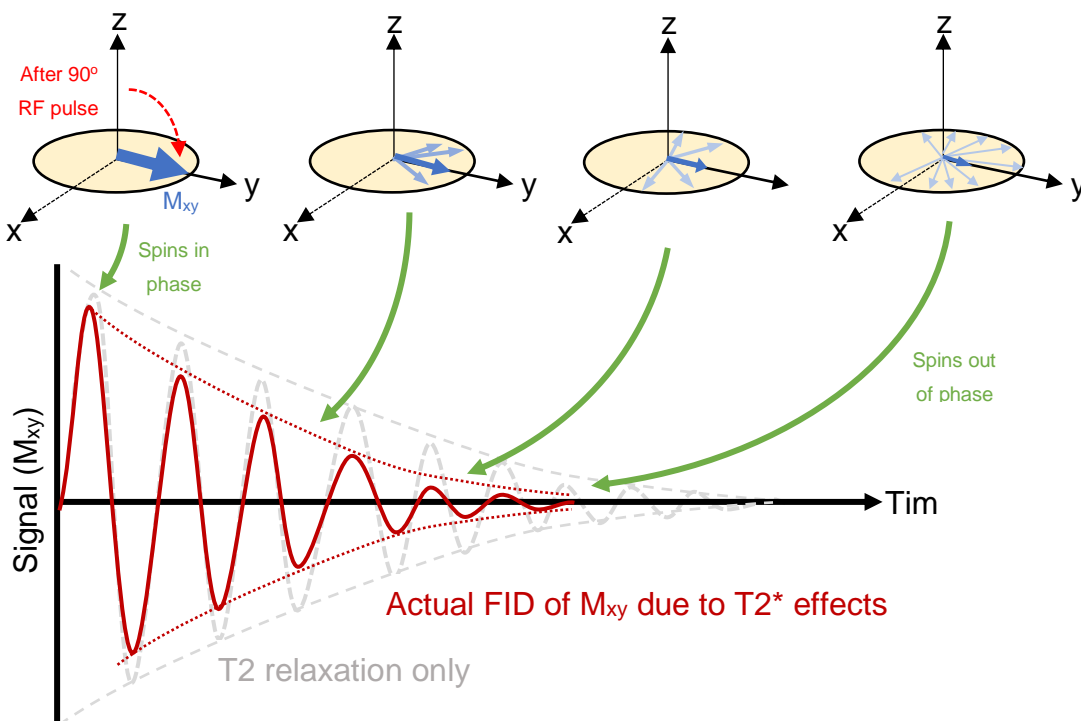
Figure 25. The T2 and T2* relation process. After a 90º pulse, transverse magnetisation (M_{xy}) is generated, and spins are coherent. Over time, spins dephase causing signal decay. Adapted from Ridgway et al (2010)[57].

The observed FID due to T2 effects is smaller than expected. This is due to several other effects which accelerate the decay of M_{xy}, such as field inhomogeneities, magnetic susceptibility and the chemical environment. Together, T2 and these local effects which contribute to the overall loss of phase coherence is called T2* relaxation. T2* incorporates both T2 effects (interactions due to molecular motion) and other local effects to better describe the discrepancy between the actual and expected FIDs.

Of importance, T2 relaxation always accompanies processes which cause T1 relaxation, which is known as "T1 in T2". However, T2 relaxation may occur without T1 relaxation due to "flip-flop" interactions and/or local field disturbances.
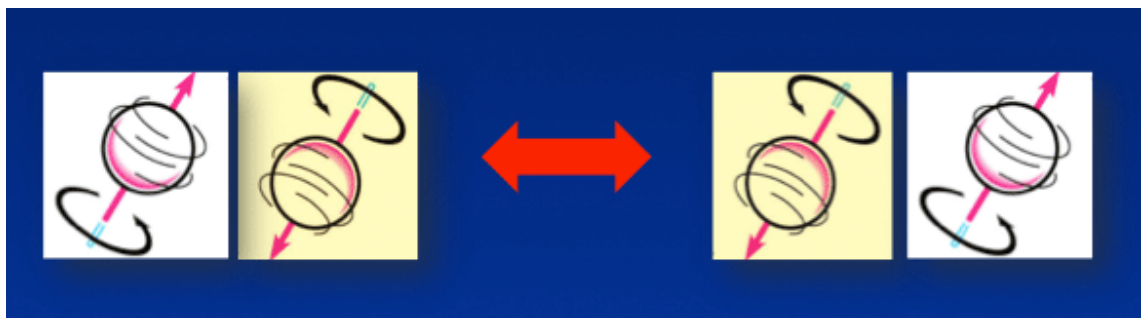
Figure 26. Spin-spin "flip-flop" whereby a pair of spins swap longitudinal angular momentum which causes no change in T1, but the interaction causes T2 relaxation . Reproduced from https://mriquestions.com/what-is-t2.html

1.3.3.4 T1 and T2 values in humans

The T1 and T2 constants are different in different tissues, ranging from tenths of seconds to several seconds. Examples of these values, relevant to peripheral nerve imaging, are shown in Table 4 based on the work of Stanisz et al (2005)[58].

Tissue	Mean (SD) time in ms			
	1.5T		3T	
	T2	T1	T2	T1
White matter (Brain)	72 (4)	884 (50)	69 (3)	1084 (45)
Gray matter (Brain)	95 (8)	1124 (50)	99 (7)	1820 (114)
Optic nerve	77 (9)	815 (30)	78 (5)	1083 (39)
Spinal cord	74 (6)	745 (37)	78 (2)	993 (47)
Skeletal muscle	44 (6)	1008 (20)	50 (4)	1412 (13)
Blood	290 (30)	1441 (120)	275 (50)	1932 (85)

Table 4. T2 and T1 Relaxation Times at 3T and 1.5T, at 37°C.

1.3.3.5 Echoes

The FID from an excitation can be measured as MR signal (which can be achieved clinically using ultrashort TE imaging) but the gradients used to spatially encode signals in typical scanners rapidly degrade the FID, so it is typically reformed and measured as an echo. The FID is one of four types of MR signal (Table 5) which are broadly categorised into spin and gradient echo.

MR signal	Method of formation
FID	1 RF pulse
Gradient echo	1 RF pulse + gradient reversal
Spin echo	2 RF pulses
Stimulated echo	3 or more RF pulses

Table 5. Types of NMR signal

Spin echoes are based upon a 90° excitatory RF pulse, followed by a 180° rephasing RF pulse between two positive gradients (Figure 27).
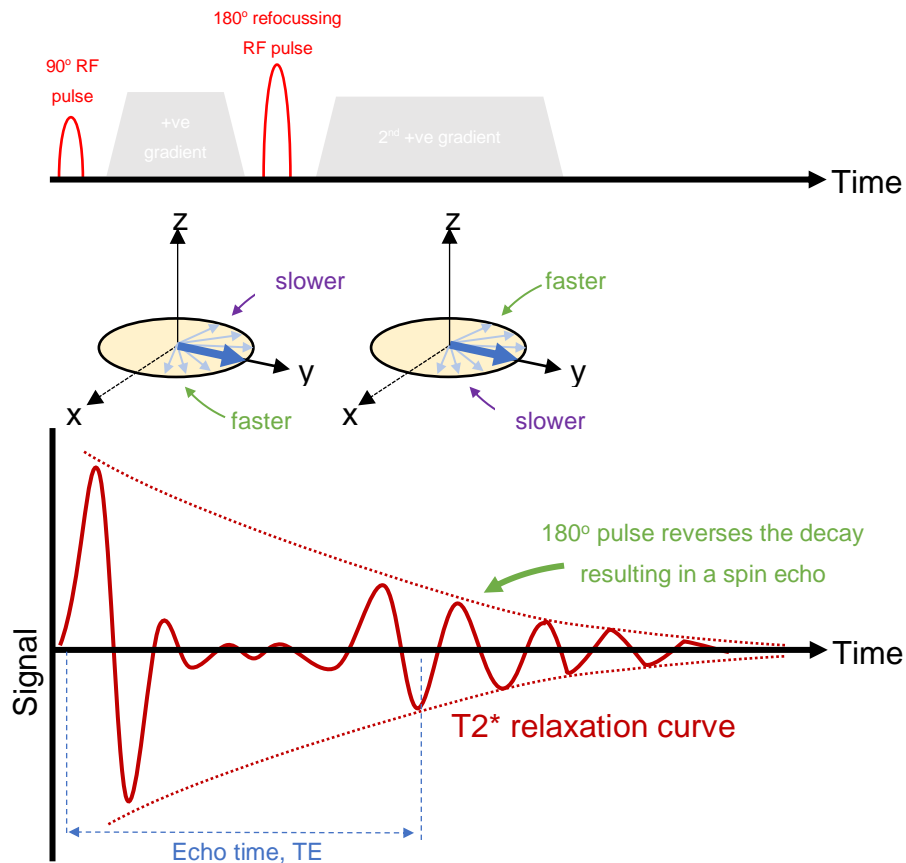
Figure 27. A diagrammatic representation of how a spin echo is generated. In areas of inhomogeneities, spins precess relatively faster or slower which accelerates dephasing and the decay of M_{xy}. The application of a 180° pulse reverses the rotation of spins such that spins re-align (coherence) and an echo of the FID is generated which can be measured as MR signal. Adapted from Ridgway et al (2010)[57].

The work presented in this thesis is based upon spin echo sequences and will be described henceforth.

1.3.4 Spatial encoding

When MR signal is measured without spatial localisation, signal measured in the coils comes from the entire sample. To localise the signal to a specific position, three separate magnetic fields are applied in three separate steps to spatially encode the signal.

1.3.4.1 Slice selection

Selection of a 2D slice can be achieved by deploying a linear gradient (perpendicular to the slice) when the excitatory RF pulse is applied (Figure 28). This causes the Larmor frequency to change along the axis of the gradient and as such, the RF pulse can be tailored to excite a certain range of frequencies representing the desired slice. In practice, the slice thickness is determined by the range (transmit bandwidth) of frequencies in the RF pulse and the steepness (strength) of the slice select gradient.
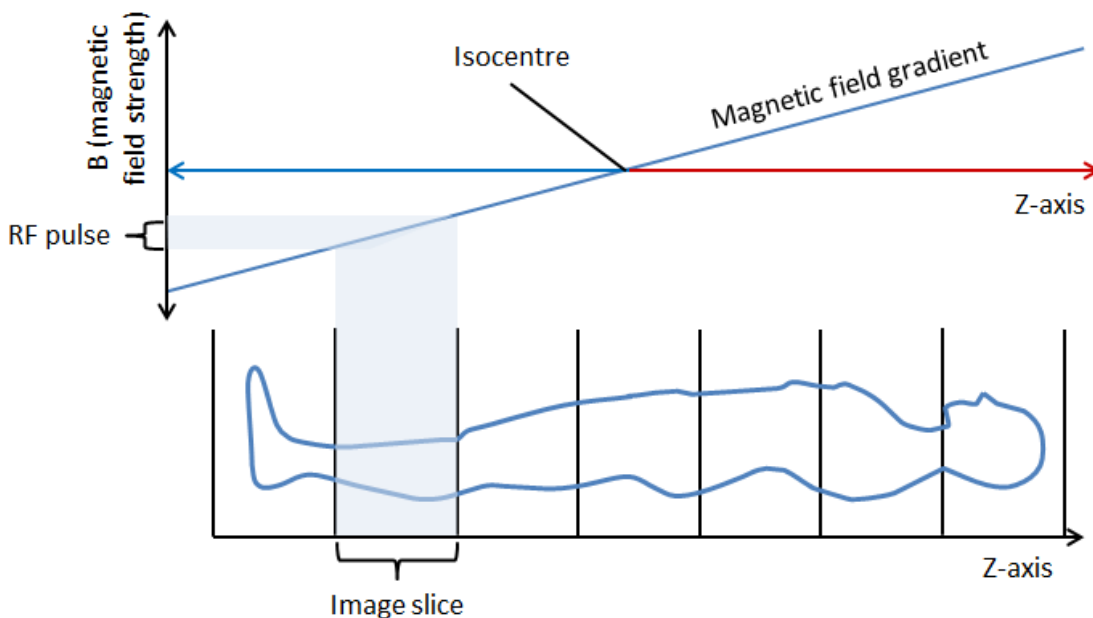
Figure 28. Slice selection (e.g., an axial slice in this instance) involves the application of a linear gradient alone the length of the patient. Reproduced from FRCR Physics Notes (https://www.radiologycafe.com/frcr-physics-notes/).

To further localise the signal in 3 dimensions (generating a grid of pixels within the 2D slice), phase and frequency encoding steps are required.

1.3.4.2 Phase encoding

Following an excitatory RF pulse in the presence of a slice selection gradient (G_s), another gradient is applied. This phase encoding gradient (G_p) causes some spins to accelerate and some to decelerate. When G_p is turned off, this relative

change in phase is encoded within the signal and can be used to partially infer spatial location.

1.3.4.3 Frequency encoding

Following the phase encoding gradient (G_p) a further frequency encoding gradient (G_f) is applied along the readout direction, which causes the precession frequency to vary linearly along that direction and as such, allows spatial encoding within the slice. The frequency encoding gradient is applied for longer than the phase encoding gradient and is applied at the same time as MR signal readout.

1.3.4.4 Spin echo pulse sequence

A basic diagrammatic representation of a pulse sequence for a single RF spin echo with echo planar imaging (EPI) readout is shown in Figure 29. This will be adapted in later sections.
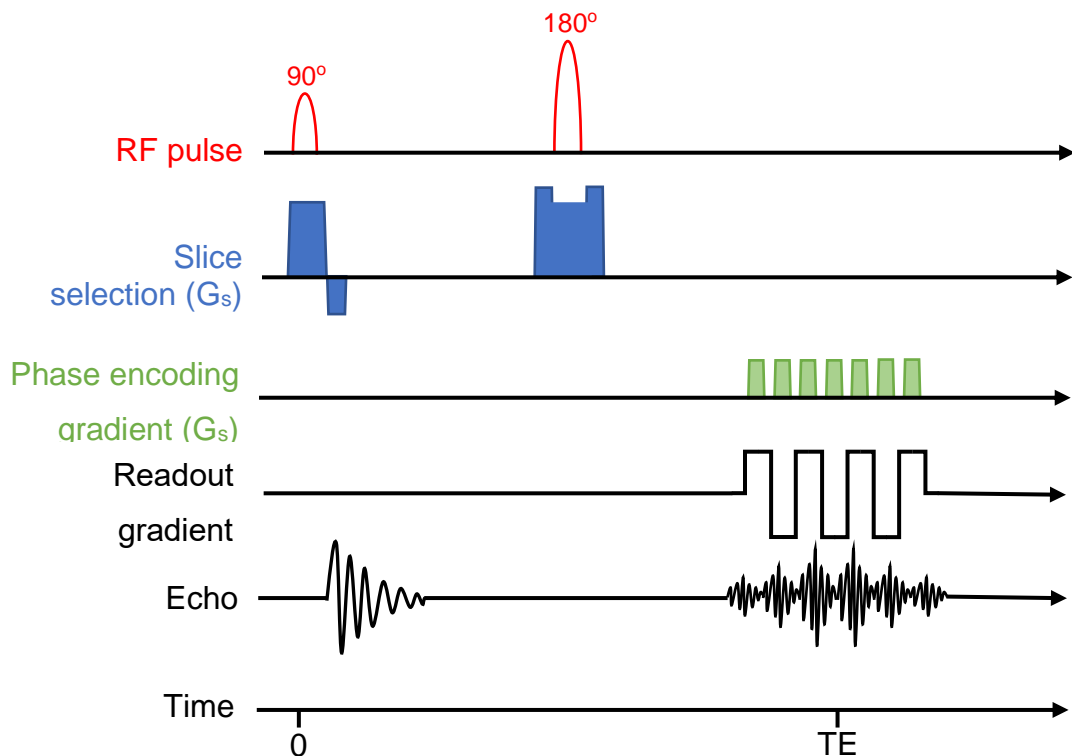
Figure 29. An example of a spin echo pulse sequence. Note that the readout gradient is blipped – this is an echo planar imaging readout gradient – it is a time efficient method of phase encoding a slice (taking a few milliseconds) from a single RF shot.

1.3.5 K-space

Data are typically stored in arrays – multidimensional grids, composed of columns and rows. Cells within an array contain the variables or datapoints. K-space is the name of the space (array) in which spatial frequencies of the MR data are stored. K-space has axes k_x and k_y which correspond to the x (horizontal) and y (vertical) axes. However, points in k-space (e.g., k_1,k_2) do not map one-to-one (i.e. directly) to pixels/voxels in the image domain (e.g., x_1,y_2). Rather, each individual point in k-space contains spatial frequency and phase information about every pixel in the magnitude image. Data in the k-space (k_x,k_y) and image (x,y) domains can be converted back-and-forth using the Fourier and inverse Fourier transformations, respectively, as shown in Figure 30.
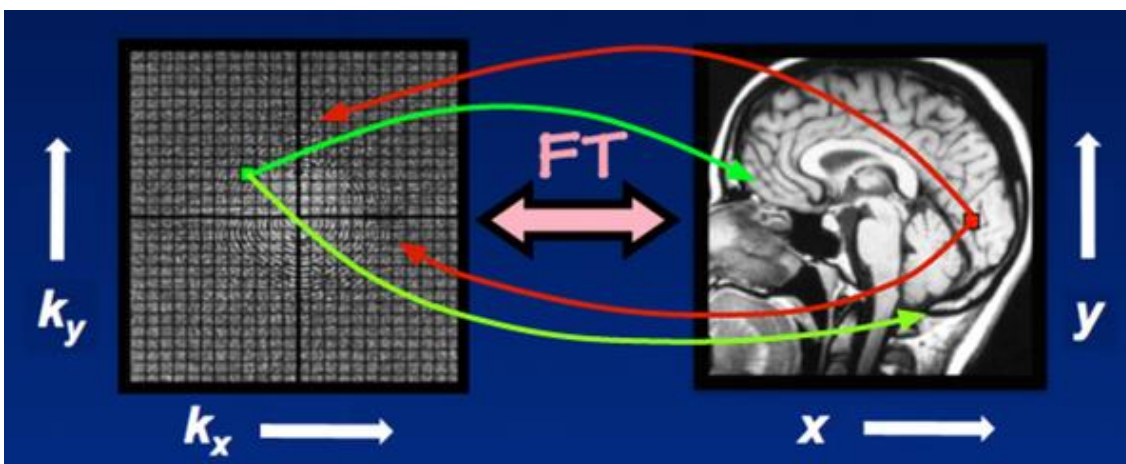
Figure 30. K-space is the domain in which spatial frequencies are stored (left) i.e., it is the spatial frequency domain. These data undergo Fourier transformation to obtain the magnitude image (right) used in clinical medicine. Reproduced from Questions and Answers in MRI (https://mriquestions.com/what-so-k-space.html).

1.3.5.1 K-space filling

Given that k-space is simply a grid, there are several methods of filling the grid (Figure 31) which have their own strengths and weaknesses. These methods are typically divided in Cartesian and non-Cartesian:

- For most 2D MRI acquisitions, k-space data are acquired on a Cartesian grid which facilitates the application of a fast Fourier transformation. The downside of Cartesian sampling is the time required to fill the entirety of k-space as only one line is populated per TR (each pink line in Figure 31

represents a single TR). This means that the scan time is proportion to the number of phase encoding steps.

- Alternatively, k-space may be filled in non-Cartesian trajectories. Generally, these formats of data require regridding for reconstruction. Some non-Cartesian sample techniques (Figure 31) include:
  - o Zig-zig sampling: in this method, the readout gradient is blipped in a long train to complete all phase encoding steps following a single RF pulse. This is known single-shot echo planar imaging (ssEPI) which is very efficient, as all phase-encoding steps can be completed after a single RF pulse. However, EPI is highly vulnerable to susceptibly artefacts and induces other artefacts (discussed in Chapter 5) which are related to the rapidly switching gradients. To reduce such artefacts, k-space can be filled segmentally, using readout-segmented EPI (rsEPI) although this comes with a time penalty whereby each segmentation requires another TR. For example, a rsEPI with segmentation factor of 2 would take twice as long as a ssEPI sequence.
  - o Radial and spiral sampling: these methods of k-space filling (which may be "spiral in" or "spiral out" or a hybridisation) are intrinsically less sensitive to subject motion and permit a shorter TE. However, because the frequency and phase-encoding directions are inseparable, they have unique artifacts, they are more vulnerable to gradient irregularities, gradient mistiming and concomitant field gradients. Moreover, image reconstruction is more complex.
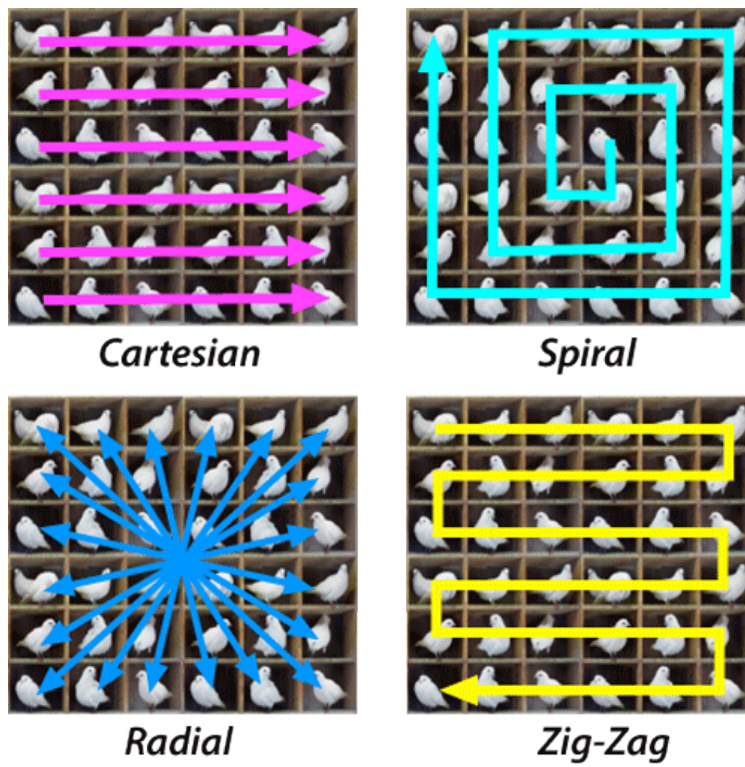
Figure 31. Methods of k-space sampling. Reproduced from Questions and Answers in MRI (https://mriquestions.com/ k-space-trajectories.html).

Chapter 4. Diffusion Weighted Imaging

This chapter provides an overview of diffusion weighted MRI, focussed on techniques used for clinical imaging of the brachial plexus.

1.4.1 Introduction

Diffusion weighted MRI (dMRI) uses the biological principles of diffusion to generate contrast in images. The contrast in dMRI images is based upon relative differences in the macroscopic and microscopic structures of tissues, which ultimately dictate the diffusion pathways. This chapter describes the fundamentals of molecular diffusion, the core elements of dMRI pulse sequences and problems associated with these modalities.

1.4.2 Brownian motion

Diffusion describes the physical random movements of molecules due to thermal collisions. The random flux of particles through space over time is known as Brownian motion and is described by the diffusion coefficient, D. The coefficient of diffusion (D) is related to the root mean squared displacement over a given time and so, typically given in units of area/time, such as mm^2/s. When diffusion is not restricted (for example, within the cerebrospinal fluid around the brain and spinal cord), the displacement profile (D) is Gaussian and described by the Einstein equation (Equation 2):

$$D = \frac{\xi^2}{6\tau}$$

Equation 2. The Einstein equation. ξ is the mean displacement length and τ is the time interval

1.4.3 Tissue anisotropy

Water in the human body is distributed between the intra and extra-cellular compartments in a ratio of approximately 1:3. Pure water has no barriers or hinderances to diffusion and so the diffusion is (very close to) isotropic. However, human tissues have biological barriers, which are typically coherently arranged (e.g., cell membranes, organelles, vascular spaces, etc) and these hinder/restrict

diffusion. Therefore, diffusion in tissues is often anisotropic (Figure 32). The degree of hindrance/restriction is determined by the size, shape and composition of the barriers, and how they are spaced.
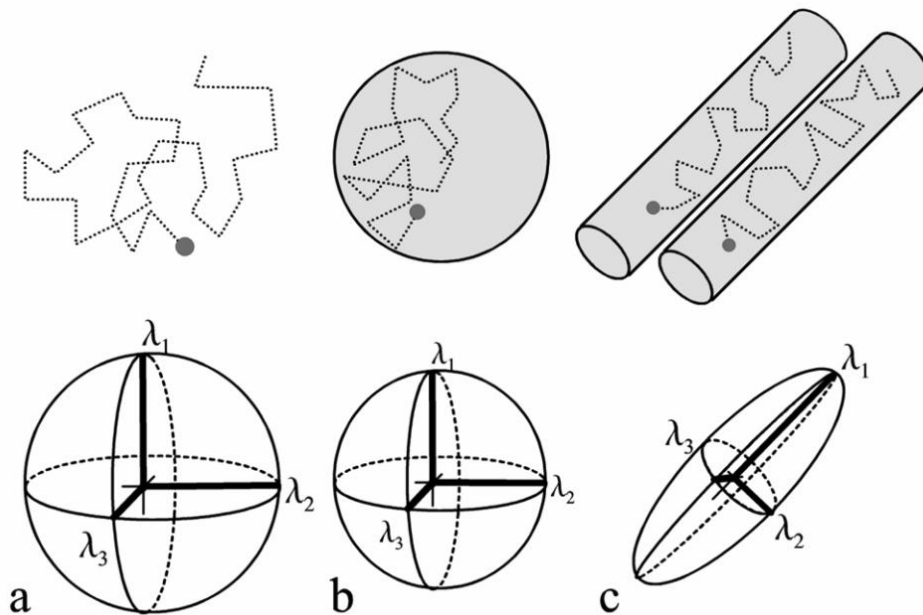
Figure 32. Schematic representation of the diffusion paths for pure water (top left), a viscous solution (top middle) and nerves (top right) with their corresponding diffusion ellipsoids. The eigenvalues (λ_1, λ_2, and λ_3) are oriented along the axes of the respective eigenvectors. Adapted from Heemskerk (2006)[59].

In-vivo measurements of diffusion are subject to fluctuations in temperature and interactions between spins, both of which vary over the diffusion time (Δ). However, Δ is typically very small (milliseconds) in clinical dMRI and so temperature fluctuations are not typically given consideration.

On the other hand, during Δ protons interact and encounter biological barriers, so experiments with longer diffusion times are more likely to sample signal from populations of restricted protons than scans with shorter diffusion times. Therefore, the measured diffusivity is strongly affected by the diffusion time of the sequence. For reasons such as this (and other experimental factors), the measured diffusivity typically differs from the true 'intrinsic' diffusion coefficient of the substance. Therefore, the term apparent diffusion coefficient (ADC) is preferred for describing the flux over space and time.

1.4.3.1 Anisotropy in peripheral nerves

In healthy peripheral nerves, the diffusion of water is highly anisotropic[60]. Several biological structures and processes contribute to the observed anisotropy of diffusion and the non-linear decay of dMRI signal. The degree of anisotropy is sensitive to nerve-specific features (axon type and diameter, the degree of myelination, the density of fibres [i.e. extracellular spacing] and their organisation[61–63]) as well as host characteristics, such as age. Each of these factors have different magnitudes of effect on the dMRI signal and how much they contribute is a matter of ongoing debate. It is difficult to resolve the hierarchical effect of different biological structures and process on anisotropy because obtaining samples of neural tissues from living humans is intrinsically disabling. Therefore, to-date, most studies which have captured both dMRI data and tissue for some form of morphological analysis (e.g., histopathology) are derived from animals, deceased humans or diseased tissues. None-the-less, there is consensus that the axonal membrane and myelin are the major biological contributors to anisotropy.

1.4.3.2 Biological origins of anisotropy in peripheral nerves

The largest contributor to the restriction of water diffusion appears to be the axonal cell membrane itself[60,64]. More to the point, it is the geometry, orientation and density of the axons[63], which influences the observed anisotropy within an imaging voxel. Whilst myelin is not a requirement for substantial anisotropy in peripheral nerves, it does modulate some of the observed anisotropy by hindering the intra-axonal diffusion of water and the effect size appears to relate to the density of the myelin sheath[65,66]. These properties and how they might affect the diffusion of water are summarised in Figure 33.
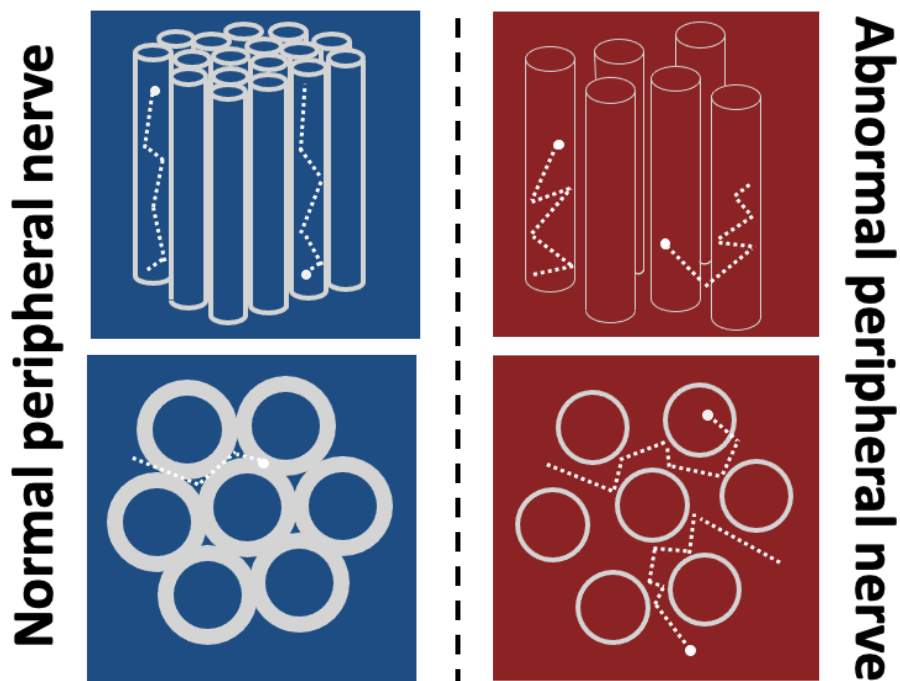
Figure 33. Pictorial representations of healthy (blue) and unhealthy (red) peripheral nerves in both longitudinal (top) and cross-section (bottom). Possible paths of water diffusing are illustrated by a dotted line.

Other nerve-related factors which may contribute to anisotropy. The cytoskeleton of nerves is composed of longitudinally oriented cylindrical neurofibrils (microtubules, Figure 6) which facilitate fast axonal transport and neurofilaments. These longitudinally oriented structures impart non-random barriers to diffusion (Figure 34) and hence reduce diffusion perpendicular ($\perp$) to the axon, such that the coefficient $D(\perp)$ would be less than diffusion occurring longitudinally $D(//)$. Experiments which eliminate these cytoskeletal structures (microtubules) have demonstrated that they have a small but observable effect on diffusion anisotropy[64]. On a related point, the axonal diameter has also been shown to influence the observable anisotropy given that larger axons typically contain more microtubules[67]. To-date, it is unknown whether axon diameter is independent of microtubule density in terms of diffusion antitropy.
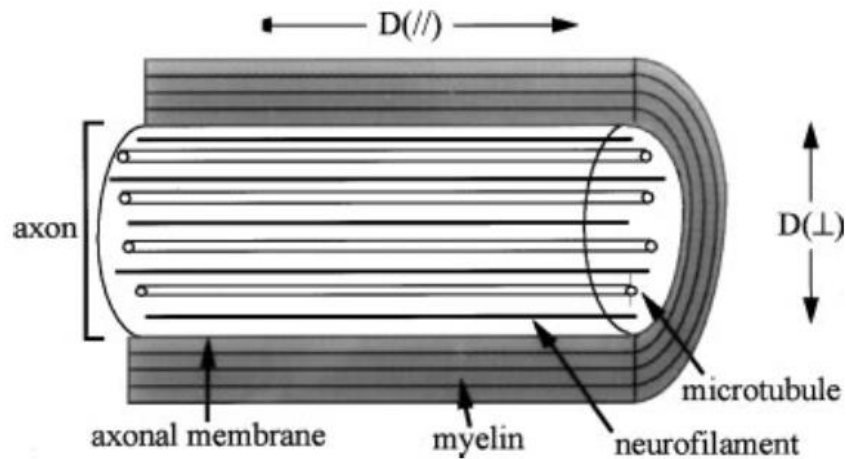
Figure 34. A longitudinal section of an axon showing how the axonal membrane, myelin and microtubules hinder diffusion perpendicular D($\perp$) to the axon, favouring diffusion parallel D($//$) to the fibre orientation. Reproduced from Beaulieu (2002)[60].

In healthy nerves, the perineurium is a highly organised lamellar structure, contributing to diffusion anisotropy. The tight junctions and desmosomes connecting adjacent perineural cells within each layer of perineurium act as a selective diffusion barriers[68–70]. Normally, the perineurium is typically very thin (0.1μm[71]) relative to the size of the axon. Recent work shows that both fibre packing/density (i.e. the amount of perineum or fibrotic tissue around nerves) and the density of cytoskeletal structures play a role in determining the anisotropy of nerves[72].

Other host factors affect the anisotropy of nervous structures. In the brain, anisotropy of white matter tracts increases from infancy through to early adulthood[73], although it is unclear whether this is due to improved myelination or coherence of fibre pathways. The converse occurs in later life whereby white matter tracts have reduced anisotropy, although again the biological/structural origins of this are unclear. This phenomenon has also been observed in peripheral nerves, whereby anisotropy reduced with advancing age; however, dMRI data from the limbs has not been collected from children or the elderly (data only exists for teenagers and adults into their 6th decade of life[74,75]), so limited inferences can be made.

1.4.4   Diffusion sensitisation

Within an external magnetic field, spins are subject to both relaxation and diffusion. For spins with net zero displacement at time т, loss of phase coherence can be reversed, and signal recovered. However, in human tissues water diffusion is hindered / restricted to different extents and in the absence of biological constraints by a cellular structure, diffusion leads to irrecoverable signal loss.

1.4.4.1 Diffusivity

To measure ADC, the most common approach involves the combination of a spin echo and pulsed field gradient. Together, this is known as pulsed gradient spin echo (PGSE), or Stejskal-Tanner diffusion-weighting (Figure 35).
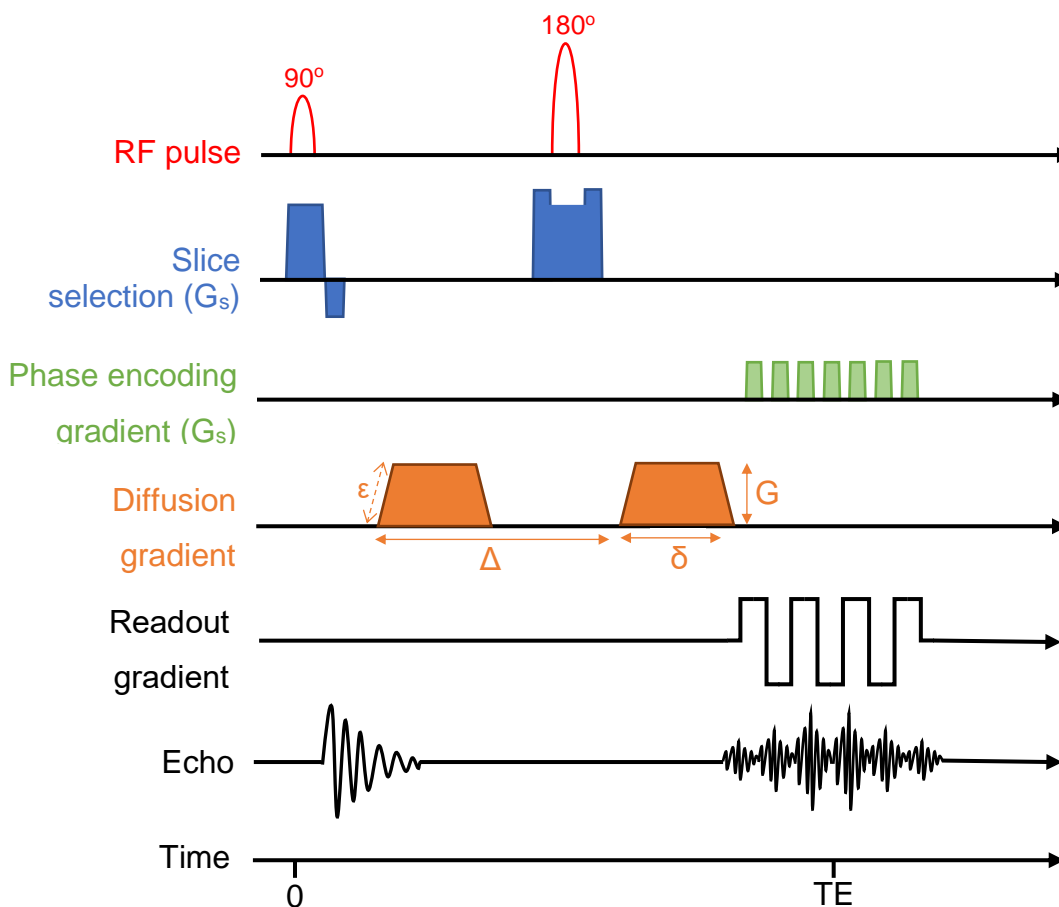
Figure 35. An example of single shot pulsed-gradient spin echo diffusion weighted sequence as described by Stejskal and Tanner. ε = slew time [measured along the x-axis, hence the dotted line], Δ = diffusion time (aka inter-gradient pulse delay), δ = diffusion encoding duration, G = gradient amplitude

The additional diffusion sensitising gradients (Figure 35, shown in orange) phase label spins by location. The 1st diffusion sensitising gradient causes spatially varying dephasing of spins (Figure 36). Spins with net zero displacement over the diffusion time (Δ) will be rephased by the 2nd diffusion sensitising gradient. Conversely, populations of spins which are not restricted/hindered will move (e.g., by diffusion, perfusion, etc) during the diffusion time and therefore not be rephased by the 2nd gradient, resulting in signal loss.
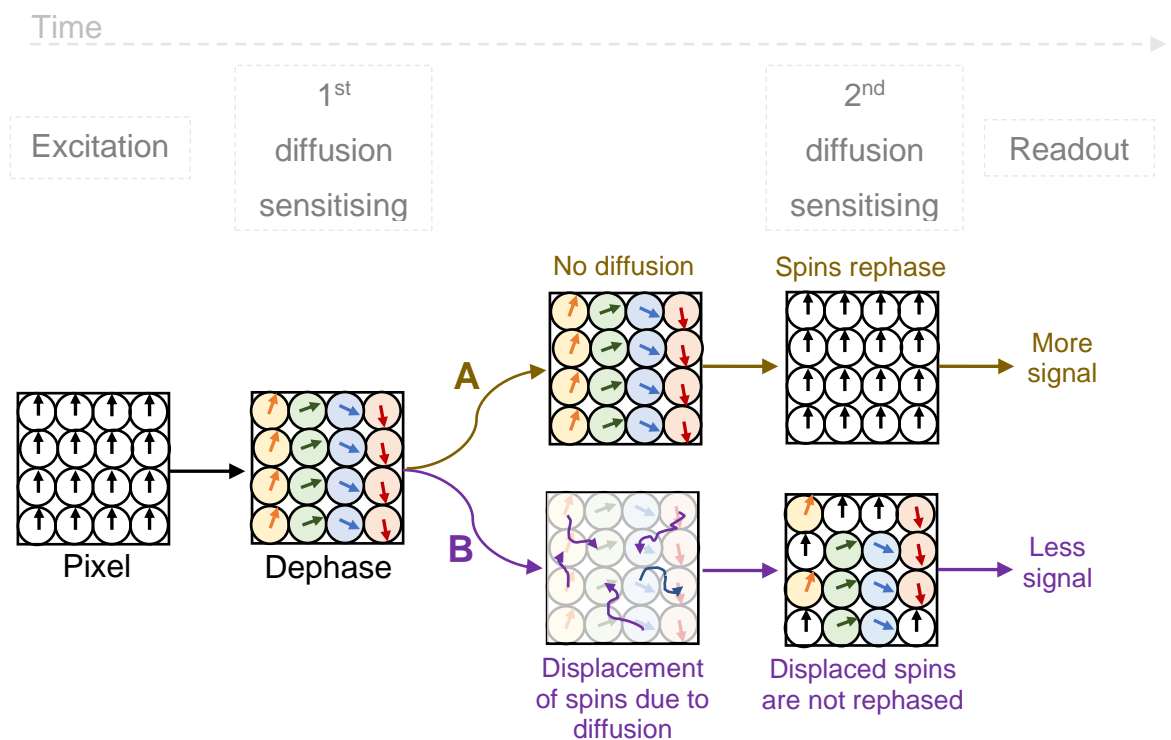
Figure 36. A graphical representation of a pixel containing a population of spins within a straight nerve. The 1st diffusion sensitising gradient causes spatially varying dephasing, shown by different colours. In A, the diffusion gradient is applied perpendicular to the long axis of the nerve (diffusion is restricted radially), so less displacement occurs and so more signal is recovered by the 2nd rephasing gradient. In B, the gradient is applied orthogonal to the nerve; as water can diffuse freely bidirectionally in the nerve, there is relatively more displacement during the diffusion time, spins experience a different field with the 2nd gradient, and there is incomplete rephasing, causing signal loss. Adapted from Mori & Zhang (2006)[76].

This method enables contrast to be generated across a spectrum of hinderance to diffusion. Importantly, these diffusion sensitising gradients can be applied in any direction and so, information about hinderance/restriction can be gathered in 3 dimensions.

1.4.4.2 b-value

The dMRI signal which is measured is related to both the diffusivity of the tissue and the amount of diffusion sensitisation applied. The amount of diffusion sensitisation is related to the strength of the applied gradient (or amplitude [G]), how quickly it is applied and removed (the slew time, ε) and duration of its application as shown in Figure 35. For PGSE, these values can be converted into a single metric which summarises the 'amount' of diffusion sensation, known as the b-value (b, Equation 3) which is measured in seconds per area (s/mm^2).

$$b - value, b = \gamma^2 G^2 \left(\delta^2 \left[\Delta - \frac{\delta}{3} \right] + \frac{\varepsilon^2}{30} + \frac{\delta \varepsilon^2}{6} \right)$$

Equation 3. Calculation of the b-value (b), whereby γ is the gyromagnetic ratio, G is the gradient amplitude, δ is the gradient pulse duration, Δ- δ/3 is the diffusion time (also known as the inter-gradient pulse delay) and ε is the gradient slew time.

1.4.4.3 dMRI signal is non-Gaussian

The decay of dMRI signal intensity (S) is non-Gaussian in human tissue. That is the signal attenuation in relation to b-value used does not follow a mono-exponential model. This reflects the biological heterogeneity of tissues whereby the diffusion displacement of water is different (typically slower) within tissue than pure water, and further hindered/restricted by barriers, compartments and other molecules. As such, the diffusion within tissues is described as having a positive diffusion kurtosis (K>0).
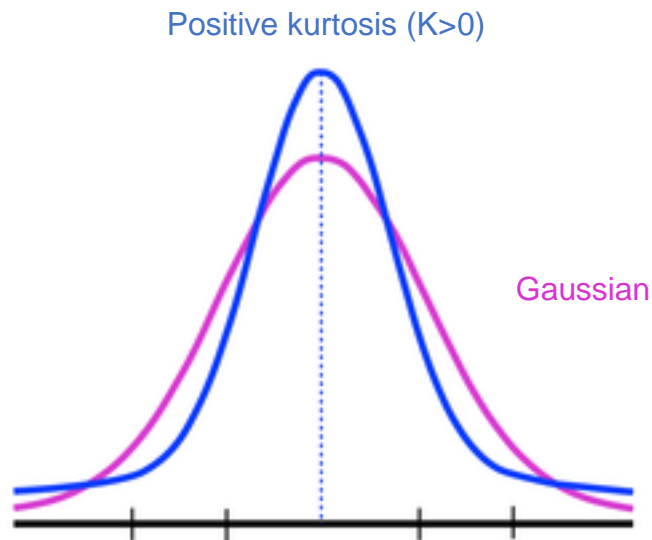
Figure 37. A probability distribution showing the displacement of water in a fixed period of time. Pure water would exhibit Gaussian diffusion. The diffusion of water in tissues exhibits positive kurtosis

Depending on the application, at very low b-values (<300 s/mm^2) signal attenuation may be greater (and the calculated ADC higher) than expected due to intra-voxel incoherent motion (IVIM, Figure 38). As such, very low b-values are rarely used (alone) to explore diffusion in clinical MRI. Between b-values of approximately 300-1000 s/mm^2 diffusion is described as hindered, because it typically follows a Gaussian displacement pattern. At larger b-values (≥1000 s/mm²) the signal attenuation (S) is less than expected due to the non-Gaussian (kurtotic) nature of the diffusion probability distribution (Figure 37). This is largely due to diffusion occurring within the intra-cellular space, bounded by axonal cytoplasmic structures and cell membrane
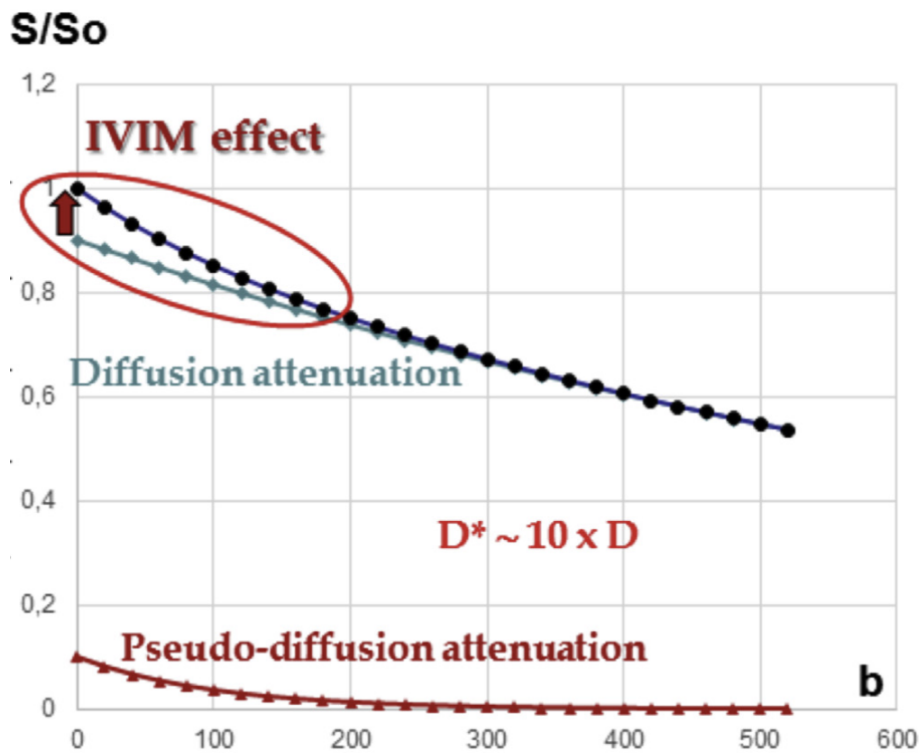
Figure 38. Signal attention (S) in relation to b-value (s/mm^2).
Reproduced from Le Bihan (2019)[77].

1.4.5 Q-space

Q-space is conceptualised as the limitless 3D space (x, y, z) used to record and model diffusivities derived from dMRI experiments. Typically, diffusivity (analogous to the diffusion coefficient) is measured in multiple directions per voxel and recorded as a function of displacement in the x, y and z planes. From this, mathematical models (such as the tensor, Figure 39) can be used to describe the shape of the diffusion displacement.
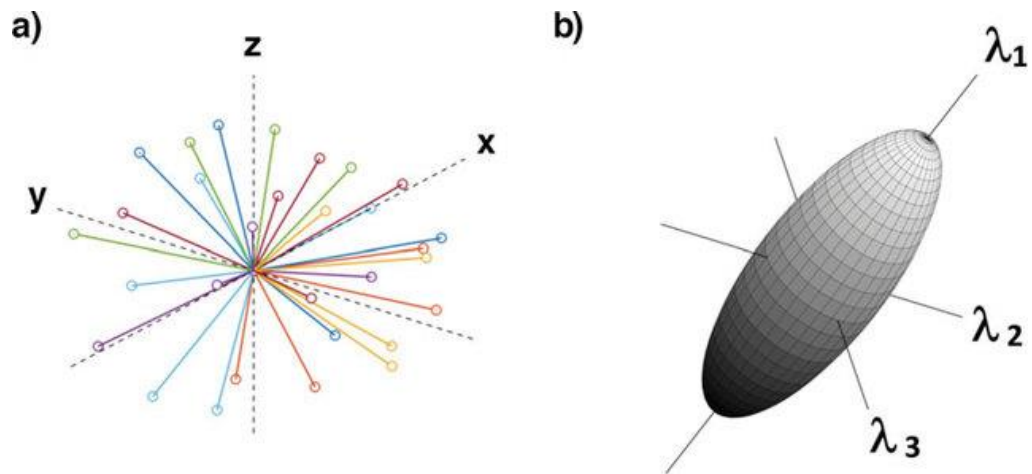
Figure 39. Graphical representation of dMRI data recorded in q-space (a) whereby each colour represents a unique direction of diffusion encoding (in the x, y, z planes) and the length of the vector is proportional to the diffusion displacement (diffusivity). In panel b, these

Furthermore, q-space can be sampled in different ways. The below graphic (Figure 40) shows an example of shell sampling of diffusion within 'q-space'. Sampling can also be free/random in q-space, according to some maximum parameters specified and this is discussed in more detail in Chapter 8.
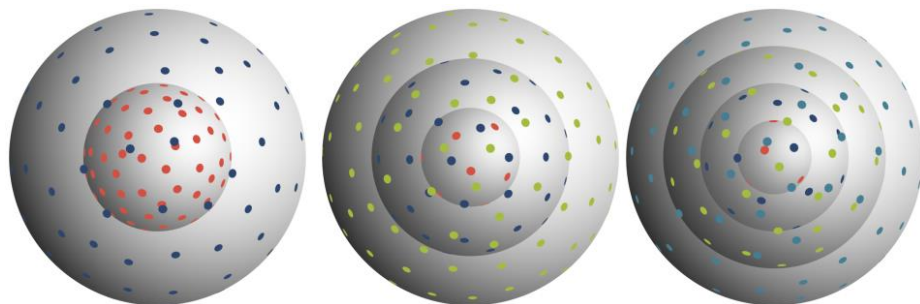
Figure 40. Sampling of q-space using 2 (left), 3 (middle) and 4 (right) distinct 'shells'. Each dot represents a unique vector of sampling. The inner shell (red) has the shortest diffusion time and so is sensitive to less restricted spins. Each successive shell typically has a longer diffusion time meaning that they are sensitive to more hindered or restricted spins e.g., intracellular water. Using the diffusivities measured at each point on the sphere, from each shell, the underlying microstructure can be inferred.

Chapter 5. Artefacts associated with dMRI

The use of EPI offers a rapid method of filling k-space after a single excitation and so, it is very appealing for dMRI. However, the use of rapidly alternating gradients (the EPI readout) over a long echo train generates several artefacts which are described and discussed below.

1.5.1 Noise

As dMRI signal is dependent on loss of phase coherence within voxels, the signal to noise ratio (SNR) can be problematic, especially in the neck where coil coverage is challenging. Signal attenuated is caused by diffusion sensitisation and T2 decay (due to the long echo times necessary to accommodate the diffusion gradients), so dMRI has an inherently low SNR. Consequently, low SNR can corrupt dMRI measurements. It is well accepted that low SNR upwardly biases estimates of FA[78] and underestimates diffusivity[79]. Simulations[80] suggest that an SNR in non-diffusion-weighted images should exceed 10 to reduce such bias[81] although in reality, a much greater SNR is desirable and other factors (such as the b-value) must be considered.

1.5.2 Susceptibility artefacts

Susceptibility describes the extent to which a tissue is magnetised within an external magnetic field (B_0). Materials that oppose the external magnetic field are described as diamagnetic (Figure 41). Materials that concentrate the field are paramagnetic, or ferromagnetic, depending on the magnitude of effect. Materials with these effects can cause signal loss from T2*-dephasing and spatial mismapping. These in turn cause susceptibility-induced changes in the B_0 and spatially vary the b-value.
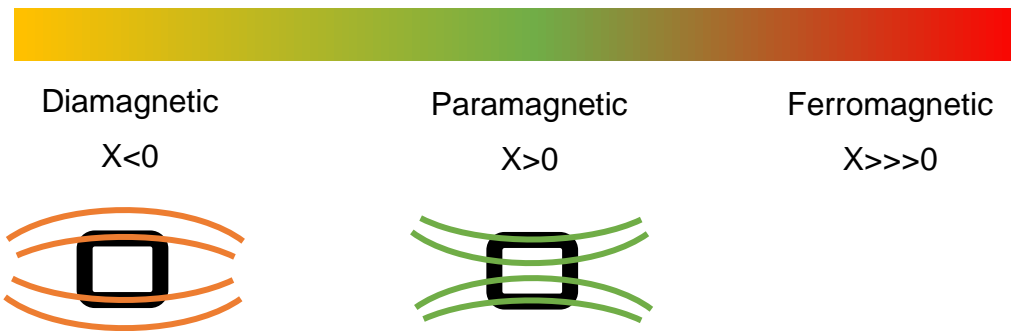
Figure 41. Graphical representation of the effect of diamagnetic (oppose/reduce the local magnetic field), paramagnetic (concentrate/add to the local magnetic field) and ferromagnetic substances.

Susceptibility artifacts are an inherent problem of single-shot echo-planar imaging sequences (ssEPI), which are typically used for dMRI experiments. This is largely due to the low bandwidth of the blipped phase-encoding gradients which enable k-space to be filled within a single TR. However, the low bandwidth phase-encoding gradients which are needed for fast imaging mean that small changes in the static magnetic field and the susceptibility of tissues can have large effects in the spatial mapping of signal. For this reason, susceptibility artefacts change in shape when the direction of the phase-encoding (and implicitly, the frequency encoding direction) are changed. Also, the shape and intensity of the artifact depends on anatomic relationships, field strength, difference in susceptibilities, the TE and bandwidth. Examples of susceptibility artefacts around the brain and neck are shown in Figure 42 and Figure 43, respectively.
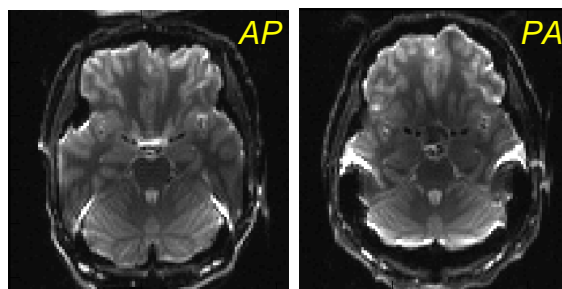
Figure 42. An axial slice through a brain taken with the phase encoding direction as anterior-to-posterior (AP, left) and posterior-to-anterior (PA, right).

In relation to the brachial plexus, there are several interfaces between nerves, air and bone which can induce distortions (Figure 43). Air is slightly paramagnetic so the interface between the 1st thoracic spinal root and the apex of the lung can distort data. Conversely, calcium within bones is diamagnetic so the interface between and the plexus and the 1st thoracic rib can again induce distortions.
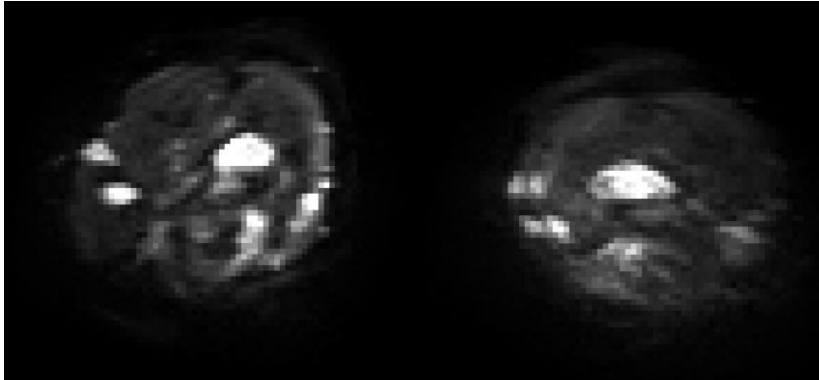
Figure 43. b0 axial slices through the neck taken with left-to-right (left) and right-to-left (right) phase encoding, using a single shot echo planar imaging sequence.

1.5.3 Eddy-currents

To acquire dMRI, magnetic field gradients are rapidly changed which in turn, according to Faraday's Law, induces a current (Figure 44). These eddy currents are unwanted, decay the magnetic fields and perturb desired gradients causing errors in k-space sampling. This results in geometric distortions and ghosting in the image.
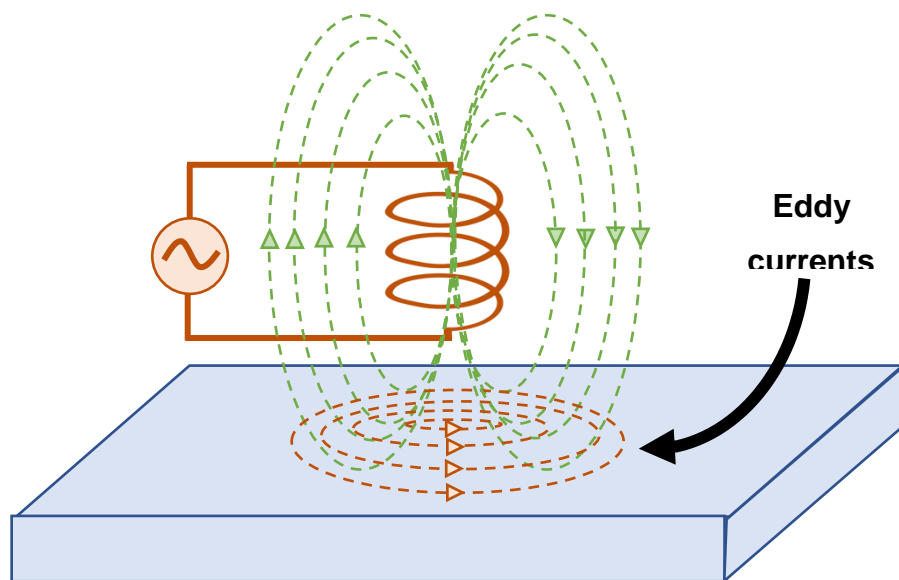
Figure 44. Eddy currents induced by an alternating current in a coil.

In clinical MRI, eddy currents may be induced in any metallic component of the scanner, devices within or on the patient or the patient as a whole. Importantly, eddy currents can cause peripheral nerve stimulation and heat tissues. These are typically limited by limits prescribed by the scanner software. The magnitude of the eddy currents depends on the rate of change of the magnetic field, so they are particularly problematic in dMRI and may induce image artefacts, such as Nyquist ghosts (Figure 45).
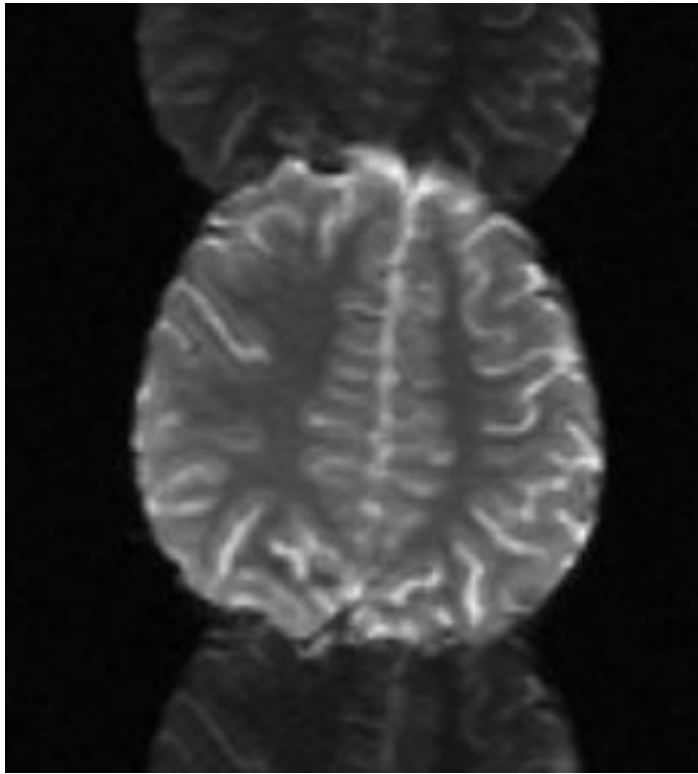
Figure 45. Nyquist ghosts of the brain

Eddy currents cannot be eliminated entirely but can be reduced by slowing the gradient slew rates, using gradient pre-emphasis and with specific pulse sequences, such as the 'bipolar' waveform shown in Figure 46.
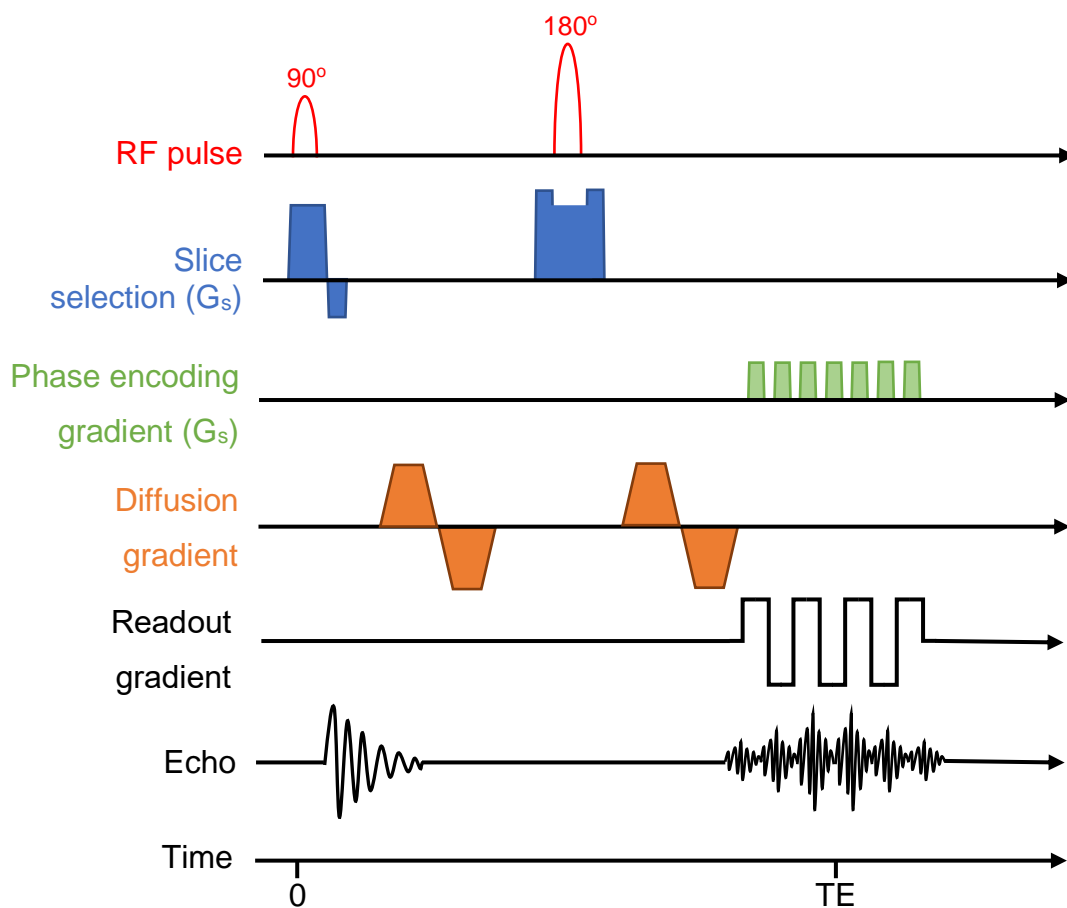
Figure 46. A modification to the Stejskal-Tanner pulse sequence with a bipolar diffusion sensitising waveform (orange).

1.5.4 **Motion**

The need to acquire numerous DW images means that dMRI experiments typically last several minutes. During such experiments, subject motion cannot be avoided. In the neck, there are several different sources of subject motions which are common. Voluntary movement due to positional discomfort is frequently seen in the form of neck forward/backward flexion – the head coil limits lateral flexion and rotation, so this is the plane in which motion is observed. The bore the scanner is air conditioned and so subject typically develop dry lips, necessitating lip licking which is often associated with bulk movement of the jaw and neck. As saliva is constantly produced, subjects must swallow which generates intrinsic neck muscle movement too. Motion related distortions arising from breathing and large vessel dilation/contraction are also captured in the neck.

Chapter 6. Pre-processing dMRI data

Pre-processing of dMRI data is a multi-step process concerned with correcting geometric and signal distortions (Figure 47). The aim is to minimise false negatives without increasing false positives in the post-processing (analysis) phase.

Figure 47. An overview of dMRI artefacts and (pre-processing) methods of correcting them. Reproduced from Tax et al (2022)[82].

It is widely accepted that attempts should be made to correct artefacts associated with dMRI before analysis. This is because pre-processing improves the accuracy of dMRI metrics and tractography (described in detail in Chapter 9)[83]. To achieve this goal, there are numerous potential steps and several different software

packages. Table 6 summarises the most commonly cited software packages for pre-processing of dMRI, with their own potential advantages, limitations and difficulties from the perspective of the user.

This chapter focuses on the most prevalent pre-processing techniques. These steps are described in the order in which they are typically performed[84]. However, it should be noted that there is still considerable uncertainty about the 'best' pipeline, which encompasses the order, requisite steps, the methods for each step and their respective settings. Consequently, the ISMRM diffusion study group is currently running an international collaborative study to address the heterogeneity of practice within the field. This study is capturing the typical practices of users worldwide regarding their pre-processing pipelines and will ultimately describe how this heterogeneity of practice effects the output dMRI metrics and tractography from a set of standardised multishell dMRI scans from the brain.

Features		MRtrix	ExploreDTI	DSI Studio	FSL	TORTOISE
						Software packages
	Graphical user interface	✗	✗	✓	✓ (limited)	✗
	Software dependencies		MATLAB	None	None	None
Compatible Operating Systems	Windows	✓	✓	✓	✓ (via a WSL or virtualisation)	✓
	Mac	✓	✓	✓	✓ (limited)	✓
	Linux	✓	✓	✓	✓	✓
Available pre-processing options	Denoise	✓ (MP-PCA[85])	✗	✗	✓ (SUSAN[86])	✓ (DIFFPREP[87])
	Susceptibility correction	✓ (using FSL's TOPUP[88])	✓	✓	✓ (TOPUP[88])	✓ (DIFFPREP[87])
	Eddy current correction	✓ (using FSL's eddy[89])	✓	✓	✓ (eddy[89])	✓ (DR-BUDDI[90])
	Outlier replacement	✓ (using FSL's eddy/repol[91])	✗	✗	✓ (eddy[89]/repol[91])	✗
	Slice-to-volume motion correction	✓ (using FSL's eddy/mporder[92])	✗	✓	✓ (topup and eddy_cuda /mporder[92])	✓ (DR-BUDDI[90])
	Susceptibility-by-movement correction	✓ (using FSL's CUDA version of eddy[93])	✓	✗	✓ (eddy_cuda/ susceptibility_by_movement[93])	✗
	Gibbs ringing correction	✓ (local subvoxel-shifts[94])	✗	✗	✗	✓ (DIFFPREP[87])
	Signal drift	? (dwicat scales signal intensity between volumes)	✓	✗	✗	✗
	Registration	✓ (using FSL's FLIRT)	✓	✓	✓ (FLIRT/epi_reg/FNIRT)	✓ (DIFFPREP[87])
	Quality assessment	✓	✓	✓	✓ (eddy_qa)	✗

Table 6. Software pipelines for pre-processing dMRI data and their functions at the time of writing.

1.6.1 Denoising

Dealing with noise is an important and longstanding problem in dMRI preprocessing. Consequently, there are numerous mathematical methods available.

Historical approaches dealt with spatially varying and non-Gaussian noise by using weighted averages of voxels. However, this typically caused loss of spatial resolution and introduces partial volume effects. Consequently, denoising was not widely performed in dMRI experiments until recent advances were made.

Modern techniques are based upon the concepts of principal component analysis (PCA) - most signal-related variance is contained within a few components of the image, whereas noise is spread over all components. Equally, noise-only eigenvalues should follow the universal Marchenko-Pastur law as a result of the random matrix theory for noisy covariance matrices. Therefore, the latest approaches for denoising dMRI datasets are based upon MP-PCA[85].

MP-PCA denoising is deployed in the open-source MRTrix3 package, via the *dwidenoise* command. After application of the algorithm, the SNR of the b0 images in adult healthy brains is typically increased by 77% to 201%, without loss in accuracy[85].

1.6.2 Correcting susceptibility artefacts

There are several methods for correcting susceptibility artefacts but the TOPUP[88] tool within the FMRIB suite[84] is the most popular approach. TOPUP takes either a field map acquired at the time of scanning, or blip-up blip-down b0 data (b0s opposing phase-encoding directions) with all other parameters held constant. From these datasets (alongside other user input information, such as the readout time) TOPUP estimates the off-resonance field and unwarps the b0(s), as shown in Figure 48 and Figure 49.
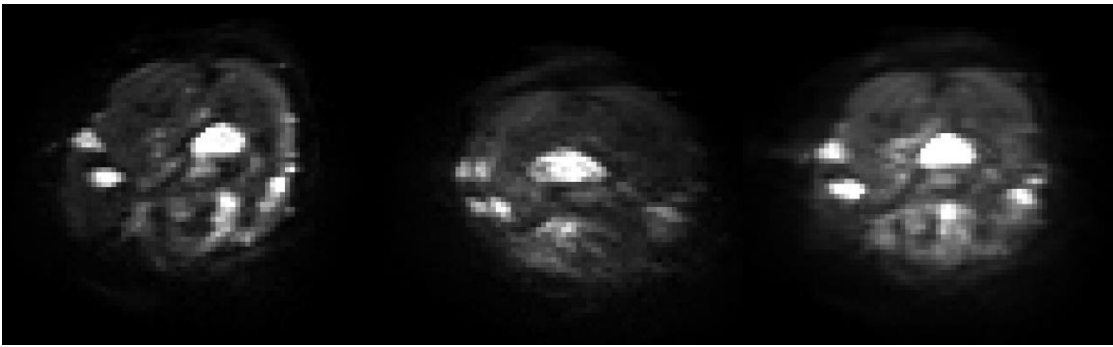
Figure 48 The same slice through the neck taken with the phase encoding direction as left-to-right (left) and right-to-left (middle). From these, an average b0 is generated (right).
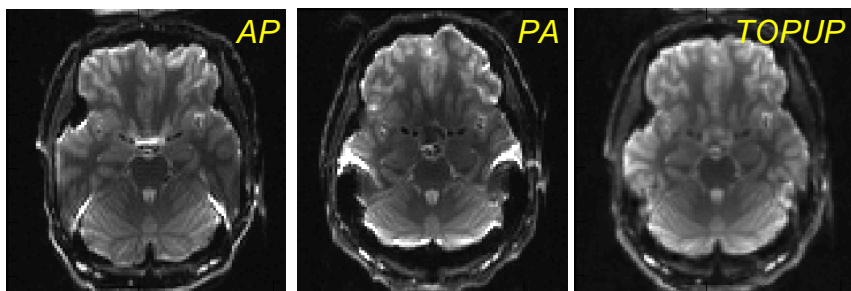
Figure 49. One axial slice through the brain taken with the phase encoding direction as anterior-to-posterior (AP) posterior-to-anterior (PA). From these, an average b0 is generated (TOPUP).

Recent iterations of TOPUP incorporated a motion-correction module that simultaneously estimates subject motion and more accurate methods of concatenating data with severe distortions.

1.6.3   Eddy-currents, motion, empty planes and signal drop-out

The most common tool for correcting artefacts arising from eddy-currents is *eddy* within the FMRIB suite[84]. The original version was release in 2016[89] and this sought to incorporate the outputs of TOPUP (estimations of the susceptibility induced off-resonance field) to correct both susceptibility artefacts and eddy-current induced distortions. Since then, there have been several updates to *eddy* and it can now also: perform motion correction, detect outlier slices and replace them with predictions made by the Gaussian Process and interpolate empty planes. Some of these processes are computationally intensive so are hardware dependent. None-the-less, the core elements are widely adopted and have also

been assimilated into several other open-source software packages, such as MRtrix via the *dwipreproc* command.

To correct motion and eddy-current induced distortions, *eddy* has the same requirements of TOPUP but make further recommends about how diffusion is sampled, including:

1. Diffusion should be sampled across the whole sphere. Whilst both half and whole sphere approaches sample diffusion in the same way (and interchangeable vector schemes can be created from either starting point), half sphere sampling does not facilitate eddy-current correction (Figure 50).
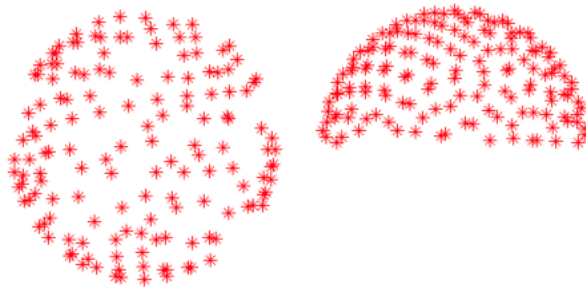
Figure 50. Diffusion sampled in q-space across the whole sphere (left) versus half sphere (right). Both have the same number of unique directions (vectors).

2. When the experiment can accommodate >120 diffusion directions, rather than acquiring many unique vectors, in one phased encoding directions (most of which will be redundant) and then using reversed b0s alone to correct eh field, acquire full DWI datasets (each with >60 directions) in opposing phase encoding directions. This approach enables the best estimation of the field(s) caused by eddy-currents whilst simultaneously improving SNR and providing sufficient angular sampling for most modelling approaches downstream.

3. Acquire interleaved b0s throughout the DWI acquisition. This approach best exploits *eddy's* motion correction modules.

Uniquely, eddy also corrects the b-table and outputs a corrected vector scheme.

Alongside these corrections, eddy provides optional extra functions, which include

- Motion correction: there are several modules which the FMRIB suite which seek to correct motion artefacts in synchrony, embedded within both TOPUP[88] and eddy[89]. Within TOPUP, the susceptibility induced field due to motion is estimated from data acquired in opposing phase-encoding directions (given that the field dependence on pitch and roll is linear). The observed variance, after correcting for gross movement and eddy currents, generates a unique susceptibility induced field for each volume. This is passed to the --susceptibility_by_movement[93] option within eddy and complements the slice-to-volume motion correction (--mporder[92]) function.

- Filling empty planes (--fep) which populates empty planes (in the reconstructed EPI images) by duplication if the previous plane is perpendicular to the frequency encode direction, or by interpolation between the previous and the wrap-around plane if perpendicular.

- The detection of outlier slices (defined as >4 standard deviations lower than the expected intensity) and replacement with predictions made by the Gaussian Process. This is enabled via the --repol[91] option.

1.6.4 Registration

As dMRI images are inherently distorted, and typically have worse spatial resolution and contrast than anatomical images, so registering dMRI datasets to non-distorted images is desirable. This ensures that regions of interest in the dMRI maps correspond to anatomy and indeed, the same region can then be interrogated on other images once images are registered.

Registration is the mathematical transformation into a common coordinate system. The process of image registration can be manual (specifying a model), semi-automated (a transformation is proposed and previewed for the user to adjust) or wholly automatic. Registration methods are typically categorised as rigid or non-rigid (affine or elastic, Figure 51).
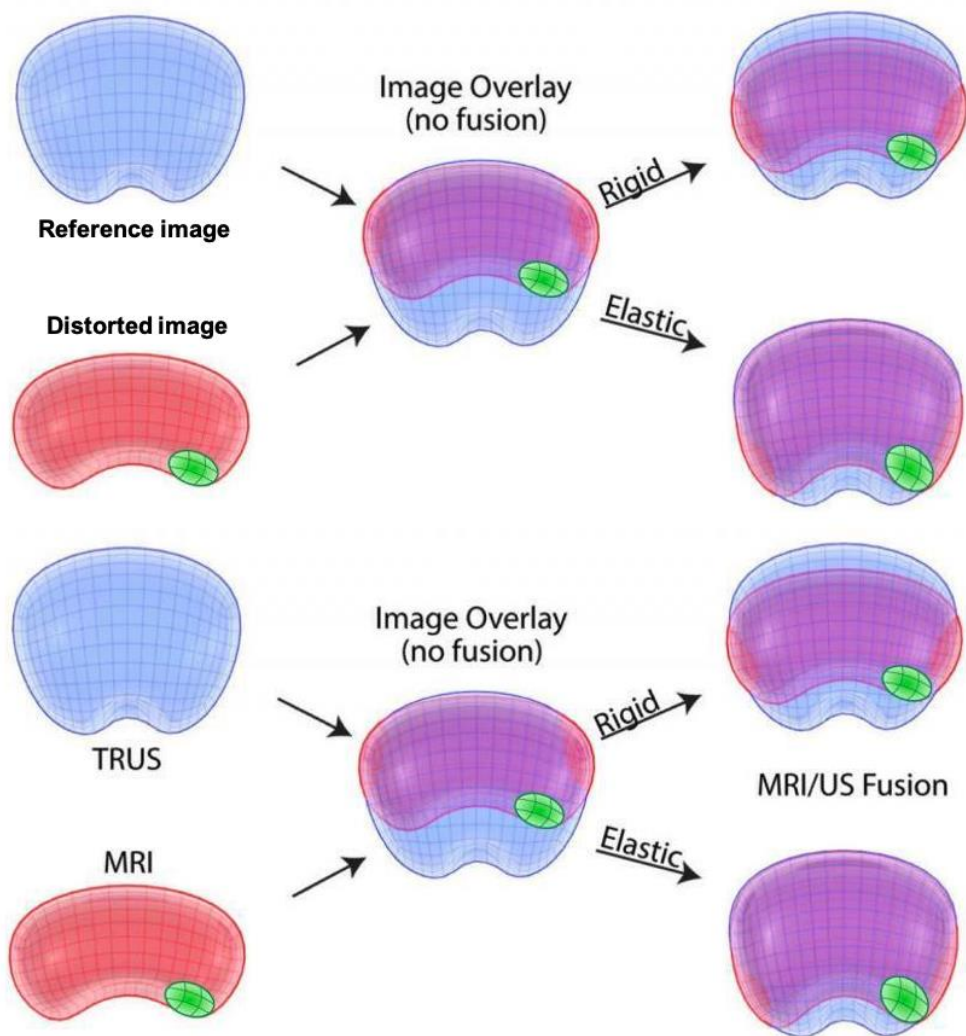
Figure 51. Examples of rigid and elastic image registration.
Modified from Logan et al (2014)[95]

Rigid transformation is used when geometric distortions are minimal or absent, as this allows for rotation and translation only. For a 3D dataset, there are 6 degrees of freedom in a rigid transformation, namely 3 axes of rotation and translation.

Affine registration methods allow for rotation, translation and scaling which corresponds to 9 degrees of freedom in a 3D dataset. Affine registration can also incorporate a 4th transformation, namely skew and this combination is sometimes referred to as elastic transformation. In a 3D dataset, affine transformation with scalings and skew has 12 degrees of freedom.

Chapter 7. Post-processing: The Diffusion Tensor

Post-processing describes the steps taken to mathematically model dMRI data for the purposes of estimating the preferred directions(s) of diffusion (orientation) and the molecular diffusion rate. As diffusion is anisotropic in tissues, it is useful to understand its 3D orientation such that inferences at the microstructure can be made. There are several mathematical methods available for modelling dMRI signal to estimate diffusivity, orientation and dispersion which are summarised and discussed below.

1.7.1 Tensors

There are numerous mathematical methods for modelling the complexities of diffusion in biological tissues, but the diffusion tensor[96] is the most common and widely used. The diffusion tensor is a 2nd order tensor that can be described as a 3x3 symmetric matrix, as shown below:

$$D = \begin{bmatrix} D_{xx} & D_{xy} & D_{xz} \\ D_{yx} & D_{yy} & D_{yz} \\ D_{zx} & D_{zy} & D_{zz} \end{bmatrix}$$

When diffusion is perfectly random (isotropic) the diagonal elements are all equal and the off-diagonal elements are zero, so a single diffusion coefficient (D) represents the overall diffusion tensor:

$$D_{isotropic} = \begin{bmatrix} D & 0 & 0 \\ 0 & D & 0 \\ 0 & 0 & D \end{bmatrix}$$

However, as diffusion in tissues is anisotropic the diagonals are unequal, and off-diagonals must be considered. Given that the diffusion tensor model assumes symmetry, mirror off-diagonals are equal (i.e., $D_{xy}=D_{yx}$, $D_{zy}=D_{yz}$, etc) and so there are 6 unique coefficients which must be estimated. Therefore, a minimum of 7 measurement are required which classically includes at least one b0 (a non or low diffusion-weighted image) and at least six non-collinear diffusion-weighted images. After processing, the tensor (Λ) is derived by regression, usually least-squares linear regression:

$$\Lambda = \begin{bmatrix} \lambda_1 & 0 & 0 \\ 0 & \lambda_2 & 0 \\ 0 & 0 & \lambda_3 \end{bmatrix}$$

The tensor can be graphically shown as a diffusion ellipsoid. In the context of dMRI data captured from a hypothetical nerve (Figure 52). The resultant glyph is an ellipsoid (Figure 53) which implies anisotropic diffusion.
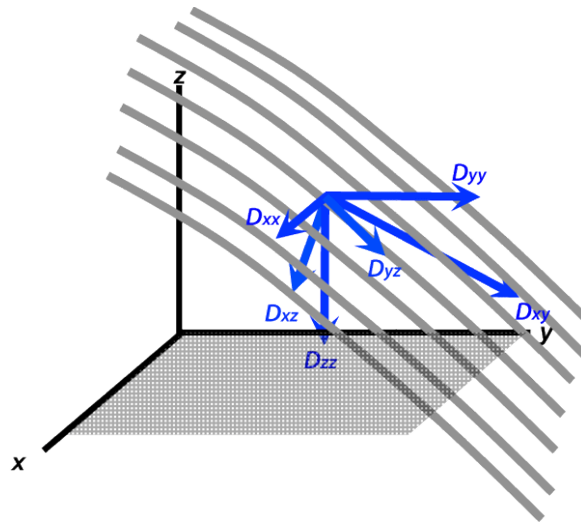
Figure 52. The curved lines represent axons of a nerve within a x-y-z frame of reference. Six unique diffusion coefficients (D_{xx}, D_{xy}, D_{xz}, etc) are measured to calculate the diffusion tensor. Reproduced from http://www.mriquestions.com
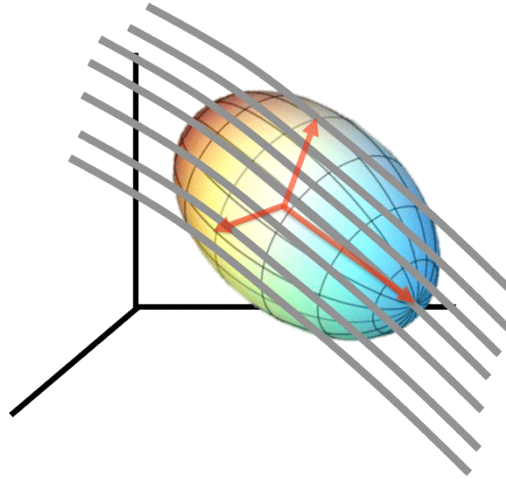
Figure 53. The above graph (and tensor) is simplified to the ellipsoid model whereby the long axis is parallel to (the tangent of) the principal direction of diffusion. Reproduced from http://www.mriquestions.com

The component eigenvalues (ε) and eigenvectors (λ) are superimposed on the glyph in Figure 54 to demonstrate their relationship to the ellipsoid.
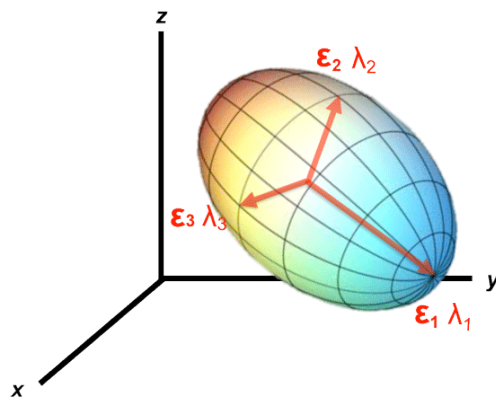
Figure 54. In the ellipsoid model of the diffusion tensor, the directions of diffusion are reduced to three vectors (ε_1, ε_2 and ε_3) which are termed principal eigenvectors each of which have a unique value/length (λ_1, λ_2 and λ_3) known as principal eigenvalues. Reproduced from http://www.mriquestions.com.

1.7.1.1 Apparent diffusion coefficient (ADC)

By holding all other parameters (TE, TR, etc) constant but varying the diffusion-weighting of the MRI experiment, it is possible to calculate the diffusivity of tissues, or more precisely the apparent diffusivity (ADC, as discussed earlier, Equation 4). The experimental time (Δ, the diffusion time) and the biological barriers to diffusion within the tissue of interest determine the coefficient of diffusion, D. Therefore, apparent diffusivity can be estimated from differently weighted images. In this way, the difference in signal attenuation in a given voxel between a b0 image and diffusion-weighted image is the apparent diffusivity.

$$ADC = \frac{ln\left(\frac{S_2}{S_1}\right)}{b_1 - b_2}$$

Equation 4. The apparent diffusion coefficient (ADC, aka trace) is related to the signal intensity in a given voxel, measured at b-values of b_1 and b_2

1.7.1.2 Mean diffusivity

Modern approaches to estimating diffusivity obtain DTI (DWIs from at least 6 non-collinear directions, or more) which estimate the size of the average diffusion tensor ellipsoid. This is done by averaging the eigenvalues (λ_1, λ_2 and λ_3) which gives a mean apparent diffusion coefficient, shortened to mean diffusivity (MD, Equation 4). This metric is typically measured in mm^2/s and typically displayed in units of x10^{-3}.

$$MD = \frac{(\lambda_1 + \lambda_2 + \lambda_3)}{3}$$

Equation 5. The mean apparent diffusion coefficient, aka mean diffusivity (MD)

Diffusion occurring along the principal eigenvector (ε_1) is the axial diffusivity (AD). Diffusion sampled perpendicular to ε_1 is the radial diffusivity (RD, Equation 6).

$$RD = \frac{(\lambda_2 + \lambda_3)}{2}$$

Equation 6. Radial diffusivity

1.7.1.3 Fractional Anisotropy

To describe the amount of anisotropy within a given voxel (based on the diffusion tensor), the fractional anisotropy (FA, Equation 7) is computed. This is a scalar value from zero to one, given by:

$$FA = \sqrt{\frac{(\lambda_1 - \lambda_2)^2 + (\lambda_2 - \lambda_3)^2 + (\lambda_1 - \lambda_3)^2}{2(\lambda_1{}^2 + \lambda_2{}^2 + \lambda_3{}^2)}}$$

Equation 7. Fractional anisotropy

When the FA is zero, diffusion within the voxel is perfectly isotropic ($\lambda_1 = \lambda_2 = \lambda_3$) and the diffusion ellipsoid is spherical (Figure 55). Nerves have coherently arranged biological barriers (e.g., cell membranes, organelles, vascular spaces, microtubules, etc) which hinder diffusion radial to the long axis. This means that diffusion within nerves is typically highly anisotropic. As diffusion becomes more anisotropic, the FA increases and the ellipsoid becomes more elongated (Figure 55).
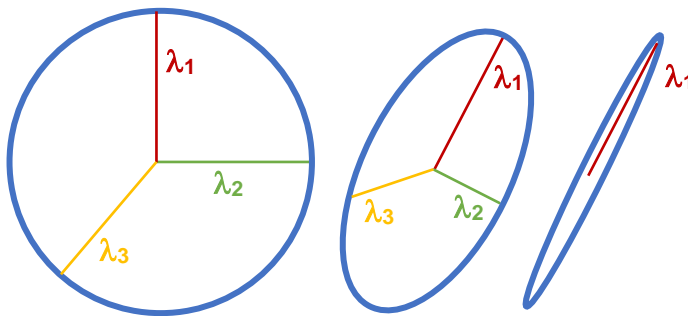
Figure 55. Examples of perfectly isotropic diffusion (left) whereby FA~0, diffusion restricted in some directions (middle) whereby the FA is >0 and highly anisotropic diffusion whereby the diffusion is restricted to one direction (right) and the FA~0.99.

1.7.2 **The limitations of DTI**

With respect to the brachial plexus, there are several important limitations to DTI:

1. It is unable to resolve crossing fibres (Figure 56 and Figure 57) which may be important in the brachial plexus, where there is fascicular exchange (Figure 15). The crossing/exchange in the brachial plexus is likely to be on a lesser scale than that observed within deep structures of the brain, where white matter tracts can cross at 90° to one another and in some areas, 3 white matter tracts can cross within an imaging voxel. None-the-less, there may be >1 fibre population within a given voxel in the brachia plexus and as such, one tensor (or at least, (ε1 aka v1) may not adequately represent the underlying microstructure. At the voxel-level, this could manifest as oblate or spherical tensors which may limit tractography.

2. It is unable to differentiate fibre coherence from the intrinsic properties of nerve microstructure (Figure 3). For example, DTI may be insensitive to the differences between one demyelinated nerve with a normal axon count, from a normally myelinated nerve with fewer axons. To-date, diffusion-tensor derived metrics have been unable to resolve differences in fibre density/coherence[81,97,98] from changes to the actual microstructure of nerves.

3. The Gaussian assumptions of tensor-based modelling fail to account for non-Gaussian diffusion in some tissues (Figure 38) at higher b-values.
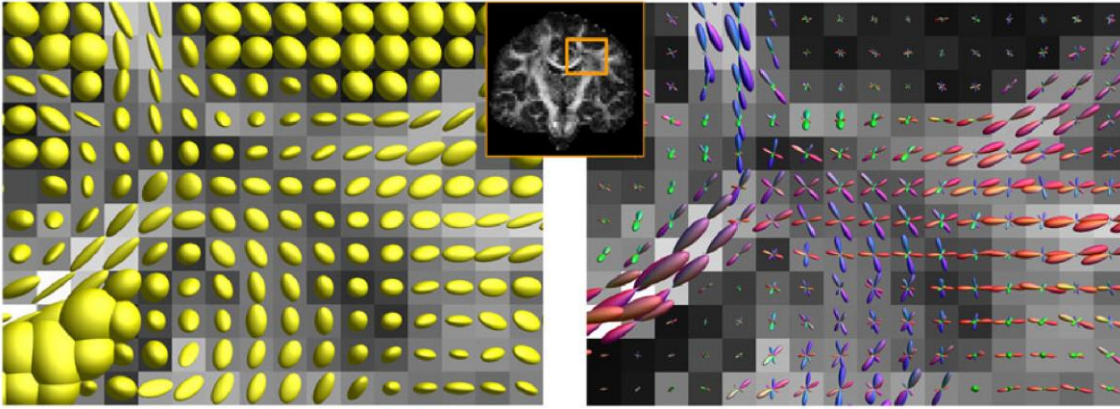
Figure 56. Two different methods of modelling dMRI signal in an area of the brain with crossing fibres. On the left, ellipsoids from DTI which describe the average profile within a voxel and so convey information on the dominant fibre population. On the right, glyphs (fibre orientation density functions, fODFs) derived from spherical deconvolution (SD) which demonstrate multiple fibre populations. Reproduced from Dell'Acqua and Tournier (2019)[99].
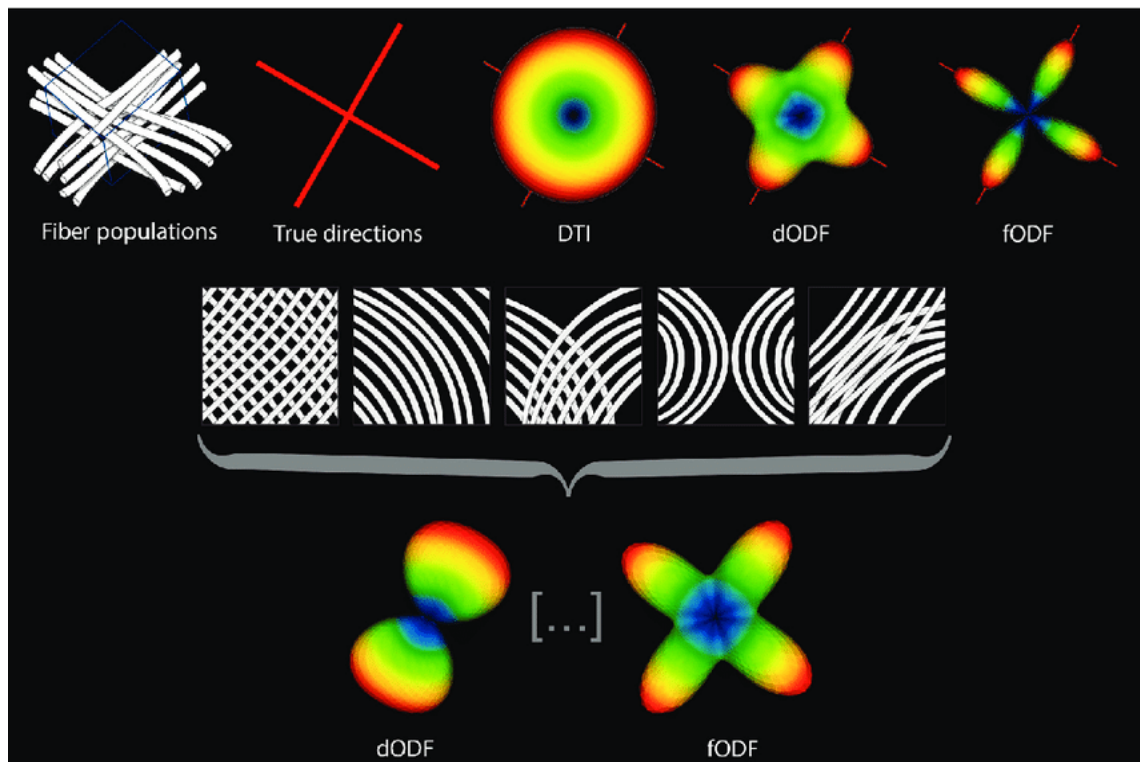
Figure 57. Graphical example of crossing nerve fibres. In this configuration, multiple peaks are expected in the dMRI signal, however the diffusion tensor is flat and thus insensitive. Orientation distribution functions (ODFs) and a fiber ODF (fODF, also known as the fiber orientation dispersion [FOD]) can be estimated using other techniques. Reproduced from Descoteaux (2015)[100].

Chapter 8. Post-processing: Beyond DTI

There are several techniques which model the diffusion propagator and enable the 3D reconstruction of crossing fibres as well as estimates of fibre density and dispersion. These include multi-tensor[101], PAS-MRI[102], Q-ball imaging[103], spherical deconvolution[104,105] and its modern constrained variants[106], ball and sticks[107], NODDI[108] and GQI[109]. These methods can largely be divided into two groups:

1. Methods based on q-space[110] (aka 'model-free' approaches) which typically estimate the diffusion orientation distribution function (diffusion-ODF, dODF)
2. Methods based on mixture models (aka 'model-based' approaches) which estimate the fibre orientation distribution function (fibre-ODF, fODF).

Both methods use spherical functions describe the diffusion signal, reconstruct multiple lobes/peaks which represent the diffusion orientation(s) and amplitude(s) which represents the diffusivity. Of note, dODF is usually closer to the real diffusion displacement profile and so their glyphs are typically less sharp. Conversely, fODF methods appear sharper as they resolve the underlying fibre orientation (Figure 58).

Figure 58. Two ODFs from the same voxel. On the left, a dODF derived from diffusion spectrum imaging. On the right, a fODF dervied from spherical deconvolution

1.8.1 Model-free (q-space imaging) methods

As a concept, "q-space imaging" was first proposed by Callaghan[110]. It is described as the Fourier relationship between the ensemble spin propagator $P(r,\Delta)$ (aka EAP), where Δ is the diffusion time and r the displacement, and the diffusion-weighted signal $S(q,\Delta)$. The Fourier relationship between signal and the spin propagator is akin to the relationship between k-space signal and spatial distribution of spins. K-space encoding (coordinates) is defined by the readout

gradient, whereas q-space encoding is defined by the diffusion gradient. As such, k-space signals have a Fourier relation with the spatial distribution of spins whereas q-space signal has a Fourier relation with the EAP (P(r,Δ)).
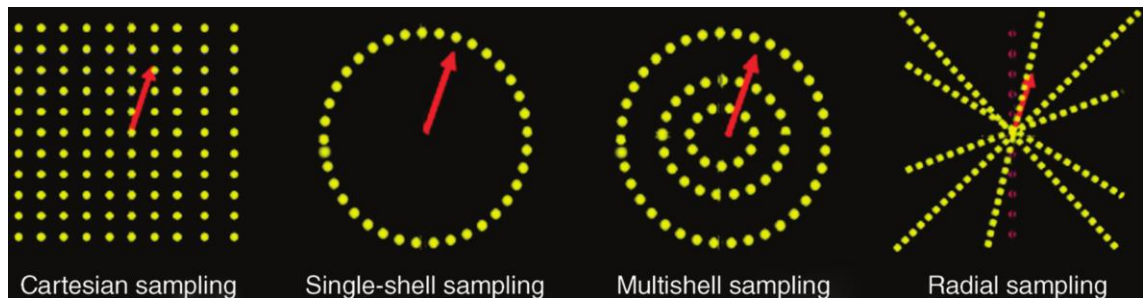
Figure 59. Diffusion sampling schemes in q-space for the proposes of diffusion propagator imaging and compartment modelling. Adapted from Descoteaux (2015)[100].

Q-space imaging aims to estimate the angular dependence of signal to estimate a dODF. Peaks in this dODF (the directions of the greatest spin displacement) are assumed to correspond to the orientation of fibres within the nerve. Whilst the methods used to estimate the dODF assume no models (hence the term model-free), when applying the dODF to model orientation of fibres, a model must be assumed. To-date, the most commonly used methods for q-space imaging include:

1.8.1.1 Diffusion spectrum imaging

Diffusion spectrum imaging (DSI)[111] was the first such technique to be described. Originally, it required complete sampling of q-space e.g., in a cartesian arrangement (Figure 59) which was profoundly time consuming and therefore, not clinically applicable. Recent developments on the acquisition techniques (e.g. radial and multishell sampling) and post-processing methods (e.g. Generalised Q-Space Imaging [GQI], Figure 60)[109] have made this approach feasible and valuable.
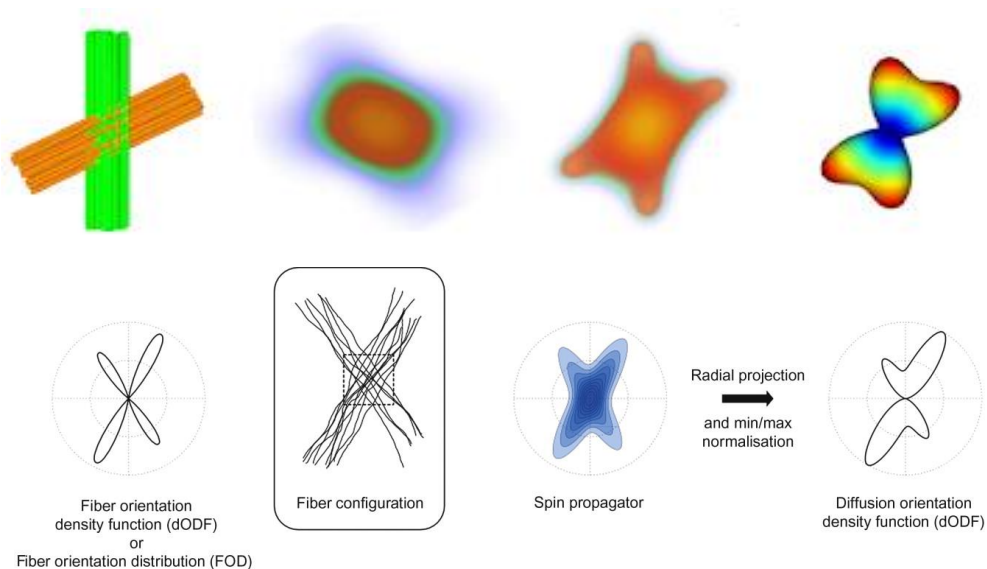
Figure 60. A graphical example of GQI (a derivative of DSI) being used to generate a dODF from q-space data. Reproduced from http://dsi-studio.labsolver.org/course/q-space-imaging-1

1.8.1.2 Q-ball imaging

Q-ball imaging[103] requires dense sampling of q-space (e.g. many vectors) at a single b-value (or q-value) to estimate the dODF using the Funk-Radon transformation. However, the angular resolution of the original approach was inferior to DSI[111] and so recent modifications have since been made, including the use of spherical harmonics (SH) to both speed up and improve the reconstruction[112,113] such that it is now equivalent to DSI. Modern constrained variants of SH (constrained spherical deconvolution, CSD)[106] is now a popular modelling choice for many and indeed, it is the default algorithm in the most popular diffusion modelling software package worldwide, MRtrix.

1.8.2 Mixture (multi-compartment) models

An alternative approach for estimating fibre orientations within a voxel is based upon the concept that the total diffusion signal observed is a summation of signal from spins within different tissue compartments. In the simple DTI model, all spins are assumed to derive from a single fibre population and thus, single compartment. In the mixture models, different tissue properties are considered whereby water than is highly restricted (e.g., intracellular water) it is assumed to generate a different amount of signal to extracellular water which may be less hindered. Some methods also include isotropic compartments to account for

partial volume effects. To-date, there are numerous models available but the most common and currently used methods include

1.8.2.1 Ball-and-stick(s)

Variations on the ball-and-sticks[107] (Figure 61) approach are common. This technique assumes that a) the ball compartment represents extracellular water (e.g., CSF) which has no preferred direction of diffusion (hence it is represented as isotopic), and b) the stick compartment which represents water within axons, with a preferred direction of diffusion.
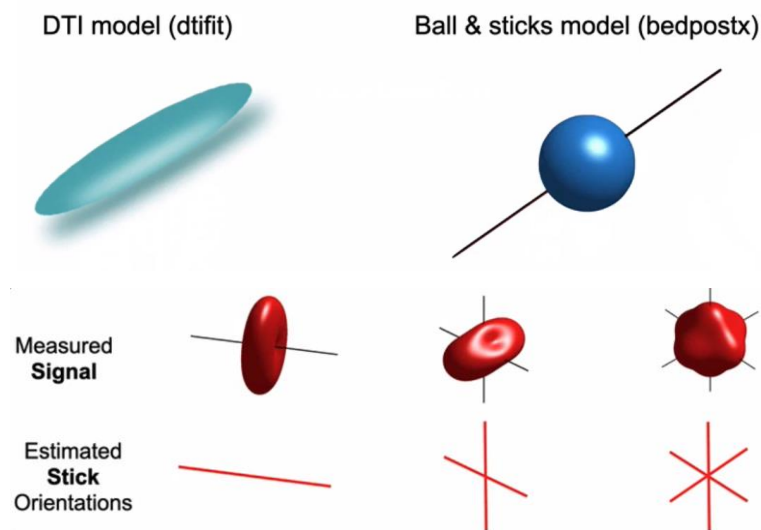
Figure 61. The ball-and-stick model implemented within the FMRIB FSL toolbox. The top tow shows the ellipsoid from DTI and how this would be represented as 1 ball and 1 stick. Below are examples (in red) of how different measured signals correspondences to different numbers of sticks. Reproduced from the FMRIB FSL teaching materials available at
https://www.youtube.com/watch?v=4dGC1kdNv1M

By taking a Bayesian approach and utilising Markov Chain Monte Carlo simulations, the model-predicted signal for multiple different fibre orientations and stick:volume fractions can be compared to the measured dMRI signal, on a voxel-by-voxel basis (Figure 62).
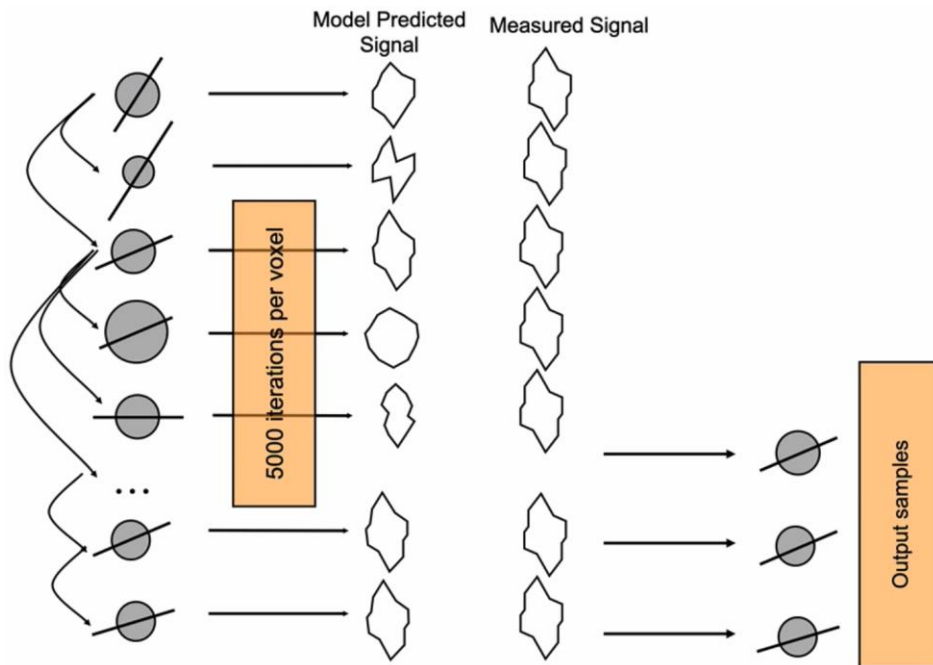
Figure 62. From the top-down, random changes to the size (volume) of the ball and orientation of the stick are generated, its dMRI signal predicted and compared to the measured signal. If the change is compatible with measured signal, then the model-prediction is accepted as plausible. Reproduced from the FMRIB FSL teaching materials available at

https://www.youtube.com/watch?v=4dGC1kdNv1M

This approach generates all possible fibre orientations that are consistent with the measured signal. Ultimately, a distribution of uncertainty around the preferred fibre orientation (a pre-specified number of sticks) are generated (Figure 63) which may be used to visualise the fibre population in a given region (e.g., with the roots of the brachial plexus, to understand if there is axonal sharing) and ultimately, for probabilistic tractography which may be superior to tensor-based deterministic tractography.
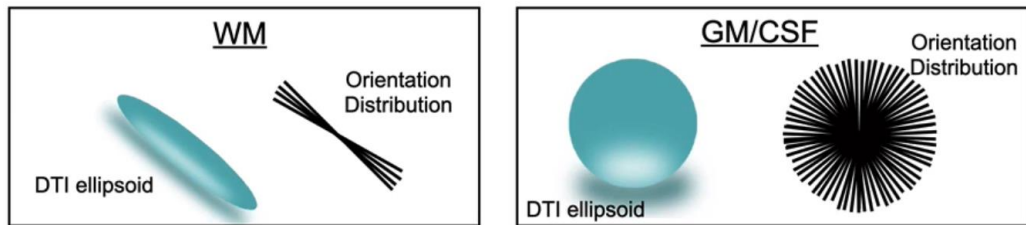
Figure 63. The predicted/simulated sticks (derived from MCMC modelling) which fit the measured dMRI signal in white matter (WM) and grey matter (GM) or CSF. Alongside these sticks, the representative diffusion tensor ellipsoid. Reproduced from the FMRIB FSL teaching materials available at
https://www.youtube.com/watch?v=4dGC1kdNv1M

1.8.2.2 NODDI

The neurite orientation dispersion and density dispersion NODDI model[108] distinguishes three non-exchanging spaces/compartments (Figure 64):

1. The intra-axonal (intra-neurite) space – signal is assumed to derive from within axons, modelled as cylinders (of zero radius), with diffusion assumed to be restricted and forming by a Watson distribution, the spherical equivalent of the Gaussian distribution.

2. The extra-axonal space – signal is assumed to derive from hindered diffusion around axons. It is modelled as anisotropic Gaussian (cylindrically symmetric tensors)

3. The extra-cellular space – signal is assumed to derive from extracellular water (e.g. CSF) which has no preferred direction of diffusion. This is analogous to the ball of the ball-and-stick model. It is modelled as isotropic Gaussian diffusion

Figure 64. The NODDI concept. Axons and dendrites are collectively known as neurites

By modelling the dMRI signal in a compartment fashion (Equation 8), NODDI outputs unique maps which show the orientation dispersion index (ODI), intra-cellular volume fraction (V_{ic}) and the isotropic volume fraction (V_{iso}) which represents cerebrospinal fluid (CSF).

$$S = F_{ia}S_{ia} + F_{ea}S_{ea} + F_{csf}S_{csf}$$

Equation 8. A simplification of the NODDI model which assumes that the observed signal (S) is a summation of some function (F) of three different compartments i.e., the intra-neurite (ia), extra-neurite (ea) and CSF.

This approach enables quantification and visualisation of new parameters and corresponding maps (Figure 65), beyond those generated by DTI.
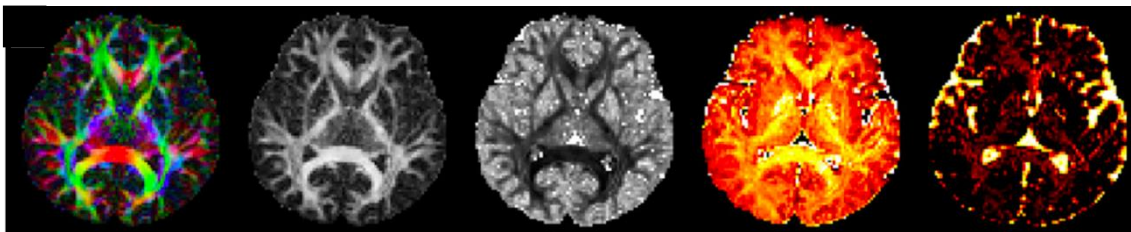
Figure 65. An axial slice through the brain reconstructed using NODDI[108] showing (from left to right) maps of the RGB-encoded principal direction, FA, orientation dispersion index (ODI), intra-cellular volume fraction (V_{ic}) and the isotropic volume fraction (V_{iso}). Reproduced from Zhang et al (2012)[108]

However, NODDI has not been applied to peripheral nerve data and it is unclear whether the modelling assumptions are appropriate.

Chapter 9. Tractography

This chapter provides an overview of tractography methods available for dMRI data, alongside their relative benefits and limitations.

1.9.1 Introduction

Tractography, also known as fibre tracking, is a method of estimating the connectivity of diffusion data. Using ODFs derived from any of the approaches described earlier (DTI, CSD, GQI, etc), the voxel-to-voxel connectivity can be estimated. To appreciate connectively within the brachial plexus (e.g., root to trunk, or trunk to division) and its connectivity to the spinal cord, performing tractography and deriving fibre-based statistics is desirable.

Foremost, there are numerous terms related to tractography which are used interchangeably in the literature. These are summarised and distilled below.

1.9.1.1 Terminology

Also known as fiber (or fibre) and streamline tracking, tractography is a mathematical exercise. It derives line segments which connect neighbouring anisotropic voxels in 3D space (Figure 70). The term "tracking" is preferable to "tracing" as the latter typically pertains to the use of injected tracers for labelling. And the spelling 'track' and 'tract' are often confused and must be differentiated. 'Tracks' are the virtual lines going voxels, whilst 'tracts' refer to actual white matter pathways in-vivo in the brain. To avoid confusion, many advocate the term streamline (which will be used henceforth) instead of track, with the aim of reminding readers that these are virtual (digital) representations of the trajectory of axons, not images of actual nerves. Furthermore, whilst streamlines are supposed to be virtual representations of axons, they rendered graphically on a much larger scale than actual axons within real tracts e.g., the corticospinal tract.

Streamlines originates from a point of interest (a seed) and are evolved/lengthened step-by-step until termination criteria are reached. There are various algorithms and approaches to generating streamlines and numerous conditions which can be used to terminate a streamline, all of which are discussed later.

Streamline bundles, clusters or pathways are all terms for a collection of several (typically hundreds or thousands of) streamlines which are packed tightly together in 3D space. These are virtual representations of the thousands or millions of actual axons within a nerve or white matter pathway. Henceforth, the term streamline bundle will be used. From such bundles, metrics can be extracted such as the average anisotropy, diffusivity or density.

Finally, a tractogram is a collection of streamlines (bundles or otherwise) which represent the overall anatomical structure.

1.9.1.2 Software

There are numerous software packages available for dMRI post-processing and the most popular for generating streamlines are shown in Figure 66. Whilst the output tractograms of these different approaches largely agree, there are important differences which should not be ignored[114].
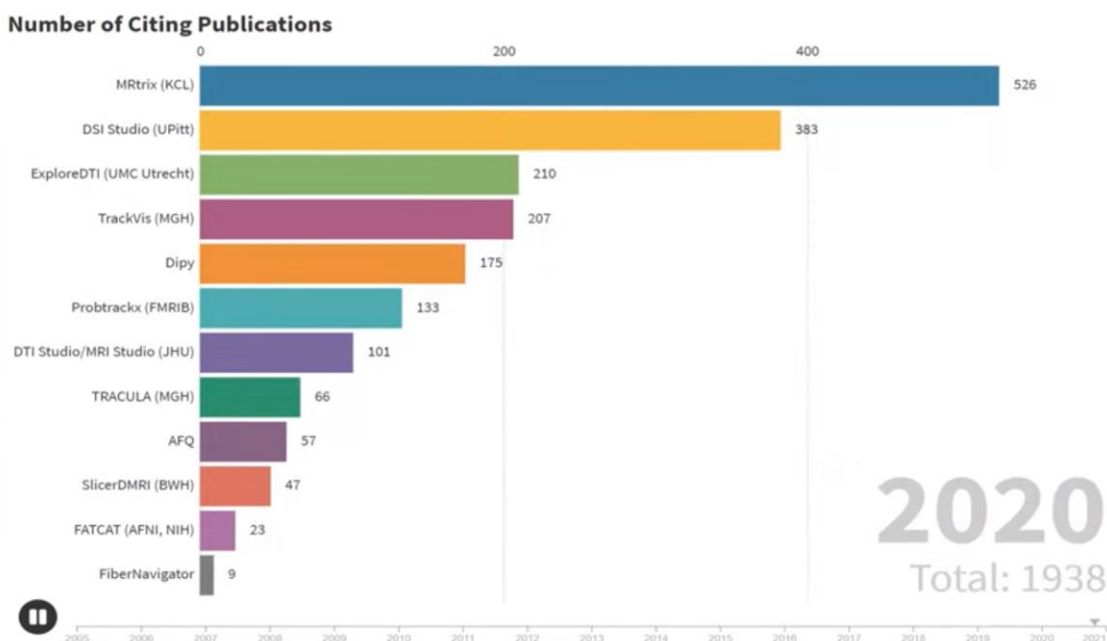
Figure 66. Bar chart showing the most popular software packages
(by citation counts) for tractography until the end of 2020.
Available at https://youtu.be/3PcUSHmgoYo

1.9.2 Deterministic tractography

The first algorithms for generating streamlines were tensor-based. These methods were based on the local orientation of diffusion, whereby the principal eigenvector (ε1 but typically shown as v1 in the tractography literature. The principal, eigenvector is the one associated with the largest eigenvalue, i.e., the direction of maximum diffusivity and this is assumed to be parallel to the underlying trajectory of axons.

1.9.2.1 FACT

The earliest algorithm, first published in 1999 was the FACT (fiber assignment by continuous tracking)[115] although this was revolutionary, the variable step size (Figure 67) and inherent difficulties dealing with sharp changes in direction limited its application.
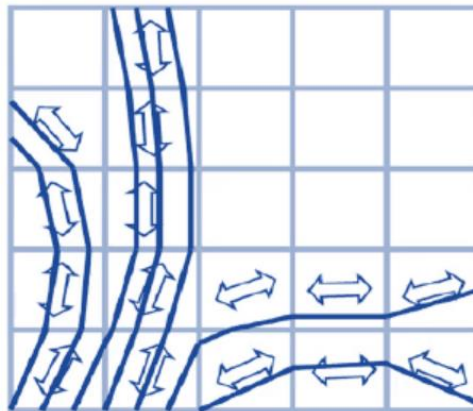
Figure 67. FACT tractography. Reproduced from Mori et al (1999)[115].

1.9.2.2 Interpolated streamlines

Soon after, in 2000, a family of algorithms were developed which are collectively known as interpolated streamline tracking[116] (Figure 68). These algorithms use a fixed (user specified) step sizes which are be considerably smaller than the dimensions of the voxel. Additionally, the trajectory of the streamlines can be smoothed by the trajectory of the incoming and outgoing streamlines. Different algorithms approach this concept differently; the most prevalent deterministic methods include the Euler technique (which uses a single differential equation) and Runge-Kutta method (which uses recurrent differential equations, typically to

the 4th order) to better estimate streamline trajectory. Both can be used on tensor-based and ODF-based data.
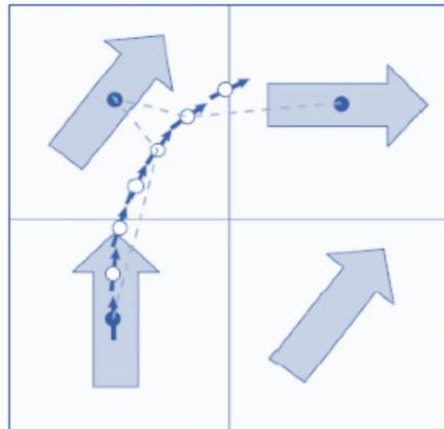
Figure 68. Interpolated streamline tractography.

1.9.2.3 Seeding methods

There are two main methods for choosing were streamlines should start (Figure 69) – this is known streamline seeding. Seeding from all possible locations within the anatomical pathway is desirable because it represents the highest chance that all true paths are represented.

Figure 69. In black (left) is the ground truth of fanning pathways. Seeding from a single central region (orange diagram) fails to demonstrate all true pathways. Seeding everywhere (right, blue diagram) with a specified waypoint (yellow) better represents the truth.

1.9.2.4 Stopping criteria

There are several ways of specifying when a streamline should stop i.e., no longer propagate into a neighbouring voxel. The most common stopping criteria are based on:

1. Anisotropy – when the anisotropy (typically fractional or quantitative anisotropy) exceeds a specified threshold tracking continues in neighbouring voxels (red in Figure 70) but when this value falls below the cut-off (e.g., FA<0.1), then tracking terminates, as shown in green.
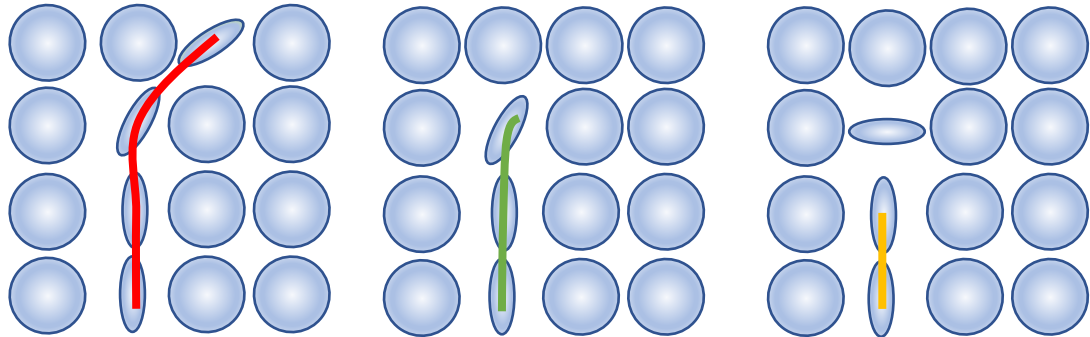
Figure 70. Simplified examples of the termination tractography based on the turning angle. On the left, the red streamline propagates through neighbouring anisotropic voxels because the turning angle is below the prespecified threshold. In the middle, an example of termination based on an anisotropy thresholding, whereby the green line terminates when the FA of the adjacent voxels exceeds the prescribed threshold. On the right, an example of angular thresholding whereby the yellow line does not propagate through the anisotropic voxel containing an orientation perpendicular to the previous voxel(s).

2. The turning angle – if the streamline is required to turn through an improbably high angle to continue (this angle is user-specified and based on the geometry of the anatomy e.g., in the brain it's typically set to 30-40º) then tracking stops, as shown in the yellow streamline in Figure 70 – although there is a neighbouring highly anisotropic voxel, it would be required to turn through 90º to continue and this angle is above the threshold. The turning/step angle depends on the imaging resolution, and algorithms used for both EAP (dMRI signal) reconstruction and tractography.

3. Anatomical constraint – using masks, streamlines can be forced to start (seed) within specific regions, pass through waypoints, terminate within

and/or avoid specific regions in any combination. In the brain, it is commonplace to seed throughout the white matter, exclude tracts that stray into the CSF and constrain endpoints to the grey matter.

1.9.3 Probabilistic Tractography

The goal of probabilistic tractography is to estimate the probably of different anatomical regions being connected, by building up a distribution of possible streamlines based on the observed dMRI data. In the context of the brachial plexus, this could be used to estimate the chance of axonal integrity in the roots and the chance that they are connected to the spinal cord.

There are less numerous but still several ODF-based methods of estimating the probability of different streamlines

1.9.3.1 Hough probabilistic tractography

The technique described by Imangi et al (2011)[117], Hough tractography is based upon Q-ball imaging[103] (Section 1.8.1.2). Normalized and dimensionless, constant, solid angle ODFs are computed prior to tractography. Typically, tens-of-thousands of streamlines are fitted and then, the Hough transformation voting process is applied to determine the best fitting streamline(s).

1.9.3.2 Bedpostx and Probtrackx

The FMRIB suite of FSL tools uses the ball-and-sticks[107] approach (Figure 61), implemented in their Bayesian Estimation of Diffusion Parameters Obtained using Sampling Techniques (Bedpostx, whereby the x stands for crossing fibres). Thereafter, the probtrackx tool generates maps of the probability of regions being connected, depending on how users have specified the tractography to occur (seeds and targets).
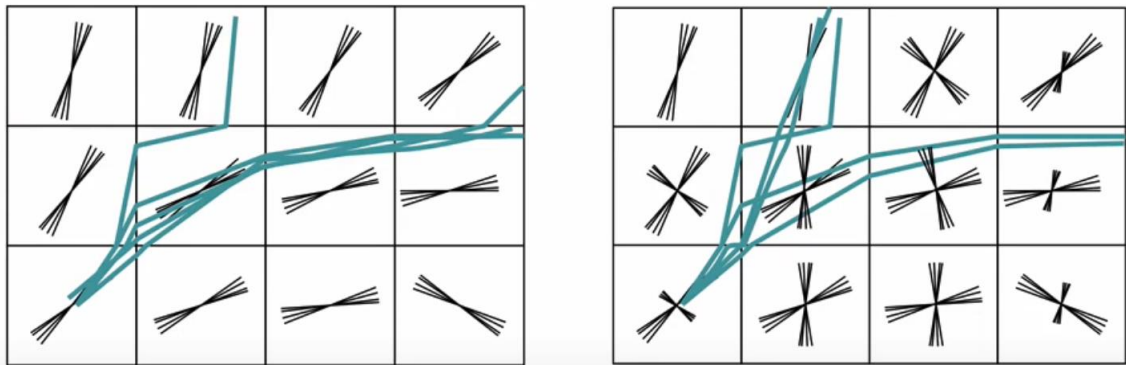
Figure 71. On the left, no crossing fibres are seen so the majority of streamlines are congruent, meaning that the probability of connectivity is high. On the right, cross fibres are seen to the streamlines are shared between different bundles. Reproduced from the FMRIB FSL teaching materials available at https://www.youtube.com/watch?v=_N8hzzo818U

1.9.3.3 Deterministic versus probabilistic tractography

The main difference between these two methods of tractography is the sampling of the local orientation at each voxel. In deterministic methods, the streamline is steered by a fixed direction, the principal eigenvector. In contrast, with probabilistic methods a distribution of orientations is estimated per voxel and streamlines are steered from a random draw from this population.

Deterministic methods are more commonplace and computationally inexpensive. However, critics of deterministic tractography cite that it cannot account for inherent uncertainty in local orientations[118], it's overly sensitive to the estimated principal direction[80] and susceptible to noise[119]. Probabilistic tractography better accounts for uncertainty[80,120,121] in the data but it is computationally intensive.

Chapter 10. The Rationale for Investigating diffusion MRI in Peripheral Nerve Injury

In section 1.4.3.1, it has been shown that the microstructure of healthy nerves (Figure 33 and Figure 34) compels the axoplasm to diffuse bidirectionally. This means that healthy nerves exhibit highly anisotropic diffusion. In this chapter, the literature on dMRI in peripheral nerve injury will be summarised, followed by the objectives for developing a clinically applicable dMRI sequence for capturing microstructural information about the brachial plexus in adults.

1.10.1.1 Diffusion in injured animal nerves

Following a traumatic peripheral nerve injury, the microstructure of a nerve changes (section 1.1.5). To-date, numerous studies have shown that diffusion becomes more isotropic in the distal stump of injured peripheral nerves in rats[122–128] and rabbits[129,130]. More specifically, in the distal nerve stump (which is disconnected from the cell body), RD rises as microstructure is lost and FA reduces (Figure 72 and Figure 74). In the proximal stump (which remains connected to the cell body so microstructure is maintained), FA and MD remain relatively unchanged in the acute phase, whilst there is potential for axon regeneration.
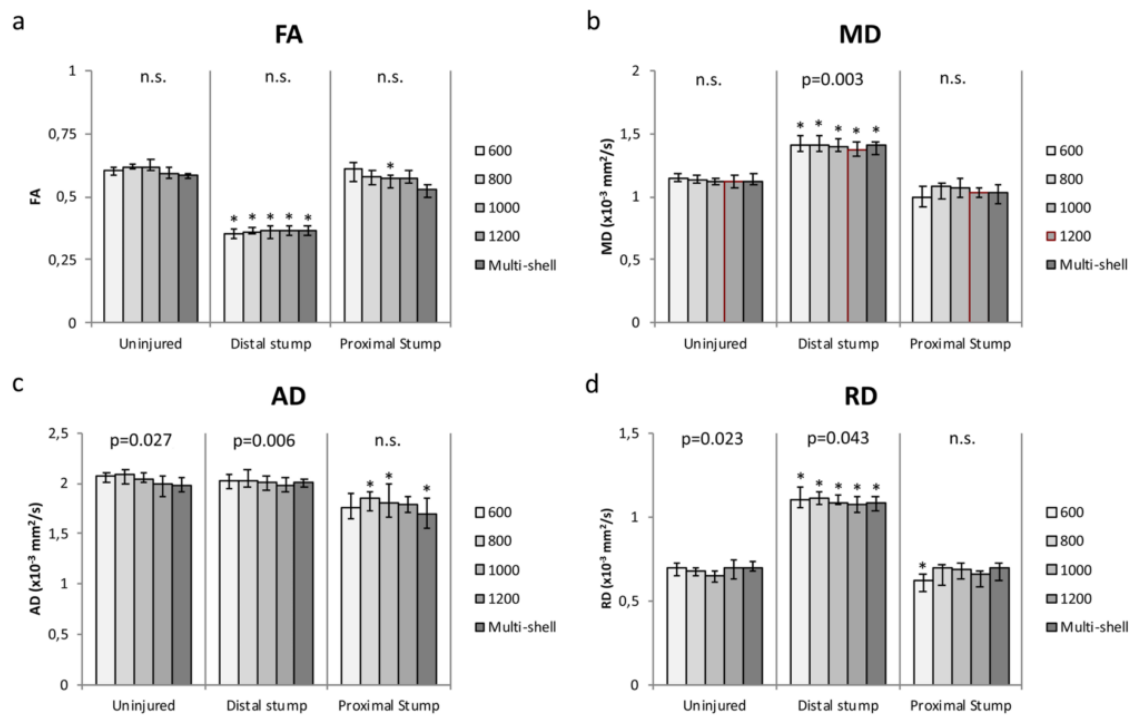
Figure 72. The median fractional anisotropy (a), and mean (b), axial (c) and radial (d) diffusivity values in the sciatic nerve of a rat change 4 weeks after injury. Reproduced from Andersson et al (2018)[123].

Changes in DTI metrics are also proportional to the severity of peripheral nerve injury (Figure 73)[124,125] and associated with limb function[122,128].
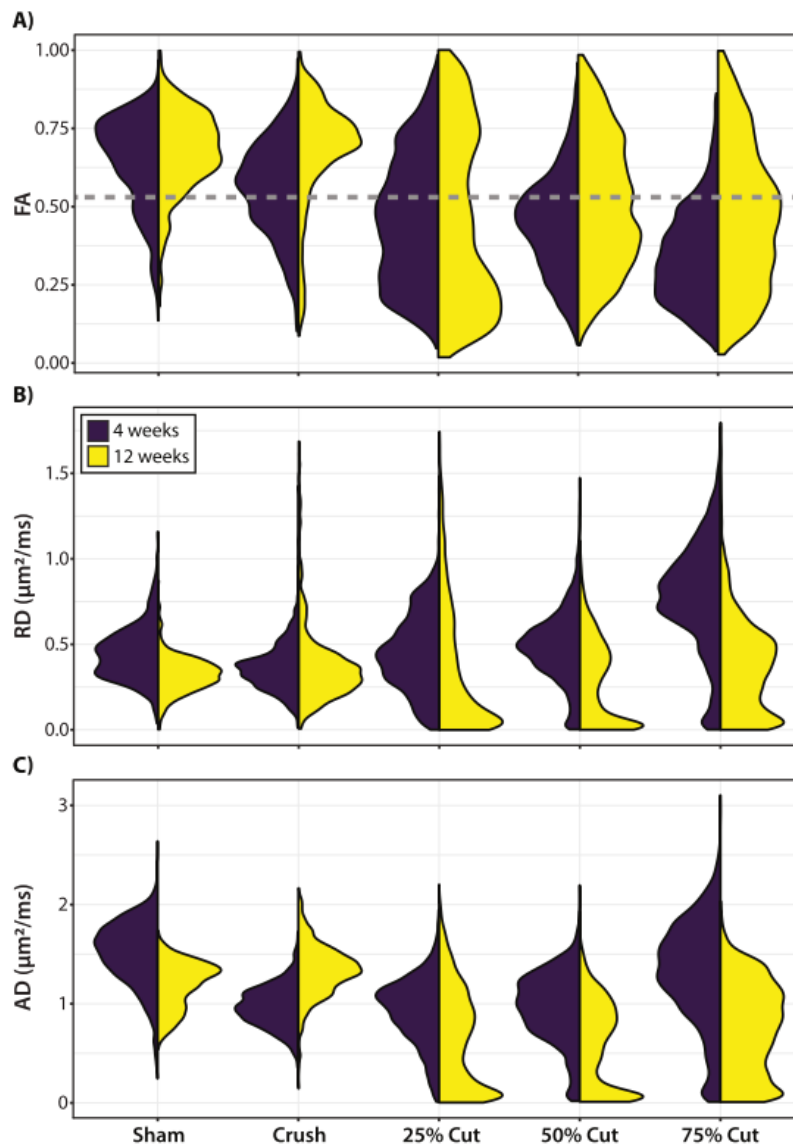
Figure 73. Split violin plots showing that FA falls and RD rises in proportion to the severity of peripheral nerve injury in rats. Reproduced from Manzanera et al (2021)[124].

Moreover, several studies have shown that dMRI is sensitive to axonal regrowth[127,130], i.e., regeneration of axons across the zone of crushing or neurorrhaphy (Figure 74).
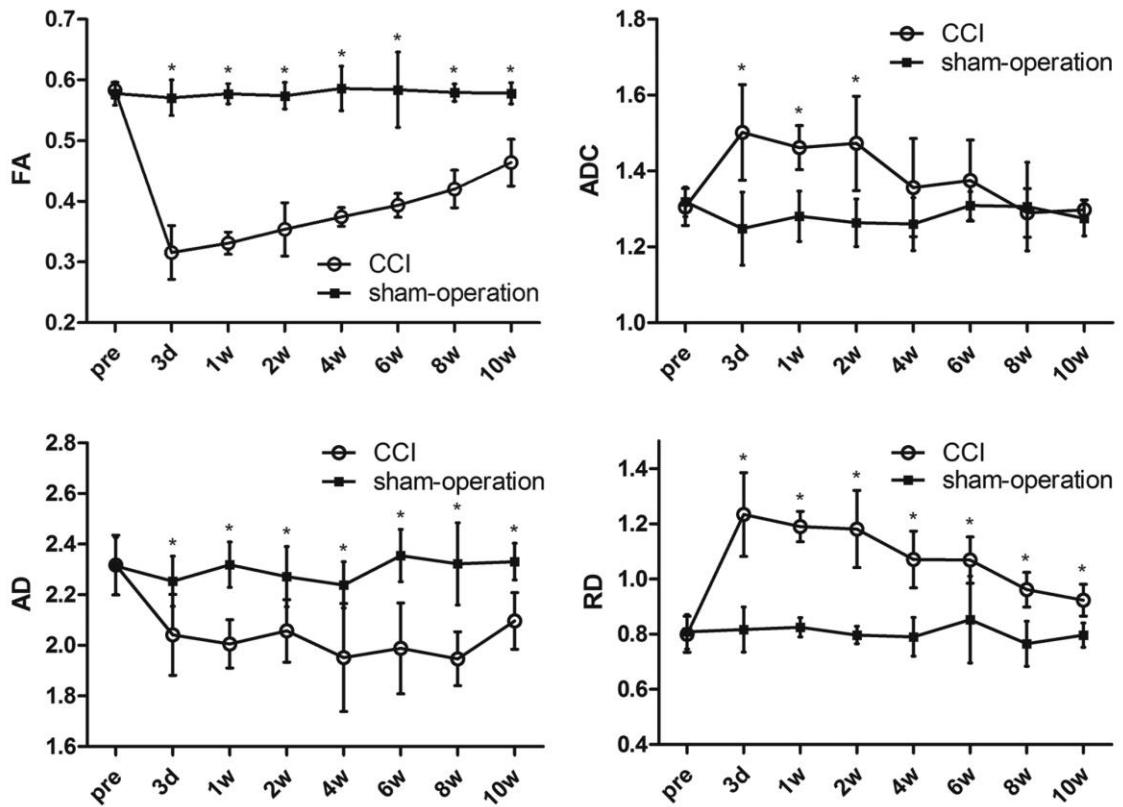
Figure 74. Changes in the DTI parameters of the sciatic nerve in rabbits who were subject to either chronic compression (CCI) or sham surgery. Diffusivity values are in ×10^{-3} mm²/s. Reproduced from Wu et al (2018)[128].

1.10.1.2   Diffusion in injured human nerves

DTI has been consistently shown to be sensitive to microstructural changes in humans with numerous peripheral nerve pathologies and outperforms standard morphological imaging[131]. Some applications of DTI in humans to-date include:

- Carpal tunnel syndrome[132] – in this meta-analysis, 32 studies of 2643 wrists, belonging to 1575 asymptomatic adults and 1068 patients with CTS were compared. Patients with carpal tunnel syndrome had a 12% lower FA than controls (95% CI 0.09, 0.16) and higher MD (mean difference 0.16×10^{-3} mm²/s [95% CI 0.05, 0.27]) than controls. Heckel et al (2015)[61] also showed that DTI in parameters carpal tunnel syndrome are strongly associated with electrophysiological parameters.
- Cubital tunnel syndrome[133–138] – numerous studies have shown that patients with ulnar nerve compression have a lower FA (of the order of 10%) and higher radial diffusivity, throughout the length of the ulnar nerve.

- Lumbosacral nerve root root compression[139] – in this meta-analysis, 10 studies of 262 patients with 285 symptomatic underwent dMRI. The DTI parameters in symptomatic (compressed) lumbosacral nerve roots were compared to asymptomatic roots. Compressed roots a 3% lower FA than healthy roots (95% CI 2.3, 3.8) and 2% higher MD (95% CI 0.9, 3.2) than healthy roots.

- Charcot-Marie-Tooth disease[140–142] – several studies have shown that DTI is sensitive to the demyelination and axonal loss which occur in this hereditary condition, manifesting as lower FA and higher diffusivity. dMRI can further differentiate subtypes of Charcot-Marie-Tooth disease (1A versus 2) which have different patterns of demyelination and axonal loss[140].
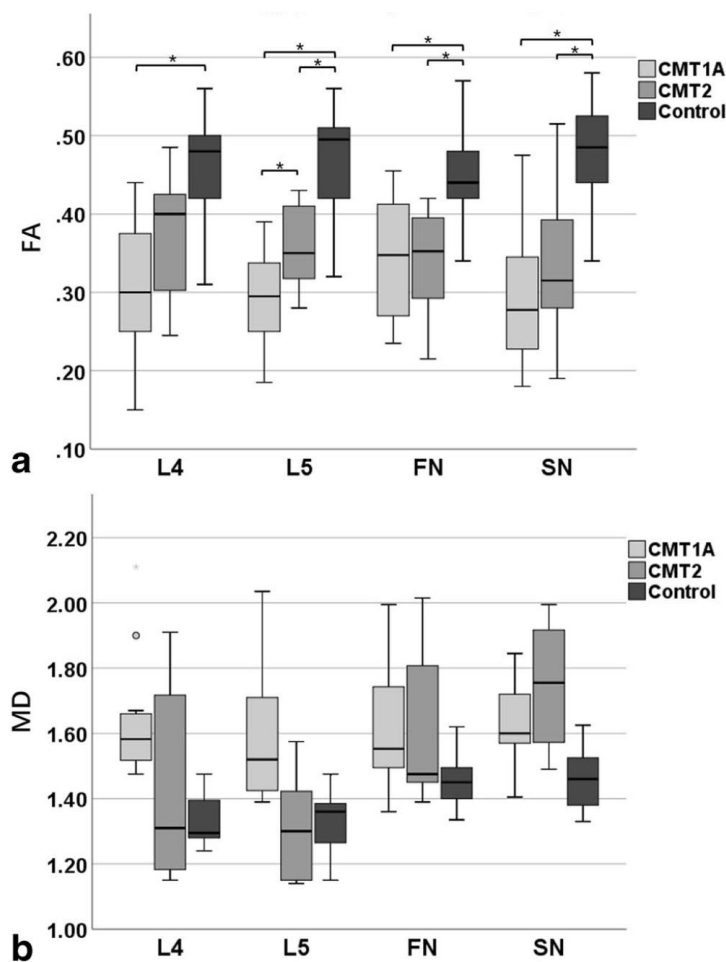
Figure 75. Boxplots showing the FA (a) and MD (b) from lumbar spinal nerve roots in patients with Charcot-Marie-Tooth (CMT) disease type 1A, type 2 and controls. Reproduced from Sun et al (2022)[140].

- Traumatic peripheral nerve injury[143] which is marked by higher MD (due to inflammation and haemorrhage), raised RD (due to loss of axonal architecture) and thus, reduced FA (Figure 76). Moreover, tractography based on dMRI can identify partial and completely divided peripheral nerves within days of injury[144].
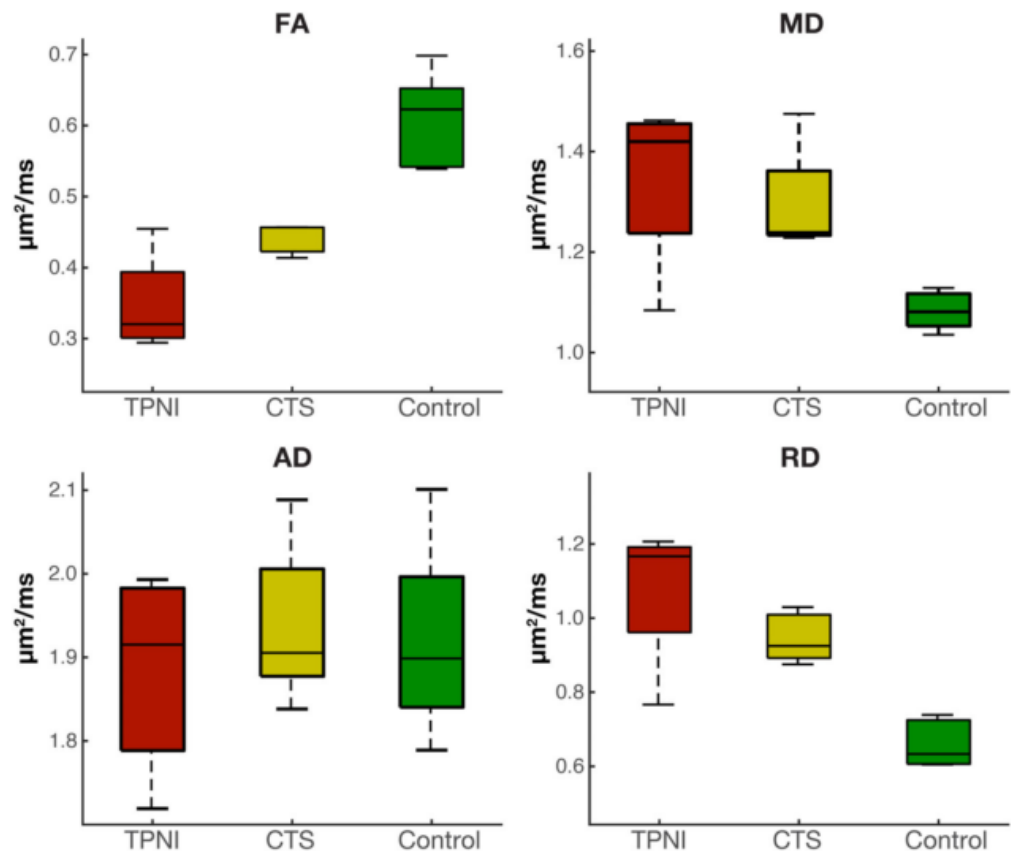
Figure 76. Boxplots showing the DTI parameters from healthy controls (green), patients with traumatic peripheral nerve injury (TPNI, red) and carpal tunnel syndrome (CTS). Reproduced from Pridmore et al (2021)[143].

- Peripheral nerve tumours[145] whereby DTI parameters in the neoplasm are substantially different to heathy nerves and tractography can help plan the approach to surgical resection.

1.10.1.3   dMRI in the brachial plexus

At the time of planning the research on which this thesis is based, five studies[146–150] had investigated DTI in the brachial plexus. Three involved healthy volunteers who were scanned at 3T[146–149], one articled considered neoplasms compressing the plexus[148] and one group[150] reported deterministic tractography in patients with brachial plexus injuries at 1.5T.

1.10.2 Why develop dMRI for brachial plexus injuries?

The diagnosis of peripheral nerve disorders (of any type) is inherently difficult because many of the medical tests available in routine clinical practice are unreliable. Moreover, many disorders, especially in the field of surgical nerve disorders, lack diagnostic criteria which is arguably due to the fact that there is no objective, accurate and repeatable medical test.

1.10.2.1   Symptoms and signs

Most of the classically described symptoms of nerve disorders (such as nocturnal paraesthesia and provocative tests such as Phalen and Tinel, scratch-collapse and sensory threshold testing in carpal tunnel syndrome[151,152]) have poor diagnostic value. This is also reflected in the brachial plexus whereby provocative tests (albeit less studied) are unreliable for grading the severity of injury[153] or predicting outcomes.

1.10.2.2   Electrodiagnostics

Despite the widespread use of electrodiagnostic studies, it is an unreliable invasive and painful test which evokes patient anxiety[154,155]. Also, there are no established normal values which immediately undermines its diagnostic application. This is why numerous studies have shown that for the most common neuropathy worldwide, carpal tunnel syndrome, it has poor diagnostic accuracy[156]. This is also the case for BPI[157]. For these reasons, surgeons ignore the results of electrodiagnostic tests when they disagree with the clinical picture[158].

1.10.2.3   Ultrasonography

Recently, sonographic measurement of the cross-sectional area of peripheral nerves has gained popularity for diagnosing abnormalities. Whilst it has good inter-rater and intra-rater reliability[159], and validity[160,161] in various applications, it has not been adopted into routine clinical practice for several potential reasons:

a) How the cross-sectional area of peripheral nerves is affected by other factors such as age, sex, diabetes, sonographer technique [pressure applied, measurement angle, etc] and the hardware is unclear,

b) Whether the epineurium should be included in the measurement and how it affects the measurement is not clear

c) How these measurements relate to injury severity, or subjective (patient-reported) and objective outcomes has not been investigated.

Moreover, sonography still only provides morphological information about nerves (their size and shape) and has few other potential applications in the contact of nerve injury. Despite these limitations, the cost is similar to that of MRI (£220 versus £389)[162].

1.10.2.4   MRI

To-date, morphological MRI has been shown to be the most accurate non-invasive test for diagnosing brachial plexus injuries[29]. MRI is superior to nerve and muscle electrophysiology studies[30], ultrasonography[31–34] and intraoperative somatosensory-evoked potentials[35]. In the UK, the cost of a non-contrast MRI of the extremity is also less than an electrodiagnostic exam (£389 versus £444).[162] Moreover, MRI has numerous other potential applications which could be valuable for patients and clinicians alike. It is the only non-invasive medical test which could also provide objective information on other tissues and broader functions to inform the management of BPI, by capturing information on:

- Macroscopic regional anatomy via morphological classical T1/2 weighted scans. This could provide an opportunity to identify incidental anomalies[163] or non-BPI injuries which typically occur simultaneously, such as rotator cuff tears[164].

- The connectivity of end organs in the upper limb to the brain, through resting-state functional MRI, supplemented with motor and sensory paradigms[165–169].

- The plasticity of the sensorimotor cortex (i.e., it's potential to recover and reinnervate end organs) via singe-voxel spectroscopy of prognostically important neurotransmitters, such as GABA (γ-aminobutyric acid)[170,171].

- Skeletal muscles, such as their T1 and T2 signal profile which changes in the acute phase of denervation, fat fraction[172] which increases in the medium-to-long term after denervation, and aberrations in elastography or iron deposition profiles. Together, these data could establish the subject-specific normal values in uninjured muscles, their state of innervation at baseline (after injury) and the likelihood of subsequent recovery if reinnervated. Unlike electromyography, this information could be captured painlessly and from multiple muscles simultaneously, at less expense to the health service.

- The vascularity to the limb. Concomitant vascular injury is an uncommon[173,174] but critically important to identify so contrast-free angiography (such as time-of-flight angiography[175]) may be valuable.

- Microstructural information from the spinal cord, brachial plexus and regional muscles via dMRI.

For these reasons, MRI appears to be the most potentially useful tests to develop and for capturing information on the 'health' of the brachial plexus, dMRI appears to be the most useful modality.

1.10.3 Research Objectives

By chapter, the primary objectives are as follows:

Chapter 1: Estimate the diagnostic accuracy of conventional, morphological MRI for diagnosing the most common form of brachial plexus injury, root avulsion, in adults subject to major trauma worldwide.

Chapter 2: Develop a clinically applicable diffusion tensor imaging sequence for the brachial plexus in adults, and compare the DTI parameters of spinal nerve roots in healthy individuals to patients with surgically confirmed brachial plexus injuries.

Chapter 3: Model the geometry of the roots of the brachial plexus in cadavers to define the required step angle(s) for dMRI tractography

Chapter 4: Explore the effect of different fractional anisotropy thresholds for deterministic tractography of the brachial plexus in healthy adults.

Chapter 5: Define the normal DTI values of the roots of the brachial plexus via meta-analysis, and explore how FA and MD vary with experimental conditions.

Chapter 6: Explore the effect of different pre-processing pipelines on DTI parameters and tractograms of the brachial plexus

Chapter 7: Investigate the possibility of multiple fibre orientations within the adult brachial plexus using multishell dMRI and how this may influence deterministic versus probabilistic tractograms, as well as future dMRI sequence development and data processing.

Part 2. Research Findings

Chapter 11. MRI for Detecting Root Avulsions in Traumatic Adult Brachial Plexus Injuries: A Systematic Review and Meta-analysis of Diagnostic Accuracy

Published at https://doi.org/10.1148/radiol.2019190218 (Appendix 2)

1.11.1 Background

MRI is the best non-invasive test for brachial plexus injuries[29] and most surgeons use pre-operative MRI in an effort to identify patients with roots avulsion. However, clinical sequences are still aimed at generating contrast between macroscopic anatomical structures (e.g., nerve and muscle, or nerve and CSF) and remain in the domain of morphological imaging. To-date, the accuracy of morphologic MRI for identifying root avulsion remains a topic of debate. Therefore, the prevailing clinical practice involves either protracted observation (for months) or surgical exploration of the brachial plexus.

Numerous studies have examined the accuracy of morphological MRI for the detection of traumatic root avulsions in the brachial plexus. This review aims to evaluate the diagnostic accuracy of morphological MRI for the identification of root avulsion(s) in adults with traumatic brachial plexus injuries.

1.11.2 Materials and Methods

This systematic review and meta-analysis was conducted in accordance with our protocol[176] (Appendix 1) and has been written in accordance with the Preferred Reporting Items for Systematic Reviews and Meta-Analyses – Diagnostic Test Accuracy (PRISMA-DTA) Statement[177].

1.11.2.1 Participants and Studies

We included studies of adults with symptomatic brachial plexus injuries sustained from non-penetrating trauma, that reported the findings of pre-operative morphological MRI examination and surgical exploration of the roots of the brachial plexus. We excluded case reports and studies concerning bilateral injuries[178,179].

1.11.2.2   Target Condition

The primary target condition is avulsion of the root(s) of the brachial plexus. The secondary target condition is a pseudomeningocoele, which is purported to be a surrogate marker of root avulsion. Our review is concerned with the ability of morphological MRI to distinguish between normal roots (no avulsions) and any frequency of root avulsion.

1.11.2.3   Index Test

The role of MRI is to detect root avulsion. This scan is typically performed within weeks of the injury and before surgery. The interpretation of MRI for root avulsion is binary with implicit threshold. Similarly, images are examined for the presence of a pseudomeningocoele (sometimes erroneously termed meningocoele) which is also a binary outcome with implicit threshold. The target conditions can be observed at any spinal level, from C4 to T2 depending on the pattern of plexus fixation. Several systematic differences are expected including the: scanner brand and model, field strength, pulse sequences, software for post-processing, display hardware and viewing environment; these differences will be investigated if possible.

1.11.2.4   Prior Tests

Patients typically undergo extensive clinical assessment and imaging. Some patients might be subject to electrodiagnostic studies (nerve conduction and electromyography). All examination and medical test findings would typically be made available to the radiologist interpreting the MRI scan.

1.11.2.5   Reference Standard

The reference standard is operative exploration of the supraclavicular brachial plexus under general anaesthesia.

1.11.2.6   Search Strategy

Medline and Embase were searched from inception on 20th August 2018, with no restrictions (Appendix 7). Citations were independently deduplicated by two authors and independently screened.

1.11.2.7 Study Selection

Two authors independently screened all citations. The full texts of potentially eligible articles were obtained and independently assessed by the same two authors[176]. Disagreements were resolved by discussion.

1.11.2.8 Data extraction

Two authors (RGW and JCRW) independently extracted data concerning demographics (age and sex); mechanism of injury; timeframes between injury, scanning and surgery; scanning protocols; surgical steps; and test statistics to construct 2x2 tables of the number of true positives (TP), false positives (FP), false negatives (FN) and true negatives (TN). The authors of two studies[180,181] provided missing data.

1.11.2.9 Methodological quality assessment

The risk of bias and applicability of included studies was assessed by two authors (RGW and JCRW) using a tailored version of the Quality Assessment of Diagnostic Accuracy Studies (QUADAS-2, Appendix 8)[176,182] and there were no disagreements.

1.11.2.10 Statistical Analysis

We used RevMan to generate forest plots and summary receiver operating characteristic (SROC) plots. Estimates of sensitivity and specificity are provided on forest plots. Using Stata version 15 (StataCorp, Texas, USA), a bivariate meta-analytical model was used to obtain summary sensitivities and specificities with the nerve as the unit of analysis[183–185]. A meta-analysis of patient-level data was not performed owing to sparse and heterogeneous data. To determine the effect of a covariate on the sensitivity and specificity of MRI we planned a bivariate meta-regression, but this was not possible due to limited data. We did not assess publication bias because the determinants are not well understood for diagnostic accuracy reviews[185] and the Deeks' test has low power in the presence of substantial heterogeneity[186]. Significance was set at 5%.

1.11.3 Results

1.11.3.1   Study selection

A total of 1688 unique articles were identified (Figure 77). Eighty-six full texts were retrieved of which 66 were excluded: narrative review (24), no reference standard (17), case report (7), opinion piece (4), no pre-operative MRI (3), a systematic review (1), a survey of brachial plexus imaging (1) or irrelevant (9). Nine articles were later excluded[187–195] due to missing outcome data[187,190–193,195], inability to disaggregate results[189,194], and a report of root avulsion within a series of patients with other nerve injuries was treated as a case report[188]. Ultimately, 11 articles (11 studies)[174,180,181,196–203] were included.
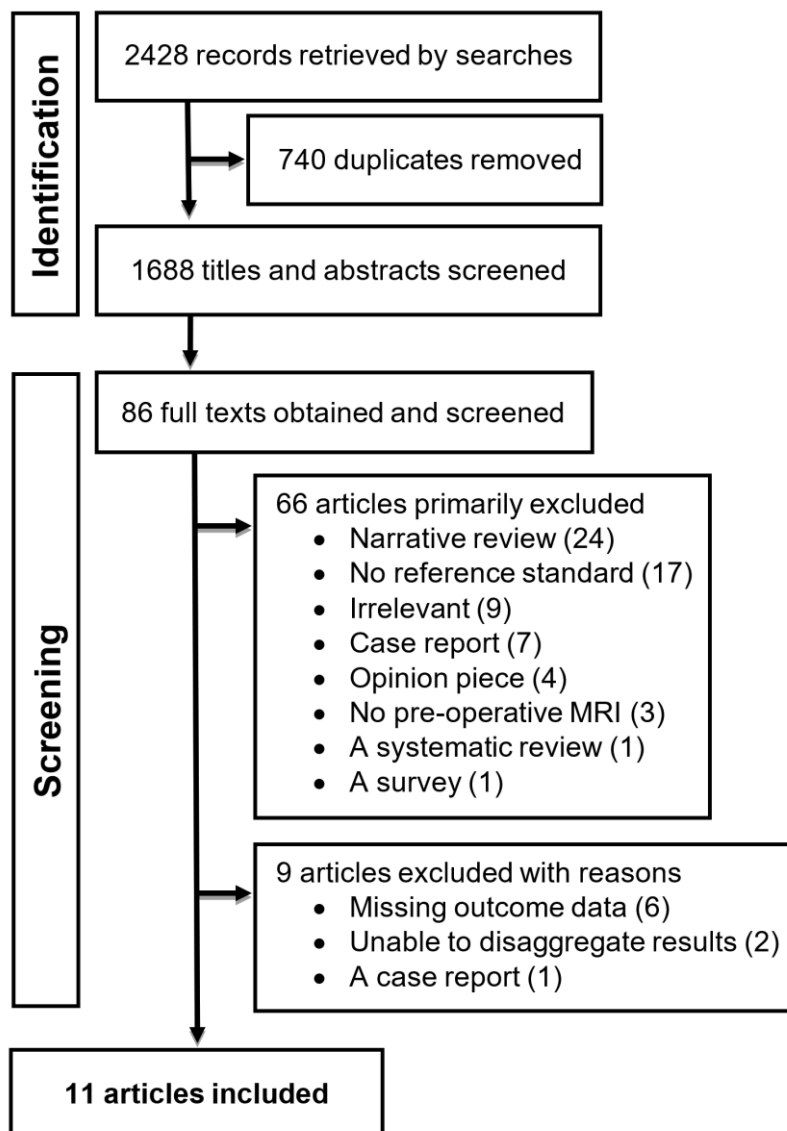
Figure 77. PRISMA flowchart

Study	Recruitment Timeframe	Location	Study Type	Participants Undergoing MRI and Surgical Exploration of the Roots of the Brachial Plexus					Description of the Surgical Exploration of the Brachial Plexus
				Number of patients	Mean Age	Males: Females	Patients With At Least One Root Avulsion (%)	Overall Frequency of Roots Avulsions (%)	
Abul-Kasim 2010[196]	2000 to 2008	Sweden	Consecutive series; retrospective research	7	29	7:0	5 (71)	15 (44)	Clavicle splitting supra- and infraclavicular exploration by the same surgeon
Chanlalit 2015[197]	1997 to 2000	Thailand	Consecutive series; retrospective research	35	25·7	35:0	35 (100)	46 (66)	Supraclavicular exploration by the senior author
Doi 2002[198]	1995 to 1997	Japan	Not described	35	25·5	Not described	Not described	Not described	Supraclavicular exploration with intraoperative spinal root sensory evoked potentials, compared to a preoperatively placed epidural electrode
Dubuisson 2002[180]	1992 to 1995	Belgium	Not described	7	27	~4:1	3 (43)	Not described	Supraclavicular and infraclavicular exploration by the same surgeon, with or without a posterior approach if needed
Gasparotti 1997[201]	1993 to 1994	Italy	Consecutive series; temporality unknown	13	26	18:2	Not described	25 (40)	Supraclavicular exploration of selected roots by two experience neurosurgeons with intraoperative recording of sensory evoked potentials
Hayashi 1998[199]	1995 to 1996	Japan	Not described	25	22.8	25:2	Not described	40 (32)	Supraclavicular exploration of extravertebral roots with intraoperative recording of sensory evoked potentials
Hems 1999[181]	1997 to 1999	UK	Consecutive series; temporality unknown	23	30	23:0	11 (48)	Not described	Supraclavicular exploration; no further details
Nakamura 1997[202]	1993 to 1996	Japan	Consecutive series; temporality unknown	10	22	9:1	10 (100)	17 (34)	Exploration with intraoperative recording of sensory evoked potentials
Qin 2016[200]	2007 to 2012	China	Not described	33	33·5	10:1	23 (70)	96 (93)	Exploration with intraoperative recording of sensory evoked potentials
Wade 2018[174]	2008 to 2016	United Kingdom	Consecutive series; retrospective research	47	29	47:0	17 (36)	56 (39)	Supraclavicular exploration and assessment under loupe and operating microscope magnification by the senior author, alongside an intraoperative nerve stimulation.
Yang 2014[203]	2006 to 2010	China	Consecutive series; retrospective research	86	29	77:9	Not described	288 (88)	Exploration of the supraclavicular plexus with intraoperative sensory evoked potentials interpreted in relation to the index test

Table 7. Characteristics of included studies

Study	Scanner Brand and Model	Field Strength (Tesla)	Descriptions of Pulse Sequence(s)	IV Contrast	Number of Reporting Radiologists	Criteria for root avulsion	Frequency of Indeterminate Tests (%)
Abul-Kasim 2010[196]	Siemens Magnetom Avanto	1.5	Sagittal and axial T1w images Axial T2w images Turbo flash gradient echo imaging Coronal STIR (n=7) or 3D CISS (n=3)	No	2	Potential features of root injury described but no thresholds or criteria were clearly defined	Not described
Chanlalit 2015[197]	GE Signa	1.5	T1w TSE images of TR 600-800ms, TE 12.8-20ms, 3mm slice thickness with gaps of 0.5-1mm, with respiratory motion compensation T2w TSE images (TR 4000-5000, TE 102) with a thickness of 3 mm, a gap of 0.5-1 mm with an ETL of 4 or 8, and fat and vessel suppression	No	2	Potential features of root injury described but no thresholds or criteria were clearly defined	Not described
Doi 2002[198]	Siemens Magnetom Harmony	1.0	Axial and coronal-oblique T2w TSE, 5 slices of 2mm thickness with 1mm overlap, TR 4000ms, TE 130ms, 6 averages, rectangular FOV 250mm, 120x256 matrix, no fat suppression	No	8	Yes	1 patient (10%)
Dubuisson 2002[180]	Unknown	Unknown	Not described	Not described	Not described	No	33 patients (83%)
Gasparotti 1997[201]	Unknown	1.5	Not described	Not described	2	Yes	Not described
Hayashi 1998[199]	Siemens Magnetom Vision	1.5	Axial and sagittal T1w SE images of TR 756ms, TE 12ms, 4mm slice thickness Axial and sagittal T2w TSE images of TR 4700, TE 112, 240x512 matrix, 210x280 FOV, ETL 15 Post contrast T1w SE, TR 525-780ms, TE 12-14ms, 4-5mm slice thickness, 256-240x512 matrix, 125x200-210 FOV with chemical fat suppression in 5/11 patients	Gadolinium	2	No	Not described
Hems 1999[181]	GE	0.5	Sagittal, coronal and axial T1w and T2w images	No	Not described	Potential features of root injury described but no thresholds or criteria were clearly defined	Not described
Nakamura 1997[202]	GE Signa	1.5	Sagittal and axial 3D T2w TSE images (TR 2000ms, TE 200ms, slice thickness 2-5 mm, FOV 24cm, 256x256 matrix; no slice gap) compiled into a MIP	Not described	Not described	No	Not described
Qin 2016[200]	Siemens Magnetom Trio	3	T1w and T2w SE 3D PSIF of TR 9.26ms, TE 4.91ms, matrix, 448x448 mm, flip angle 180°, FOV 280x280 mm; bandwidth 686 Hz/px; slice thickness 2 mm, in-plane resolution 1.1x1.5 mm; 2 acquisitions)	Not described	2	No	Not described
Wade 2018[174]	Siemens Magnetom Avanto	1.5	Axial and sagittal T1w and T2w TSE Coronal CISS (0.7mm slice thickness, TR 11.5ms, TE 5.7ms, 320 matrix, flip angle 28°)	No	1	Yes	9 (24%)
Yang 2014[203]	Siemens Magnetom Trio	3	Coronal T1w, T2w, T2*w multi-echo and STIR imaging to compile MIPs and multiplanar reconstructions	Not described	2	Potential features of root injury described but no thresholds or criteria were clearly defined	Not described

Table 8. Characteristics of the Index Test. CISS = constructive interference in steady state, ETL = echo train length, FOV = field of view, MIP = maximum intensity projection, PSIR = phase sensitive inversion recovery, SE = spin-echo, STIR = short tau inversion recovery, T1w = T1-weighted, T2w = T2-weighted, TE = time to echo, TR = repetition time, TSE = turbo/fast spin echo

1.11.3.2   Study characteristics

Study characteristics are presented in Table 7 and Table 8. Studies originated from the UK[174,181], Sweden[196], China[200,203], Japan[198,199,202], Belgium[180], Italy[201] and Thailand[197]. All studies were small with a median sample size of 23 (interquartile range [IQR] 9, 31; range 7 to 86) and conducted between 1992 and 2016. One study was reported as retrospective[174] whist the remainder did not describe the design.

Overall, 275 adults with traumatic brachial plexus injuries were considered of which, 83% were men (229/275). The mean age of participants was 27 years[174,180,196,197,199–203] and 84% were injured during a motorcycle collision (145/173)[174,197,199–202].

The unit of analysis and therefore the prevalence of root avulsion varied between studies (Table 7 and Table 8). Five studies[174,196,197,200,202] reported the accuracy of MRI for patients and nerves; two studies[180,181] reported results only at the patient level; three studies[199,201,203] reported the accuracy with the nerve as the exclusive unit of analysis; and the unit of analysis was unclear in one study[198] so did not contribute to summary estimates. With the patient as the unit of analysis[174,180,181,196,197,200,202], 104 out of 144 patients (median 72%; IQR 53%, 86%) had at least one root avulsion. With the nerve as the unit of analysis[174,196,197,199–203], 583 out of 918 roots were avulsed (median 55%; IQR 38%, 71%).

The time from injury to MRI was reported in six studies[174,181,196,197,200,202] and varied considerably, with a median delay of 36 days (IQR 26, 66; range 0 to 840 days). The time from injury to exploratory surgery was reported in four studies[174,196,197,203] and also varied, with a median delay of 67 days (IQR 52, 74; range 6 to 399 days).

1.11.3.3   Risk of bias and applicability concerns

The risk of bias and applicability assessment are summarized in Figure 78.

	Risk of Bias				Applicability Concerns		
	Patient Selection	Index Test	Reference Standard	Flow and Timing	Patient Selection	Index Test	Reference Standard
Abul–Kasim 2010	+	?	?	+	+	?	?
Chanlalit 2005	?	?	?	+	?	?	?
Doi 2002	?	+	?	?	?	+	?
Dubuisson 2002	?	–	?	?	?	–	?
Gasparotti 1997	?	+	?	?	?	?	?
Hayashi 1998	–	–	?	?	+	–	?
Hems 1999	+	?	?	+	+	?	?
Nakamura 1997	?	–	?	+	+	–	?
Qin 2016	?	–	?	+	+	–	?
Wade 2018	+	+	?	+	+	+	?
Yang 2014	–	?	?	+	?	?	?

– High ? Unclear + Low

Figure 78. The risk of methodological bias and applicability concerns for included studies

Six studies[180,197,198,200–202] were at unclear risk of selection bias because the sampling strategy was unclear or patients were inappropriately excluded. Hayashi[199] was at high risk of selection bias due to the retrospective exclusion of (an unknown number of) patients whose MRI images were suboptimal. Yang[203] was also at high risk of selection bias as they inappropriately excluded individuals with concomitant injuries. Eight studies[180,181,196,197,199,200,202,203] were at risk of bias concerning the MRI; four studies[180,199,200,202] at high risk because no definition or threshold was described and four studies[181,196,197,203] were at unclear risk because potential features of root avulsion were described but no criteria provided. All eleven studies were at unclear risk of bias regarding the reference standard because the surgeons performing the exploration had knowledge of the

MRI findings; additionally, partial verification bias was present in five studies[198–201,203]. There was an unclear risk of bias in the flow and timing of four studies[180,198,199,201] owing to a lack of information about the time between injury and MRI or surgery.

Five articles[180,197,198,201,203] were of unclear concern regarding the applicability of patient selection due to non-consecutive recruitment. There were applicability concerns for the MRI in nine studies[180,181,196,197,199–203]; four studies[180,199,200,202] were of high concern because no MRI criteria or thresholds were described and five studies[181,196,197,201,203] were of unclear concern because multiple radiologists reported the images[196–201,203], the methods were not described[180,181,202], the description of the MRI protocol was different to the parameters shown in figures[197] or the pulse sequences were not adequately described[180,181,196,200–203]. All eleven studies had unclear applicability concerns regarding the reference standard because surgeons had knowledge of the MRI findings.

1.11.3.4   Synthesis of results

Figure 79 shows the forest plots of the sensitivity and specificity of MRI for root avulsion, according to the unit of analysis. There was no apparent influence of field strength on diagnostic accuracy when the patient was the unit of analysis (Figure 79). When the nerve was the unit of analysis, 3T systems appeared to improve the sensitivity and reduce the specificity (Figure 79). Of note, all studies performed at 3T reported the diagnostic accuracy with the nerve as the unit of analysis, whilst studies at lower field strengths (0.5T and 1.5T) used patients.

Root Avulsion: Unit of Analysis = Patients

Study	TP	FP	FN	TN	Field Strength	Sensitivity (95% CI)	Specificity (95% CI)
Hems 1999	7	0	4	12	0.5T	0.64 [0.31, 0.89]	1.00 [0.74, 1.00]
Nakamura 1997	8	2	0	0	1.5T	1.00 [0.63, 1.00]	0.00 [0.00, 0.84]
Abul–Kasim 2010	4	1	0	2	1.5T	1.00 [0.40, 1.00]	0.67 [0.09, 0.99]
Chanlalit 2005	35	0	0	0	1.5T	1.00 [0.90, 1.00]	Not estimable
Wade 2018	17	2	2	8	1.5T	0.89 [0.67, 0.99]	0.80 [0.44, 0.97]
Dubuisson 2002	3	1	1	2	Unknown	0.75 [0.19, 0.99]	0.67 [0.09, 0.99]
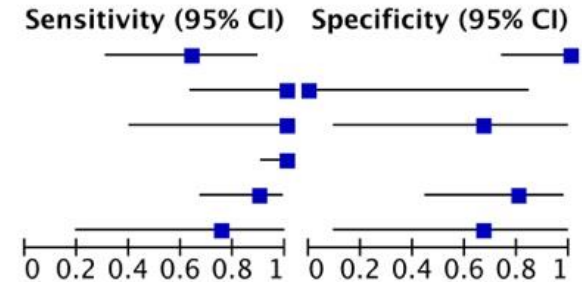
Root Avulsion: Unit of Analysis = Nerves

Study	TP	FP	FN	TN	Field Strength	Sensitivity (95% CI)	Specificity (95% CI)
Gasparotti 1997	21	4	6	32	1.5T	0.78 [0.58, 0.91]	0.89 [0.74, 0.97]
Nakamura 1997	16	4	1	29	1.5T	0.94 [0.71, 1.00]	0.88 [0.72, 0.97]
Abul–Kasim 2010	13	2	2	17	1.5T	0.87 [0.60, 0.98]	0.89 [0.67, 0.99]
Chanlalit 2005	46	24	0	0	1.5T	1.00 [0.92, 1.00]	0.00 [0.00, 0.14]
Wade 2018	30	9	17	89	1.5T	0.64 [0.49, 0.77]	0.91 [0.83, 0.96]
Hayashi 1998	37	42	3	168	3T	0.93 [0.80, 0.98]	0.80 [0.74, 0.85]
Yang 2014	266	11	22	29	3T	0.92 [0.89, 0.95]	0.72 [0.56, 0.85]
Qin 2016	93	3	3	4	3T	0.97 [0.91, 0.99]	0.57 [0.18, 0.90]
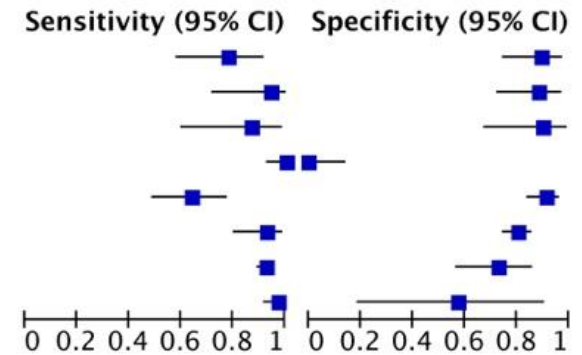
Figure 79. Forest plots of the sensitivity and specificity of MRI for root avulsion with a) patients as the unit of analysis and b) nerves as the unit of analysis. FP = false positive; FN = false negative; TP = true positive; TN = true negative.

Using the nerve as the unit of analysis, the mean sensitivity of MRI for root avulsion was 93% (95% CI 77%, 98%) with a mean specificity of 72% (95% CI 42%, 90%) as shown in Figure 80.

144
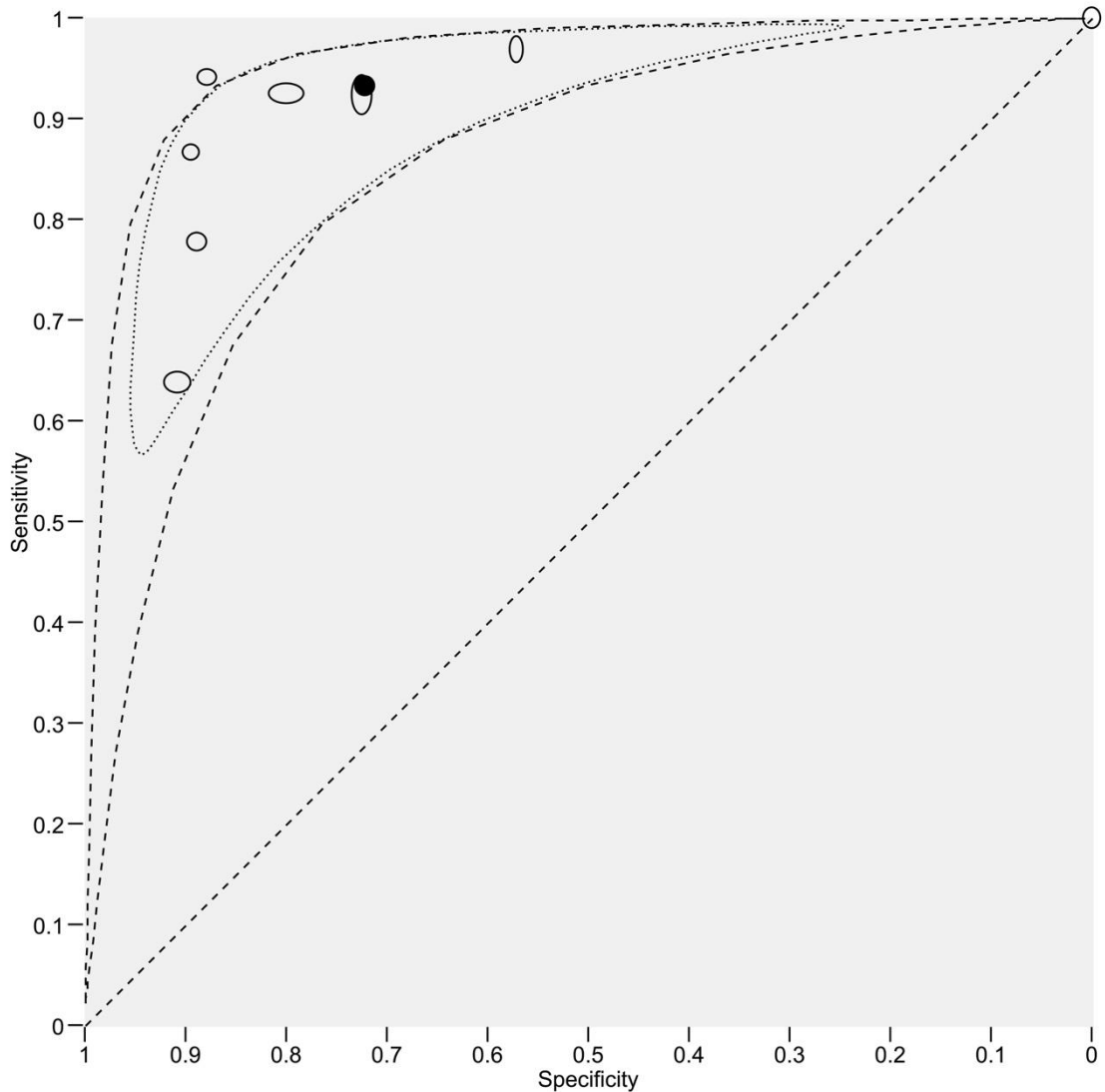
Figure 80. Summary receiver operating characteristic plot of MRI for root avulsion, with the nerve as the unit of analysis. Markers denote studies and are scaled by sample size to indicate the precision of the estimates of sensitivity and specificity from each study. The dotted and dashed regions around the solid (summary) point represent the 95% confidence and 95% prediction regions.

The accuracy of MRI using the patient as the unit of analysis is summarized in a forest plot (Figure 79) and SROC plot below (Figure 81), and varies considerably; a meta-analysis was not possible owing to sparse and heterogenous data. There was insufficient data to estimate the effect of a covariate (e.g., field strength) on the accuracy of MRI.
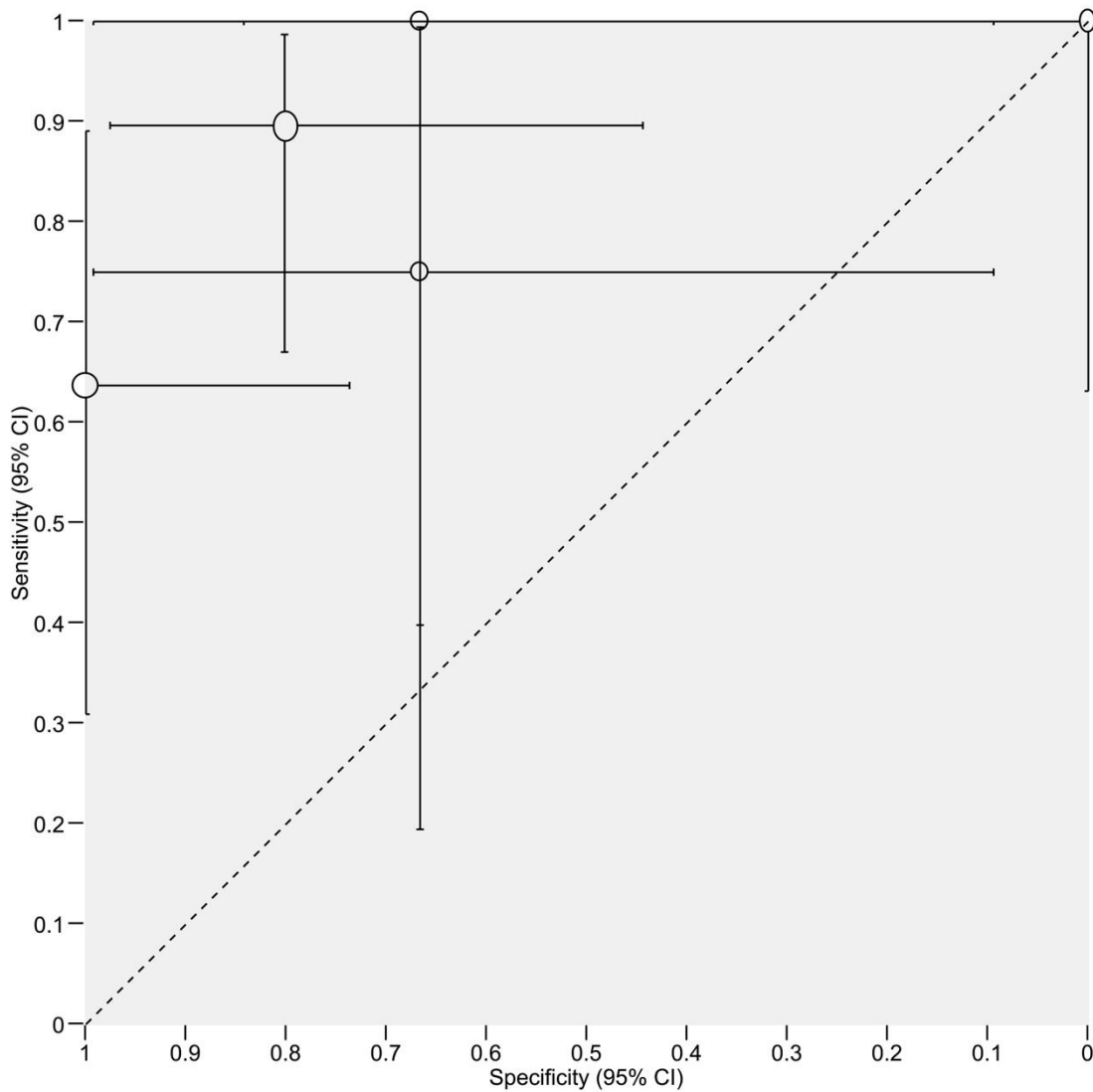
Figure 81. A summary receiver operating characteristic plot of MRI for root avulsion, with patients as the unit of analysis. Markers denote studies and are scaled by sample size to indicate the precision of the estimates of sensitivity and specificity from each study, with 95% confidence intervals.

Forest plots of the sensitivity and specificity of pseudomeningocoeles as a surrogate marker of root avulsion are shown in Figure 82. No meta-analysis was performed owing to the substantial heterogeneity and sparsity of data.

Pseudomeningocoele: Unit of Analysis = Patients

Study	TP	FP	FN	TN	Field Strength	Sensitivity (95% CI)	Specificity (95% CI)
Hems 1999	7	0	4	12	0.5T	0.64 [0.31, 0.89]	1.00 [0.74, 1.00]
Wade 2017	12	3	7	7	1.5T	0.63 [0.38, 0.84]	0.70 [0.35, 0.93]
Qin 2016	15	8	8	2	3T	0.65 [0.43, 0.84]	0.20 [0.03, 0.56]

Pseudomeningocoele: Unit of Analysis = Nerves

Study	TP	FP	FN	TN	Field Strength	Sensitivity (95% CI)	Specificity (95% CI)
Wade 2017	22	12	34	77	1.5T	0.39 [0.26, 0.53]	0.87 [0.78, 0.93]
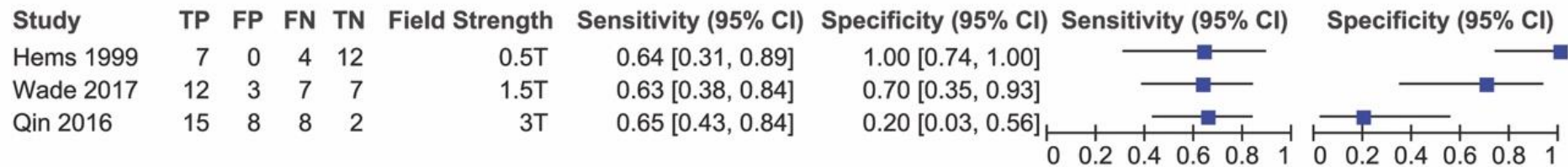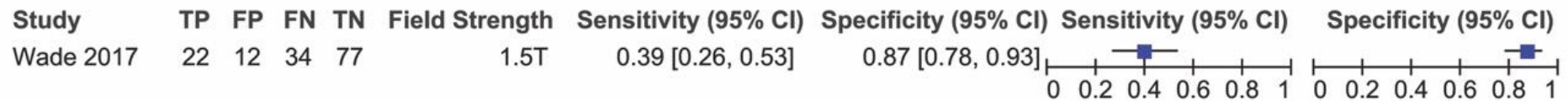
Figure 82. Forest plots of the sensitivity and specificity of MRI for pseudomeningocoeles with a) patients as the unit of analysis and b) nerves as the unit of analysis. FP = false positive; FN = false negative; TP = true positive; TN = true negative.

The clinical consequences of using MRI to diagnose root avulsion are summarised in Table 9 using the median prevalence.

The diagnostic accuracy of MRI for detecting root avulsions in adults with traumatic brachial plexus injuries

Patient population	Adults with symptomatic traumatic brachial plexus injuries.
Prior testing	Highly variable. Patients may experience any of the following: history and mechanism of injury, focussed ultrasound in trauma (FAST), repeated clinical examinations, plain radiographs, computed tomography +/- myelography by lumbar puncture, electrodiagnostic (nerve conduction or electromyography).
Settings	Inpatients in major trauma centres specialising in brachial plexus injuries.
Index test	Preoperative MRI of the brachial plexus.
Reference standard	Surgical exploration and visual inspection of the supraclavicular roots of the brachial plexus under general anaesthesia.
Target condition	Root avulsion(s) of the brachial plexus.
Included studies	11 cross-sectional studies of 275 adults with traumatic brachial plexus injuries that reported the findings of pre-operative MRI and surgical exploration of the roots of the brachial plexus.
Risk of bias and applicability concerns	There was potential for bias in patient selection. The diagnostic criteria for root avulsion were poorly reported. The applicability concerns regarding the reference standard were unclear in all studies.
Data synthesis	The unit of analysis differed between studies. Six studies reported both per-patient and per-nerve analysis. A total of 6 studies reported per-patient while 8 studies reported per-nerve. Meta-analysis was not performed at the patient level due to sparse and heterogeneous data.
Limitations	The study samples may not represent the population. There was poor reporting of diagnostic thresholds. Investigation of heterogeneity was not possible due to limited data. Due to limited and heterogenous data, it is difficult to determine the extent to which the review findings can be applied to clinical practice.

					Consequences per 100 nerves		
Unit of analysis	Studies	Nerves (avulsions)	Mean sensitivity (95% CI)	Mean specificity (95% CI)	Prevalence*	Missed avulsions (95% CI)	Nerves explored unnecessarily (95% CI)
					38 per 100	3 (1, 9)	45 (26, 56)
Nerve	8	918 (583)	93% (77%, 98%)	72% (42%, 90%)	55 per 100	4 (1, 13)	32 (19, 41)
					71 per 100	5 (1, 16)	21 (12, 26)

*Table 9. Summary of findings *These values are the median and interquartile range estimated from the included studies.*

1.11.4 <u>Discussion</u>

Conventional morphological MRI for traumatic brachial plexus root avulsion has a mean sensitivity of 93% (95% CI 77%, 98%) and mean specificity of 72% (95% CI 42%, 90%). This means that MRI fails to identify 7 in 100 avulsed nerves and incorrectly classifies 28 in 100 nerves as avulsed when they are in continuity. Our data suggests that pseudomeningocoeles are an unreliable marker of root avulsion. Moreover, the performance of MRI and the clinical consequences vary depending on the prevalence (Table 2).

1.11.4.1   Diagnostic accuracy

MRI appears to have modest diagnostic accuracy for root avulsions in adults with traumatic brachial plexus injuries, which is unlikely to be acceptable to patients or surgeons given that a false negative may cause irreversible morbidity. Moreover, it is probable that the diagnostic accuracy of morphological MRI is worse than suggested because there were several methodological concerns.[204] Eight studies (73%, 8/11) were at risk of selection bias[197–203] meaning that the samples may not be representative: For example, one study excluded patients whose images were suboptimal[199], which will upwardly bias the accuracy[205]. Furthermore, there were issues in the reporting of MRI in all studies which hampers critical appraisal and translation to practice. We decided to ascribe an unclear risk of bias when surgeons knew the MRI findings because the effect of reviewer bias is inconsistent.[205] Additionally, the lack of detail on pulse sequences limits both the reliability and external validity. Overall, the quality of the included studies in our review was poor because 71% of all QUADAS domains were assessed as high or unclear risk, which is 15% worse than the DTA review data in other fields[206].

1.11.4.2   Prevalence of root avulsion

Our review suggests that root avulsions are found in approximately three in four patients but given the variability of the estimates and quality of the original data, this is unlikely to be reliable. There are several clinical and artefactual factors that might reduce the apparent prevalence of root avulsions and therefore, the accuracy of MRI.[207] Patients with a brachial plexus injury are typically victims of polytrauma who undergo several tests that may identify a problem obscuring or superseding the brachial plexus injury. Polytrauma patients are typically

managed by clinicians who do not specialize in nerve injury, so the intrinsic threshold for identifying the condition and referring the patient might be lower. Moreover, most surgeons do not perform hemilaminectomy when exploring the supraclavicular brachial plexus, so the status of the root proximal to the exit foramen is unknown which might further underestimate the prevalence. Overall, several factors suggest that the true prevalence of root avulsion could be higher than observed, which may have important clinical ramifications.

1.11.4.3   Sensitivity versus specificity

Currently there is no evidence nor consensus to suggest whether a more sensitive or specific test is preferable. A more sensitive test would enable clinicians to rule-out root avulsions (potentially avoiding unnecessary exploratory surgery) although the fiscal and functional cost of false-negatives are substantial, notably lifelong disability[18–22], pain[23–25], mental illness[26,27] and impaired quality of life[18,20,28]. A more specific test might rule-in root avulsion, enabling clinicians to avoid exploration and proceed directly to nerve transfer whilst eliminating prolonged surveillance [37,38,208]. Furthermore, avoidance of unnecessary surgery would reduce morbidity for patients and costs for health services. We accept that a proportion of patients who are root-avulsion negative may have other nerve injuries that warrant reconstruction; however, the diagnosis of root avulsion is of paramount importance. Therefore, improving the specificity of MRI for root avulsion appears to be most desirable.

1.11.4.4   Unit of analysis

In upper extremity nerve surgery, there is no consensus on the unit of analysis (patient, limb or nerve). This is a common issue but profoundly important in upper extremity research.[209,210] In this situation, if the patient is the unit of analysis then MRI would classify patients as either negative (avulsion-free) or positive (between one and five avulsions), which fails to discriminate between distinct patterns of roots injury and wrongly apportions one to five avulsions the same result, introducing composite bias[211]. Conversely, if the root is the unit of analysis, then composite bias is avoided and five clinically meaningful and distinct results are provided. Therefore, we advocate the nerve as the unit of analysis.

1.11.4.5 Conflicting data

There is one systematic review related to this topic which compares the performance of MRI to CT myelography for the diagnosis of root avulsions.[212] The authors concluded that MRI is "*an excellent test for assessing traumatic brachial plexus injuries*"; however, this statement is not substantiated because all three studies were judged to be at risk of methodological bias and no meta-analysis was performed. Their review had no protocol and was not reported in accordance with recommended guidelines. Further, CT myelography carries a demonstrable risk of cancer induction. Therefore, we disagree with the authors findings and suggest that their conclusion is too optimistic[213], and the hazards of CT myelography outweigh the potential benefits as compared to MRI.

1.11.4.6 Limitations

Whilst 20 potentially relevant articles were identified, data extraction was impossible from nine[187–195]. Retrospective studies of medical tests tend to report inflated estimates of diagnostic accuracy[204]; our review included four retrospective studies[174,196,197,203] and seven articles that incompletely described the timeframes between injury, scanning, and surgery. Similarly, studies recruiting non-consecutive (non-random) samples are prone to selection bias and inflated estimates of accuracy[204]; our review included four such articles[180,198–200]. We expected the accuracy of MRI to improve over time, in line with technological and methodological advances, although this is not appreciable (Figure 3). This discord is likely multifactorial and certainly, high-quality prospective research is needed.

1.11.5 Conclusions

In conclusion, based on limited and heterogenous data, morphological MRI offers modest diagnostic accuracy for traumatic brachial plexus root avulsion(s) and it is recommended that early operative exploration remains as the diagnostic method.

Based on this information, we judged that there was a clinical need to develop MRI and as described in section Part 1: Chapter 10, dMRI appears to hold the greatest potential value.

Chapter 12.   Diffusion Tensor Imaging in Adults with Traumatic Brachial Plexus Root Injuries: A Proof-of-Concept Study

1.12.1 Introduction

Approximately 1% of adults involved in major trauma sustain a brachial plexus injury (BPI)[17] which cause disability[18,20], pain[25], psychological morbidity[26] and impaired quality of life[18,20].

Root avulsions are the most prevalent form of injury in traumatic BPI[41]. Root avulsions are high-force injuries which affect all neural elements including the anterior horn cells[42], fibres in the transitional zone and free rootlets, all of which precludes re-implantation[43] and mandates reconstruction by nerve transfer. Nerve transfers are cost-effective[44], low morbidity procedures which significantly improve function[45]. Early diagnosis is of critical importance because early reconstruction improves outcomes[37,38] and might mitigate the chronic neuropathic pain[39], which is experienced by 95% of patients with BPIs[40]. Therefore, early and accurate diagnosis of root avulsion(s) is of paramount importance.

Magnetic resonance imaging (MRI) is the best non-invasive test for diagnosing traumatic brachial plexus root avulsion(s); however, the accuracy of morphological imaging (using conventional sequences which are concerning with resolving macroscopic anatomy) is modest at-best. Moreover, morphological MRI misclassifies approximately 28% of in-continuity nerves as avulsed and fails to identify approximately 7% of true avulsions[41]. Further, there is no consensus (nor data) on the ideal time to scan such patients or which sequences are most accurate. Therefore, there is a pressing need to improve MRI techniques to better evaluate the roots of the brachial plexus.

Diffusion tensor imaging (DTI) characterises tissue microstructure and generates reproducible[114,214–217] proxy measures of nerve 'health' which are sensitive to

myelination, axon diameter, fibre density and organisation[61–63]. DTI is outlined in section 1.7.1 and how DTI metrics change following injury is described in Part 1, Chapter 10. Therefore, we postulate that DTI may be useful for diagnosing nerve injuries, such as root avulsion. The literature concerning DTI of the brachial plexus is sparse, but includes healthy volunteer studies performed at 3T [146–149], injured patients studies at 1.5T [150] and neoplasms [148]. There is a lack of DTI research on adults BPIs performed at 3T, and the typical measurements of diffusivity and anisotropy in these structures following injury is yet to be determined. The potential for DTI to provide a meaningful supplemental assessment of the roots (alongside current sequences) for adults with traumatic BPIs and the deficit of research on this important problem forms the rationale for this proof-of-concept study.

Our hypothesis was that at the level of a root avulsion, diffusion tensor imagin may be sensitive to changes in tissue microstructure (where morphological MRI is insensitive) and tractography would demonstrate breaks in streamlines which may represent the zone of injury. Therefore, we aimed to develop a DTI sequence to visualise the roots and compare the findings between healthy and injured patients.

1.12.2 Methods

This cross-sectional study was designed and reported in accordance with the STARD guidance[218], taking into account the domains of the QUADAS-2[182] and PRISMA-DTA[219] tools. This study was approved by the National Health Service Health Research Authority (16/YH/0162) and written informed consent was provided by all participants.

1.12.2.1   Subjects

After a period of sequence development, DTI data from 7 prospectively recruited healthy individuals (4 males and 3 females, with a mean age of 28 years [standard deviation, SD 9] which represents the population at-risk) were acquired. Thereafter, we recruited 12 adults (all male) with unilateral brachial plexus root avulsions who were surgically exploration by a single surgeon between 2009 and 2014 (with a median of 6 years [IQR 4, 7] between surgery to DTI); these patients had not had any form of reconstruction in the neck (when injured, they had

received distal nerve transfers) and had since been discharged from clinical services. Ten patients sustained their injuries in motorcycle collisions, one man fell from a 1st story window and one pedal-cyclist was hit by a car. The mean age at the time of injury was 30 years (SD 9) and mean age at the time of DTI was 35 (SD 10), neither of which was statistically different to the age of healthy volunteers. Individuals were excluded for standard MRI-safety concerns, claustrophobia, the inability to lie still (e.g. due to athetoid movements, dystonias, chorea, etc), a bilateral BPI and any other neurological disorder which impaired the affected limb.

1.12.2.2 Image acquisition

We were concerned with the ability of deterministic tractography from DTI to differentiate normal roots (no root avulsion) from abnormal roots (suspected root avulsion). DTI data were acquired at a field strength of 3T using a Siemens Magnetom Prisma (Siemens Healthcare Limited, Erlangen, Germany) and single-shot echo-planar imaging (ssEPI) sequence. The acquisition parameters were as follows: 45 axial slices of 2.5m, thickness, $2.5mm^2$ in plane resolution, field-of-view 305×305×105mm from the C3/4 to T2/3 intervertebral discs. Twenty diffusion directions using twice refocused spin echoes were used, with ten averages of the b0, a b-value of 1000 s/mm^2, a TrueForm B1 shim and up to 2nd order B_0 shimming was performed, with the shim and imaging volumes matched to improve B_0 homogeneity. An AP phase encoding direction was used with 4 repetitions averaged inline. The repetition time was 4300ms, echo time 66ms, echo spacing 0.5ms, echo train length 445ms, GRAPPA factor 2, receiver bandwidth 2276Hz, interleaved with motion correction on, distortion correction off and strong fat saturation. A 64-channel head and neck coil in combination with posterior spine coils were used. The acquisition time was 6 minutes 41 seconds.

1.12.2.3 Image reconstruction

We sought to test tractography without pre-processing, using software on the operator console (Siemens NeuroLab 3D). Seeding regions were manually placed to cover the cervical spinal cord in cross-section. Streamlines were propagated using polylines with the following termination thresholds: FA 0.06 or 35° angle. There were 4 samples per voxel and the step length was 1.15mm.

Tractograms were viewed by a single musculoskeletal radiologist (JJR) with 20 years of experience in brachial plexus and spinal imaging. The test was considered positive for root avulsion when there was a visible lack of continuity between the streamlines in the spinal cord and the brachial plexus or an absence of streamlines attaching to the spinal cord. The diagnosis of root avulsion was binary with implicit threshold. The mean (and SD) fractional anisotropy (FA) and mean diffusivity (MD) were calculated from a region of interest (ROI) which consisted of five 2.5mm^2 pixels (Figure 83) covering the lateral recess of the vertebral foramen. Values for the cervical cord were derived from the corresponding cervical level.

Figure 83. Axial MD map showing the placement of ROIs in the lateral recess of the vertebral foramina

1.12.2.4   Reference standard

All patients underwent surgical exploration of all roots (C5-T1) prior to recruitment. Hemilaminectomy was not performed. Somatosensory evoked potentials were not used. Avulsion was a binary outcome with implicit threshold, defined by any combination of the following: the absence of a nerve root in the exit foramina; relaxation, attenuation and displacement of a scarred proximal nerve trunk or a visible dorsal root ganglion; no identifiable nerve fascicles on exploration of the nerve root; empty proximal nerve sheaths. If there was a neural structure in the foramen but it was easily pulled away, then avulsion was diagnosed. Other MR sequences were not used at the reference standard

because these too may be inaccurate; the best possible method of determining the integrity and suitability of the root for reconstruction is direct visualisation by surgical exploration.

1.12.2.5 Statistical analysis

Data were analysed using Stata v15 (StataCop LLC, Texas). Age was skewed so is represented by the median and interquartile range (IQR) and compared using the Wilcoxon rank-sum test. Other scaled variables are represented by the mean (and standard deviation, SD) and compared using independent samples t-test. The true positive (TP), false positive (FP), true negative (TN) and false negative (FN) vales are calculated based on the findings of the index and reference tests. Significance was set at 5%.

1.12.3 Results

1.12.3.1 Deterministic tractography

The normal brachial plexus is shown in four volunteers in Figure 84. Four different patterns of root avulsions are shown in Figure 85. The diagnostic accuracy of deterministic DTI for root avulsions is shown in Table 10, with an overall diagnostic accuracy of 71% (95% CI 54, 85).

Diagnostic test accuracy statistics

	Avulsion at operation		Sensitivity (95% CI)	Specificity (95% CI)	Positive Predictive Value (95% CI)	Negative Predictive Value (95% CI)
	Yes	No				
Suspicion of at least one root avulsion	Yes	12	11	100	58	52	100
	No	0	15	(74, 100)	(37, 78)	(31, 73)	(78, 100)
Absent C5 tract	Yes	3	1	50	97	75	91
	No	3	31	(12, 88)	(84, 100)	(19, 100)	(76, 98)
Absent C6 tract	Yes	6	0	67	100	100	91
	No	3	29	(30, 93)	(88, 100)	(52, 100)	(79, 96)
Absent C7 tract	Yes	8	1	89	97	89	97
	No	1	28	(52, 100)	(82, 100)	(54, 98)	(81, 99)
Absent C8 tract	Yes	7	7	100	77	49	100
	No	0	24	(60, 100)	(59, 90)	(34, 65)	(83, 100)
Absent T1 tract	Yes	5	14	100	58	26	100
	No	0	19	(48, 100)	(39, 75)	(19, 34)	(79, 100)

Table 10. Diagnostic accuracy of DTI deterministic tractography
(19 individuals, 190 cervical roots). The 2x2 contingency table
(with column and row headings of yes and no) show the true
positive, false positive, false negative and true negative values.
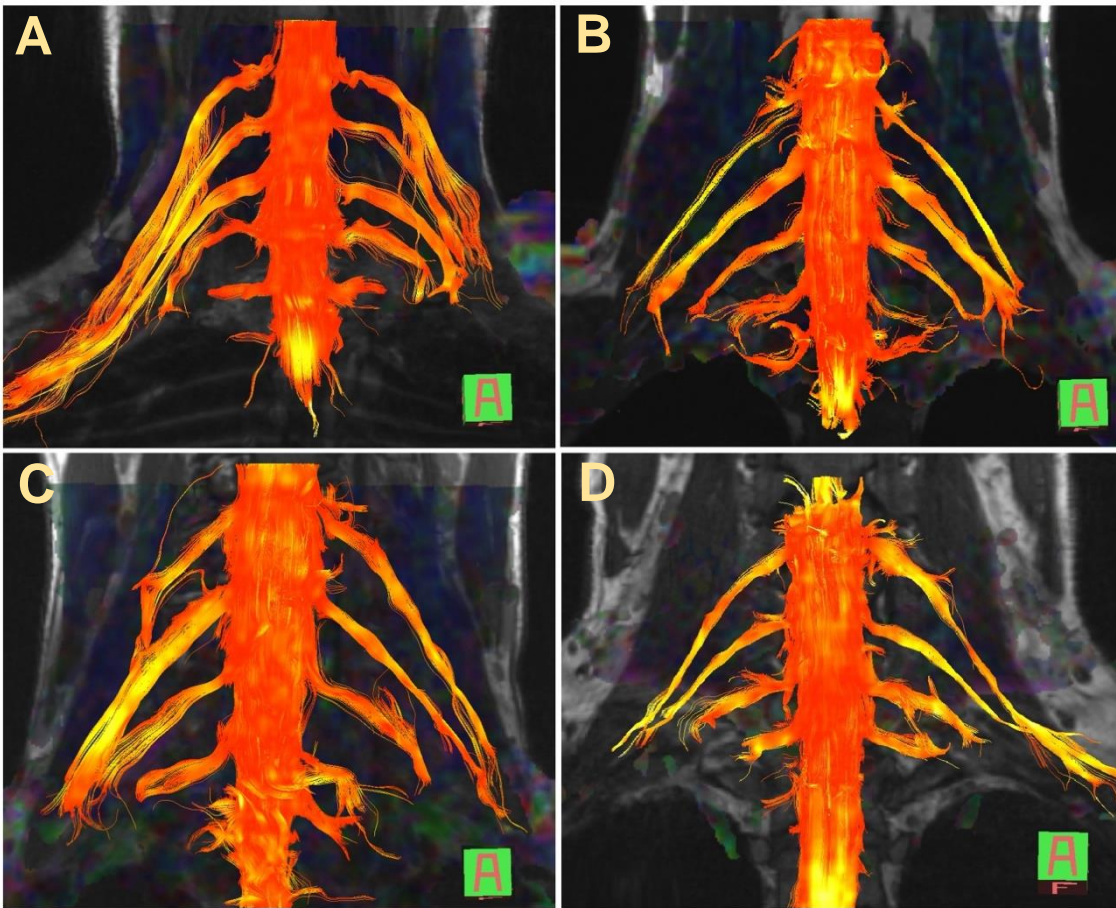
Figure 84. DTI deterministic tractography of the cervical cord and brachial plexus in four healthy volunteers.

Typically, streamline bundles representing the C5-8 roots were consistently visualised which is reflected in the high positive predictive values. However, streamlines representing the T1 root were less often visualised (5/14 T1 roots in healthy controls and 7/10 T1 roots on patients' uninjured side).

Four patients had Horner's syndrome and when this was observed, the probability of absent streamlines representing the T1 root was 100% (PPV 100%). However, if there were no features of Horner's syndrome, there was a 3% probability of an absent T1 root tract (NPV 97%; 95% CI 85, 100).
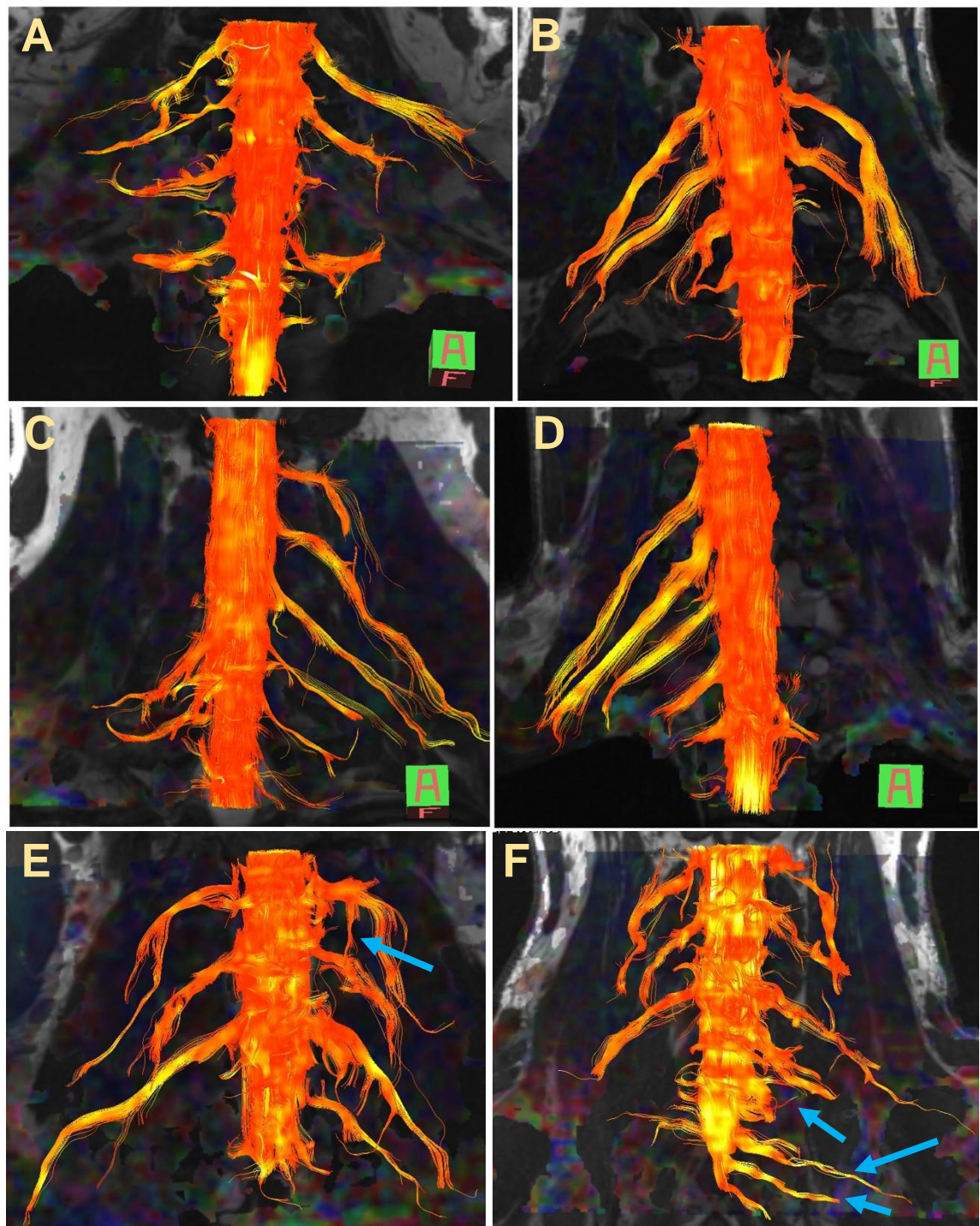
Figure 85. DTI deterministic tractography of the cervical cord and brachial plexus. A-D show tractograms from four patients in which the streamlines matched the clinical findings. A) Isolated left C7 avulsion, B) Left C7, C8 and T1 avulsions, D) Right C5, C6 and C7 avulsions and E) Left panplexus avulsion. Panels E and F show tractograms with spurious false streamlines (blue arrows) and show instances where streamlines were generated for the right C5 root despite the fact that both were found to be avulsed at operation.

Diffusion tensor imaging metrics

Table 2 shows the FA and MD for the roots and corresponding levels of the cervical cord. Compared to healthy roots, the MD was 0.32 x10^{-3} mm^2/s higher (95% CI 0.11, 0.53; p<0.001; Figure 86) and the FA 10% lower in avulsed roots (95% CI 7%, 13%; p<0.001; Figure 87). The MD and FA values from the cervical cord at levels subject to avulsion injury compared to uninjured levels were not significantly different (Table 11).
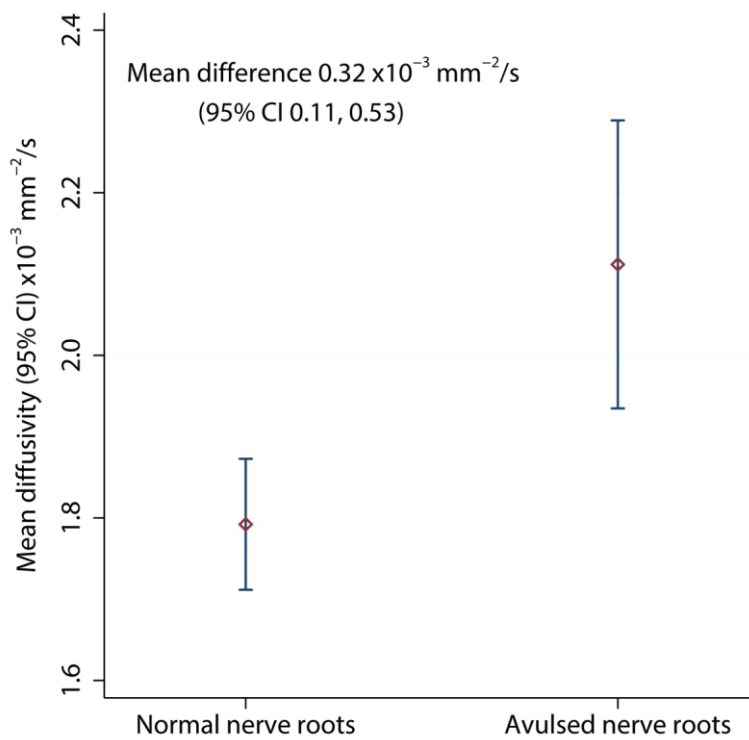
Figure 86. The mean diffusivity of the lateral recess of the vertebral foramen, housing either normal or avulsed C5-T1 nerve roots.
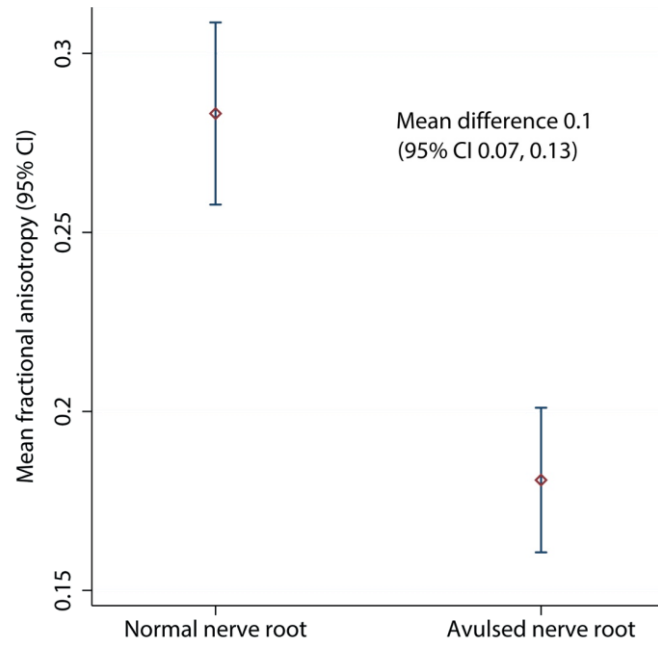
Figure 87. The fractional anisotropy of the lateral recess of the vertebral foramen, housing either normal or avulsed C5-T1 nerve roots.

Mean (SD) DTI parameters

Anatomical structure	Level	Mean Diffusivity in mm^2/s x10^{-3}			Fractional Anisotropy		
		Normal roots[¥]	Root avulsions[*]	p-value	Normal roots[¥]	Root avulsions[*]	p-value
Spinal cord	C5	1.25 (0.25)	1.09 (0.23)	0.2	0.49 (0.10)	0.54 (0.09)	0.3
	C6	1.24 (0.25)	1.20 (0.21)	0.8	0.53 (0.07)	0.50 (0.07)	0.7
	C7	1.31 (0.31)	1.27 (0.22)	0.8	0.47 (0.09)	0.45 (0.08)	0.7
	C8	1.33 (0.29)	1.26 (0.21)	0.6	0.48 (0.09)	0.52 (0.09)	0.7
	T1	1.31 (0.31)	1.22 (0.24)	0.3	0.53 (0.01)	0.49 (0.10)	0.6
	Overall[∞]	1.29 (0.28)	1.21 (0.22)	0.1	0.50 (0.09)	0.51 (0.08)	0.8
Lateral recess of the vertebral foramen	C5	1.90 (0.43)	1.94 (0.33)	0.9	0.28 (0.07)	0.21 (0.08)	0.5
	C6	1.82 (0.37)	2.06 (0.40)	0.2	0.28 (0.08)	0.17 (0.05)	0.09
	C7	1.80 (0.35)	2.25 (0.39)	0.03	0.21 (0.06)	0.16 (0.03)	0.05
	C8	1.75 (0.37)	2.17 (0.27)	0.05	0.28 (0.08)	0.20 (0.05)	0.2
	T1	1.68 (0.34)	2.07 (0.43)	0.1	0.30 (0.09)	0.18 (0.05)	0.1
	Overall[∞]	1.79 (0.18)	2.11 (0.36)	0.002	0.28 (0.08)	0.18 (0.06)	0.008

*Table 11. Diffusion measurements from the spinal cord and roots of the brachial plexus. * Defined by the reference standard of operative exploration. ¥ In patients this is defined by the reference standard of operative exploration of the injured sides or the normal (non explored side; all roots were defined as normal in healthy volunteers. ∞ The arithmetic mean of the five levels*

1.12.4 Discussion

This study demonstrates the potential clinical utility of diffusion tensor imaging for capturing information on the microstructure of the roots of the brachial plexus. Furthermore, deterministic tractography appears to help visualise the continuity of the roots of the brachial plexus and differentiate adults with established root avulsion from healthy controls. This technique may supplement conventional MRI sequences (which have modest accuracy[41]) and provide readily interpretable tractograms alongside diffusion metrics.

1.12.4.1   Tractography in healthy adults

Our findings are in agreement with the limited literature concerning DTI of the brachial plexus at 3T[146,147,149], all of which report deterministic tractography in healthy volunteers. We based our pulse sequence and tracking methods on that of [149]); their work captured FA values of 0.27 to 0.43 (mean 0.34) and MD values of 1.4×10^{-3} to 1.8×10^{-3} mm^2/s (mean 1.6×10^{-3} mm^2/s), although they omitted to describe which anatomical structure from which these values were derived which might explain the disparity with our data. It's possible that these values were from extraforaminal sections of the roots, or the average value from streamlines or otherwise. Ho et al., (2017)[147] used a 1.9mm isotropic ssEPI sequence with 30 diffusion directions, a b-value of 800 s/mm^2 and longer TE/TR values than us. In their report, their FA values were approximately 10% higher and MD 0.2×10^{-3} mm^3/s lower than our data. Similarly, Oudeman et al., (2018)[146] used 3mm isotropic EPI with 15 diffusion directions, a b-value of 800 s/mm^2 and longer TE/TR values than us. Their FA and MD values were derived from the trunks and are comparable to ours (0.33 ± 0.04 vs 0.28 ± 0.08) although again, their MD values were approximately 0.5×10^{-3} mm^2/s lower. The differences in the MD between Ho's and Ouderman's work compared to ours and Tagliafico's might be explained by differences in the b-value[220] and other experimental conditions (e.g. methods of averaging, partial volume effects, etc). Overall, our data adds to the literature and suggests that deterministic tractography and FA/MD extraction from the brachial plexus is both possible and of potential clinical utility.

1.12.4.2 Tractography in root avulsions

Aside from the present work, Gasparotti et al., (2013)[150] assessed the agreement between conventional diffusion-weighted and diffusion tensor imaging for diagnosing root avulsion(s). Their offline processing corrected for artefacts and distortions caused by eddy-currents and motion, whilst we corrected for the latter inline and tested a more streamlined approach which may be preferable from a clinical perspective. Our findings suggest that universal exportation of data and pre-processing in 3rd party software may not be imperative to yield clinically meaningful tractograms of the brachial plexus. Nonetheless, more work is needed on the topics of acquisition optimisation, pre-processing and if/how these DTI-specific metrics relate to nerve microstructure.

1.12.4.3 Diagnostic accuracy

Specificity is arguably of paramount importance in imaging adult brachial plexus injuries[41]. Gasparotti et al., (2013)[150] showed that DTI had an overall specificity of 99% and sensitivity of 85%; however, they used another form of diffusion-weighted MRI as the reference standard which is probably less accurate than surgical exploration, which is likely to inflate the estimates of accuracy. Similarly, our estimates of diagnostic accuracy may be overstated because we had knowledge of the results of the reference test (exploration).

1.12.4.4 The T1 root

There are a number of potential reasons to explain why we and others[146,147,149] are currently unable to have confidence in diffusion data acquired from the T1 root. The T1 root will be affected by susceptibility artefact due to the diamagnetic and paramagnetic effects of 1st rib and air in the apical lung, respectively, causing signal loss due to T2*-dephasing and mis-mapping. The proximity between the T1 root and the subclavian artery may cause flow and partial volume effects. Respiratory motion may cause mis-mapping, which cannot be fully corrected by inline or offline motion correction. Similarly, eddy-currents may cause distortion or misregistration due to spatial nonlinearities and frequency/phase shifts. Overall, our data are similar to the works of [146221], [149222] and [147223]. In comparison, Gasparotti[150] visualised the T1 root in all cases (except three cases which were degraded by undefined artefact) which might in-part be due to the lower (1.5T)

field strength and pre-processing they performed. In the future, we intend to experiment with different acquisition parameters and offline corrections for eddy-currents, motion and distortion to explore if this improves the visualisation of the T1 root.

1.12.4.5   Limitations

The diagnostic accuracy in this study is likely to be upwardly biased because we knew the pattern of avulsions and the sample was non-consecutive (non-random)[204]; future work by our group is investigating the utility of preoperative DTI on a consecutive series of patients with traumatic BPIs subject to the reference standard of exploratory surgery. We imaged patients years after their injury whereas clinicians need this information is in the weeks/months after injury. DTI parameters reflect changes in the proximal and distal stumps of peripheral nerves in animals within days of injury[61,62,144].

DTI is sensitive to Wallerian degeneration in the injured spinal cord of animals[224–227] and humans[228–231] within 3 days and for up to 1 year, respectively. DTI is also sensitive to degenerative changes in the white matter tracts of the brain over several years[232]. Notwithstanding, there is a lack of research concerning DTI parameters years following peripheral nerve injury and so the effect of time can only be surmised. We believe that as the avulsed distal nerve degenerates, diffusion in the structure would regress to a similar isotropy of connective tissue (scar). Furthermore, whether DTI is useful in the acutely injured patient remains unknown and this is the subject of ongoing prospective research by our group.

Different protocols and techniques for tractography of DTI data can generate substantial variability in tractograms. The Diffusion Study Group of the International Society for Magnetic Resonance in Medicine (ISMRM) formed an international collaborative of 144 dMRI experts, who analysed 57 unique datasets to generate 3138 fibre bundles of major white matter pathways in the brain[233]. This group interrogated the inter-protocol, intra-protocol and inter-subject variability of such bundles to understand how different approaches to tractography altered the outputs. Overall, they showed variability in both the inter-protocol (different researchers using protocols) and intra-protocol (different researchers using the same protocol) experiments (Figure 88). The FA within a

bundle varied by 8-12% across protocols. However, when FA was weighted by the density of fibres in the voxel, the variability reduced to 4-7%. This is an important finding for imaging of the brachial plexus roots because the fibres in healthy adults' spinal roots are normally coherent, densely packed and have distinct anatomical boundaries. Importantly, this work demonstrated that the largest variability in tractography output was between subjects, which implies that standardisation of analysis is needed to minimise residual variance and enable comparisons between subjects.
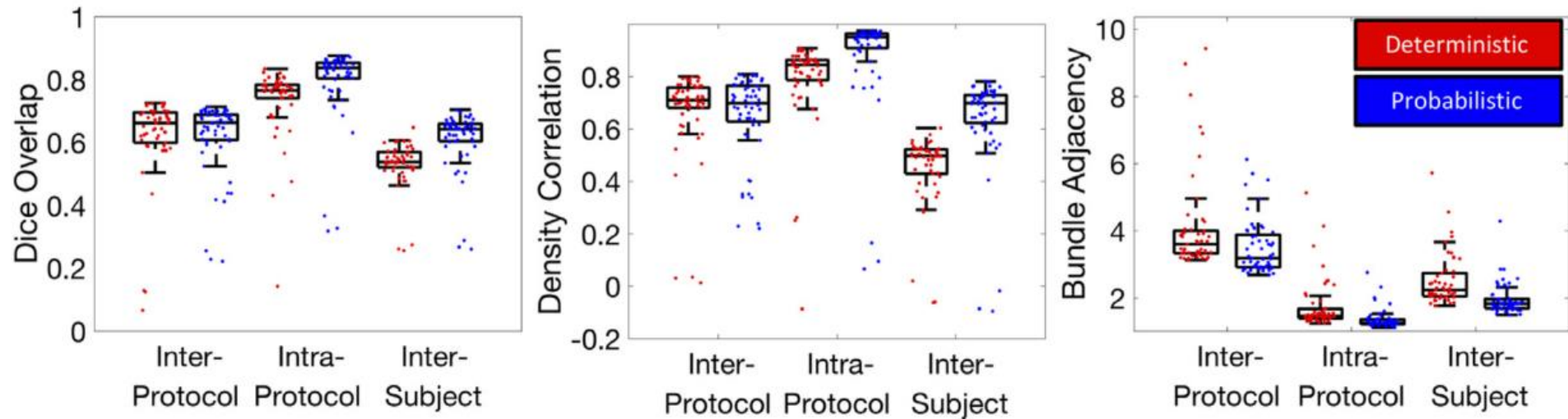
Figure 88. Box plots of Dice overlap (left), density correlation (middle), and bundle adjacency quantify (right) for inter-protocol, intra-protocol and inter-subject variability (deterministic: red; probabilistic: blue). Reproduced from Schilling et al (2021)[233].

Our proof-of-concept work on DTI in the brachial plexus, in comparison to prior dMRI works on this anatomical area has highlighted important variability in data acquisition, tractography methods and consequently, DTI metrics. In the same way that international collaboratives are seeking to standardise the preprocessing steps and tractography methods[233] for dMRI brain, we suggest that standardisation of dMRI in the brachial plexus can only be beneficial. In the following chapters, we outline work which explores the effects of signal averaging, different pre-processing software pipelines, altering the step angle and FA thresholds used for streamline propagation and how these effect the resultant tractograms and DTI metrics extracted from the roots.

1.12.5 **Conclusions**

This early work demonstrates that the diffusion tensor imaging (without pre-processing) appears to be sensitive to the microstructural differences of healthy and chronically injured roots in adults. However, this work has also highlighted several uncertainties including requisites for data acquisition, how best to pre-process data and what thresholds are required for tractography which will be examined in subsequent chapters.

Chapter 13. The Geometry of the Roots of the Brachial Plexus

1.13.1 Introduction

There has been a recent surge in the development of diffusion tensor imaging of the brachial plexus[234,235] given the ability to generate tractograms which can convey also information about local diffusivity through colour (Figure 89).
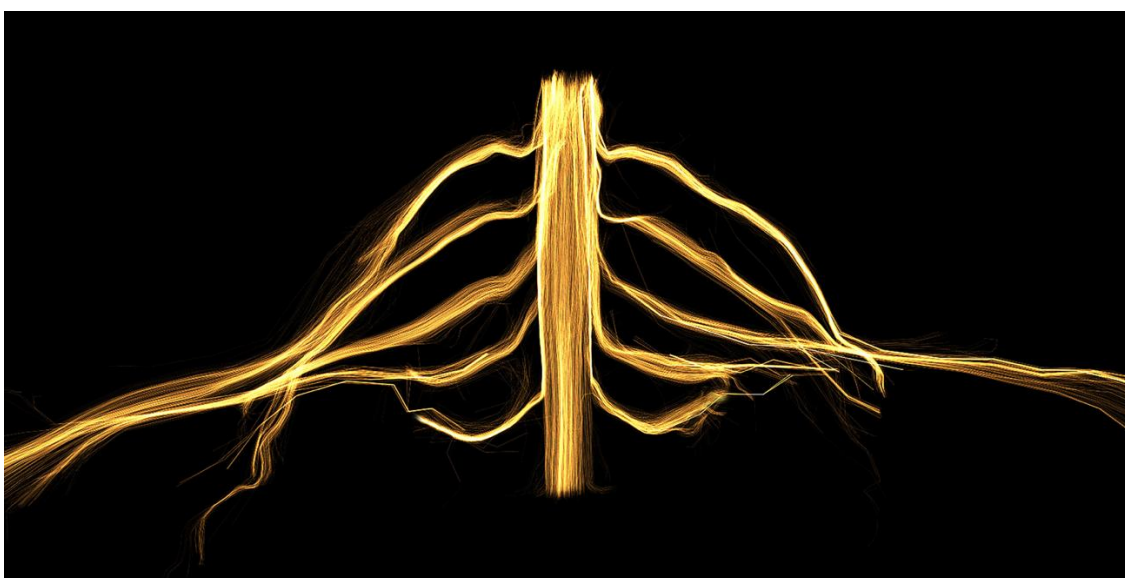
Figure 89. A deterministic tractogram of the cervical spinal cord and brachial plexus in a healthy adult.

A simplification of the process involved in creating a tractogram from DTI data is shown in Figure 90 and demonstrates the importance of the turning/step angle in generating streamlines[236]. The step angle is an important factor to consider when tracking tortuous structures across adjacent voxels (rather than structures which may be tortuous at the microscopic, intra-voxel level). If the user selects a step angle which is excessively high, then numerous non-valid and looping streamlines may be produced. If the step angle is too low then streamlines will not propagate. Therefore, when performing tractography on tortuous structures (such as the roots of the brachial plexus) it is important to select a step angle which is sufficient to propagate valid streamlines but not higher than necessary, to minimise non-valid streamlines.
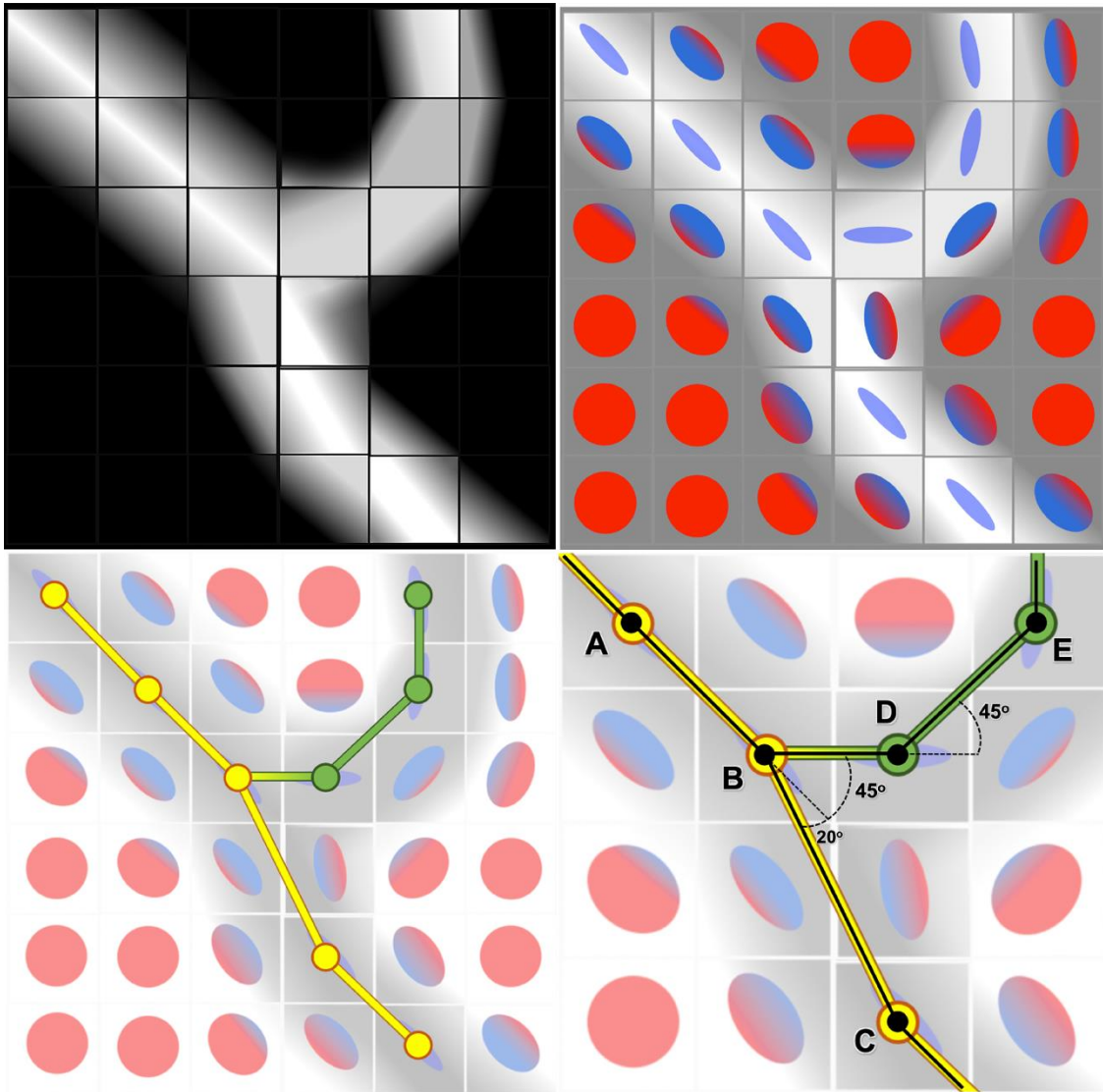
Figure 90. A simplification of DTI tractography. A) A 2D artistic example of a diffusion weighted image through an imaginary bifurcating nerve. B) Diffusion is modelled by a tensor and shown as an ellipsoid, whereby the colour denotes the direction and the shape describes the degree of anisotropy. C) Streamlines (line segments) are propagated along voxels with locally aligned primary eigenvectors which exceed a specified FA. D) A zoomed section of Panel C shows that users must specify the maximum angle allowed between new line segments (the step angle aka turning angle). To track the yellow portion of the nerve (line segment $\overrightarrow{ABC}$) a threshold of ≤25° would be sufficient but to track the green section of the nerve also (line segment $\overrightarrow{ABDE}$), a higher step angle would be needed.

Two anatomical studies have investigated the geometry of the brachial plexus in adult cadavers[237,238]. Xiang et al. (2008)[237] summarised the microanatomy of the dorsal root entry zone and dorsal rootlets, showing that the average angle between the inferior rootlets of T1 and the median sulcus of the spinal cord was 66° in the coronal plane; this angle decreased in a cranial direction with the C4 root branching at 20°. Xiang et al. (2008)[237] provided a valuable insight into the step angle needed to propagate streamlines of the rootlets but their study only considered the most proximal 1.5cm (the rootlets) of the brachial plexus. More recently, Zhong et al. (2017)[238] performed similar dissections although they only acquired a single measurement of the angle between the median sulcus of the spinal cord and each spinal root at the level of the dorsal root ganglion in the coronal plane (Figure 91), which substantially underestimates the complexity of the geometry of the roots.
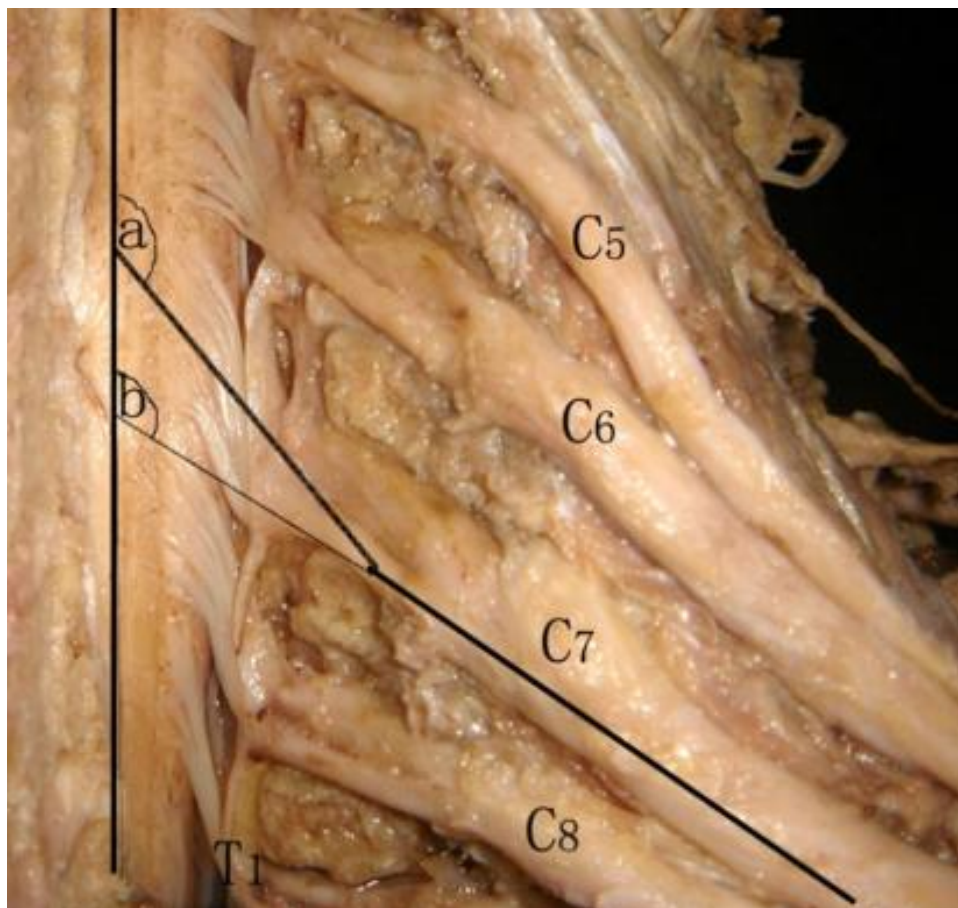
Figure 91. The methods used by Zhong et al (2017)[238] to measure the acute angle between the median sulcus of the spinal cord and the spinal roots of the brachial plexus.

The published anatomical studies provide limited information on the geometry of the brachial plexus, which is why there is wide variation in the step angles (14° to 70°) used in DTI studies of the brachial plexus to-date[239–243]. The need for precise and detailed geometric information, which can be translated to tractography, represents the rationale for this study.

1.13.2 Methods

This anatomical study, which was conducted between June and August 2019, included ten adult cadavers (of mean age 85 years) donated to the Leeds Medical School. Each donor had given written consent to donation and to the use of their body for research purposes. Approval for the work was granted by the University of Leeds Anatomy Access Committee (Reference 200619). The study complied with the Human Tissue Act (2004).

1.13.2.1 Objectives

The primary objective was to detail the geometry of the rootlets and spinal roots of the brachial plexus in two dimensions (in the coronal plane).

1.13.2.2 Embalming process

Donors were perfused through the left common carotid or femoral artery with approximately 30-50 litres of a premixed preservation fluid consisting of 1.6% formaldehyde, 3.8% Methanol, 9% water, 10% Phenol and 75.6% Ethanol. Cadavers were stored at 4°C until dissection.

1.13.2.3 Dissection

The spinal cord and brachial plexus were demonstrated bilaterally via a posterior approach, with osteotomies through the pedicles of C4-T1. The dorsal and ventral rootlets have an identical length, and angles in both the coronal and axial planes within the spinal canal[238], so to preserve the exact course of dorsal rootlets and spinal roots, the anterior (ventral) rootlets were not dissected (Figure 92). None of the cadavers had any relevant pathology.

Figure 92. A posterior dissection of the spinal cord and roots of the brachial plexus.

1.13.2.4   Photography and image analysis

All specimens were photographed under fixed conditions using the same camera consistently positioned orthogonal to the imaging plane at 30 cm from the C7 cord level to the lens. A ruler with 1mm increments was included in the field of view adjacent to the roots. Images were imported to MATLAB R2019b (The Mathworks, Inc., Natick, Massachusetts, United States of America), calibrated and a 2.5mm^2 cartesian grid overlaid. Twenty-one points were placed at 2.5mm intervals along the left-right direction, starting from the respective dorsal root entry zone and extending for 5cm along each of the C5-T1 nerve roots (Figure 93). We chose to trace the mid-point of the rootlets/roots because this approach provided the lowest possible estimate of the step angle through the course of the nerves. Further, when tractography algorithms are tracking into nearby voxels of similar anisotropy, streamlines will preferentially propagate into the voxel with the lowest

step angle. The line segments between points were plotted and the step angles and gradient of each line were resolved.
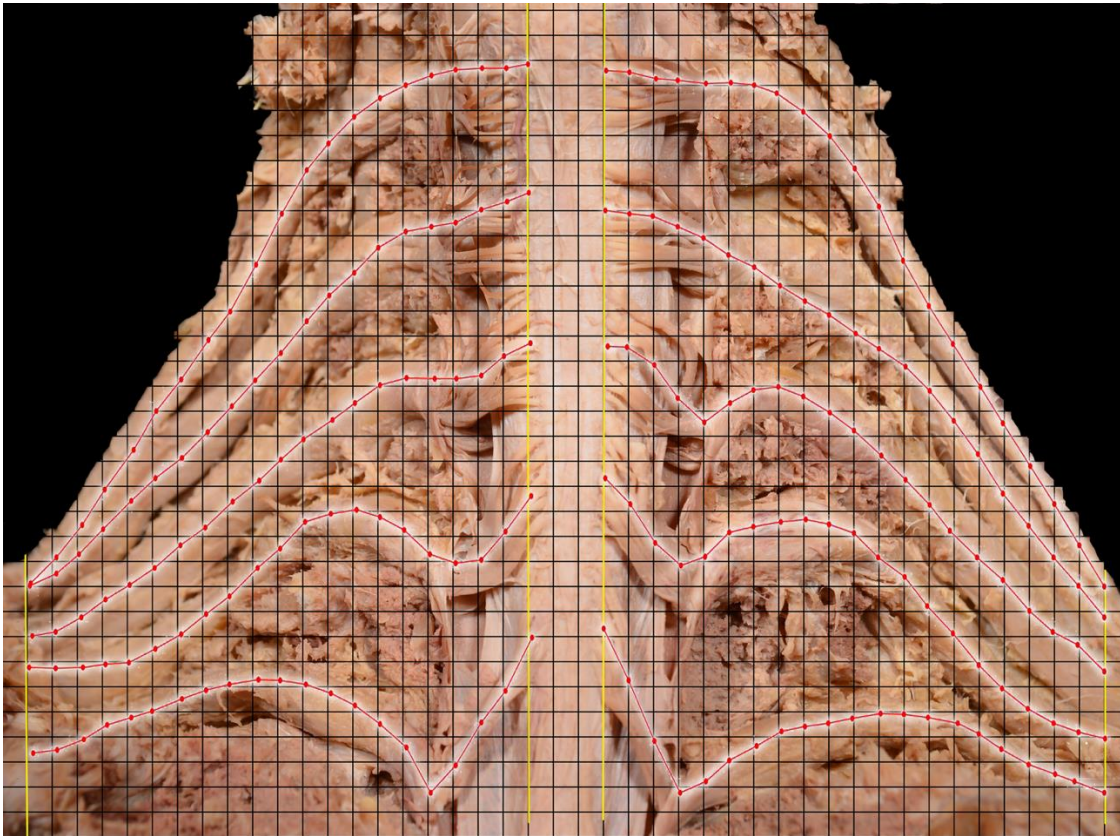
Figure 93. Cadaveric dissection of the posterior aspect of the
spinal cord, rootlets and roots of the brachial plexus with a
2.5mm^2 grid overlaid

1.13.2.5   Statistical analysis

Data were analysed in Stata/MP v15 (StataCorp LLC, College Station, Texas, United States of America). As this research was concerned with generating estimates of the normal geometry of the roots of the brachial plexus and there were no formal hypotheses to test, there was no role for a power calculation. The sample size was based upon the availability of cadavers and staff time within the dissection room. Step angles are skewed so summarised by the geometric mean and 99% confidence intervals (CI). Non-parametric regression was used to model step angles data. To estimate how the geometry differed between the five roots (C5 to T1), between sides (left and right) and between individuals (ten cadavers), these were modelled as categorical fixed-effects in a multivariable non-

parametric regression. To quantify the tortuosity of roots, the residual variance from the multivariable non-parametric regression was calculated and summarised per root.

Twelve points were placed at 2.5mm intervals, from the dorsal root entry zone laterally for 3cm into the postganglionic section. The angle (in degrees) between each point was resolved with respect to the horizontal.

1.13.3 Results

The summary trace of ten cadavers (Figure 94) and non-parametric regression plots (Figure 95) demonstrate that the tortuosity of spinal roots increased in the caudal direction (Table 3; p<0.001). There was no statistically significant difference in the geometry of left versus right roots (p=0.170).
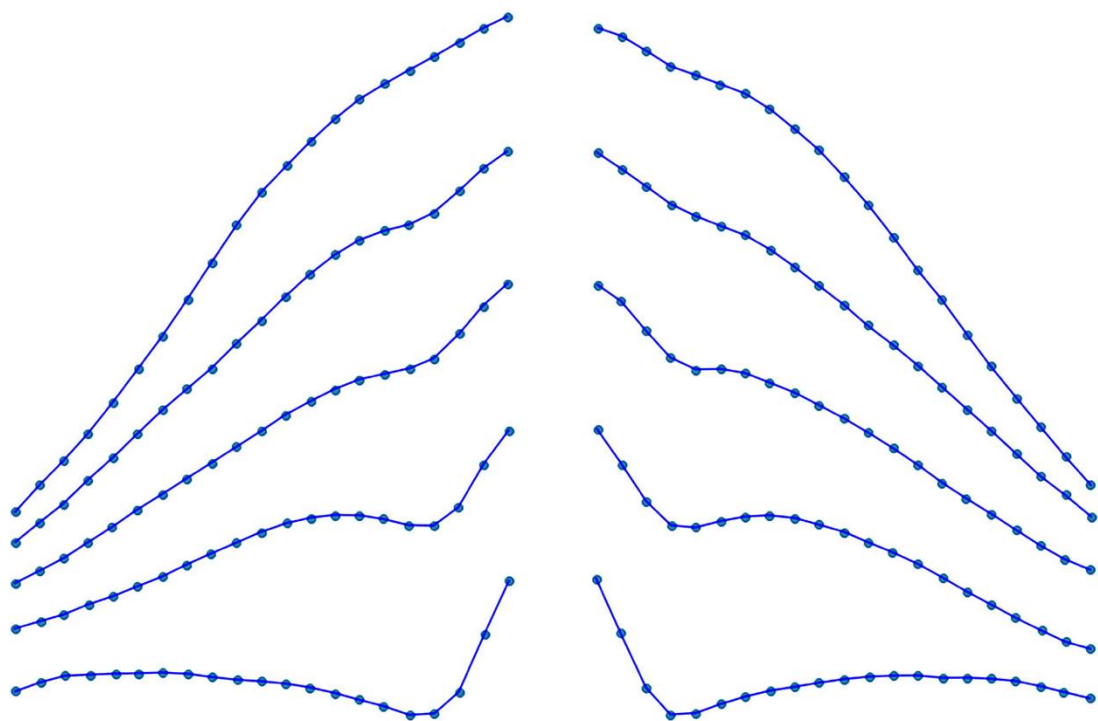
Figure 94. A summary plot of the course of the roots of the brachial plexus in 10 cadavers.

Left C5
μ residuals 872

Right C5
μ residuals 922

Left C6
μ residuals 1226

Right C6
μ residuals 1280

Left C7
μ residuals 1605

Right C7
μ residuals 1643

Left C8
μ residuals 1683

Right C8
μ residuals 2009

Left T1
μ residuals 2464

Right T1
μ residuals 2454
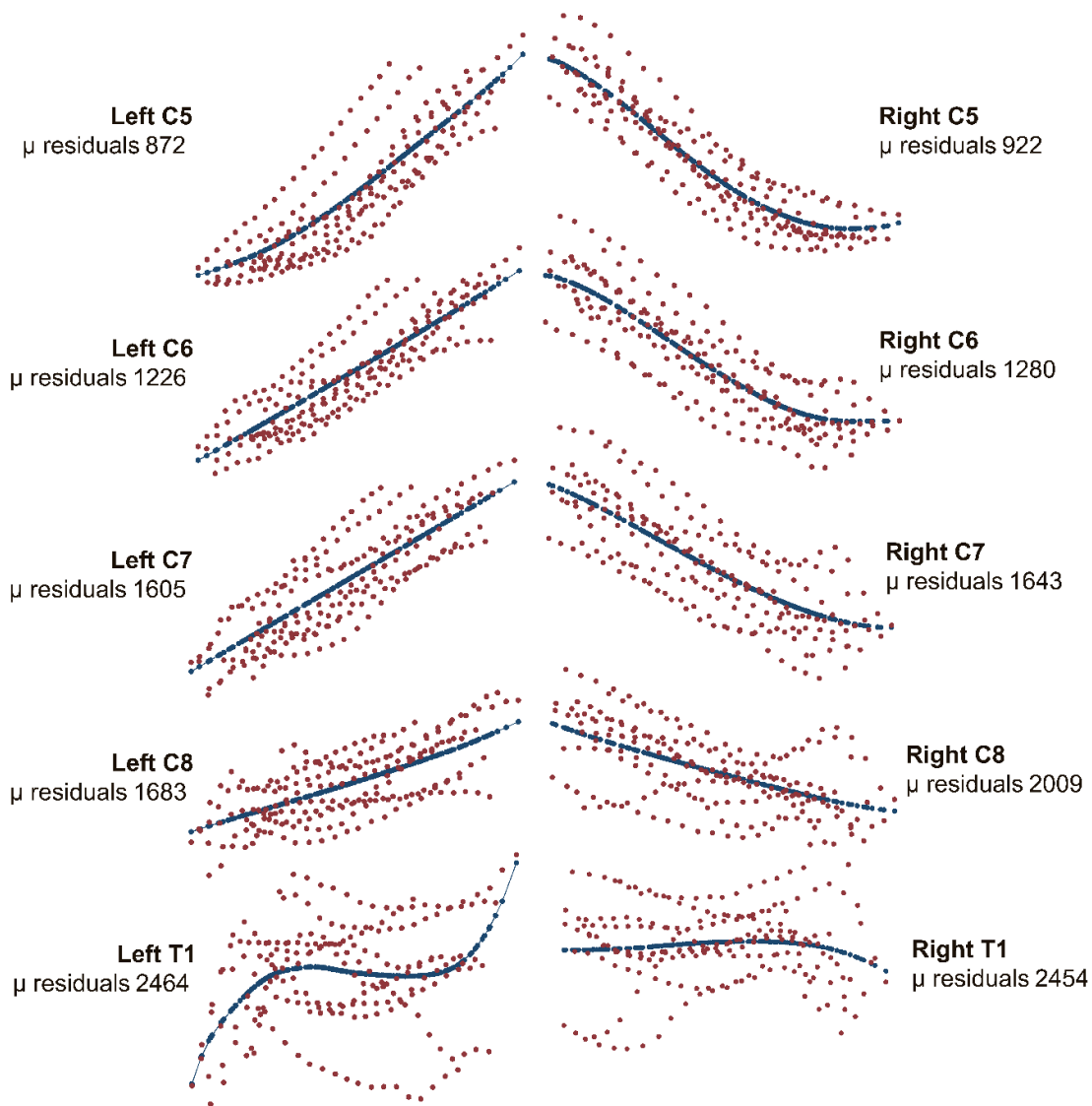
Figure 95. Scatter plots of traces for each root (red dots) with a non-parametric regression line of fit (blue). The mean (μ) of the residual variance is provided to quantify the tortuosity, whereby a higher mean residual variance implies a more tortuous nerve.

Root	Mean step angle in degrees (99% CI)	Maximum step angle in degrees (99% CI)
C5	7 (6, 9)	20 (15, 25)
C6	8 (7, 9)	25 (21, 30)
C7	9 (7, 12)	32 (23, 43)
C8	11 (10, 13)	44 (34, 57)
T1	12 (11, 13)	56 (44, 70)

Table 12. The mean (and 99% confidence intervals) of the step angles (acute angle between points) of the roots of the brachial plexus, at 2.5mm^2 resolution

The C5 and C6 roots had very similar geometry (p=0.906), with little variability throughout their course and a small step angle (Table 12 and Figure 95). Conversely, the T1 root had the greatest maximum step angle with a mean of 56° (99% CI 44° to 70°) as well as the greatest variability throughout its course (Figure 95 and Figure 96). Compared to the C5/6 roots, for every 2.5mm the C7 root turned an additional 2° (99% CI 1° to 4°); the C8 turned an additional 4° (99% CI 2° to 5°) and the T1 root turned an additional 4° (99% CI 3° to 5°).
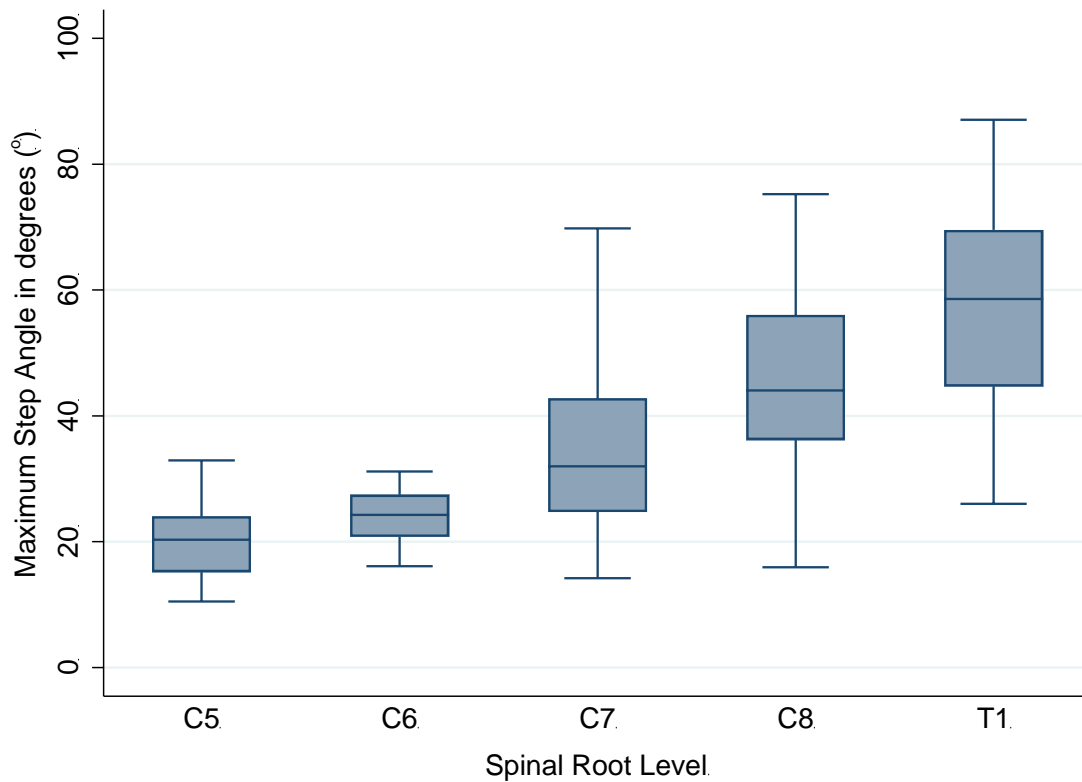
Figure 96. Boxplots showing the maximum angles (averaged across cadavers) for each root of the brachial plexus.

The majority of the variability in the course of the C7, C8 and T1 roots was observed in the medial two quintiles (medial 2cm) which turned an addition 5° per 2.5mm [99% CI 4° to 6°] compared to the lateral three quintiles (Figure 97). There was no statistically significant difference between the step angles measured in the 1st and 2nd quintiles (p=0.926). There were no statistically significant differences between the step angles measured in the 3rd, 4th or 5th quintiles. This implies that the majority of the tortuosity is observed within the intradural and intraforaminal portions of the brachial plexus.

Boxplot of the step angle (in quintiles, from medial to lateral) for each root of the brachial plexus
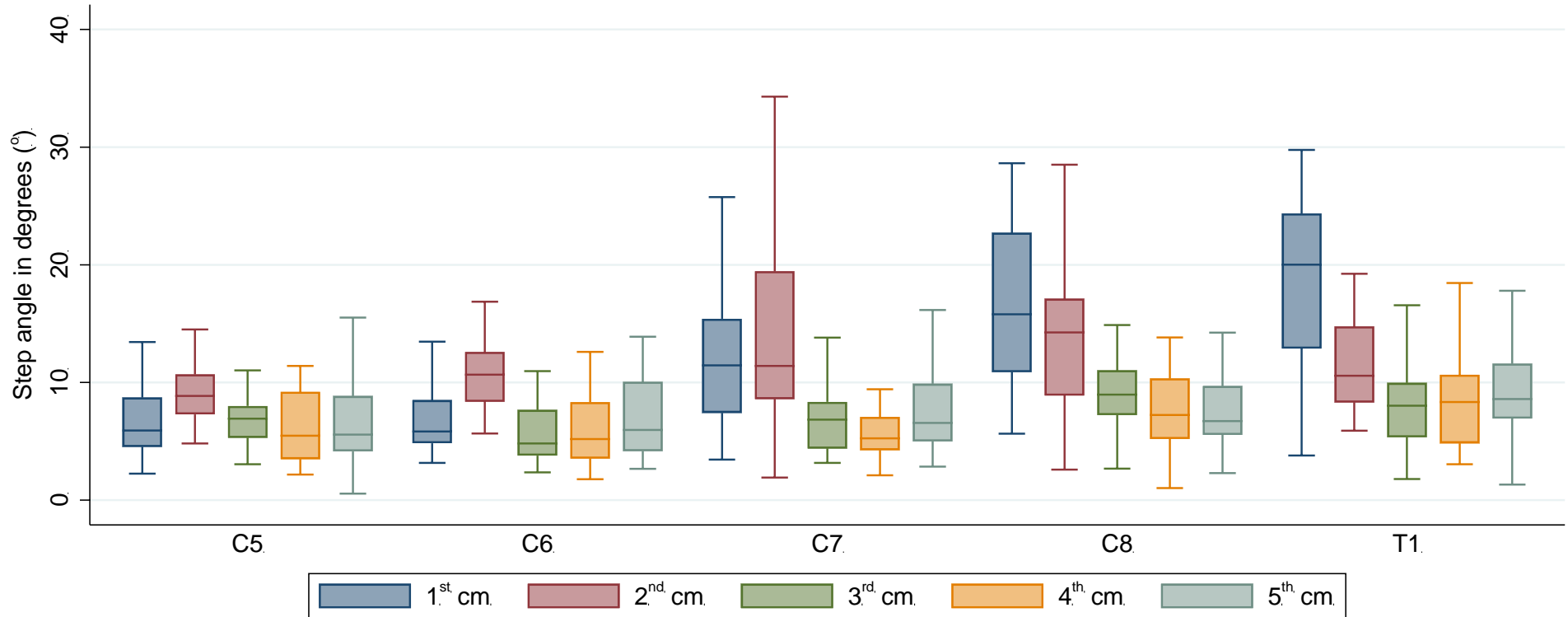
Figure 97. Boxplots of the angles of each root, divided into quintiles (from medial to lateral) showing that the majority of the variability in the measured angles is observed within the medial 2cm.

As some sections of nerves are more vertically oriented than others (e.g. the rootlets of the T1 are more vertical than the C5 rootlets), we correlated step angles with the gradients of the line segments to understand if we had introduced a bias in our methods, given that the effective resolution was modified. No statistically significant association was observed (r=0.017, p=0.065; Figure 98) implying that no bias was introduced by our methods.
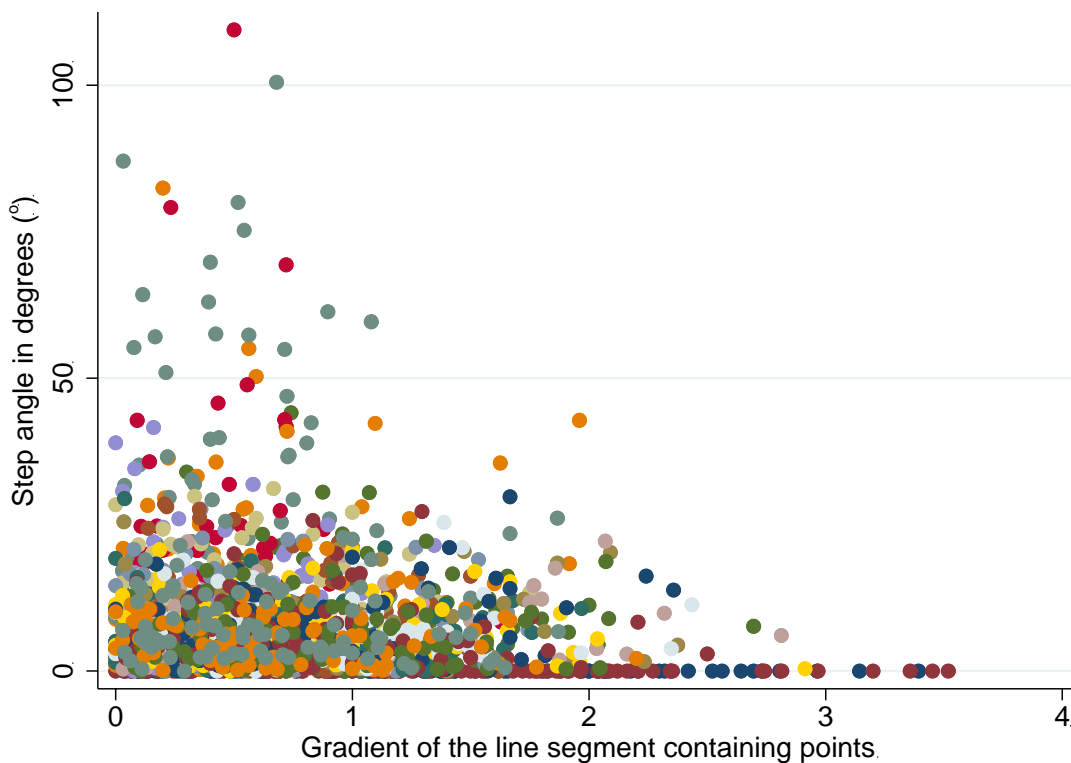
Figure 98. A scatterplot showing no correlation between the measured step angle and gradient of the line segments. This shows that no bias was introduced by our tracing methods. Such a potential bias might have meant that horizontal segments of nerves were shorter than vertical segments of nerves through change of the effective resolution.

Translating these measurements to clinical DTI tractography (Figure 99), shows that 50% of step angles are ≤20º and fewer than 1% exceed 70º. Therefore, to plot 99% of streamlines representing the roots of the brachial plexus, a step angle of 70º is likely to be sufficient to render streamlines of 99% of roots. To

demonstrate this concept, the summary plot from all cadavers is overlaid onto an example tractogram derived from a healthy adult (Figure 100).
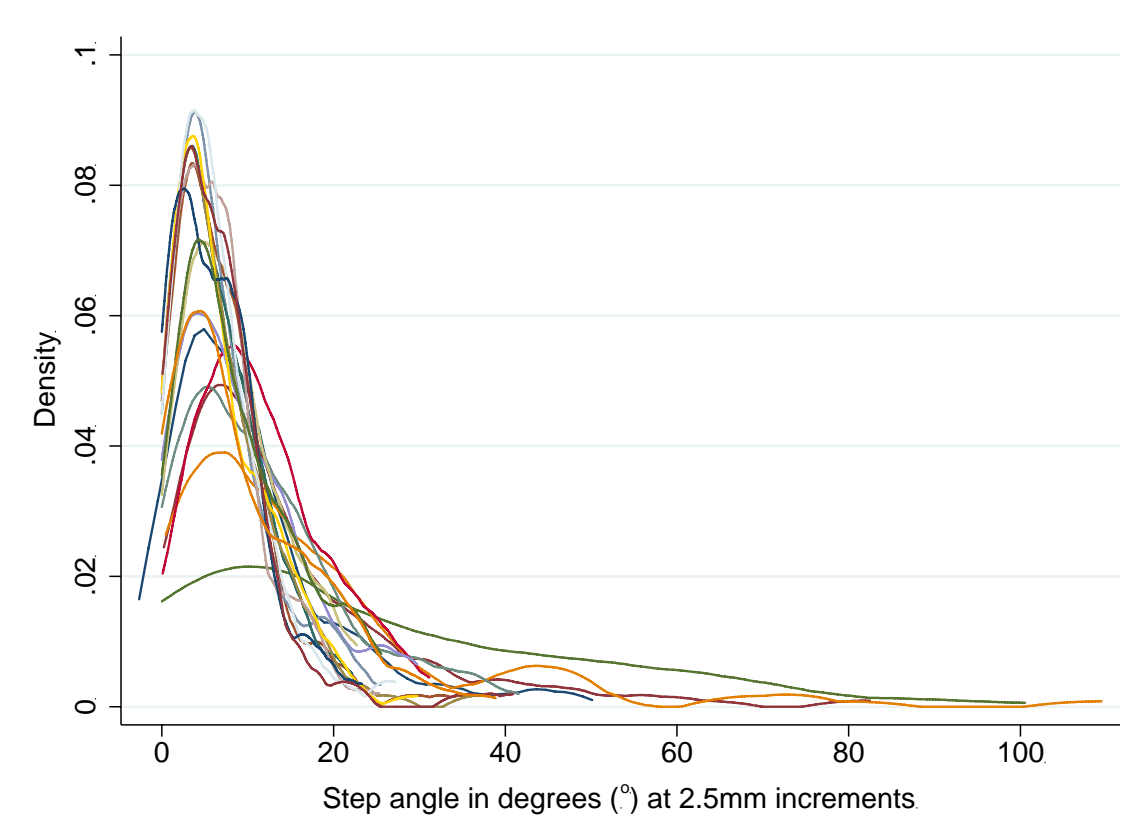
Figure 99. A kernel density plot of all angles calculated from all traces. Each coloured line represents one of the 21 points on the 10 nerve traces. The plot shows that over 50% of angles are less than 20 degrees and fewer than 1% are over 70 degrees.

1.13.4 Discussion

When reconstructing the brachial plexus using diffusion tensor imaging tractography, a step angle of 70° is likely to enable the propagation of 99% of streamlines representing the roots. Our findings agree with the two cadaveric studies of the geometry of the brachial plexus whereby Xiang et al. (2008)[237] showed that the rootlets of the T1 had a step angle of 66° over 15mm and Zhong et al. (2017)[238] showed that both the dorsal and ventral rootlets had a step angle of approximately 70°. However, our study adds more detailed information to the literature regarding the microscopic geometry of the pre- and postganglionic

brachial plexus which can be readily translated to clinical imaging. Our findings might be applied in one of two ways:

a) When tractography software requires a fixed step angle for a session of tractography then the 99% confidence interval value (70°) could be used, accepting that some false streamlines may be generated, necessitating manual or automatic pruning[244]

b) If a bespoke step angle can be prescribed per root, then the upper value of the root-specific 99% confidence intervals could be selected (e.g. 25° for C5, 30° for C6, 43° for C7, 57° for C8 and 70° for T1; Table 12). This approach mightminimise the probability of generating false streamlines whilst maximising the probability of representing the true geometry of the roots.

DTI tractography has gained attention globally given its unparalleled ability to generate high fidelity maps of neural pathways from non-invasive imaging and provide objective proxy measures of nerve health. However, to be able to differentiate healthy from diseased or injured sections of nerve, it is necessary to define the normative DTI parameters and tractography conditions for the brachial plexus. To-date, six studies report the findings of DTI tractography of the brachial plexus in healthy adults[239–243] but a wide array of step angles were used to reconstruct streamlines representing the pre- and postganglionic brachial plexus. Vargas et al. (2010)[239] used a 30° step angle and reconstructed the C5-T1 roots in all volunteers, although the C5 roots were not apparent in their published tractograms. Gasparotti et al. (2013)[241] used a step angle of 35-45° to propagate streamlines of the C5-T1 roots in all individuals; however, their published tractograms showed the T1 streamlines terminating close to the spinal cord. Wade et al. (2020)[243] used a step angle of 35° although 4% of C5-C8 and 46% of T1 roots did not propagate. Oudeman et al. (2018)[242] used a step angle of 14° which reconstructed all C5-C8 streamlines but failed to propagate T1 streamlines in 52%. Neither Tagliafico et al. (2011)[240] or Su et al. (2019)[245] described the step angle used for tractography or the proportion of streamlines generated; their articles contained data on the C5-C8 roots and did not describe why the T1 root data was excluded. We hope that future DTI tractography studies can produce more reliable tractograms using the information within our report.

1.13.4.1 Limitations

A 2D study of the geometry of the brachial plexus incompletely describes its complex course. Although our mathematical summary of the geometry of the roots appear to agree with DTI tractograms (Figure 100), 3D modelling of the geometry of the gross anatomy would (in theory) be superior; however, a) the techniques for generating 3D structure from motion are immature and would require the attachment of circumferential beacons, meaning further dissection and perturbed anatomy, b) the angles through which the roots of the plexus turn in the axial and sagittal planes are substantially less than in the coronal plane. Therefore, thresholding would need to be based on the coronal angles, rendering measurements of angles in any other 2D plane irrelevant. In Supplementary Figure 4 we overlay the summary plot from all cadavers onto a DTI tractogram from a single healthy adult, so formal assessments of agreement cannot be made. Ideally, DTI would be acquired on a recently deceased non-embalmed donors[246] and subsequent dissection would facilitate an assessment of agreement between the tractogram and anatomy. However, dMRI in fixed tissues is particularly challenging given that the formalin-based fixatives dramatically reduce the T1 and T2, meaning that protracted scanning or customised sequences are needed. The translation of our findings may be limited because the geometry of the plexus in younger individuals may be different to the adults we studied and furthermore, the normal variation within the population may not be adequately captured by our relatively small sample.

A DTI tractogram of the brachial plexus (Figure 89) is the result of a multistep process, with numerous assumptions and uncertainties [81]. The principal eigenvector of the tensor cannot be assumed to be an accurate representation of the actual fibre orientation(s) because it cannot resolve crossing, diverging or converging axons (section 0) so is likely that erroneous streamlines will be generated – further work is needed to understand whether multishell acquisitions (to resolve crossing fibres) are needed in the brachial plexus and whether probabilistic approaches to tractography are more accurate.
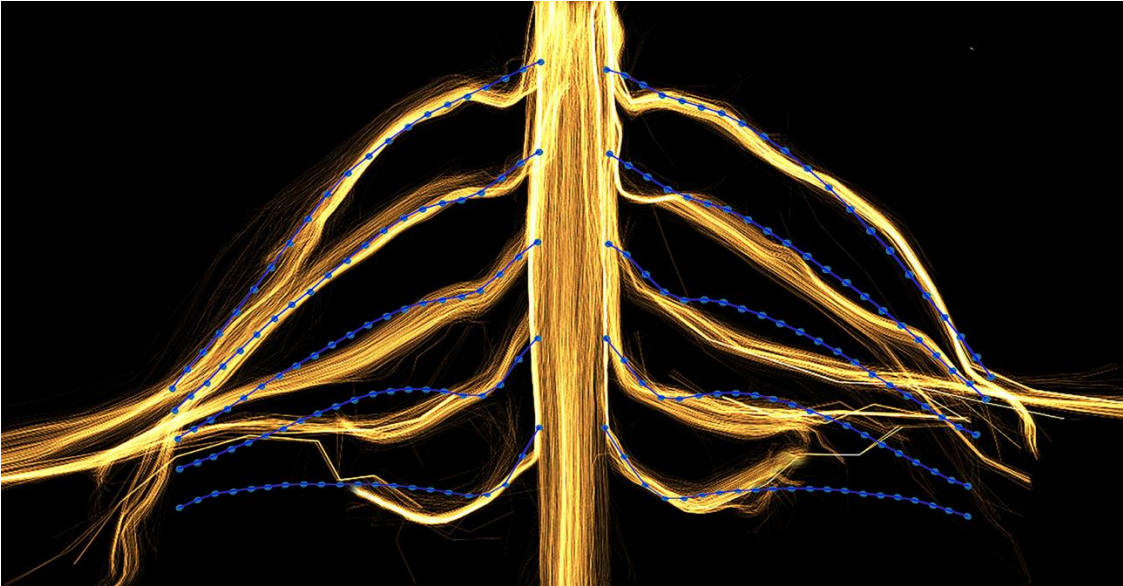
Figure 100. The summary plot of nerve traces from cadavers in this study overlaid on the spinal cord and brachial plexus of a healthy adult reconstructed from diffusion tensor magnetic resonance imaging, using example data acquired by our group.

1.13.5 Conclusions

The geometry of the roots of the brachial plexus increases in complexity in the caudal direction. When reconstructing the roots of the brachial plexus using tractography based on dMRI, a step angle of 70º is likely to plot 99% of streamlines representing the roots although this must be balanced against the noise of false streamlines.

Future work should examine the relationship between tractograms and gross anatomy in post-mortem subjects, as well as the utility of probabilistic versus deterministic tractography.

Chapter 14. Diffusion Tensor Imaging of the Roots of the Brachial Plexus: A Systematic Review and Meta-Analysis of Normative Values

Published at https://doi.org/10.1007/s40336-020-00393-x

1.14.1 Introduction

Before researchers and clinicians can use DTI parameters to identify abnormal roots of the brachial plexus, there is a need to define the population "normal" values. Numerous studies have examined aspects of DTI of the brachial plexus in healthy adults. This review aims to summarise the values observed in health and explore discrepancies in the reported measurements.

1.14.2 Methods

This review is registered with PROPSERO (ID CRD42019155788), it was designed and conducted in accordance with the Cochrane Handbook of Systematic Reviews[247] and has been authored in accordance with the PRISMA checklist[248].

1.14.2.1 Types of studies

We included all studies which report the findings of diffusion tensor magnetic resonance imaging of the roots of the brachial plexus in healthy adults. Case reports were excluded.

1.14.2.2 Participants

Asymptomatic adults (aged ≥16 years) with no known pathology (past or present) affecting the spinal cord or brachial plexus were the population of interest.

1.14.2.3 Image acquisition

Studies must report diffusion tensor imaging parameters from the roots of the brachial plexus.

1.14.2.4 Search strategy

The NICE Healthcare Databases (hdas.nice.org.uk) was searched using the terms "diffusion tensor" OR "DTI" AND "brachial plexus". This yielded 67 hits in PubMed, 36 in Embase, 8 in CINAHL, 2 in CENTRAL and 2 in ClinicalTrials.gov the on 13th November 2019. After de-duplication, 78 unique citations were independently screened by two review authors. The full texts of all potentially relevant articles were obtained. The reference lists for included articles were also scrutinised for potentially relevant papers. The final lists of included articles were compared and disagreements resolved by discussion.

1.14.2.5 Study selection

Two review authors (RGW and AW) independently screened titles and abstracts for relevance, in accordance with the eligibility criteria. The full texts of potentially eligible articles were obtained and again independently assessed by the same two authors. Disagreements were resolved by discussion. Eligible articles were imported to Review Manager® version 5 (The Nordic Cochrane Centre, The Cochrane Collaboration, 2014) and categorised as included or excluded for subsequent analyses.

1.14.2.6 Data extraction

Two review authors (RGW and AW) independently extracted data concerning the demographics, scanner, pulse sequence, pre-processing, tensorial reconstruction, measurement conditions and the outcomes of interest. The nerve root was the unit of analysis[41] and root level estimates of DTI -parameters were extracted. Where data was missing or unclear, the corresponding author was contacted by email and/or phone and if no reply was received, 4 weeks later all authors were contacted in addition to re-contacting the corresponding author. The authors of one study[243] provided additional information (measurements form the extraforaminal roots using identical methods) for the purposes of this review.

1.14.2.7 Outcomes

The primary outcome is to estimate the normal FA of the extraforaminal roots of the brachial plexus in healthy adults. The secondary outcomes include: a) to estimate the normal MD of the extraforaminal roots of the brachial plexus in

healthy adults, and b) to explore the associations between DTI parameters and participants age, the SNR and related factors such as the b-value(s), echo time(s), TE and resolution (in cubic millimetres, mm^3) and the number of diffusion sensitising gradient directions (N_D) sampled per shell.

1.14.2.8   Methodological quality assessment

The risk of bias was assessed by two review authors (RGW and AW) using the ROBINS-I tool[249] and displayed graphically using robvis[250]. Disagreements were resolved by discussion.

1.14.2.9   Statistical analysis

Data were analysed in Stata/MP v15 (StataCop LLC, Texas). To estimate the effect of experimental/participant factors on the FA and MD, generalised linear modelling (GLM) was used with gaussian families. As the TE, b-value and resolution are functions of SNR, the fixed-effects were selected to be SNR, age in years and the N_D all of which were handled as continuous variables. The random-effects in the GLM varied by the study. Estimates were bootstrapped using lossless non-parametric resampling with replacement, with 1000 iterations. There was insufficient data to meaningfully assess the effect of different tensor fitting methods or components of the b-value (diffusion time, magnitude or interval) on DTI parameters. To visualise the association of FA with N_D, and MD with age, scatterplots of the aggregate estimates were generated using the *metareg* package; the circles are root-level estimates and the sizes are dependent on the precision (inverse variance) of the estimate. To estimate the pooled normal FA and MD of the spinal roots, meta-analyses were performed using the *metan* package. Cohen's method was used because both FA and MD were homoscedastic. Dersimonian and Laird random-effects were used given the clinical heterogeneity. Analyses were subgrouped by both the N_D and spinal root (C5, C6, C7, C8, T1). Confidence intervals (CI) were generated to the 95% level. To assess the possibility of small-study effects we constructed a funnel plot using the *metafunnel* package, which is a scatterplot of the effect size against precision; symmetry implies the absence of small-study effects. To adjust for multiplicity of testing, the family-wise error rate was revised down to $p < 0.001$ and the term

statistical significance is avoided in favour of extrapolation of average effects and their variability/uncertainty (as shown by the CIs).

1.14.3 Results

After reviewing 27 full texts, 15 were excluded (Appendix 9) and 9 articles (of 9 unique studies) were included[149,239,242,243,251–255] (Figure 101).
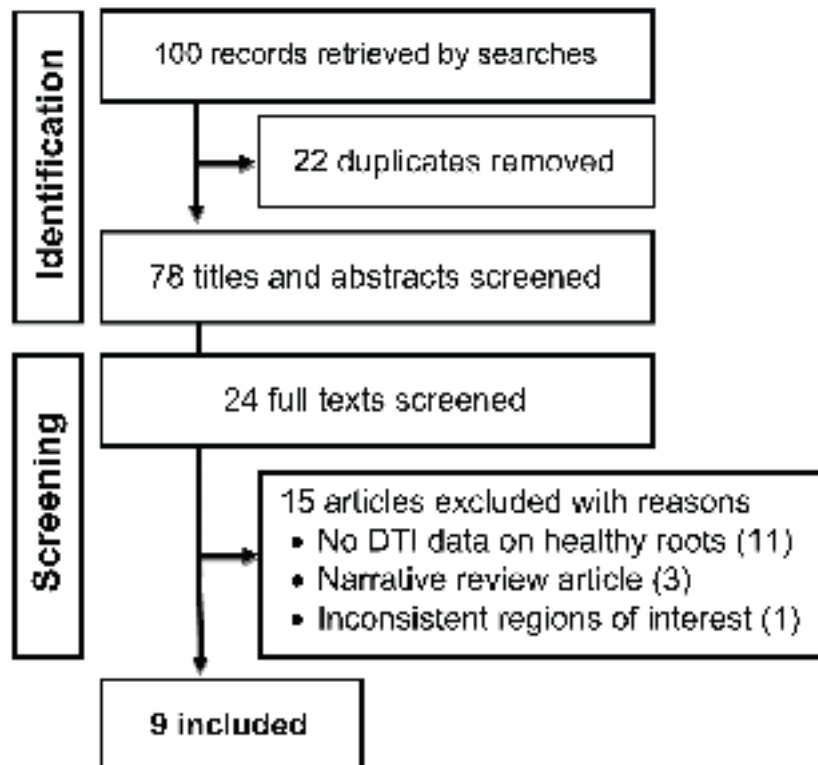
Figure 101. PRISMA flowchart

1.14.3.1   Study characteristics

Overall, 316 adults were included. The ratio of males:females was approximately 1:1 (156:154). The mean age of participants was 35 years (SD 6). The characteristics of included studies are shown in .

Population parameters				Scanner details		Data acquisition	DTI reconstruction		Measurement conditions			
Study	**Location**	**N (M:F)**	**Age**	**Make & Model**	**Field Strength**	**Sequence**	**Pre-processing / corrections**	**Tensorial calculation**	**Mean SNR (SD)***	**ROI position**	**ROI size**	**No. raters**
Chen (2012)[253]	China	32	33.5	Philips Intera Master	1.5	ssEPI: b0/700/9001000s/mm^2, 32 directions, 2 averages, TE 77ms, TR 9000ms, 2mm isotropic, axial slices.	Not described	Not described	b700 = 18.3 (7.4) b900 = 17.0 (6.9) b1000 = 14.1 (5.1)	Not described	Not described	Not described
Ho (2017)[252]	Switzerland	10	30.6	Siemens Magnetom Skyra	3	ssEPI: b0/800s/mm^2, 30 directions, one acquisition (no averages), TE 67ms, TR 5600ms, 1.9mm isotropic.	Not described	Not described	Not described	Distal to the ganglia	11m^2	2
Ho (2019)[251]	Switzerland	10	29.2	Siemens Magnetom Skyra	3	rsEPI: b0/900s/mm^2, 4 averages, TE 57ms, TR 3030ms, 2.4mm isotropic, *number of directions not described.* ssEPI: b0/900s/mm^2, 4 averages, TE 59ms, TR 5800ms, 2.4mm isotropic, *number of directions not described.*	Not described	Not described	rsEPI ≈ 6.5 (2) ssEPI ≈ 6.1 (2.4)	Distal to the ganglia	Bespoke	2
Oudeman (2018)[242]	Netherlands	30	44	Philips Ingenia	3	ssEPI: b0/800s/mm^2, 15 directions, TE 77ms, TR 5969ms, 6 averages, 3mm isotropic.	Correction for Rician noise, motion and eddy currents in DTItools	Weighted Least Linear Squares	21 (8)	Close to the ganglia	Not described	2
Su (2019)[254]	China	163	38	Siemens Magnetom Aera	3	rsEPI: 0/900 s/mm^2, 20 directions, 4 averages, TE 92ms, TR 6000ms, 2x2x3mm voxels	Not described	Not described	Not described	Postganglionic roots	Not described	2
Tagliafico (2011)[149]	Italy	40	44.5	GE, model not described	3	ssEPI: b0/1000s/mm^2, 32 directions, averaging not described, TE "minimum", TR 16675ms, 2mm slice thickness.	Correction for eddy currents using the General Electric Functool v6.3.1	Not described	Not described	Not described	2mm^2	4
Vargas (2010)[239]	Switzerland	12	41	Siemens Avanto	1.5	ssEPI: b0/900s/mm^2, 30 directions, TE 78ms, TR 9000ms, one acquisition (no averages), 2mm isotropic, iPAT 2, axial slices.	Not described	Not described	Not described	At the level of the proximal roots	2mm^2	3
Wade (2020)[255]	UK	10	28	Siemens Magnetom Prisma	3	ssEPI: b0/1000 s/mm^2, 64 bipolar directions (twice refocused spin echo), TE 66ms, TR 4300ms, 8 averages (4 per phase encoding direction), 2.5mm isotropic, 2nd order in-line motion correction, axial slices.	Correction for susceptibility artefacts in DSI Studio	Linear least squares	67.6 (45)	Extraforaminal roots, 3cm lateral to the midline of the spinal cord	5mm^3 (8 voxels)	2
Wade (2020)[243]	UK	7	28	Siemens Magnetom Prisma	3	ssEPI: b0/1000 s/mm^2, 20 monopolar directions, 4 averages, TE 66ms, TR 4300ms, 2.5mm isotropic, 2nd order in-line motion correction, axial slices.	None	Linear least squares	36.0 (16)	Extraforaminal roots, 3cm lateral to the midline of the spinal cord	5mm^3 (8 voxels)	2

Table 13. Study Characteristics. *Study-level signal-to-noise ratio (SNR) derived from non-diffusion-weighted (b0) images; readout segment echo-planar imaging*

1.14.3.2 Risk of bias within studies

The risk of bias for the included studies are summarised in Figure 102.

	D1	D2	D3	D4	D5	D6	D7	Overall
Chen 2012	❌	➕	➕	➕	❓	❌	❓	❌
Ho 2017	❌	➕	➕	➕	❓	➕	❓	❌
Ho 2019	❌	➕	➕	➕	❓	❌	❓	❌
Oudeman 2018	❌	➕	➕	➕	❓	➕	❓	❌
Su 2019	❌	➕	➕	➕	❓	❓	➕	❌
Tagliafico 2011	❌	➕	➕	➕	❓	❓	❓	❌
Vargas 2010	❌	➕	➕	➕	❓	➕	❓	❌
Wade 2020a	❌	➕	➕	➕	➕	➕	➕	❌
Wade 202b	➖	➕	➕	➕	➕	➕	➕	➖

Domains:
D1: Bias due to confounding.
D2: Bias due to selection of participants.
D3: Bias in classification of interventions.
D4: Bias due to deviations from intended interventions.
D5: Bias due to missing data.
D6: Bias in measurement of outcomes.
D7: Bias in selection of the reported result.

Judgement
❌ Serious
➖ Moderate
➕ Low
❓ No information

Figure 102. The summary risk of bias plot for included studies.
Red = high risk, yellow = unclear risk, green = low risk.

Eight of the included studies[149,239,242,243,251–253,256] were at risk of bias due to confounding because there was no adjustment for a) effect-modifiers such as age, weight and the experimental factors described above, and b) repeated-measures, i.e. ten estimates of the FA (one from each spinal root, bilaterally) taken from the same individual will be highly correlated and without adjustment, the sample-level estimates will have falsely small variances. Seven studies[149,242,251–254] provided no information about missing data and so the risk of bias is unclear. Two studies[251,253] were judged to be at high risk of bias in the measurement of FA and MD because a bespoke region of interest was used to calculate the FA and the number of diffusion sensitising gradients used was not described[251]. Three studies[149,242,254] were at unclear risk of bias in the measurement of FA and MD because information was lacking about pre-processing, tensorial reconstruction or how the estimates of the FA and MD were

derived from images (e.g. region of interest size and position). One study[253] was at high risk of reporting bias because three b-values were tested (700, 900, 1100 mm/s) but it is unclear which yielded the estimates of FA and MD reported in the manuscript or whether they are an average of the three. The risk of bias due to selective outcome reporting was unclear in six studies[239,242,251–253,257] because no information was provided regarding the exclusion criteria, attrition due to scan intolerance, dataset exclusion (e.g. for uncorrectable motion artefact) or otherwise and there were no published protocols to consult.

1.14.3.3   Evidence synthesis

There were no associations between experimental factors and the FA or MD on univariable modelling (Table 14).

DTI parameter	Experimental factors	Unadjusted coefficients (95% CI)	p-value	Adjusted coefficients (95% CI)	p-value	Resampled Adjusted coefficients (95% CI)	Resampled p-value
Fractional Anisotropy	SNR	0.0001 (-0.0003, 0.0004)	0.662	0.0001 (-0.0001, 00004)	0.257	0.0001 (-0.001, 0.002)	0.840
	Age in years	0.0003 (-0.006, 0007)	0.926	0.001 (0.001, 0.002)	0.001	0.001 (-0001, 0.003)	0.236
	Number of Diffusion Directions	-0.002 (-0.005, 0001)	0.183	-0.001 (-0.002, -0.001)	<0.001	-0.001 (-0.002, -0.0004)	0.002
	Echo time (ms)	0.002 [0.00001, 0.004])	0.174	*	*	*	*
	b-value (mm/s)	-0.0004 (-0.001, 0.0001)	0.098	*	*	*	*
	Resolution (mm^3)	0.008 (0.003, 0.013)	0.126	*	*	*	*
Mean Diffusivity (x10^{-3} mm^2/s)	SNR	-0.001 (-0.003, 0.0005)	0.154	-0.001 (-0.003, 0)	0.055	-0.001 (-0.012, 0.01)	0.799
	Age in years	-0.01 (-0.03, 0.01)	0.303	-0.025 (-0.030, -0.021)	<0.001	-0.03 (-0.042, -0.01)	0.003
	Number of Diffusion Directions	0.005 (-0003, 0013)	0.234	0.001 (-0.001, 0.002)	0.238	0.001 (-0.005, 0.006)	0.723
	Echo time (ms)	-0.012 (-0.019, -0.005)	0.174	*	*	*	*
	b-value (mm/s)	0.001 (0.0004, 0.002)	0.003	*	*	*	*
	Resolution (mm^3)	0.004 (0.002, 0.007)	0.562	*	*	*	*

*Table 14. Mixed-effects generalised linear modelling showing the unadjusted, multivariable and bootstrapped multivariable effect estimates of co-variables on fractional anisotropy and mean diffusivity of the roots of the brachial plexus. *Excluded due to multicollinearity*

Multivariable modelling showed that the angular resolution was strongly associated with FA, whereby every additional 10 diffusion sensitising gradient directions sampled reduced the FA by 0.01 (95% CI 0.01, 0.03; Figure 103).
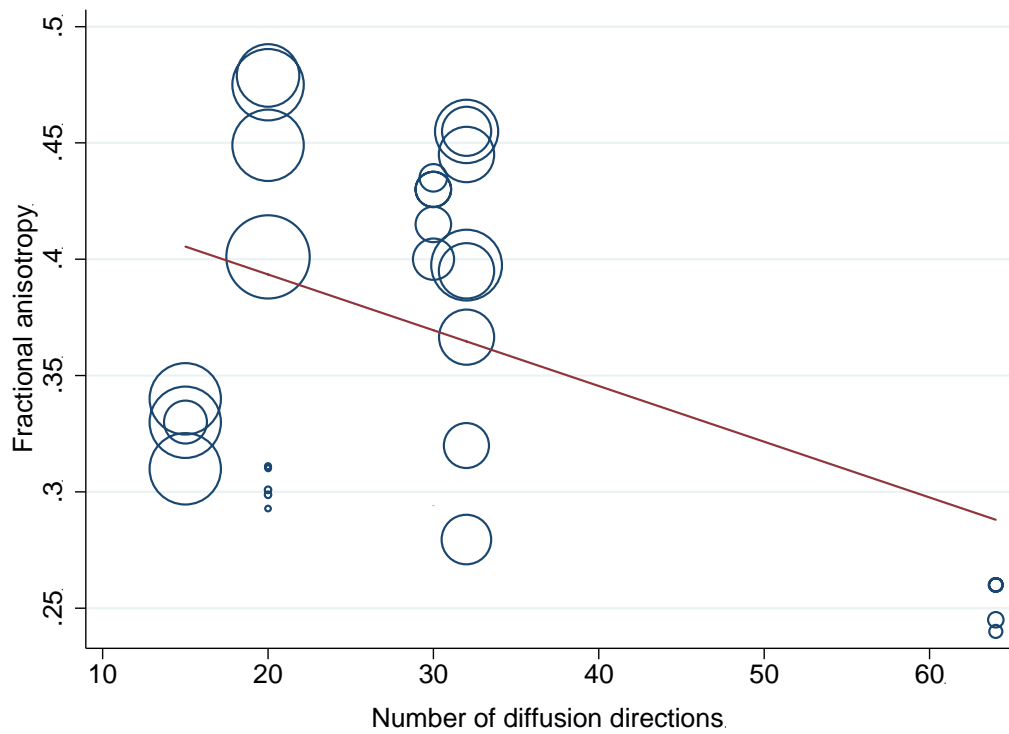
Figure 103. A scatterplot showing the negative association between the mean fractional anisotropy of the roots of the brachial plexus and the number of diffusion sensitising gradient directions.

Furthermore, multivariable modelling showed that each year of life reduced the MD by 0.03 x10^{-3} mm^2/s (95% CI 0.01, 0.04; Figure 104). Bootstrapping did not change these estimates.
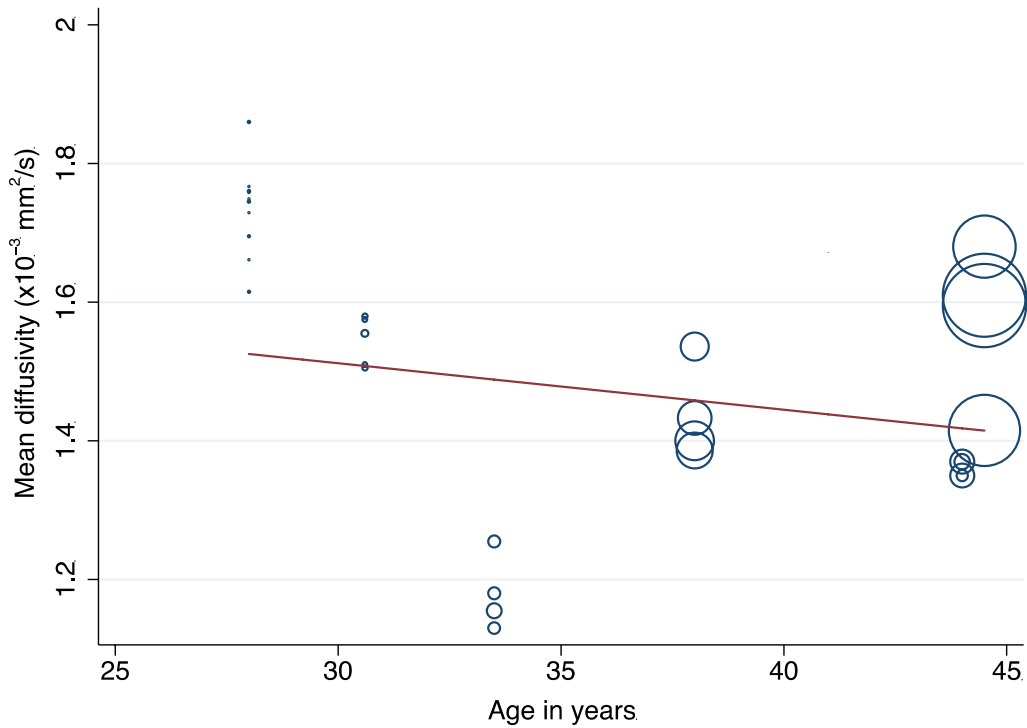
Figure 104. A scatterplot showing the negative association between the mean diffusivity of the roots of the brachial plexus and the mean age of adults in the included studies.

Seven studies[149,242,243,251,252,255,256] were included in the meta-analysis of the normal FA of the roots of the brachial plexus at 3T; one study[239] did not provide estimates of the variance so could not be included. The pooled estimate of the normal FA of the root was 0.36 (95% CI 0.34, 0.38; Figure 105).

Study	N	EPI	b-value	Spinal root		ES (95% CI)	% Weight
15 directions							
Oudeman 2018	30	ssEPI	800	C5		0.31 (0.30, 0.32)	3.05
Oudeman 2018	30	ssEPI	800	C6		0.33 (0.32, 0.34)	3.05
Oudeman 2018	30	ssEPI	800	C7		0.34 (0.33, 0.35)	3.05
Oudeman 2018	30	ssEPI	800	C8		0.33 (0.31, 0.35)	3.00
Subtotal (I^2 81%, p=0.001)						0.33 (0.31, 0.34)	12.16
20 directions							
Su 2019	163	ssEPI	900	C5		0.40 (0.39, 0.41)	3.06
Su 2019	163	ssEPI	900	C6		0.45 (0.44, 0.46)	3.05
Su 2019	163	ssEPI	900	C7		0.48 (0.47, 0.49)	3.04
Su 2019	163	ssEPI	900	C8		0.47 (0.46, 0.49)	3.05
Wade 2020a	7	ssEPI	1000	C5		0.30 (0.18, 0.42)	1.44
Wade 2020a	7	ssEPI	1000	C6		0.30 (0.18, 0.42)	1.45
Wade 2020a	7	ssEPI	1000	C7		0.31 (0.18, 0.44)	1.31
Wade 2020a	7	ssEPI	1000	C8		0.31 (0.18, 0.44)	1.25
Wade 2020a	7	ssEPI	1000	T1		0.29 (0.15, 0.43)	1.18
Subtotal (I^2=95%, p<0.001)						0.41 (0.38, 0.45)	18.84
30 directions							
Ho 2017	10	ssEPI	800	C5		0.41 (0.39, 0.44)	2.97
Ho 2017	10	ssEPI	800	C6		0.44 (0.41, 0.46)	2.89
Ho 2017	10	ssEPI	800	C7		0.43 (0.41, 0.45)	2.97
Ho 2017	10	ssEPI	800	C8		0.43 (0.41, 0.45)	2.97
Ho 2017	10	ssEPI	800	T1		0.40 (0.38, 0.42)	3.00
Subtotal (I-squared = 45.8%, p = 0.117)						0.42 (0.41, 0.43)	14.79
32 directions							
Tagliafico 2011	40	ssEPI	1000	C5		0.40 (0.39, 0.41)	3.05
Tagliafico 2011	40	ssEPI	1000	C6		0.37 (0.35, 0.38)	3.03
Tagliafico 2011	40	ssEPI	1000	C7		0.32 (0.30, 0.34)	3.01
Tagliafico 2011	40	ssEPI	1000	C8		0.28 (0.26, 0.29)	3.02
Subtotal (I^2=98%, p = 0.000)						0.34 (0.29, 0.39)	12.11
64 directions							
Wade 2020b	10	ssEPI	1000	C5		0.25 (0.20, 0.29)	2.56
Wade 2020b	10	ssEPI	1000	C6		0.26 (0.20, 0.32)	2.45
Wade 2020b	10	ssEPI	1000	C7		0.26 (0.20, 0.32)	2.45
Wade 2020b	10	ssEPI	1000	C8		0.26 (0.20, 0.32)	2.39
Wade 2020b	10	ssEPI	1000	T1		0.24 (0.18, 0.30)	2.39
Subtotal (I^2=0%, p=0.977)						0.25 (0.23, 0.28)	12.25
Unknown number of directions							
Ho 2019	10	ssEPI	900	C5		0.38 (0.36, 0.40)	3.01
Ho 2019	10	ssEPI	900	C6		0.37 (0.35, 0.39)	3.00
Ho 2019	10	ssEPI	900	C7		0.37 (0.35, 0.39)	3.00
Ho 2019	10	ssEPI	900	C8		0.36 (0.34, 0.38)	3.01
Ho 2019	10	ssEPI	900	T1		0.34 (0.33, 0.36)	3.02
Ho 2019	10	rsEPI	900	C5		0.38 (0.36, 0.40)	3.02
Ho 2019	10	rsEPI	900	C6		0.36 (0.34, 0.38)	2.96
Ho 2019	10	rsEPI	900	C7		0.36 (0.34, 0.38)	2.95
Ho 2019	10	rsEPI	900	C8		0.35 (0.33, 0.38)	2.91
Ho 2019	10	rsEPI	900	T1		0.35 (0.33, 0.37)	2.99
Subtotal (I^2=48%, p=0.044)						0.36 (0.36, 0.37)	29.86
Overall (I^2=98%, p<0.001)						0.36 (0.34, 0.38)	100

Figure 105. Forest plot summarising the normal fractional anisotropy of the roots of the brachial plexus at 3-Tesla.

There were no statistically significant differences between the five roots. However, there was significant statistical heterogeneity between studies (I^2 98%) which may be related to the experimental conditions described above. The pooled

estimates of the normal FA subgrouped by spinal root (including the study performed at 1.5T which had usable data[253]) is shown in Figure 106.

Study	Field (Tesla)	N	EPI	Directions	b-value	ES (95% CI)	% Weight
C5							
Chen 2012	1.5	32	ssEPI	32		0.46 (0.44, 0.47)	2.71
Oudeman 2018	3	30	ssEPI	15	800	0.31 (0.30, 0.32)	2.72
Ho 2017	3	10	ssEPI	30	800	0.41 (0.39, 0.44)	2.64
Su 2019	3	163	ssEPI	20	900	0.40 (0.39, 0.41)	2.73
Ho 2019	3	10	ssEPI		900	0.38 (0.36, 0.40)	2.68
Ho 2019	3	10	rsEPI		900	0.38 (0.36, 0.40)	2.69
Wade 2020a	3	7	ssEPI	20	1000	0.30 (0.18, 0.42)	1.29
Tagliafico 2011	3	40	ssEPI	32	1000	0.40 (0.39, 0.41)	2.72
Wade 2020b	3	10	ssEPI	64	1000	0.25 (0.20, 0.29)	2.29
Subtotal (I-squared = 97.8%, p = 0.000)						0.37 (0.34, 0.41)	22.47
C6							
Chen 2012	1.5	32	ssEPI	32		0.46 (0.44, 0.47)	2.69
Oudeman 2018	3	30	ssEPI	15	800	0.33 (0.32, 0.34)	2.72
Ho 2017	3	10	ssEPI	30	800	0.44 (0.41, 0.46)	2.58
Su 2019	3	163	ssEPI	20	900	0.45 (0.44, 0.46)	2.72
Ho 2019	3	10	ssEPI		900	0.37 (0.35, 0.39)	2.67
Ho 2019	3	10	rsEPI		900	0.36 (0.34, 0.38)	2.64
Wade 2020a	3	7	ssEPI	20	1000	0.30 (0.18, 0.42)	1.30
Tagliafico 2011	3	40	ssEPI	32	1000	0.37 (0.35, 0.38)	2.70
Wade 2020b	3	10	ssEPI	64	1000	0.26 (0.20, 0.32)	2.19
Subtotal (I-squared = 97.8%, p = 0.000)						0.38 (0.34, 0.42)	22.21
C7							
Chen 2012	1.5	32	ssEPI	32		0.44 (0.43, 0.46)	2.70
Oudeman 2018	3	30	ssEPI	15	800	0.34 (0.33, 0.35)	2.72
Ho 2017	3	10	ssEPI	30	800	0.43 (0.41, 0.45)	2.64
Su 2019	3	163	ssEPI	20	900	0.48 (0.47, 0.49)	2.71
Ho 2019	3	10	ssEPI		900	0.37 (0.35, 0.39)	2.67
Ho 2019	3	10	rsEPI		900	0.36 (0.34, 0.38)	2.63
Wade 2020a	3	7	ssEPI	20	1000	0.31 (0.18, 0.44)	1.18
Tagliafico 2011	3	40	ssEPI	32	1000	0.32 (0.30, 0.34)	2.68
Wade 2020b	3	10	ssEPI	64	1000	0.26 (0.20, 0.32)	2.19
Subtotal (I-squared = 98.2%, p = 0.000)						0.37 (0.33, 0.42)	22.12
C8							
Chen 2012	1.5	32	ssEPI	32		0.40 (0.38, 0.41)	2.70
Oudeman 2018	3	30	ssEPI	15	800	0.33 (0.31, 0.35)	2.67
Ho 2017	3	10	ssEPI	30	800	0.43 (0.41, 0.45)	2.64
Su 2019	3	163	ssEPI	20	900	0.47 (0.46, 0.49)	2.72
Ho 2019	3	10	ssEPI		900	0.36 (0.34, 0.38)	2.68
Ho 2019	3	10	rsEPI		900	0.35 (0.33, 0.38)	2.59
Wade 2020a	3	7	ssEPI	20	1000	0.31 (0.18, 0.44)	1.13
Tagliafico 2011	3	40	ssEPI	32	1000	0.28 (0.26, 0.29)	2.69
Wade 2020b	3	10	ssEPI	64	1000	0.26 (0.20, 0.32)	2.14
Subtotal (I-squared = 98.5%, p = 0.000)						0.36 (0.31, 0.41)	21.97
T1							
Ho 2017	3	10	ssEPI	30	800	0.40 (0.38, 0.42)	2.67
Ho 2019	3	10	ssEPI		900	0.34 (0.33, 0.36)	2.69
Ho 2019	3	10	rsEPI		900	0.35 (0.33, 0.37)	2.66
Wade 2020a	3	7	ssEPI	20	1000	0.29 (0.15, 0.43)	1.06
Wade 2020b	3	10	ssEPI	64	1000	0.24 (0.18, 0.30)	2.14
Subtotal (I-squared = 89.6%, p = 0.000)						0.34 (0.30, 0.38)	11.22
Overall (I-squared = 97.8%, p = 0.000)						0.37 (0.35, 0.39)	100.00

Figure 106. A forest pot summarising the normal fractional anisotropy of the roots of the brachial plexus, subgrouped by cervical root.

Six studies[149,242,243,252,255,256] contributed to the meta-analysis of the normal MD of the roots of the brachial plexus at 3T; one study[239] did not provide estimates of the variance and one study[251] did not report the MD of any roots. The pooled

estimate of the normal MD of the roots of the brachial plexus was 1.51 $\times 10^{-3}$ mm^2/s (95% CI 1.45, 1.56; Figure 107); however, there was high statistical heterogeneity between studies (I^2 99%) which may be related to the experimental conditions described above.

Study	N	EPI	b-value	Spinal root	ES (95% CI)	% Weight
15 directions						
Oudeman 2018	30	ssEPI	800	C5	1.37 (1.32, 1.42)	5.50
Oudeman 2018	30	ssEPI	800	C6	1.37 (1.34, 1.40)	5.65
Oudeman 2018	30	ssEPI	800	C7	1.35 (1.32, 1.38)	5.65
Oudeman 2018	30	ssEPI	800	C8	1.35 (1.28, 1.42)	5.30
Subtotal (I^2=0%, p=0.808)					1.36 (1.34, 1.38)	22.11
20 directions						
Su 2019	163	ssEPI	900	C5	1.54 (1.51, 1.56)	5.68
Su 2019	163	ssEPI	900	C6	1.43 (1.41, 1.46)	5.71
Su 2019	163	ssEPI	900	C7	1.40 (1.38, 1.42)	5.72
Su 2019	163	ssEPI	900	C8	1.39 (1.36, 1.41)	5.72
Wade 2020a	7	ssEPI	1000	C5	1.66 (1.03, 2.29)	0.67
Wade 2020a	7	ssEPI	1000	C6	1.76 (1.10, 2.41)	0.62
Wade 2020a	7	ssEPI	1000	C7	1.77 (1.10, 2.43)	0.61
Wade 2020a	7	ssEPI	1000	C8	1.73 (1.05, 2.41)	0.58
Wade 2020a	7	ssEPI	1000	T1	1.75 (1.09, 2.40)	0.63
Subtotal (I^2=91%, p<0.001)					1.45 (1.39, 1.51)	25.94
30 directions						
Ho 2017	10	ssEPI	800	C5	1.58 (1.41, 1.74)	3.85
Ho 2017	10	ssEPI	800	C6	1.51 (1.35, 1.67)	3.80
Ho 2017	10	ssEPI	800	C7	1.50 (1.35, 1.66)	4.00
Ho 2017	10	ssEPI	800	C8	1.58 (1.43, 1.73)	4.05
Ho 2017	10	ssEPI	800	T1	1.55 (1.44, 1.67)	4.66
Subtotal (I^2=0%, p=0.937)					1.55 (1.48, 1.61)	20.35
32 directions						
Tagliafico 2011	40	ssEPI	1000	C5	1.68 (1.67, 1.69)	5.75
Tagliafico 2011	40	ssEPI	1000	C6	1.60 (1.59, 1.60)	5.76
Tagliafico 2011	40	ssEPI	1000	C7	1.41 (1.40, 1.43)	5.75
Tagliafico 2011	40	ssEPI	1000	C8	1.61 (1.60, 1.62)	5.76
Subtotal (I^2=100%, p<0.001)					1.57 (1.47, 1.68)	23.02
64 directions						
Wade 2020b	10	ssEPI	1000	C5	1.62 (1.25, 1.98)	1.64
Wade 2020b	10	ssEPI	1000	C6	1.70 (1.32, 2.07)	1.56
Wade 2020b	10	ssEPI	1000	C7	1.75 (1.40, 2.09)	1.76
Wade 2020b	10	ssEPI	1000	C8	1.76 (1.43, 2.09)	1.83
Wade 2020b	10	ssEPI	1000	T1	1.86 (1.52, 2.20)	1.79
Subtotal (I^2=0%, p=0.909)					1.74 (1.58, 1.90)	8.58
Overall (I^2=99%, p<0.001)					1.51 (1.45, 1.56)	100

Figure 107. Summary estimates of the normal mean diffusivity of the roots of the brachial plexus at 3-Tesla.

The pooled estimates of the normal MD subgrouped by spinal root (including the study performed at 1.5T which had usable data[253]) is shown in Figure 108.

197

Study	N	Field (Tesla)	EPI	Directions	b-value		ES (95% CI)	% Weight
C5								
Chen 2012	32	1.5	ssEPI	32			1.15 (1.10, 1.21)	4.43
Oudeman 2018	30	3	ssEPI	15	800		1.37 (1.32, 1.42)	4.44
Ho 2017	10	3	ssEPI	30	800		1.58 (1.41, 1.74)	3.28
Su 2019	163	3	ssEPI	20	900		1.54 (1.51, 1.56)	4.56
Wade 2020a	7	3	ssEPI	20	1000		1.66 (1.03, 2.29)	0.63
Tagliafico 2011	40	3	ssEPI	32	1000		1.68 (1.67, 1.69)	4.61
Wade 2020b	10	3	ssEPI	64	1000		1.62 (1.25, 1.98)	1.50
Subtotal (I-squared = 98.9%, p = 0.000)							1.49 (1.32, 1.65)	23.45
C6								
Chen 2012	32	1.5	ssEPI	32			1.13 (1.06, 1.20)	4.32
Oudeman 2018	30	3	ssEPI	15	800		1.37 (1.34, 1.40)	4.54
Ho 2017	10	3	ssEPI	30	800		1.51 (1.35, 1.67)	3.24
Su 2019	163	3	ssEPI	20	900		1.43 (1.41, 1.46)	4.58
Wade 2020a	7	3	ssEPI	20	1000		1.76 (1.10, 2.41)	0.59
Tagliafico 2011	40	3	ssEPI	32	1000		1.60 (1.59, 1.60)	4.61
Wade 2020b	10	3	ssEPI	64	1000		1.70 (1.32, 2.07)	1.44
Subtotal (I-squared = 98.7%, p = 0.000)							1.44 (1.31, 1.57)	23.33
C7								
Chen 2012	32	1.5	ssEPI	32			1.18 (1.12, 1.24)	4.34
Oudeman 2018	30	3	ssEPI	15	800		1.35 (1.32, 1.38)	4.54
Ho 2017	10	3	ssEPI	30	800		1.50 (1.35, 1.66)	3.39
Su 2019	163	3	ssEPI	20	900		1.40 (1.38, 1.42)	4.59
Wade 2020a	7	3	ssEPI	20	1000		1.77 (1.10, 2.43)	0.58
Tagliafico 2011	40	3	ssEPI	32	1000		1.41 (1.40, 1.43)	4.61
Wade 2020b	10	3	ssEPI	64	1000		1.75 (1.40, 2.09)	1.61
Subtotal (I-squared = 91.2%, p = 0.000)							1.37 (1.32, 1.42)	23.65
C8								
Chen 2012	32	1.5	ssEPI	32			1.25 (1.19, 1.32)	4.34
Oudeman 2018	30	3	ssEPI	15	800		1.35 (1.28, 1.42)	4.30
Ho 2017	10	3	ssEPI	30	800		1.58 (1.43, 1.73)	3.42
Su 2019	163	3	ssEPI	20	900		1.39 (1.36, 1.41)	4.58
Wade 2020a	7	3	ssEPI	20	1000		1.73 (1.05, 2.41)	0.55
Tagliafico 2011	40	3	ssEPI	32	1000		1.61 (1.60, 1.62)	4.61
Wade 2020b	10	3	ssEPI	64	1000		1.76 (1.43, 2.09)	1.67
Subtotal (I-squared = 98.8%, p = 0.000)							1.47 (1.33, 1.61)	23.48
T1								
Ho 2017	10	3	ssEPI	30	800		1.55 (1.44, 1.67)	3.86
Wade 2020a	7	3	ssEPI	20	1000		1.75 (1.09, 2.40)	0.60
Wade 2020b	10	3	ssEPI	64	1000		1.86 (1.52, 2.20)	1.63
Subtotal (I-squared = 33.7%, p = 0.222)							1.65 (1.44, 1.85)	6.09
Overall (I-squared = 98.9%, p = 0.000)							1.46 (1.40, 1.51)	100.00

1   1.5   2
mm²/s x10³

Figure 108. Summary estimates of the normal mean diffusivity of the roots of the brachial plexus, subgrouped by cervical root.

There was no evidence of small-study effects (Figure 109).

Funnel plot with pseudo 95% confidence limits

Figure 109. A funnel plot showing no evidence of small-study effects

1.14.4 <u>Discussion</u>

We have shown that the roots of the brachial plexus in adults have a mean fractional anisotropy of 0.36 (95% CI 0.34, 0.38) and mean diffusivity of 1.51 x10^{-3} mm^2/s (95% CI 1.45, 1.56). However, there is substantial heterogeneity and the estimates appear to be affected by experimental conditions such as the field strength, b-value and N_D as well as patient factors, such as age.

Although we provide no direct comparisons, this work reinforces the generally accepted concept that the DTI parameters of peripheral nerves are different to those of the central white matter tracts of the brain[255]. The systematic reviews by Label[73] and Yap[258] showed that in health, the white matter tracts of the brain have a mean FA of approximately 0.36 to 0.54 and mean MD of 0.84 to 1.43 x10^{-3} mm^2/s, depending on the fibre bundle measured and the age of the individual. We find that the roots of the brachial plexus have a substantially lower average FA (between 0.34 and 0.38 with 95% confidence) and higher MD (95% CI 1.45 to 1.56 mm^2/s x10^{-3}), which are comparable to the lower bounds of the central white matter values. We believe that these discrepancies are likely to be related

to differences in the axon density (the corpus callosum has 38,000 myelinated fibres per mm^2 whereas the brachial plexus has approximately 8348 fibres per mm^2)[16,259] and that there is extensive intraneural fascicular sharing/crossing within the brachial plexus[15,260].

Several experimental factors[261] are known to affect DTI parameters, including: a) scanning conditions such as the SNR[79], components of the b-value[262,263], N_D[246,264]; b) pre-processing pipelines for denoising, correcting artefacts arising from susceptibility, motion and eddy currents[265,266] and tensor fitting methods[79], and c) the size and position of ROIs which vary in their sensitivity to partial volume effects[267]. Despite these limitations, the TraCED challenge[114] and several phantom studies[214–216] have demonstrated that very high reproducibility across scanners, sequences and sessions for tractography from DTI was possible. With more sophisticated sequences (e.g., high b-value multishell schemes), the reasons for the disparities between central and peripheral fibre diffusion parameters may become apparent. Nonetheless, we have shown DTI parameters are related to experimental conditions and therefore, we suggest that researchers and clinicians interpret our summary values with both caution and respect to their particular circumstances.

1.14.4.1   Diffusion sensitising gradient directions and FA

In this study, the N_D was strongly related to the FA whereby fewer directions were associated with higher estimates of the FA. This is a well-known phenomenon[264] and likely to be explained by the association between noise (which can couple to give rise to anisotropy) and artefactually high estimates of the FA[79]. Whilst the observed FA values in the studies with relatively fewer directions and lower SNR appear plausible (rather than e.g. 0.9 which would clearly be artefactual), it is possible that such studies are more susceptible to bias and their estimates of FA are falsely high. Equally, our model may still be subject to collinearity because studies with higher N_D tended to also have a higher SNR. Conversely, as MD measures the size of the diffusion ellipsoid[268], we expected[264] MD to be independent of the N_D and this is what we observed.

1.14.4.2   Age and anisotropy

As humans age, axons lose their integrity, peripheral nerves demyelinate and there is a corresponding increase in extra-cellular fluid. Consequently, advancing aging is typically associated with reduced FA and increased diffusivity in white matter structures[258,269]. Prior work by Kronlage et al (2018)[270] on the peripheral nerves in the forearm showed that the FA reduced with age (as in the brain[258]). We observed no statistically significant association between age and the FA of the roots of the brachial plexus but this may be due to the narrow age range of participants in our study. Whilst Kronlage[270] found that MD increased with age, we found that MD was slowed by 0.03 x10^{-3} mm^2/s with each year of life (Figure 5). Our findings are in agreement with the wider literature on age-related diffusivity changes in the brain[269] and compatible with the biological mechanisms of aging. Specifically, we observed that the MD of the roots of the brachial plexus slowed in the 3rd and 4th decade of life, which has also been observed in the healthy senescent adult brain[269]. It is unclear why Kronlage's work differs but this might be due to discrepancies in the age range of the sample (adults in this review were aged 28-45 years versus 20-80 years in Kronlage's[270]) and aspects of the scanning because Kronlage[270] used non-isotropic voxels (4.0mm through plane, 1.5mm^2 in plane) which might underestimate the FA and overestimate the MD[266].

1.14.4.3   Limitations

The main limitation of this review is the pooled estimation of FA and MD. We decided to perform meta-analyses in the presence of high statistical heterogeneity because a) the generated outputs provide an important graphical representation of the variability of measurements in relation to experimental conditions which are easy to interpret, and b) the forest plots provide a pictorial representation of the deleterious effects of failing to adjust study-level estimates for repeated measures. Eight studies[149,239,242,243,251–253,256] did not use multilevel models, so the standard errors of the mean (and thus, their CIs) are almost certainly falsely small. We believe that if studies had appropriately adjusted for clustering/repeated measures, the CIs would be wider, overlaps the aggregate means from other studies and the measures of statistical heterogeneity (e.g. I^2) would fall.

We show a negative association between MD and age; however, readers should note that the range of aggregate ages in the included studies is narrow (28 to 45 years) and so the estimates may not be generalisable to the population.

1.14.5 Conclusions

The roots of the brachial plexus in adults appear to have a pooled mean fractional anisotropy of 0.36 (95% CI 0.34, 0.38) and pooled mean diffusivity of 1.51×10^{-3} mm^2/s (95% CI 1.45, 1.56), although these parameters are dependent on experimental conditions and vary slightly from C5 to T1.

Now that the ground truth for the step angle and normal DTI metrics have been delineated, by holding these factors constant other covariables can be explored.

Chapter 15.   The Fractional Anisotropy Threshold for Deterministic Tractography of the Brachial Plexus

1.15.1 Introduction

Previous studies have shown the feasibility of DTI tractography of the brachial plexus in adults[146,150,239,243,254,271] and others have shown the reproducibility of DTI metrics without tractography[147,272]. Tagliafico[271] and Vargas[239] used different FA thresholds for tractography across patients, citing thresholds of 0.15 +/- 0.05 but it is unclear how and from where these values were measured, and what the +/- 0.05 represents. Tagliafico[271] does not report the frequency of propagated streamlines whilst Vargas[239] propagated C5-T1 streamlines in all healthy volunteers. Conversely, work from our group[243] and Oudeman[146] used fixed FA thresholds of 0.06 and 0.1, respectively. Oudeman[146] reconstructed fibres representing the C5-C8 root in all cases, but in 52% of datasets, the 1st thoracic root was not reconstructed. Similarly, we propagated streamlines of the C5-C8 roots in 96% of cases, although the T1 root was only visualised in 54% of datasets. Neither Gasparotti[150] or Su[254] described the FA thresholds they used for tractography, with the former reconstructing all roots in all subjects and the latter only reporting on the C5-8 roots.

It is widely accepted that the FA threshold has a significant effect on white matter tractography. Based on the work shown in Chapter 14 which defined the 'normal' FA and diffusivity of the spinal roots (which differ to the white mater of the brain) there is precedent to suspect that the FA threshold(s) needed to generate streamlines representing real nerves are different to the accepted thresholds in the brain. Equally, the effect of different FA thresholds on tractograms of the brachial plexus remains unclear which represents the rationale for this study.

1.15.2 Methods

This single-centre study was designed and reported in accordance with the STARD guidance, taking into account the domains of the QUADAS-2 and PRISMA-DTA tools. Approval was gained from the National Research and Ethics

Service of the United Kingdom (reference 16/YH/0162) and informed written consent was obtained from all participants.

1.15.2.1 Participants and recruitment

We recruited ten healthy adults who had no prior injuries or pathology affecting the brachial plexus. All volunteers were colleagues working within the institutions of the authors. They were recruited via posters, email circulars or word-of-mouth. All persons were assumed to have in-continuity roots.

1.15.2.2 Image Acquisition

DTI was acquired at a field strength of 3T using a Siemens Magnetom Prisma (Siemens Healthcare Limited, Erlangen, Germany). A 64-channel head and neck coil in combination with posterior spin coils were used. Single-shot echo-planar imaging (ssEPI) was used with TR 4300ms, TE 66ms, in-plane resolution 2.5mm^2 and gapless axial slices of 2.5mm thickness. The field-of-view was 305x305x105mm from the C3 to T2 bodies, so as to include the origins of the rootlets for the 5-8th cervical and 1st thoracic spinal nerve roots. We used a b-value of 1000 s/mm^2, 64 directions, twice refocused spin echo (Seimens "bipolar" waveform), 4 interleaved b0s and acquired 4 signal averages. We used a TrueForm b1 shim, echo spacing 0.5ms, echo train length 445ms, GRAPPA factor 2, receiver bandwidth 2276Hz/px, 1st order motion correction and strong fat saturation. Two full diffusion-weighted datasets were acquired with opposing phase encoding directions; anterior-posterior and posterior-anterior. The acquisition time was 48 minutes in total.

1.15.2.3 Pre-processing

Data were exported and pre-processed in DSI Studio. To correct for susceptibility and eddy-current artefacts datasets with opposing phase encoding directions were combined and concatenated.

1.15.2.4 Tractography

We used DSI Studio for tractography given its superior performance in generating valid streamlines[273]. The diffusion data were reconstructed by DTI using a deterministic fiber tracking algorithm[274]. The FA thresholding started at 0.1 and

was reduced in decrements of 0.01 down to 0.04. At an FA threshold of 0.04 no new streamlines representing the roots were propagated in any subject at any spinal level. Therefore, the FA thresholds studied were 0.04, 0.05, 0.06, 0.07, 0.08, 0.09 and 0.10, which is in keeping with other studies. The angular threshold was 70 degrees which is justified by cadaveric studies of the geometry of the roots[275]. Streamlines were propagated from a single seeding region covering the entire spinal cord. The rootlets/roots of the brachial plexus traverse approximately 3cm from the cephalad longitudinal axis of the spinal cord to the exit foramen[238] where they have a mean cross-sectional area 9mm^2 (minimum 5.6mm^2)[276]. Therefore, a region of interest (ROI) measuring 5mm^3 (4 voxels per slices; 8 voxels total) was placed over each root ~3cm lateral to the midline of the cord, lateral to the exit foramina on FA maps (Figure 110, Figure 111 and Figure 112). Subvoxel seeding was used with a step size of ≤1.25mm. A total of 250 streamlines were propagated per root. Streamlines shorter than 30mm were discarded. Topology-informed pruning[244] was applied with 10 iterations. DTI metrics were calculated at the region of interest (ROI) for all 10 of the spinal nerve roots individually. This process was performed by RGW and repeated in full by a 2nd independent author (GA; 6 years of DTI experience) to test the inter-rater reliability. Streamlines representing the spinal nerve roots were considered valid if the tract(s) originated cranially within the spinal cord and terminated beyond the ROI which covered the root (Figure 113). Furthermore, our regions of interest overlying the roots were set as "ROI" within DSI Studio, which meant that streamlines had to originate within the seeding region covering the spinal cord, but also both enter and exit the regions of interest overly the spinal nerve roots, meaning that we reduced the probability of rendering short (potentially false) streamlines which terminated within the ROI.
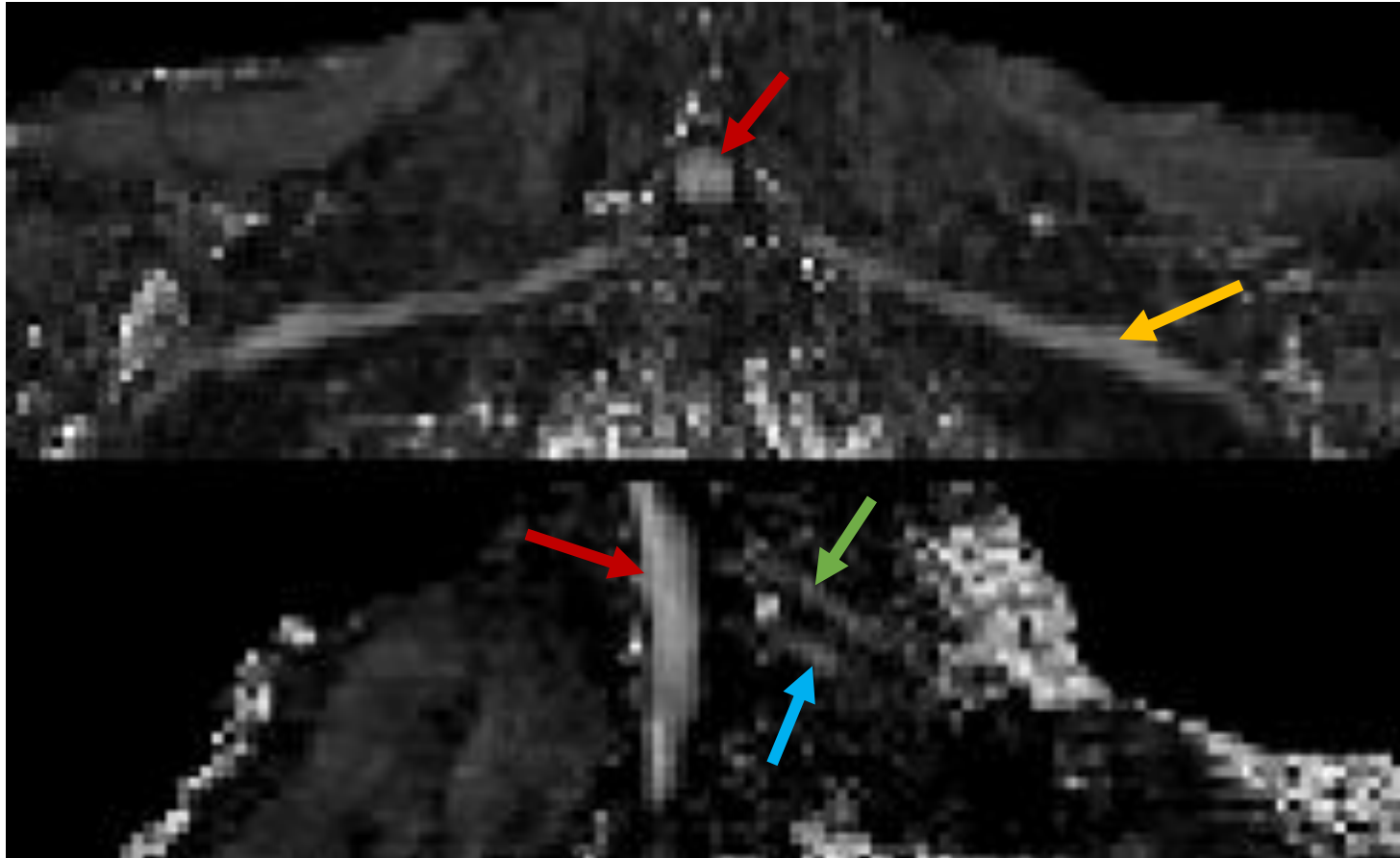
Figure 110. FA maps from a single volunteer. The top image is an axial-oblique slice showing the 7th cervical root arising from the spinal cord (red arrow) transitioning into the middle cord (yellow arrow) laterally. The lower image is a coronal-

oblique slice showing the spinal cord (again, red arrow) as well as the left 5th and 6th cervical roots (green and blue arrow, respectively).
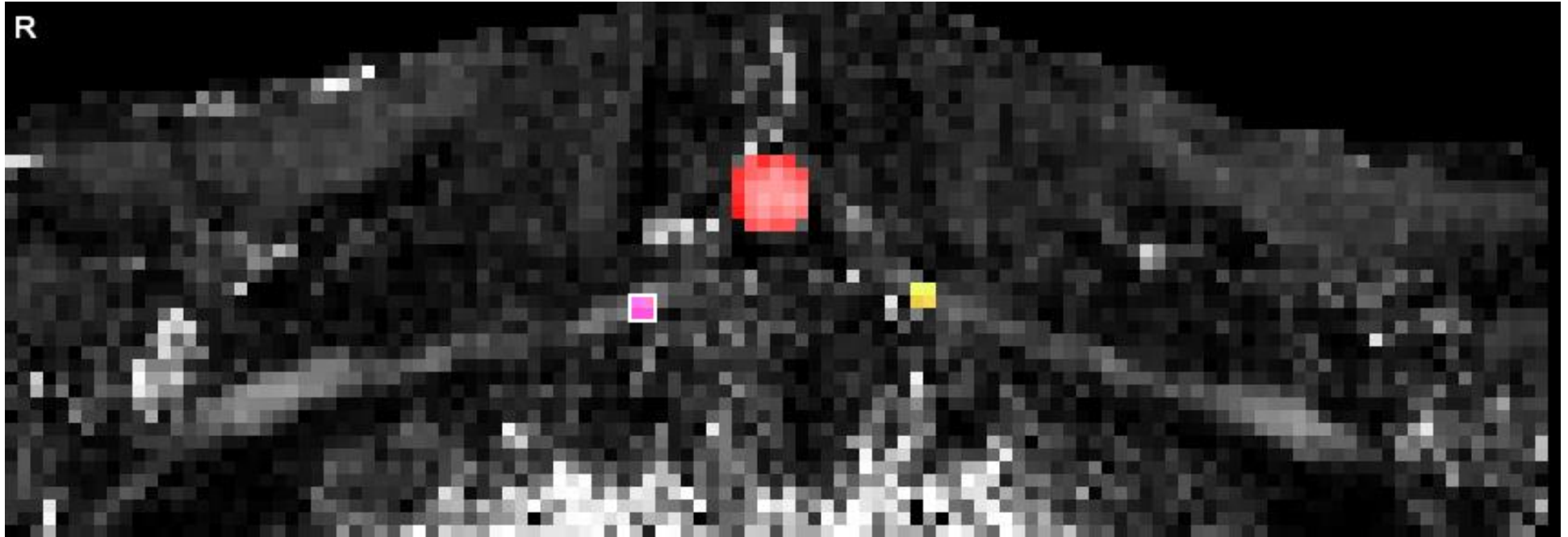
Figure 111. The same axial-oblique FA map as shown in Figure 110, with the regions of interest drawn over the spinal cord (red), left C7 root (yellow) and right C7 root (pink).
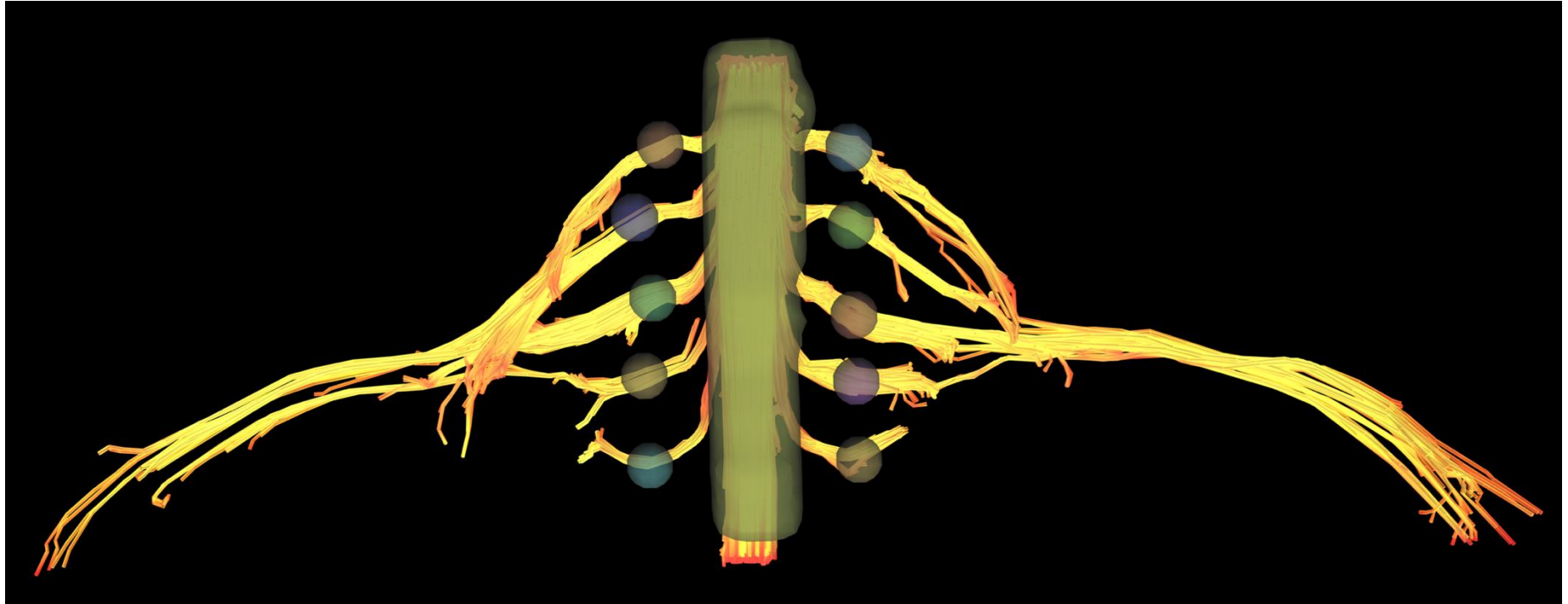
Figure 112. A deterministic tractogram with regions of interest overlaid. Each root was tracked individually. Streamlines representing each root were generated individually; streamlines were required to originate in the seeding region over the spinal cord and pass through (enter and exit) a spherical waypoints overlying the roots.
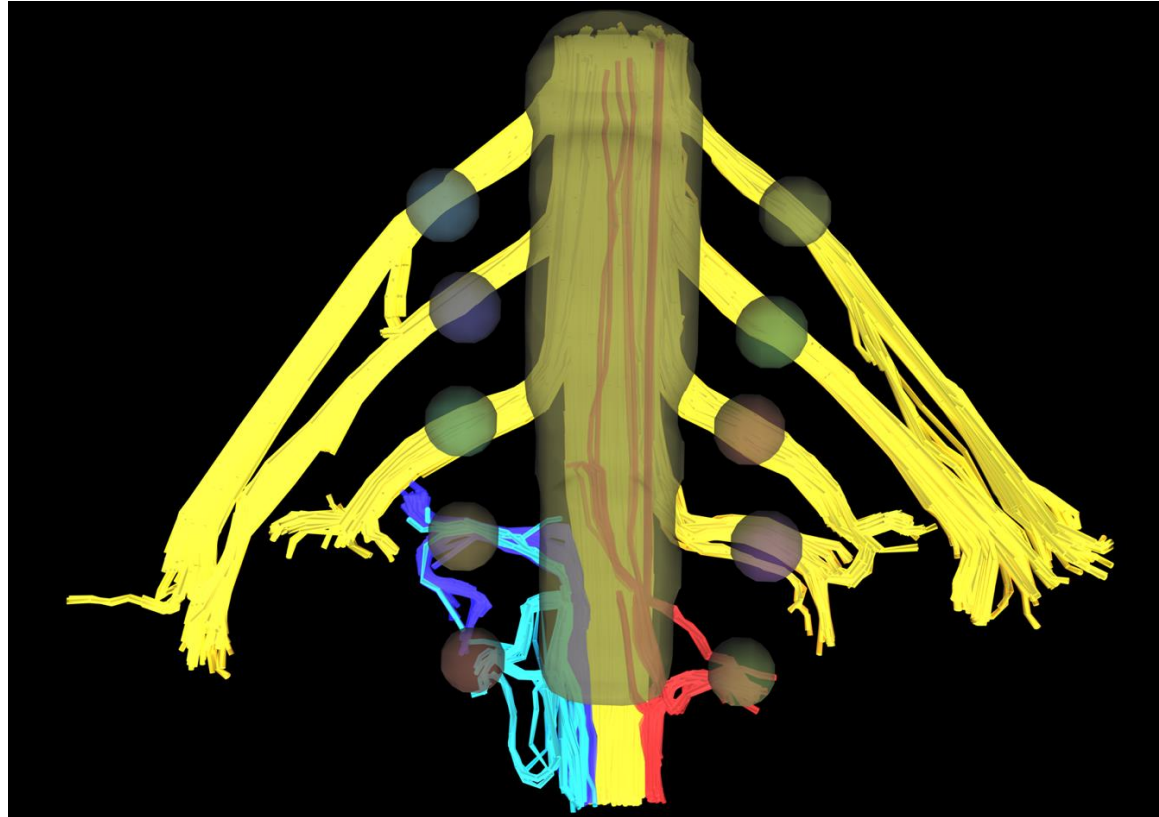
Figure 113. A deterministic tractogram from one volunteer with regions of interest overload. Streamlines coloured yellow were defined as "valid". The left T1 (red) tract-bundle was considered valid despite the caudally originating (false) streamlines which could be manually pruned, if desired. Both the dark and light blue coloured streamlines representing the right C8 and right T1 roots were considered "invalid" (by both raters) because the bundles originated caudally and there were numerous looping streamlines which do not resemble the true anatomy.

Data were analysed using Stata v15 (StataCop LLC, Texas). Age was skewed so is represented by the median and interquartile range (IQR) and compared using the Wilcoxon rank-sum test. Other scaled variables are normal so represented by the mean (and standard deviation, SD). DTI metrics were estimated using multilevel multivariable linear regression, with sex, side, hand dominance and root level comprising the fixed effects and (because measurements from each root are correlated as they derive from a single individual) the random effect varied by volunteer. The cluster level variance and covariance parameters were estimated using the restricted maximum likelihood. Agreement was assessed using Cohen's kappa for binary events (tract presence). To estimate the agreement (intraclass correlation coefficient, ICC) between rates measurements of DTI metrics, the rater was added as a fixed effect to the multilevel multivariable linear regression and the agreement between the estimates are summarised in a Bland Altman plot.

1.15.3 Results

There were eight males and two females. The mean age was 28 years (SD 4, range 21-34). Eight were right-handed. DTI metrics from the roots are shown in Table 15.

| Level | Side | Mean (SD)* DTI values Derived from Propagated Streamlines | | | |
		Fractional Anisotropy	Mean Diffusivity (mm^2/s x10^{-3})	Axial Diffusivity (mm^2/s x10^{-3})	Radial Diffusivity (mm^2/s x10^{-3})
C5	Right	0.24 (0.07)	1.62 (0.58)	2.04 (0.64)	1.40 (0.56)
	Left	0.25 (0.07)	1.61 (0.59)	2.04 (0.65)	1.40 (0.57)
C6	Right	0.26 (0.08)	1.70 (0.61)	2.18 (0.69)	1.45 (0.58)
	Left	0.26 (0.08)	1.69 (0.60)	2.16 (0.68)	1.45 (0.58)
C7	Right	0.26 (0.09)	1.81 (0.57)	2.33 (0.67)	1.55 (0.54)
	Left	0.26 (0.09)	1.68 (0.54)	2.15 (0.64)	1.45 (0.50)
C8	Right	0.26 (0.10)	1.79 (0.48)	2.30 (0.57)	1.53 (0.46)
	Left	0.26 (0.09)	1.73 (0.50)	2.23 (0.62)	1.48 (0.46)
T1	Right	0.25 (0.11)	1.84 (0.55)	2.33 (0.60)	1.60 (0.56)
	Left	0.23 (0.09)	1.88 (0.55)	2.35 (0.63)	1.66 (0.53)
All roots	Right	0.26 (0.09)	1.74 (0.56)	2.23 (0.64)	1.50 (0.54)
	Left	0.25 (0.08)	1.72 (0.55)	2.19 (0.64)	1.48 (0.52)
	Overall	**0.25 (0.09)**	**1.73 (0.56)**	**2.21 (0.64)**	**1.49 (0.53)**

Table 15. DTI metrics from all volunteers tabluated by the root

1.15.3.1   Variability in DTI metrics between subjects

There was significant variability between subjects DTI metrics (Table 16). The mean FA varied between subjects by 2% (95% CI 1%, 3%); ICC 0.16, $p<0.001$). The mean MD varied by a mean of 0.15 mm^2/s x10^{-3} (95% CI 0.09, 0.24); ICC 0.40, $p<0.001$). The mean AD varied by a mean of 0.18 mm^2/s x10^{-3} (95% CI 0.11, 0.29); ICC 0.37, $p<0.001$). The RD varied by a mean of 0.14 mm^2/s x10^{-3} (95% CI 0.09, 0.22); ICC 0.40, $p<0.001$).

Volunteer	Side	Mean (SD)* DTI values Derived from Propagated Streamlines			
		Fractional Anisotropy	Mean Diffusivity (mm²/s x10⁻³)	Axial Diffusivity (mm²/s x10⁻³)	Radial Diffusivity (mm²/s x10⁻³)
1	Right	0.27 (0.09)	1.88 (0.65)	2.42 (0.72)	1.60 (0.63)
	Left	0.27 (0.09)	1.85 (0.65)	2.39 (0.75)	1.57 (0.62)
2	Right	0.29 (0.10)	1.83 (0.58)	2.40 (0.69)	1.54 (0.55)
	Left	0.29 (0.10)	1.77 (0.57)	2.33 (0.67)	1.50 (0.54)
3	Right	0.23 (0.09)	1.90 (0.62)	2.41 (0.71)	1.64 (0.60)
	Left	0.24 (0.08)	1.86 (0.61)	2.32 (0.66)	1.64 (0.59)
4	Right	0.26 (0.09)	1.78 (0.56)	2.26 (0.59)	1.54 (0.56)
	Left	0.25 (0.09)	1.78 (0.55)	2.27 (0.60)	1.54 (0.54)
5	Right	0.31 (0.11)	1.71 (0.46)	2.31 (0.55)	1.41 (0.45)
	Left	0.27 (0.08)	1.67 (0.47)	2.17 (0.56)	1.42 (0.45)
6	Right	0.28 (0.10)	1.50 (0.51)	1.96 (0.57)	1.28 (0.5)
	Left	0.26 (0.09)	1.49 (0.46)	1.90 (0.51)	1.29 (0.45)
7	Right	0.27 (0.09)	1.79 (0.53)	2.30 (0.62)	1.52 (0.50)
	Left	0.26 (0.09)	1.87 (0.47)	2.41 (0.68)	1.61 (0.57)
8	Right	0.29 (0.09)	1.54 (0.57)	2.02 (0.69)	1.29 (0.52)
	Left	0.29 (0.09)	1.48 (0.47)	1.96 (0.57)	1.25 (0.43)
9	Right	0.25 (0.09)	1.90 (0.59)	2.41 (0.64)	1.65 (0.60)
	Left	0.27 (0.09)	1.99 (0.63)	2.56 (0.72)	1.70 (0.60)
10	Right	0.24 (0.09)	1.80 (0.51)	2.26 (0.56)	1.57 (0.50)
	Left	0.24 (0.09)	1.77 (0.55)	2.23 (0.62)	1.55 (0.53)

Table 16. DTI metrics from all roots the brachial plexus tabulated by individual

1.15.3.2 Variability in DTI metrics between sex, side, and handedness

The FA was higher on the right side, although the absolute difference was very small (mean difference 0.01 [95% CI 0.002, 0.02]). Similarly, the FA was higher in the roots of the dominant limb (mean difference 0.01 [95% CI 0.01, 0.2]) although the absolute difference was again very small. There was no significant interaction between hand dominance and side (p=0.05). There was no

statistically significant difference in the FA measurements from the roots of men and women (mean difference -0.01 [95% CI -0.04, 0.02]).

The MD was higher on the right side (mean increase 0.02 mm^2/s x10^{-3} [95% CI 0.002, 0.04]) and in the roots of the non-dominant limb (mean increase 0.02 mm^2/s x10^{-3} [95% CI 0.005, 0.04]), although the absolute differences were very small. There was no interaction between hand dominance and side (p=0.05). There was no difference in the MD of the roots between men and women (mean difference 0.08 mm^2/s x10^{-3} [95% CI -0.16, 0.32]).

The AD was higher on the right side (mean increase 0.05 mm^2/s x10^{-3} [95% CI 0.03, 0.07]) and in the non-dominant limb (mean increase 0.05 mm^2/s x10^{-3} [95% CI 0.03, 0.08]), although the absolute differences were very small. There was no interaction between hand dominance and side (p=0.05). Again, there was no difference in the AD of the roots between men and women (mean difference 0.07 mm^2/s x10^{-3} [95% CI -0.22, 0.36]).

There was no difference in the RD between the right and left side (mean difference 0.003 mm^2/s x10^{-3} [95% CI -0.01, 0.02]), the dominant limb and non-dominant limbs (mean difference 0.008 mm^2/s x10^{-3} [95% CI -0.008, 0.03]), or men and women (mean difference 0.08 mm^2/s x10^{-3} [95% CI -0.13, 0.31]).

1.15.3.3   FA thresholds: Tractography

Overall, at higher FA thresholds fewer streamlines were propagated (Figure 114); this was principally due to the failure to render streamlines representing the T1 root (Figure 115) and to a lesser extent the other cervical roots (Figure 116 and Figure 117).
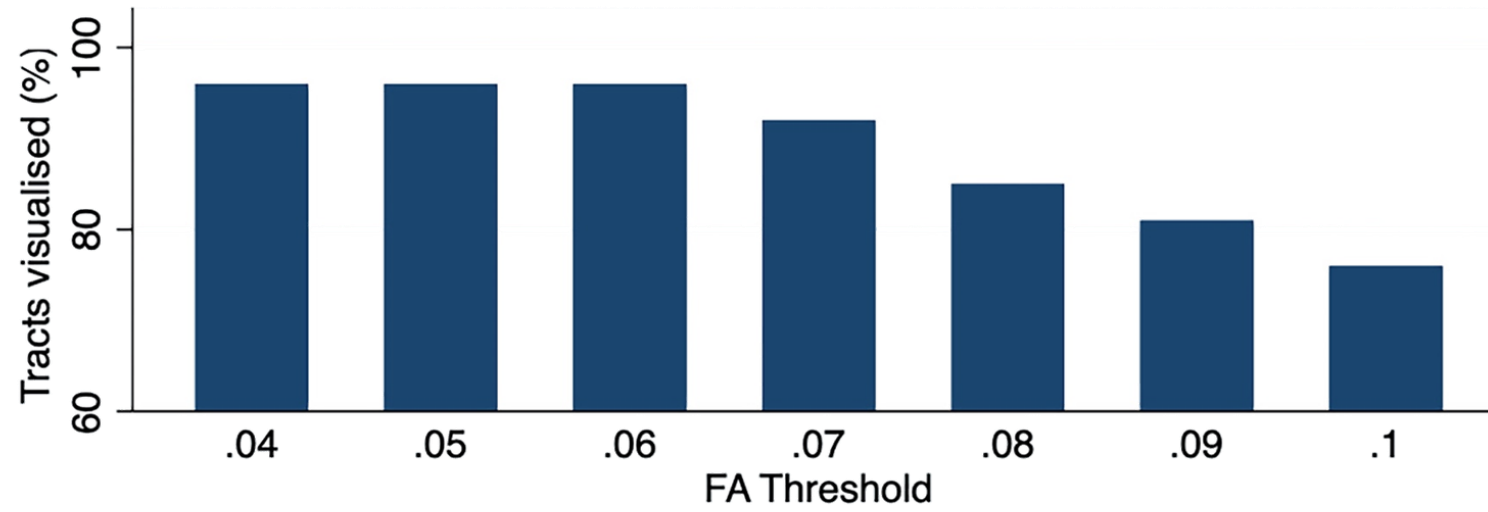
Figure 114. The overall proportion of visualised streamlines representing roots of the brachial plexus at different FA thresholds.
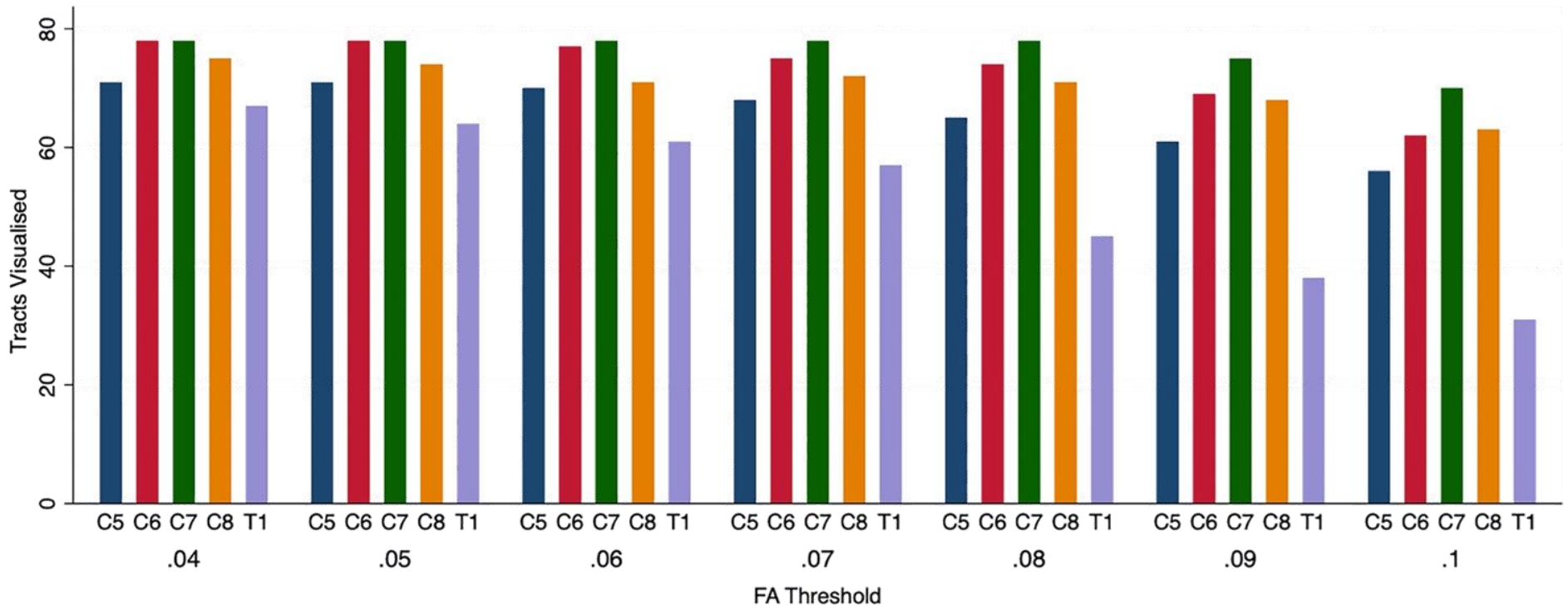
Figure 115. The proportion of streamlines visualised representing specific roots of the brachial plexus at different FA thresholds

FA 0.04　　　FA 0.06

FA 0.08　　　FA 0.1
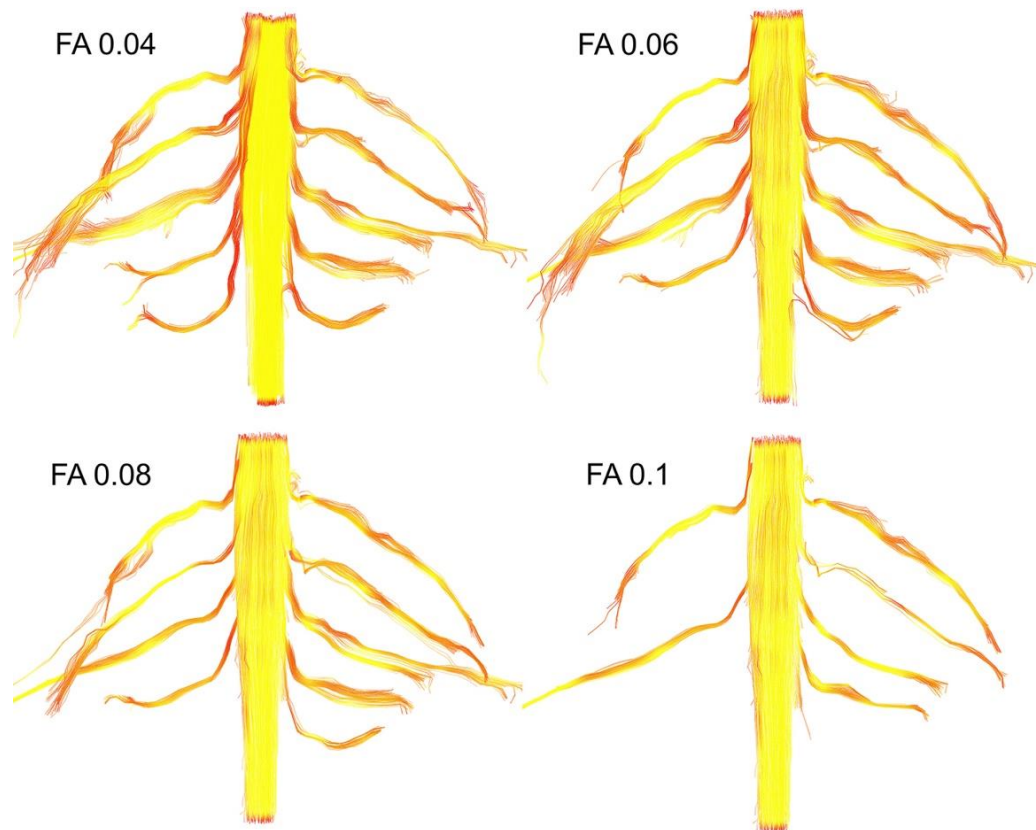
Figure 116. Tractography of the roots of the brachial plexus at different FA thresholds showing that at higher FA thresholds, numerous roots are not visualised. The colour of the tract is determined by the local FA whereby yellow denotes a high FA (0.5), scaled to red which denotes low FA (0).
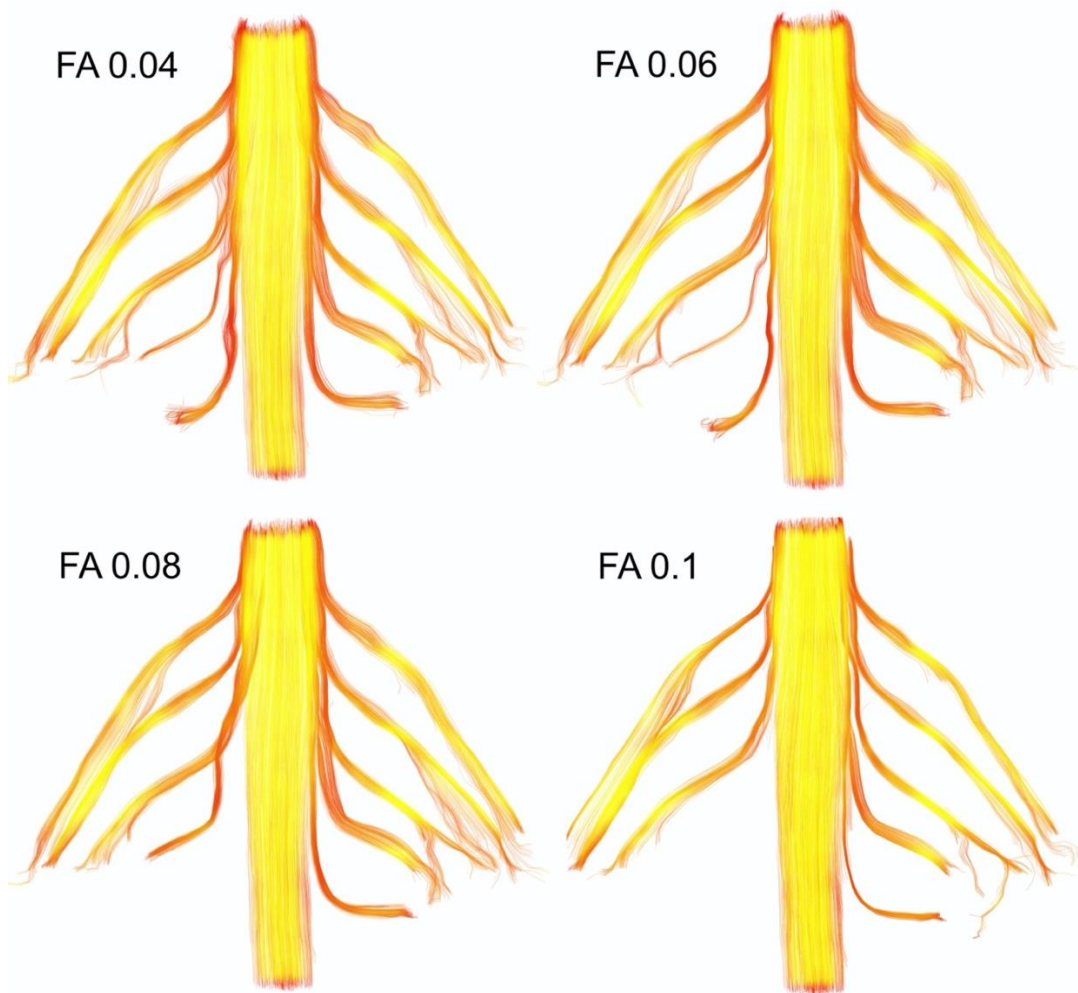
Figure 117. Tractography of the roots of the brachial plexus showing that at higher FA thresholds the right C8 and T1 roots are not propagated. The colour of the tract is determined by the local FA whereby yellow denotes a high FA (0.5), scaled to red which denotes low FA (0).

There was no statistically significant difference in the proportion of streamlines rendered at FA thresholds of 0.04, 0.05 or 0.06. Overall, at FA thresholds of ≤0.06 streamlines representing the roots were propagated for 96% of spinal levels (Figure 114 and Figure 115). In comparison, thresholding the FA at 0.07 yield 4% fewer streamlines (p=0.2), 0.08 yield 11% fewer streamlines (p=0.008), 0.09 yield 15% fewer streamlines (p=0.001) and 0.1 yield 20% fewer streamlines (p<0.001). This appears to be due to partial volume effects (reduce by cerebrospinal fluid) as the FA in the rootlets is substantially lower than the spinal cord and extraforaminal portions of the spinal roots (Figure 116 and Figure 117).

FA thresholds: Tract length

Overall, the FA threshold was strongly associated with tract length (Figure 118), whereby for every unit increase in the FA threshold, propagated streamlines were 2mm shorter (95% CI 1.3, 2.7).
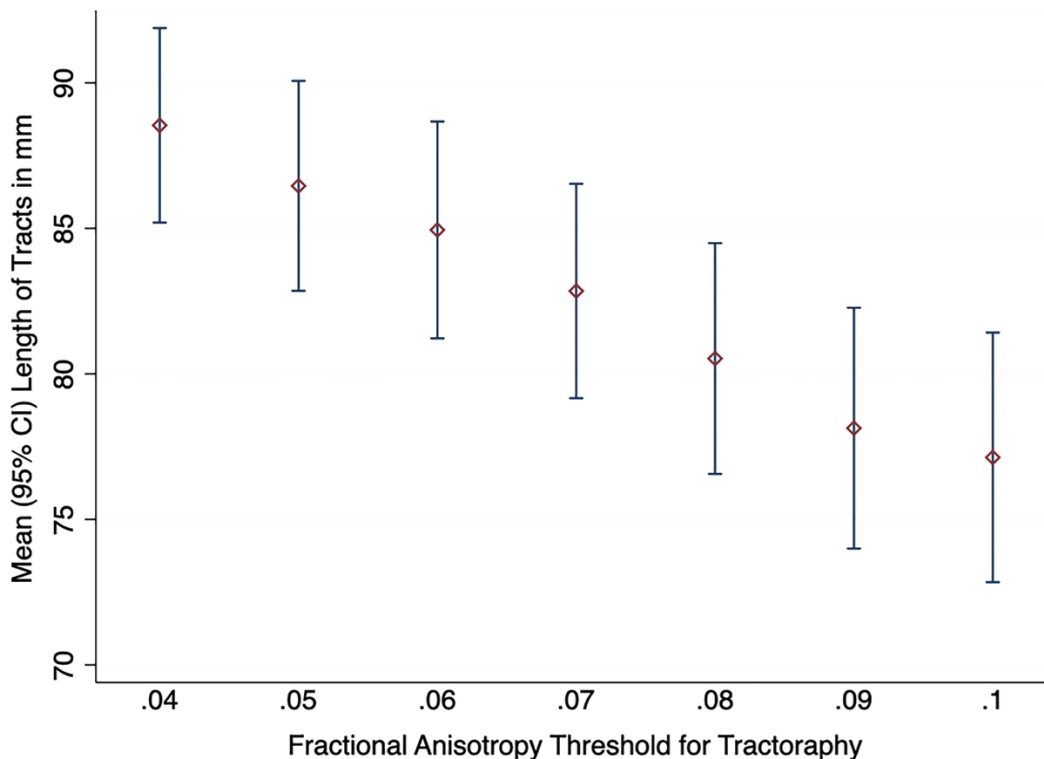
Figure 118. The mean length of streamlines (in mm) by FA threshold.

Using a FA threshold of 0.06, there was no significant difference in the length of streamlines between the left and right side (mean difference 1.37 mm [95% CI -3.22, 6.00]), the dominant and non-dominant limb (mean difference 2.24 mm [95% CI -2.00, 6.47]); or males and females (mean difference 5.30 mm [95% CI -0.10, 10.7]).

Inter-rater Agreement

There was 99% agreement between raters' assessment of the presence of a tract representing the roots at different FA thresholds (Cohen's kappa 0.92, p<0.001). There was strong agreement between raters' FA measurements from the roots

(Figure 119) with <0.1% variability (mean difference 0.008 [95% CI -0.004, 0.01]; ICC 0.001).
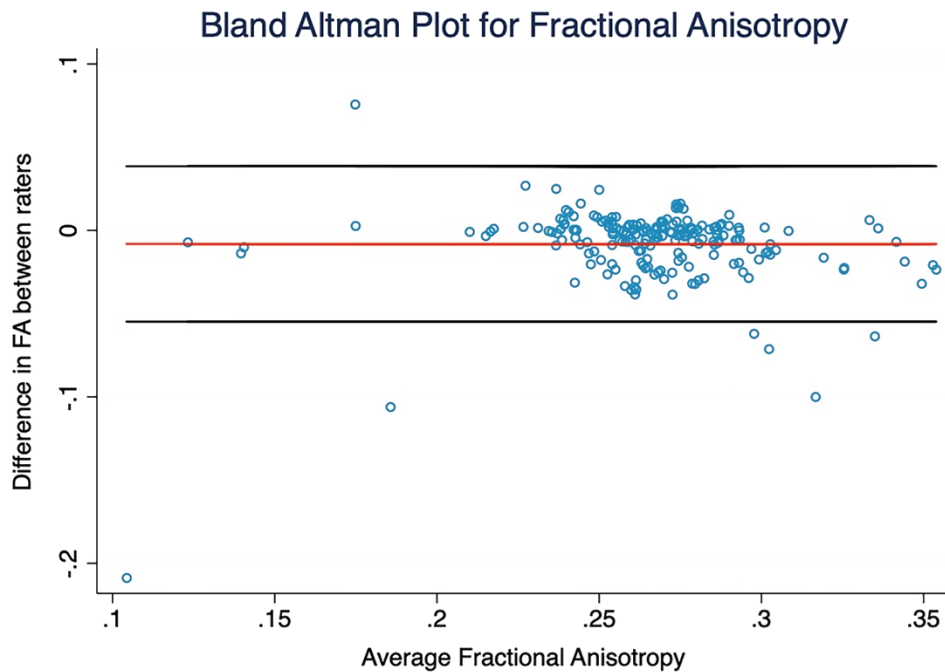
Figure 119. Bland Altman Plot showing strong agreement in the assessment of the fractional anisotropy of the roots between raters.

There was strong agreement between raters' assessment of MD (mean difference 0.02 [95% CI -1.7, 0.4]; ICC 0.016), AD (mean difference 0.01 [95% CI -2.1, 0.5]; ICC 0.02) and RD (mean difference 0.06 [95% CI -1.5, 0.4]; ICC 0.01).

1.15.4 Discussion

This work helps to define the ideal FA threshold for tractography of the roots of the brachial plexus in healthy adults. We show that an FA threshold of 0.06 maximises the visualisation of all five roots and recommend this as a starting point for tractography. This information may be used to inform future DTI studies which may consider the normal or abnormal roots of the brachial plexus in adults.

We have shown that the DTI metrics and FA threshold for tractography of the brachial plexus appear to be different from the white matter streamlines in the brain. Lebel and colleagues[73] showed that the mean FA of white matter

streamlines in the adult brain is 0.36 to 0.54, depending on the structure. However, we have shown that the extraforaminal roots have a lower mean FA. Whilst the brachial plexus roots are akin to white central matter streamlines (in that they are myelinated and highly ordered), the fascicular arrangement in the roots is substantially different in two main ways:

1. The density of axons (per mm^2) in the roots of the brachial plexus is 5 times less than the genu of the corpus callosum[259] and half that of the pyramidal tracts of the spinal cord[277]. In the corpus callosum there are approximately 38,000 myelinated fibres per mm^2 (70% are <1μm in diameter and highly restrictive to diffusion). In the spinal cord there are 10-20,000 axons per mm^2 (depending on the spinal level) and 52% are <1μm in diameter[278]. The roots of the brachial plexus have a mean of 8348 per mm^2; this estimate is based upon the work of Won and colleagues[276] who showed that the cross-sectional area of the brachial plexus roots ranged from 5.7mm^2 (C5) to 10.8mm^2 (C8). Gesslbauer et al[16] showed that the axon counts ranged from 38,000 (C5) to 90,000 (T1). The cross-sectional area of the T1 root is approximately 6.1mm^2 (based on a linear regression of the above data[16,276]) and has an axon density of 10,000 per mm^2. So on average, the spinal roots of the brachial plexus have an axon density of ~8348 per mm^2. Compared to the central nervous system, the lower axon count and density in the roots of the brachial plexus partly explains the lower FA.

2. Numerous histological studies have shown that the topography of the nerves of the brachial plexus changes every few millimetres and there is substantial fascicular sharing/cross-over[15,260]. Unlike the central white matter tracts, axons and fascicles in the roots bifurcate, merge, weave and exchange throughout the brachial plexus from the level of the intradural rootlets to the target organ[279]. These intraneural and interfascicular connections will increase signal dispersion and further explain why the FA is lower in the roots of the brachial plexus than in central white matter tracts.

Although our findings are broadly agree with the metrics reported in many DTI studies of the brachial plexus[146,147,150,254,271,272], our FA values are slightly lower. FA is a function of numerous factors such as the b-value and number of diffusion

encoding directions[246,264]. Reproducibility studies have shown that smaller b-values and fewer directions yield upwardly biased estimates of the FA[262,280]. We sampled more of q-space so our individual direction data may have lower signal-to-noise than other studies. Our higher b-value means a relatively lower signal-to-noise compared to those studies using a b-value of <1000 mm/s^2. Further, the rootlets are bathed in the cerebrospinal fluid so our data will be more influenced by partial volume effects (as shown by the red portions [lower FA] in Figure 3 and Figure 4) than Ho[147], for example. Therefore, it is plausible that other studies (of all which use smaller b-values and fewer directions) may be reporting upwardly biased estimates of the FA which underestimate dispersion and are more susceptible to noise. Further, no other study made the necessary adjustment for clustering (because numerous measurements of DTI metrics from one individual will be highly correlated) meaning their standard errors are falsely small. Future studies should consider reporting adjusted estimates from model-free methods (such as q-space imaging).

FA threshold	Level	Tract properties		
		Streamlines visualised (%)	Length (mm)	Tract Volume (mm^{-3})
0.04	C5	19 (95)	75 (18)	3192 (903)
	C6	20 (100)	86 (17)	3582 (868)
	C7	20 (100)	88 (17)	3581 (868)
	C8	19 (95)	84 (16)	3234 (803)
	T1	18 (90)	84 (21)	2893 (807)
	Overall	96 (96)	87 (3)	3410 (179)
0.05	C5	19 (95)	73 (17)	2044 (875)
	C6	20 (100)	85 (17)	2501 (896)
	C7	20 (100)	88 (16)	3429 (756)
	C8	19 (95)	84 (16)	3071 (769)
	T1	18 (90)	80 (23)	2711 (781)
	Overall	96 (96)	84 (4)	3198 (193)
0.06	C5	19 (95)	73 (17)	3029 (920)
	C6	20 (100)	85 (17)	3392 (914)
	C7	19 (95)	87 (16)	3353 (774)
	C8	19 (95)	84 (16)	2937 (813)
	T1	18 (90)	79 (24)	2510 (875)
	Overall	96 (96)	81 (4)	3002 (208)
0.07	C5	18 (90)	71 (17)	2903 (919)
	C6	20 (100)	84 (17)	3196 (917)
	C7	20 (100)	86 (17)	3188 (731)
	C8	19 (95)	84 (17)	2792 (758)
	T1	15 (75)	75 (26)	2199 (840)
	Overall	92 (92)	81 (4)	2903 (201)
0.08	C5	16 (80)	71 (17)	2730 (819)
	C6	19 (95)	83 (18)	3110 (903)
	C7	20 (100)	84 (18)	2977 (743)
	C8	19 (95)	81 (18)	2594 (772)
	T1	11 (55)	70 (27)	1922 (813)
	Overall	85 (85)	81 (4)	2747 (224)

	C5	15 (75)	69 (17)	2587 (740)
	C6	18 (90)	81 (17)	2893 (916)
0.09	C7	20 (100)	81 (18)	2870 (814)
	C8	18 (90)	80 (19)	2375 (705)
	T1	10 (50)	68 (26)	1780 (693)
	Overall	81 (81)	80 (5)	2473 (230)
	C5	15 (75)	67 (14)	2264 (739)
	C6	17 (85)	81 (18)	2759 (845)
0.1	C7	19 (95)	81 (19)	2582 (738)
	C8	16 (80)	76 (22)	2158 (669)
	T1	9 (45)	72 (23)	1643 (630)
	Overall	76 (76)	78 (5)	2280 (220)

Table 17. DTI metrics by the FA threshold used for tractography and root

DTI metrics vary subtly across scanners and pulse sequences[261]. However, the recent TraCED challenge[114] and numerous phantom studies[214–216] have shown this to have little/no deleterious effect on the reliability of tractograms because the majority strongly agree and there is very high reproducibility across scanners, sequences and sessions. This gives us confidence that our tractograms may be replicated elsewhere given similar experimental conditions. However, the application of this technology to clinical medicine remains guarded because despite decades of research and vast progress in the field, the DTI Challenge[281] showed that the utility of tractography in the brain is still uncertain. Similar work may be needed in the field of peripheral nerve surgery before clinical translation is widely accepted.

As with different regions of the brain, the ideal tractography conditions for peripheral nerves differ from region-to-region. Therefore, it is important that researchers and clinicians have evidence on which to base their selection of brachial plexus tracking thresholds so as to propagate streamlines which represent real connections and equally, avoid propagating false streamlines, e.g. into skeletal muscle which has a similar and positively correlated FA[282]. The typical FA thresholds used for tractography in the brain is ≥0.1, but this is too high

for the roots of the brachial plexus because the microstructure is different and thus, streamlines representing real connections would not propagate[146]. Similar studies of FA thresholding in the brain have shown that it has considerable effect on the number, density and directionality of streamlines, as well as tract-based estimates of anisotropy and diffusivity[283–285]. Furthermore, one study showed that with conventional FA thresholds (of $\geq$0.1), modern tractography algorithms which are robust to crossing-fibres missed clinically-important streamlines in the brain, whereas real-time threshold reductions to a FA of 0.06 yielded more meaningful and clinically-useful tractograms[285]. Therefore, we argue that using a FA threshold generalised from tractography studies in the brain or elsewhere is inappropriate. We provide estimates of the probability of streamline propagation using different metrics to demonstrate the ideal FA threshold for tractography of the healthy brachial plexus.

1.15.4.1   Limitations

The VoTEM and ISMRM Tractography challenges[235,273] showed that whilst DTI is largely reproducible, reliable and provides the best reconstructions which are closest to the ground truth, with the greatest valid:non-valid connection ratio[234], the prevalence of false connections remains high. We used topology-informed pruning[244] to remove false streamlines but this technology has not be validated in peripheral nerve tractography so our findings warrants cautious interpretation; we recommend that future studies examine the association between tractograms with different levels of pruning applied and the ground truth of 2D/3D photographs from anatomical dissections of uninjured adults.

The literature is lacking reliable human research concerning DTI metrics in peripheral nerve injury, degeneration, and regeneration and until this is known, the translational value of our work can only be speculated. We advocate the development of a biobank for diffusion MRI of peripheral nerves; ideally this would contain data from healthy adults, recently deceased donors and soft-fixed cadavers to permit comprehensive analysis of the effects of numerous co-variables on DTI metrics.

The 1st thoracic root was the least frequently reconstructed tract perhaps due to: low SNR given its distance from the receive coil, residual/uncorrected eddy current and/or susceptibility artefacts from the lung apex and 1st rib over which it courses, flow and partial volume effects due to the adjacent great vessels and spatial mis-mapping from apical breathing, therefore, inferences are less reliable. Future work should assess the effect of different pre-processing pipelines (e.g. DSI Studio, FSL TOPUP and eddy or DR BUDDI) and how different data combinations (full phase-opposed datasets versus reversed b0) affect the results.

Our DTI protocol is long (to optimise SNR for the purposes of defining the ideal tractography conditions) which may not be tolerable for patients. Future work from our group will explore the ideal sampling strategy for q-space, requisite number of signal averages to balance image quality against scan time, the role of multiband (simultaneous multislice imaging) and the utility of different pre-processing pipelines in an effort to reduce the scan time.

1.15.5 Conclusions

This study shows that the FA threshold has import implications in the genesis of tractograms. As hypothesised, the FA threshold required to consistently generate valid streamlines (~0.06) was lower than that which is conventionally used in the brain (~0.1). Also, the area with the lowest anisotropy appears to reside in the region between the spinal cord and extraforaminal roots which may be due to crossing fibres or partial volume effects given that the rootlets are bathed in CSF which is addressed in the final chapter.

Chapter 16.   The Effect of Different Pre-processing Pipelines on Diffusion Tensor Imaging of the Brachial Plexus

1.16.1 Introduction

The most common method of acquiring dMRI data in the clinical setting is by spin-echo with echo-planar imaging readout. Whilst this enables rapid imaging with excellent signal-to-noise (SNR), it is susceptible to field inhomogeneities, eddy currents, and artefacts due to subject motion and physiological noise. To combat these limitations, pre-processing of dMRI data is generally recommended.

Pre-processing of dMRI data is a multi-step process concerned with correcting geometric and signal distortions. The aim of pre-processing is to minimise false negatives without increasing false positives in the post-processing (analysis) phase. There are several possible actions/corrections that can be attempted within the pre-processing phase and each correction can be in several different ways (Figure 47).

Although it is widely accepted that pre-processing should be performed because it improves the accuracy of dMRI metrics and tractography[83], there are currently no accepted standards. Consequently, practices and pipelines vary substantially which generate important differences in tractograms[114] and negatively impact the reproducibility of studies[286,287].

The majority of researchers and clinicians agree that correcting for eddy-current and susceptibility related artefacts are of paramount importance. Most of the available tools which perform this function synchronously correct other artefacts. The ways to achieve such corrections fall into 3 broad categories: a) registration-based methods which simply register the dMRI data to structural (non-distorted) images, b) fieldmap-based methods which seek to estimate B_0 inhomogeneity to correct the dMRI data, and c) phase encoding based methods which involve capturing additional data with the phase encoding direction reversed. Numerous studies have shown that phase encoding methods outperform other methods[288,289], at the cost of longer scan time. The best corrections are provided

when full dMRI datasets are acquired in opposing phase-encoding directions (that is, b0s and all gradient directions)[290] although similar results can be achieved with reversed b0s-only. If no phase-reversed data (DWIs or b0s) were acquired then in the brain, deep-learning synthesised reversed b0s are valuable alternatives[291].

There are several software packages which provide phase-encoding based tools for correcting dMRI data, including animaDistortionCorrection[292], animaBMDistortionCorrection[293], DR-BUDDI[90,294], DSI Studio[295], EPIC[296], HySCO[297] and FMRIB FSL's TOPUP[88] and eddy[89]. The two most popular software packages for post-processing (e.g., tractography, Figure 66) also have tools embedded for pre-processing. MRtrix is the most popular post-processing tool globally, and it implements FSL's TOPUP[88] and eddy[89] for pre-processing via *dwipreproc*. DSI Studio is the 2nd most popular tool worldwide, deploying its own pre-processing steps which aim to correct susceptibility, motion and eddy current artefacts.
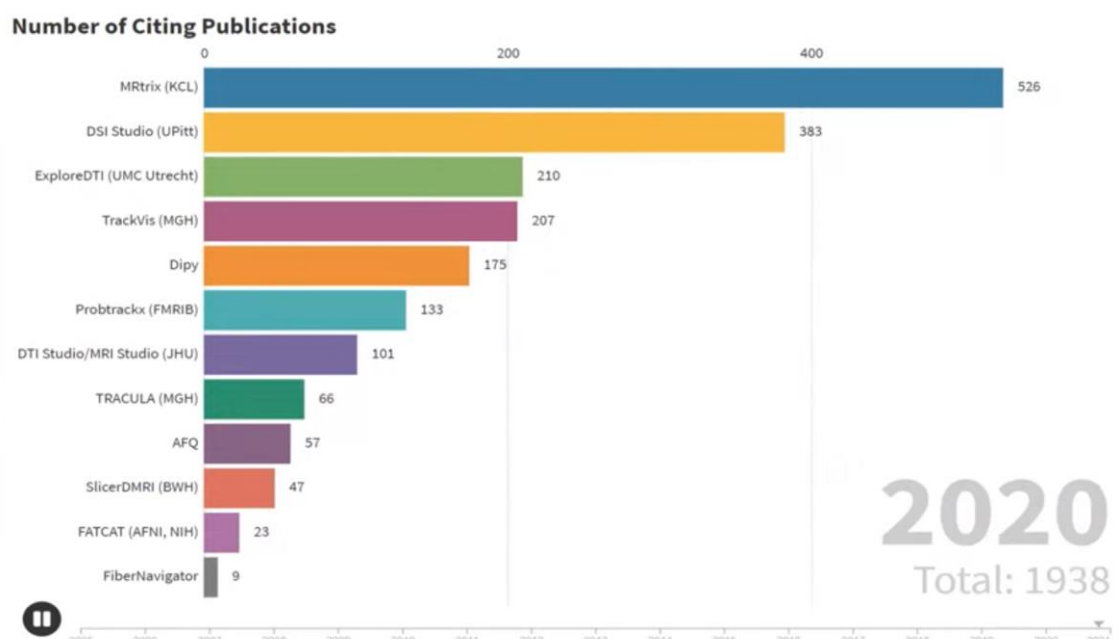
Figure 120. Bar chart showing the most popular software packages (by citation counts) for tractography until the end of 2020. Available at https://youtu.be/3PcUSHmgoYo

In this study, we compare the effect of pre-processing using the two most common packages worldwide, FSL's TOPUP[88] and eddy[89] (which is implemented in MRtrix) against DSI Studio[295], to investigate how these change DTI metrics and tractograms.

1.16.1.1 Objectives

The objectives were as follows:

1. Compare the root-level diffusion metrics between packages
2. Compare streamline diffusion metrics between packages
3. Compare the similarity of streamline bundles

1.16.2 Methods

The institutional approvals, recruitment strategy, consent procedures, characteristics of the participants, and image acquisition steps have already been described in sections 1.14.2 and 1.15.3.

1.16.2.1 Pre-processing

DICOMs were converted to nifti format using dcm2niix[298]. Each 4D volume files was then denoised using the MRtrix3 implementation of MP-PCA[85]. The datasets (with the bval and bvec files) were then passed to the respective software packages for concatenation and correction. In DSI Studio[295] (using the November 16th 2021 release), the "Correct AP-A scans" option was used, followed by motion correction and exported as in nifti format. In FSL v6.0, TOPUP[88] was run with the default settings. A mask was generated from the corrected b0 using bet. These files were then passed to eddy[89] (eddy_cuda) with the following options (https://fsl.fmrib.ox.ac.uk/fsl/fslwiki/eddy/UsersGuide) and configurations. The eddy current-induced fields were modelled using a quadratic function (--flm=quadratic) which specifies that the eddy current-induced fields can be modelled as a combination of the linear and quadratic gradients (x, y, z, x^2, y^2, z^2, xy, xz and yz), which is more complex than the linear default. The method used to concatenate data with opposing phase was by least-squares resampling (--resamp=lsr) which is the default. We enabled the "fill emply planes" option (--fep) such that eddy would duplicate the previous plane if the plane was perpendicular to the frequency-encode direction and by interpolation between the previous and

the 'wrap-around plane' if the plane was perpendicular to the phase encoding direction. We elected to replace outlier slices (with signal intensities at least 4 standard deviations from the expected) with predictions made by the Gaussian Processes using the --repol option, which is not enabled by default. We performed slice-to-volume motion correction using the –mporder options, specifying 15 degress of freedom per the developers recommendations. We also enabled the option --estimate_move_by_susceptibility whereby susceptibility-induced field change due to subject motion is estimated and corrected using a first order Taylor expansion of the static field, with respect to pitch and roll.
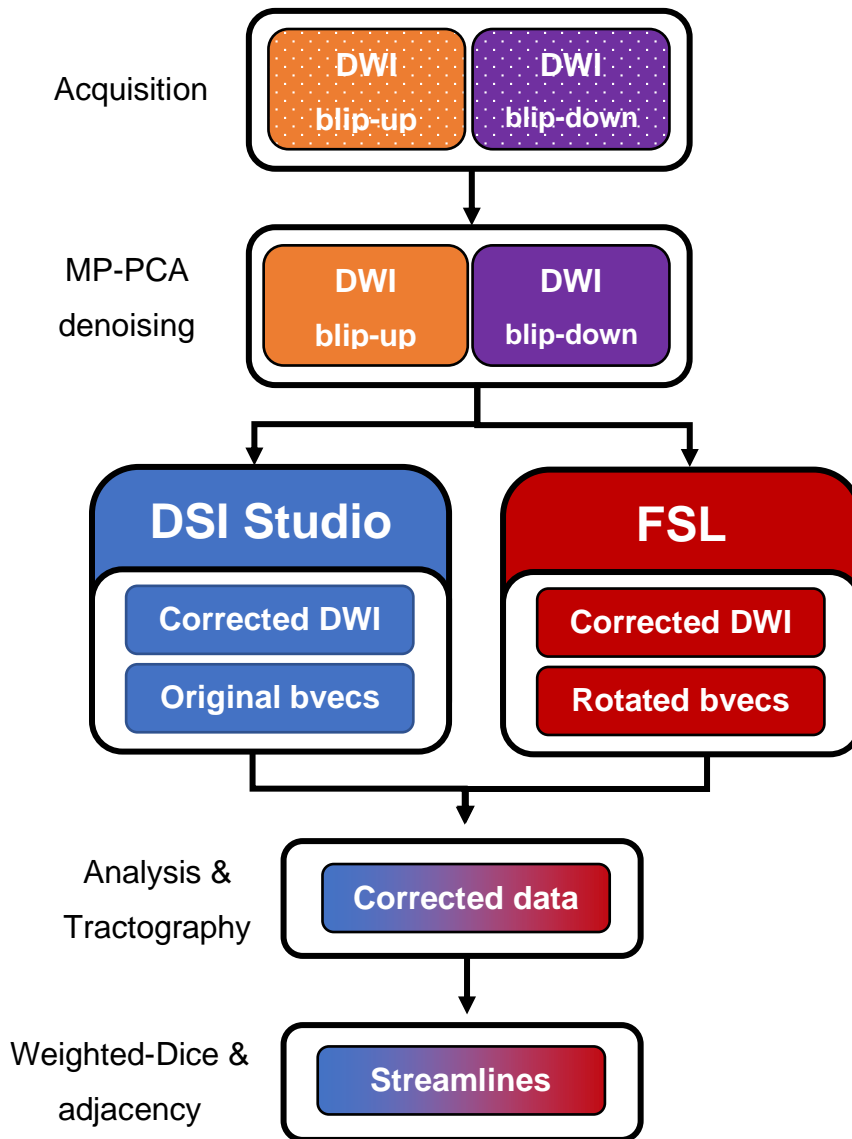
Figure 121. The steps used to pre-process the data and compare the outputs from using the two most popular software packages worldwide. Note that FSL's eddy generates a corrected bvecs file (using the same rigid body transformation used for DWIs to b0s) whilst DSI Studio does not perform this function.

1.16.2.2   Post-processing

Data were reconstructed using a least-squares tensor model in DSI Studio. Regions of interest (ROIs, functioning as waypoints) were placed over the spinal nerve roots, approximately 3cm from the cephalad longitudinal axis of the spinal cord[238] and measuring 2x2x2 voxels (5mm^3) because the spinal nerve roots have a mean cross-sectional area 9mm^2 (minimum 5.6mm^2)[276]. DTI metrics were extracted from these ROIs. ImageJ was used to compute the signal to noise ratio

(SNR, defined as mean signal in the voxels covering the nerves divided by the standard deviation of the noise)[299] in the b0 images, at every root, using the same ROIs. The noise was calculated from a ROI covering a large area (with non-zero voxels) outside the body.

1.16.2.3 Tractography

We used DSI Studio for tractography given its superior performance in generating valid streamlines[273]. A deterministic (Runge-Kutta 4th order) tracking algorithm[274] was used. Random subvoxel seeding was used, throughout the diffusion space. The anisotropy threshold and step size were randomised. To minimise false tracts, the step angle was set to 45° for C5-7, 60° for C8 and 70° for T1[275]. Streamlines shorter than 5cm were discarded. Seeding continued until 1000 streamlines were reached, per root or terminated manually if 10 million seeds has been reached. Streamlines were smoothed by averaging the propagation direction with 99% of the previous direction. To explore if and how topology informed pruning[244] changed the diffusion parameters of streamlines and their overall shape (Figure 122)[300], streamlines were also maximally pruned.
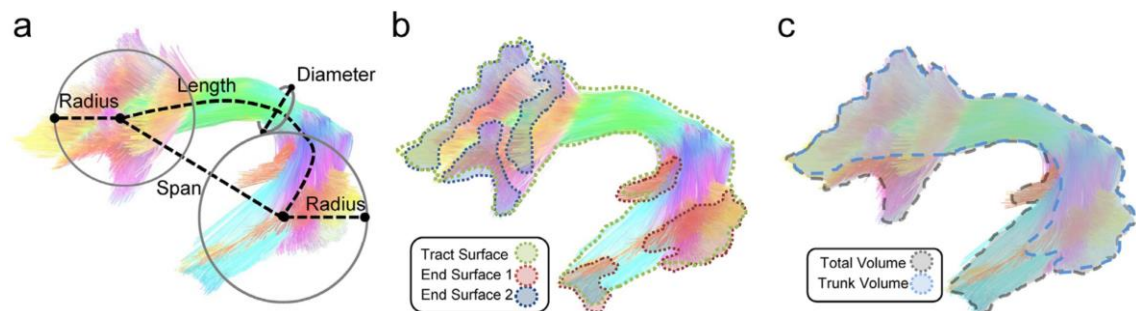
Figure 122. Streamline bundle shape metrics. Reproduced from Yeh et al (2020)[300].

1.16.2.4 Comparing streamlines

To calculate the morphological similarity of streamlines from data corrected within DSI Studio vs FSL, we used the Sherbrooke Connectivity Imaging Lab (SCIL) toolbox[301]. Sörenson-Dice coefficients were calculated per streamline bundle (where each spinal root was a single bundle of streamlines. This means that for each participant, 20 .trk files were generated – 10 from DSI Studio and 10 from FSL, given that there are 5 pairs of spinal roots. The .trk files (e.g., C5 from DSI

Studio vs FSL) were converted into binary masks and a Dice coefficient calculated. A Dice value of 0 means no overlapping voxels containing streamlines, whilst a value of 1 means perfect overlap of streamlines. However, without further adjustment, small and spurious streamlines would have a large impact on the Dice and so we also weighted the Dice by streamline density[302,303]. To complement these measures, we calculated bundle adjacency to measure the spatial agreement (in mm) of streamlines from each root, between software packages. A bundle adjacency of 0 mm is desirable because it means that streamlines generated from DSI Studio and FSL were spatially identical. Conversely, a bundle adjacency of 10 mm for the C6 root for example would mean that the streamlines in DSI Studio and FSL were in different positions, spaced apart by a mean of 10 mm. Together, the weighted-Dice and bundle adjacency can be used to understand the similarity of streamlines between datasets from different pipelines. The ideal situation is that the Dice and weighted-Dice are high, and the bundle adjacency is low (close to 0 mm).

1.16.2.5   Statistical analysis

Data were analysed using Stata v16/MP (StataCop LLC, Texas). Scaled variables approximating the normal distribution are represented by the mean (and standard deviation, SD), otherwise the geometric mean (denoted by an *) and its 95% confidence interval (CI) are used. The relationship between continuous variables which approximated the normal distribution (e.g., FA, MD, etc) and the pre-processing pipelines used were explored using multilevel multivariable linear regression. The fixed effects were the software used (DSI Studio or FSL) and the cervical root levels (5 categories) and selected based on the use of directed acyclic graphs. Restricted maximum likelihood was used to estimate the cluster-level (volunteer) variance. The variance and covariance parameters were unstructured and so, distinctly estimated. Agreement between the FSL and DSI Studio parameters are summarised in a Bland Altman plot. To explore the effect of pruning, sensitivity modelling was performed with the addition of pruning as a binary fixed effect. To display the FA and diffusivity values together on a single graph, the parameters were z-transformed. The relationship between skewed continuous variables (e.g., SNR, streamline bundle volume in mm^3, etc) and the pre-processing pipeline used was modelled using non-parametric (Epanechnikov

kernel) regression, with standard errors estimated using resampling with replacement with 1000 repetitions.

1.16.3 Results

Overall, datasets had sufficient SNR but data pre-processed with FSL had higher SNR (median increase 42 [IQR 24, 59]) at all levels (Table 18). As expected, SNR reduced in the caudal direction, as the distance between anatomy and coil-elements increased.

Root	Mean* SNR (95% CI)		Mean difference (95% CI)
	FSL	DSI Studio	
C5	182 (152, 215)	62 (52, 75)	136 (113, 158)
C6	155 (123, 195)	66 (53, 83)	137 (116, 162)
C7	91 (74, 112)	61 (50, 75)	92 (79, 106)
C8	72 (58, 89)	48 (37, 63)	75 (64, 87)
T1	38 (30, 48)	30 (22, 41)	46 (39, 54)

Table 18. SNR measurements at each spinal root level

1.16.3.1   ROI-based metrics

Overall, pre-processing with DSI Studio yielded estimates of FA which were 2% higher (mean difference 0.019 [95% CI 0.011, 0.028]) than the FSL datasets (Table 19).

After adjustment for the spinal root level, SNR did not explain the discrepancy in FA between DSI Studio and FSL pre-processed datasets (adjusted ß for SNR 4.5 x10^{-4} [95% CI -4.5 x10^{-4}, 2.5 x10^{-4}]).

Root	Metrics*	FSL	DSI Studio	Adjusted mean difference (95% CI)
C5	FA	0.23 (0.05)	0.23 (0.04)	-0.004 (-0.018, 0.011)
	MD x10⁻³ mm²/s	1.43 (0.16)	1.51 (0.19)	-0.087 (-0.141, -0.034)
	RD x10⁻³ mm²/s	1.25 (0.15)	1.32 (0.16)	-0.071 (-0.124, -0.020)
	AD x10⁻³ mm²/s	1.77 (0.19)	1.88 (0.26)	-0.118 (-0.180, -0.056)
C6	FA	0.24 (0.03)	0.26 (0.03)	-0.024 (-0.036, -0.013)
	MD x10⁻³ mm²/s	1.54 (0.11)	1.59 (0.21)	-0.047 (-0.095, 0.001)
	RD x10⁻³ mm²/s	1.34 (0.10)	1.36 (0.18)	-0.023 (-0.065, 0.020)
	AD x10⁻³ mm²/s	1.94 (0.15)	2.04 (0.27)	-0.095 (-0.159, -0.031)
C7	FA	0.25 (0.03)	0.27 (0.04)	-0.024 (-0.036, -0.011)
	MD x10⁻³ mm²/s	1.60 (0.13)	1.70 (0.19)	-0.100 (-0.151, -0.048)
	RD x10⁻³ mm²/s	1.39 (0.12)	1.45 (0.17)	-0.065 (-0.111, -0.019)
	AD x10⁻³ mm²/s	2.03 (0.15)	2.20 (0.24)	-0.168 (-0.234, -0.101)
C8	FA	0.24 (0.05)	0.27 (0.03)	-0.040 (-0.058, -0.022)
	MD x10⁻³ mm²/s	1.54 (0.11)	1.59 (0.21)	-0.099 (-0.158, -0.038)
	RD x10⁻³ mm²/s	1.34 (0.10)	1.36 (0.18)	-0.051 (-0.108, 0.006)
	AD x10⁻³ mm²/s	1.94 (0.15)	2.04 (0.27)	-0.192 (-0.270, -0.115)
T1	FA	0.21 (0.06)	0.22 (0.07)	-0.010 (-0.037, 0.016)
	MD x10⁻³ mm²/s	1.66 (0.29)	1.65 (0.29)	-0.024 (-0.116, 0.069)
	RD x10⁻³ mm²/s	1.48 (0.24)	1.46 (0.26)	-0.010 (-0.090, 0.069)
	AD x10⁻³ mm²/s	2.02 (0.40)	2.04 (0.39)	-0.051 (-0.019, 0.083)

*Table 19. The *mean (SD) DTI metrics from ROIs placed over the spinal nerve roots.*

After adjustment, datasets pre-processed with DSI Studio had higher estimates of diffusivity (Figure 123); mean diffusivity was 0.07% greater (0.067 x10⁻³ [95%

CI 0.029, 0.105]), RD was 0.04% greater (0.042 [95% CI 0.008, 0.075]) and AD was 0.12% greater (0.118 [95% CI 0.067, 0.169]) than datasets pre-processed using FSL.
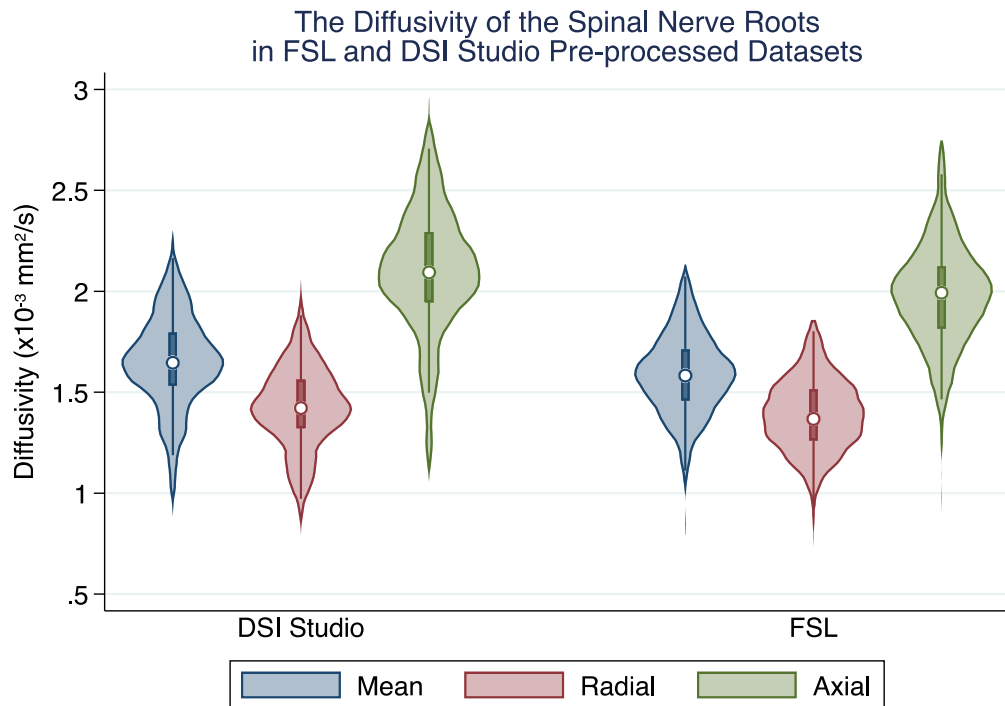
Figure 123. A violin plot showing the that estimates of the mean, axial and radial diffusivities within the spinal roots

1.16.3.2   Topology Informed Pruning of streamlines

On average, maximal pruning removed 46 (5%) streamlines per root, which had the effect of making bundles smaller in diameter and volume, without biasing their overall length and shape (Table 20).

Streamline Metrics	No Pruning	Maximal Pruning	Adjusted mean difference (95% CI)
Mean number of streamlines (SD)	986 (110)	941 (68)	46 (29, 63)
Mean volume in mm^3 (SD)	4273 (2191)	3356 (1309)	908 (607, 1209)
Mean length in mm (SD)	75 (14)	75 (14)	0.3 (-2.2, 2.8)
Mean diameter in mm (SD)	8.27 (1.85)	7.42 (1.31)	0.83 (0.56, 1.11)
Mean curl (SD)	3.02 (0.65)	2.97 (0.55)	0.04 (-0.03, 0.12)
Mean FA (SD)	0.24 (0.05)	0.24 (0.05)	0.002 (-0.006, 0.01)
Mean MD x10^{-3} mm^2/s (SD)	1.61 (0.23)	1.62 (0.23)	0.013 (-0.02, 0.05)
Mean RD x10^{-3} mm^2/s (SD)	1.40 (0.20)	1.41 (0.20)	0.01 (-0.02, 0.04)
Mean AD x10^{-3} mm^2/s (SD)	2.03 (0.31)	2.05 (0.30)	0.02 (-0.02, 0.06)

Table 20. The effect of topology informed pruning on streamline metrics

Consequently, pruning had no effect on diffusion metrics of streamline bundles (Figure 124) and 93% of streamline bundles resembled spinal roots (in their size, shape and course) whether topology informed pruning was applied or not.

Maximal Versus No Topology Informed Pruning of Streamlines
in Datasets Pre-Processed using FSL and DSI Studio

*Figure 124. A violin plot showing that maximal pruning did not
cause any meaningful changes in the estimates of the mean FA,
MD, AD or RD of streamlines.*

Similarly, multivariable modelling showed that maximal pruning made no difference to the weighted-Dice (adjusted ß 0.01 [95% CI 0, 0.02], p=0.126) or the bundle adjacency (adjusted ß 0.12mm [95% CI -0.08, 0.40], p=0.177) of tractograms derived from FSL vs DSI Studio pre-processing (Figure 125).

Figure 125. A violin plot showing the normalised (by variance)
bundle adjacency and weighted-Dice of streamlines for datasets
which were maximally pruned compared to those not pruned.

Given that topology informed pruning did not meaningfully bias the shape, length
or diffusion metrics of bundles, we use the pruned bundles hereafter for the
comparisons of FSL and DSI Studio, to mitigate any potential biases arising from
small or spurious streamlines which we may be underpowered to detect.

1.16.3.3   Streamline statistics and similarity

The choice of software used to pre-process data did not affect the number of
streamlines, their diameter, curl or irregularity (Table 21). However, streamlines
propagated in the FSL datasets were shorter (by 11 mm), had a smaller span
(3.9mm) and lesser volume (by 189mm^3). The differences in length, span and
volume meant that diffusion parameter estimates from the different pipelines had
poor agreement (Figure 126 and Figure 127) and there was small but clinically
important variability in FA (2%), MD (7%), RD (4%) and AD (1%) (Table 21).

Streamline Bundle Metrics	FSL	DSI Studio	Adjusted mean difference (95% CI)
Mean* number of streamlines (95% CI)	933 (880, 979)	958 (941, 976)	0.06 (-0.40, 0.55)
Mean* volume in mm^3 (95% CI)	3061 (2855, 3282)	3838 (3627, 4060)	189 (264, 90)
Mean* length in mm (95% CI)	69 (67, 70)	80 (78, 82)	11 (9, 13)
Mean diameter in mm (SD)	3443 (1811)	4172 (1844)	0.24 (-0.05, 0.53)
Mean span in mm (SD)	24 (5.4)	28 (5.8)	3.9 (2.88, 4.80)
Mean* surface irregularity (95% CI)	4.89 (4.72, 5.06)	4.80 (4.62, 4.98)	0.002 (-0.003, 0.007)
Mean curl (SD)	2.95 (2.88, 3.03)	2.95 (2.89, 3.01)	0.001 (-0.001, 0.003)
Mean FA (SD)	0.23 (0.12, 0.33)	0.25 (0.13, 0.41)	0.02 (0.01, 0.03)
Mean MD x10^{-3} mm^2/s (SD)	0.58 (0.85, 2.07)	1.64 (0.94, 2.24)	0.07 (0.04, 0.10)
Mean RD x10^{-3} mm^2/s (SD)	1.39 (0.79, 1.80)	1.43 (0.75, 2.01)	0.04 (0.01, 0.07)
Mean AD x10^{-3} mm^2/s (SD)	1.98 (0.97, 2.67)	2.09 (1.14, 2.88)	0.12 (0.08, 0.17)

Table 21. Streamline diffusion and shape metrics from datasets pre-processed with FSL versus DSI Studio.
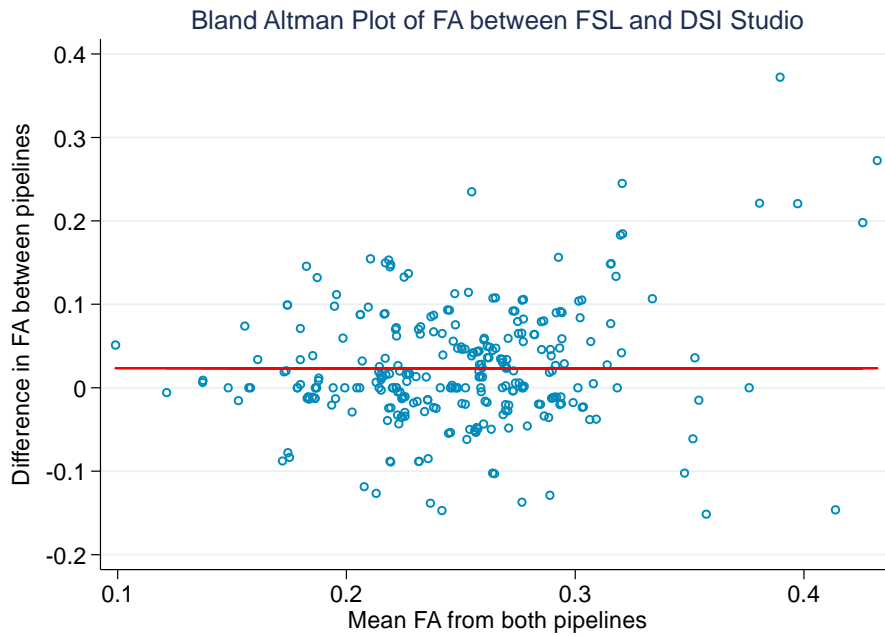
Figure 126. A Bland Altman plot showing the agreement of FA between FSL and DSI Studio pre-processed datasets
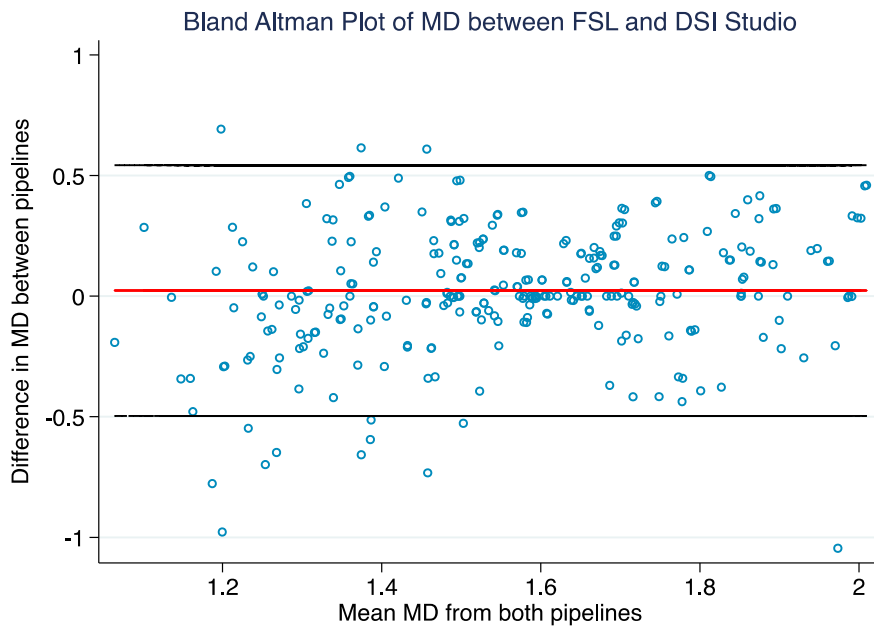
Figure 127. A Bland Altman plot showing the agreement of MD between FSL and DSI Studio pre-processed datasets

Despite maximal pruning, the similarity of streamlines between FSL and DSI Studio was generally modest (median Dice 0.37 [IQR 0.25, 0.43]). Whilst

weighting by streamline density increased the Dice coefficient, the similarity was still modest (median weighted-Dice 0.50 [IQR 0.35, 0.63], Figure 128).
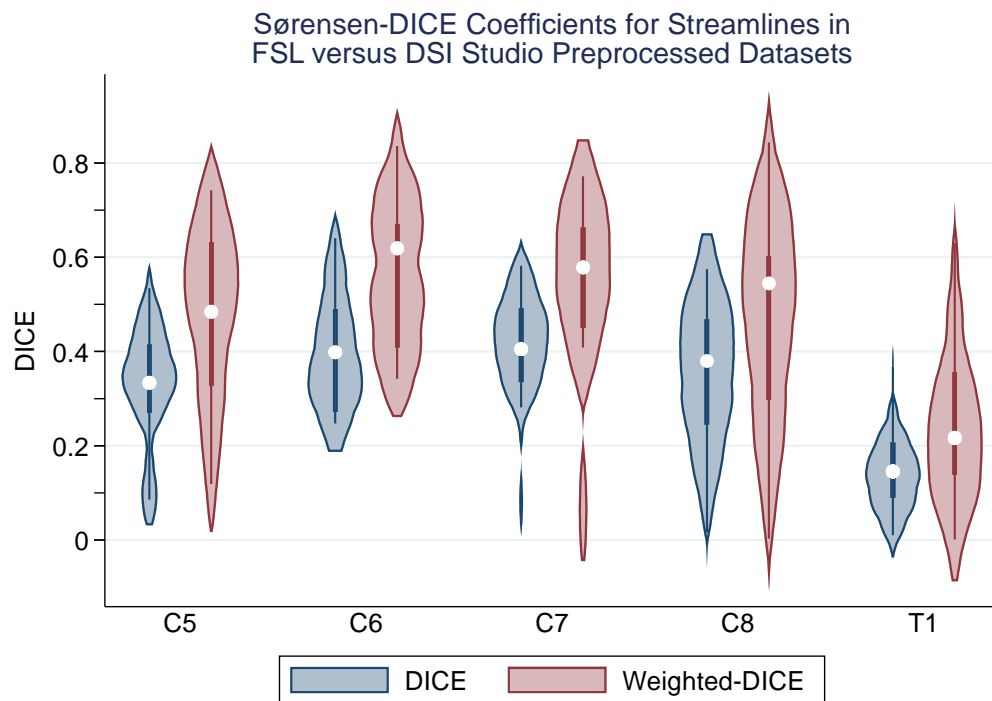
Figure 128. A violin plot showing the Dice and weighted-Dice of each spinal nerve root

Streamlines from datasets pre-processed using FSL versus DSI Studio were a mean 5.56 mm (SD 1.70) displaced and the discrepancy increased in the caudal direction, with the T1 root being the most different (Figure 129).
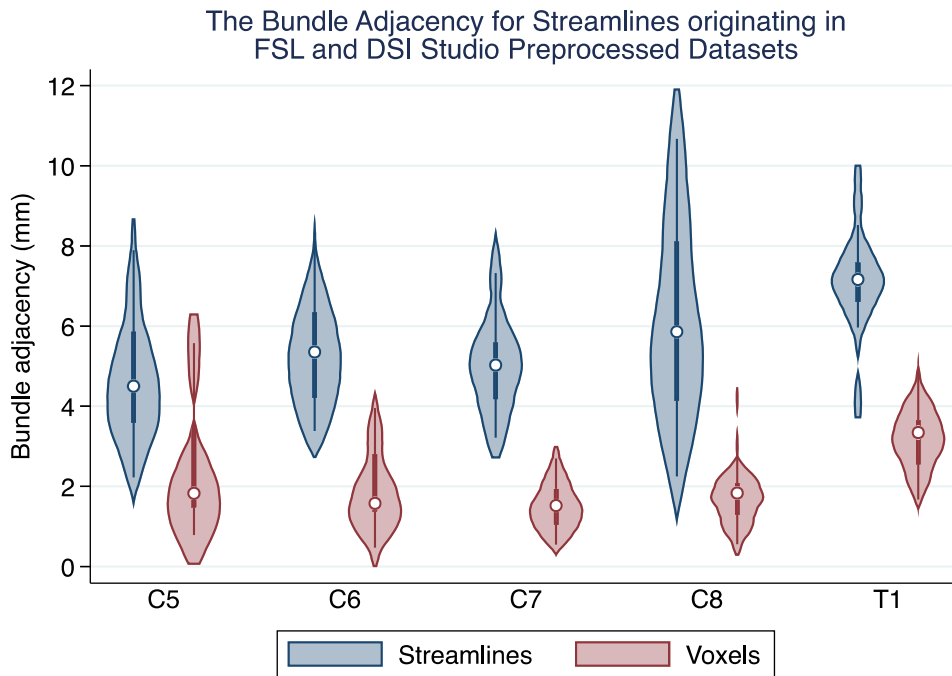
Figure 129. A violin plot showing the bundle adjacency (in mm) of streamlines and voxels occupied by streamlines

1.16.4 Discussion

This work shows that the choice of pre-processing pipeline affects the results of diffusion tensor imaging of the healthy adult brachial plexus. We show that when FSL was used for pre-processing, estimates of the anisotropy and diffusivity, both at the voxel-level and within streamlines, were a mean 2% and 7% lower (but up to 10% and 17%), respectively. This translated into differences in tractograms whereby streamlines differed in their spatial location by at least 2 voxels on average (5.56 mm, Figure 130). Moreover, streamlines from FSL-corrected datasets were shorter, and bundles had a smaller span and volume. The ideal pre-processing pipeline remains a matter of debate and until consensus is reached, users should be aware of the potential for pre-processing bias and interpret their findings accordingly.
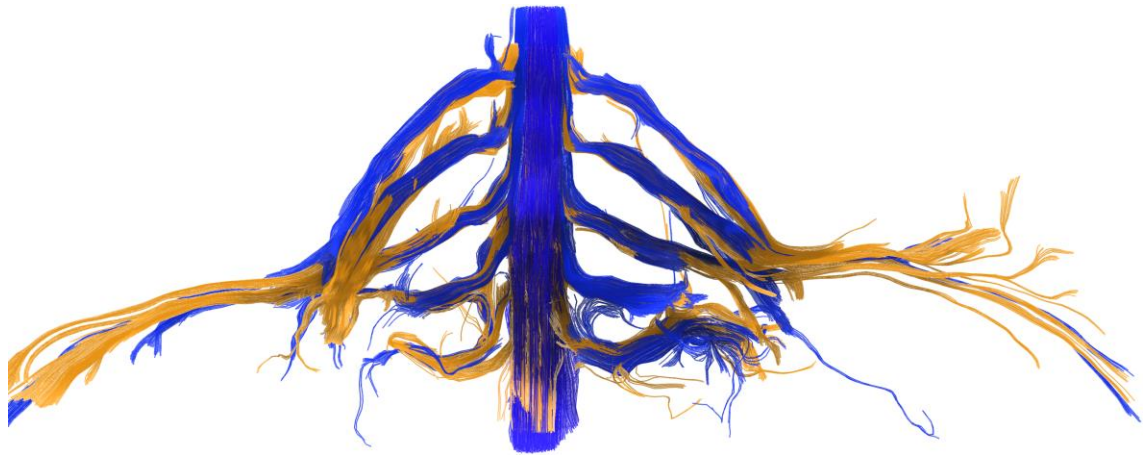
Figure 130. Tractograms overlaid derived from pre-processing with DSI Studio (blue) versus FSL (yellow). The loss of cranial slices (due to the motion correction module within FSL) and therefore, the absence of streamlines within the proximal spinal cord is conspicuous.

The issue of pre-processing variability is topical and important. In 2021, the ISMRM Diffusion Study Group assembled a group of 232 international scientists and clinicians to address this problem. Participants were first surveyed regarding their practices and then invited to pre-process 13 multi-shell spin-echo epi dMRI datasets from the brain, from multiple different vendors 3T systems (GE SIGNA, Siemens Connectom and Philips Achieva) from multiple sites and sessions. The findings are not yet available but should provide important insight into the scale of the problem and the foundations for standardising the pre-processing steps and tractography methods[233] for dMRI within the brain. When this research is complete then a summary of global practice will be shared alongside performance metrics of different pipelines. Thereafter, a Delphi process will likely follow whereby clinicians and academics may vote upon (combinations of) methods in search of consensus over the 'ideal' pipeline for brain dMRI pre-processing. Whilst one pipeline and combination of functions within is likely to perform best statistically (or at least better than others, in terms of similarity to ground-truth datasets or otherwise) this may not be of paramount importance and may lead people to vote in favour of or against specific software. Other features such as the user experience, stability, developer support, etc must be considered too. For example, in relation to the comparison of FSL to DSI Studio

1) DSI Studio's graphical user interface may be perceived as more user-friendly to those without substantial experience of coding, considering that FSL is largely terminal based. Therefore, the graphical user interface of DSI Studio may be more appealing to clinical users without a background in coding.

2) The FSL suite of tools provides many other applications which are not offered by DSI Studio and integrations with other imaging modalities, such as MR spectroscopy and functional MRI.

3) Pre-processing a dataset with DSI Studio takes minutes and the software accepts many formats of files from different vendors, whereas FSL requires data to be converted to nifti first, then pre-processing may take hours-days depending on the user's hardware and how they have scripted the processes.

4) DSI Studio runs natively on all major operating systems (Windows, MacOS and Linux) from a single downloadable executable with point-and-click installation. In comparison, FSL requires a Python-based installation which may be an obstacle for some users. In Windows, FSL requires a virtual machine or Linux subsystem to run and in all operating systems, the GPU-accelerated features require additional libraries. This is impossible in recent versions of MacOS due to lack of NVIDIA support.

Our sensitivity analyses suggest that topology informed pruning[244] is not detrimental in the brachial plexus, given that it removed 5% of potentially-false streamlines which caused bundles to be smaller (in diameter and volume) without biasing the overall shape or diffusion properties. Conversely, we cannot rule out the possibility that this automatic pruning algorithm removed small but real connections (e.g., smaller terminal branches from the roots or trunks) which ultimately reduces the sensitivity of tractography. This means that the benefits of pruning may be at the expense of tracking small nerves. Until more sophisticated pruning algorithms are developed, we feel that this function in DSI Studio provides a useful way of removing potentially false streamlines without biasing the results.

1.16.5 Conclusions

The choice of software for pre-processing dMRI data biases estimates of the anisotropy and diffusivity in brachial plexus by up to 10% and 17%, respectively. This bias has important downstream effects on tractography. Until a consensus is reached on the ideal pre-processing pipeline, users should be aware of the potential for pre-processing bias and interpret their findings accordingly.

Chapter 17.   Multishell dMRI of the Roots of the Brachial Plexus

1.17.1 Introduction

Diffusion weighted MRI provides information about the microstructure of peripheral nerves which are sensitive to axon type, axon diameter, myelination, axon density and their organisation[61–63]. The diffusion tensor (diffusion tensor imaging, DTI) is the most common method of modelling the diffusion propagator. However, as discussed in section 0, there are limitations to the use of DTI in the brachial plexus.

Fascicular exchange is known to occur throughout the brachial plexus (page 55, Figure 15) and so it is plausible that there may be >1 fibre orientation within any given voxel covering the brachial plexus. This means that a single tensor (or at least the principal eigenvector $\varepsilon 1$ aka v1) may not adequately represent the true microscopic complexity. Whilst peripheral nerves might appear macroscopically straight, at the microscopic level axons are not perfectly straight (Figure 131) and again, the diffusion tensor may underestimate the true architecture. Finally, DTI may be adversely affected by the isotropic diffusion of cerebrospinal fluid (CSF) around the rootlets in the intrathecal space. At the voxel-level, these issues could manifest as oblate or spherical tensors (as shown Chapter 15, whereby the FA of streamlines exiting the spinal cord were considerably lower than elsewhere) and limit tractography.
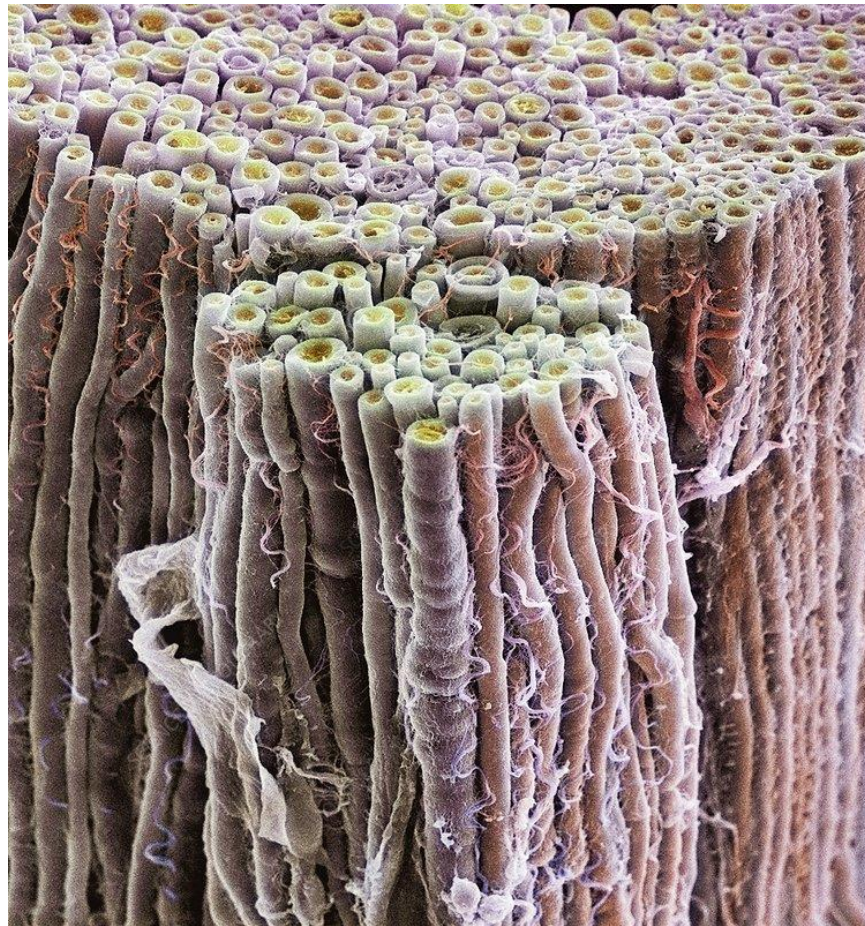
Figure 131. Electron micrograph of myelinated axons in the optic nerve. Reproduced from www.education.vetmed.vt.edu

There are several techniques which can model the diffusion propagator and crossing fibres (Chapter 8), and some of the tools commonly used today include multiple-tensors[101], Q-ball imaging[103], constrained spherical deconvolution[106], ball-and-sticks[107], NODDI[108] and GQI[109]. These methods are typically divided into 'model-free' (based on q-space[110] and estimate the dODF) and 'model-based' (using multi-compartment models to estimate the fODF).

We hypothesis that there are multiple fibre orientations within the brachial plexus, and these might be resolved by techniques 'beyond-DTI'.

1.17.1.1   Objectives

1. Develop a clinically oriented diffusion scheme for the brachial plexus which
   a. Captures multiple b-values whilst avoiding over sampling in the lower shells and under sampling in the higher shells.

b. Can be pre-processed by common open-source software

c. Is compatible with multiple methods of ODF modelling

2. Apply and compared the findings of model-free and model-based ODF estimation techniques in healthy volunteers to explore whether the brachial plexus has multiple fibre orientations

1.17.2 Methods

This single-centre study was designed and reported in accordance with the STARD guidance, considering the domains of the QUADAS-2 and PRISMA-DTA tools. Approval was gained from the National Research and Ethics Service of the United Kingdom (reference 16/YH/0162). Informed written consent was obtained.

1.17.2.1   Participants

We recruited 17 healthy adults (10 females and 7 males) of mean age 30 years (SD 10, range 19-56) by public advertisement. They had no history of injury or known pathology affecting the brachial plexus.

1.17.2.2   Acquisition

We elected to use a shell-based q-space sampling scheme with uniform coverage rather than a grid-sampling scheme for the following reasons. Although grid-sampling avoids under sampling at high b-values, oversampling and low b-values, enables more b-values to be acquired within the same timeframe and has uniformly distributed density in q-space, data acquired using grid-sampling have important limitations:

a) Distortions associated with ssEPI (Chapter 5) cannot be corrected with FSL's eddy[89] because there is insufficient redundancy for interpolation. Therefore, the only way to mitigate eddy current artefacts is with a bipolar pulse which is suboptimal[304], adversely affects SNR (due to TE prolongation) and may limit translation.

b) Several methods of modelling the ODF (such as spherical harmonics[104,105] and constrained variants[106], ball-and-sticks[107], etc) cannot be generated from dataset which used grid-sampling, which might limit the translational value of the sequence and findings of the work.

The chosen b-value(s) has an important impact on the resultant ODF and therefore, the ability to resolve multiple fibre orientations (Figure 132). Higher b-values (with sufficient sampling of q-space) provide greater angular resolution and therefore a better opportunity to detect multiple fibre orientations. However, the desire for higher b-values must be balanced against the need for adequate SNR within an acceptable scan time, and with distortions which are correctable. This is particularly challenging in the neck (compared to the head) given that the anatomy of interest is further from the (fewer) receiver coil elements, the neck is subject to additional flow/motion/susceptibility artefacts, and this culminates in less signal and more distortions. Also, simultaneous multislice acquisition is not optimised/available.
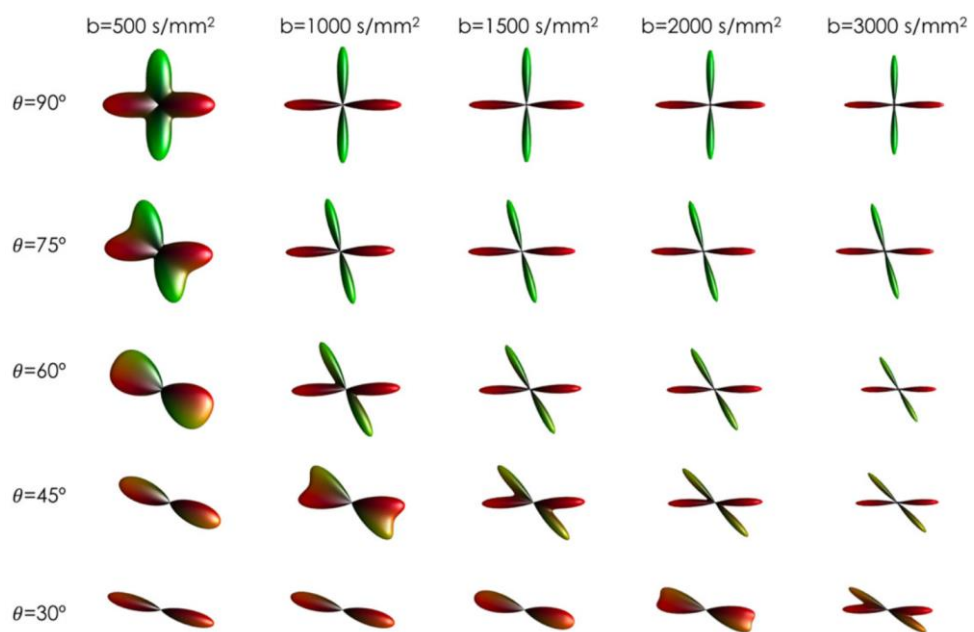
Figure 132. The relationship between b-value and fODF.
Reproduced from Dell'Acqua and Tournier (2019)[99].

After a period of testing different schemes, we observed that the following consistently generated adequate SNR within an acceptable scan time and with distortions that were readily correctable. Data were acquired at a field strength of 3T using a Siemens Magnetom Prisma (Siemens Healthcare Limited, Erlangen, Germany). A 64-channel head and neck coil, a 16-channel body coil and the posterior elements of the spine coils were used. Single-shot echo-planar imaging (ssEPI) was used. Using a Caruyer scheme[305], we acquired 142 unique directions

with uniform coverage over 3 shells: b700 24 directions, b1400 47 directions and b2100 71 directions. Eight interleaved b0s were acquired. The diffusion waveform was set to twice refocused spin echo (Siemen's "bipolar"). Other parameters included: TR 8000ms, TE 79ms, in-plane resolution 2.3mm^2, 50 gapless-slices of 2.3mm thickness, field-of-view 300×300mm, matrix size 130×130, GRAPPA factor 2, partial Fourier 6/8, TrueForm b1 shim, epi factor 130, echo spacing 0.72ms, receiver bandwidth 2564/px, 1st order motion correction and strong fat saturation. The imaging volume included the C2 to T2 vertebral bodies. The adjustment (shimming) volume was manually set as a cube within the neck and proximal to the apex of the lung. One signal was acquired in opposing (right-to-left and left-to-right) phase-encoding directions for a total of two signals. A matched T1-weighted volume was also acquired: TE 7.5ms and TR 639ms, 1.4mm slice thickness, 1.2mm^2 in-plane resolution, 121° flip angle, no acceleration or partial Fourier applied.

To explore whether greater sampling of q-space via more sensitising gradient directions (N_D) or higher b-values demonstrated more fibre orientations, we captured four additional scans in 4 subjects for sensitivity analyses. Two subjects were scanned using the same Caruyer scheme[305] but with 192 unique directions over 3 shells: b700 32 directions, b1400 64 directions and b2100 96 directions. The third subject was scanned using a b-max of 3000 s/mm^2 (b1000 24 directions, b2000 47 directions and b3000 71 directions) using Siemen's "monopolar" waveform and so a reduced TE of 72ms. The fourth subject was scanned using a b-max of 3000 s/mm^2 (b1000 24 directions, b2000 47 directions and b3000 71 directions) using twice refocused spin echo (Siemen's "bipolar") which warranted a longer TE of 85ms and TR of 8900ms.

1.17.2.3   Pre-processing

DICOMs were converted to nifti format using dcm2niix[298] and then denoised using the MRtrix3 implementation of MP-PCA[85]. Using the FMRIB FSL suite v6.0, TOPUP was run with the default settings and passed to eddy_cuda[89] with the following configurations: flm=quadratic, resamp=lsr, fep and repol enabled, mporder=15 and estimate_move_by_susceptibility enabled.

ImageJ was then used to compute the SNR (defined as mean signal divided by the standard deviation of the noise over an area of mean 21cm^2)[299] in the corrected b0s, at every root level, using the ROIs described below. The mean SNR was 98 (SD 46).

1.17.2.4   Reconstruction

In DSI Studio[295], restricted diffusion was quantified using restricted diffusion imaging[306] and reconstructed using GQI[109] with the default diffusion sampling length ratio of 1.25. In FSL, a ball and 3-stick model was fitted using the GPU accelerated version of bedpost (*bedpostx_gpu*)[107], excluding sticks with a volume fraction of <5%.

1.17.2.5   Waypoints for streamlines

Regions of interest (ROIs, functioning as waypoints) were placed over each spinal nerve roots, approximately 3cm from the cephalad longitudinal axis of the spinal cord[238] and measuring 2x2x2 voxels (5mm^3) because the spinal nerve roots have a mean cross-sectional area 9mm^2 (minimum 5.6mm^2)[276]. The same waypoints were used for all tractography methods (Figure 133). Diffusion metrics were extracted from these ROIs in each dataset.
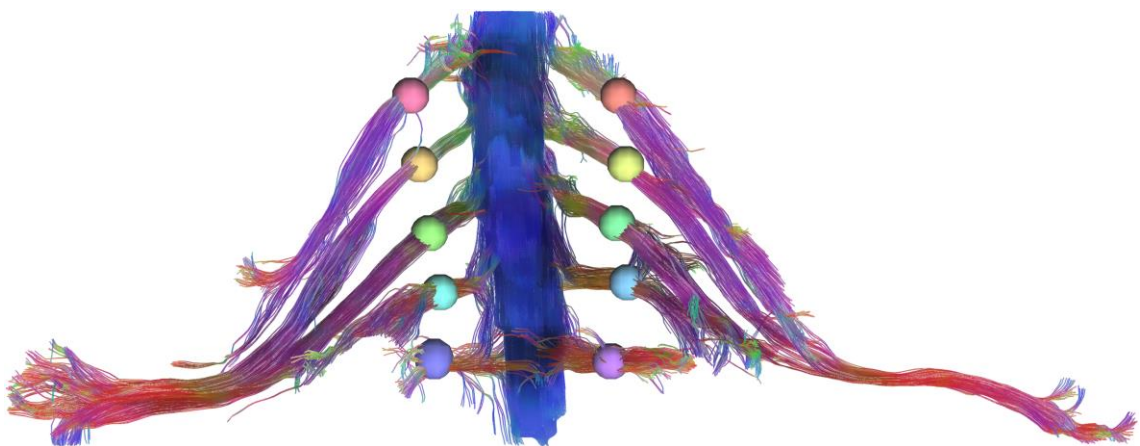
Figure 133. The size and position of waypoints used for tractography of each spinal nerve root, overlaid on an example of deterministic tractography from data reconstructed by GQI

1.17.2.6   Deterministic tractography

We used DSI Studio for tractography given its superior performance in generating valid streamlines[273]. A deterministic (Runge-Kutta 4th order) tracking algorithm[274] was used with trilinear interpolation. Randomised subvoxel seeding was used throughout the diffusion space. The anisotropy threshold (QA) was set to 0.01. The step size was 0.5mm. The step angle was 45° for C5-7, 60° for C8 and 70° for T1[275]. Tracking continued until 1million seeds were reached. Streamlines shorter than 10cm were discarded. Streamlines were smoothed by averaging the propagation direction with 99% of the previous direction. Maximal topology informed pruning[244] was applied.

1.17.2.7   Probabilistic tractography

In FSL the GPU-accelerated version of probtrackx (*probtrackx2_gpu*) was used. The default 1000 burn-in samples and 5000 estimates were generated, per root. The subsidiary fibre volume threshold was 0.1 (default) and loop check was enabled. The step length was matched to the deterministic methods (0.5mm). The default curvature threshold (0.2) was used, anisotropy constraint was turned off and modifier Euler streamlining was enabled. Streamlines shorter then 10cm were discarded.

1.17.2.8   Comparing deterministic streamlines and probabilistic pathways

As there is no common file format for each software, streamlines from GQI and paths from probtrackx were converted to binary masks for each of the 10 spinal roots and the Sörenson-Dice similarity co-efficient was calculated. A Dice value of 0 means no overlapping voxels containing streamlines, whilst a value of 1 means perfect overlap of streamlines. As probtrackx path files contain numerous regions within, representing the distribution of possible connections, these were merged to facilitate comparison with GQI streamlines (Figure 134).
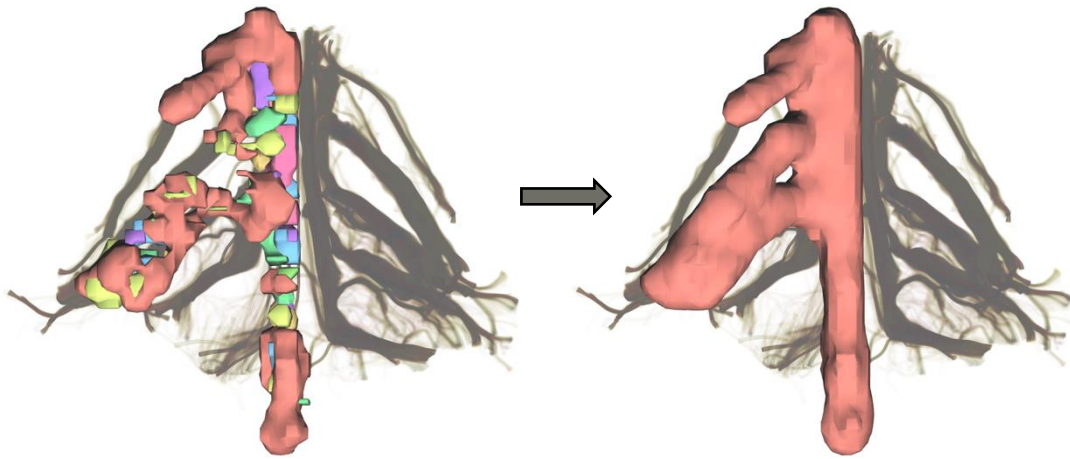
Figure 134. Conversion of probtrackx probability paths for the right

7th cervical root into a binary mask

1.17.2.9   Estimating the volume of the brachial plexus with multiple fibre orientations

To calculate the percentage of the spinal cord and brachial plexus containing crossing fibres (multiple orientations), the outputs of bedpostx (dyads1, dyads2 and dyads3) were converted to binary masks. To restrict the analysis to voxels representing the spinal cord and brachial plexus only, the probtrackx outputs were merged into a single mask and used to truncate the dyads masks by intersection.

1.17.2.10   Statistical analysis

Data were analysed using Stata v16/MP (StataCop LLC, Texas). Scaled variables approximating the normal distribution are represented by the mean (and standard deviation, SD), otherwise the geometric mean (denoted by an *) and its 95% confidence interval (CI) are used. The relationship between the Dice coefficient (as the independent variable), the b-value and number of diffusion sensing gradient directions (N_D) (as continuous covariables) was explored using mixed-effects linear regression. Restricted maximum likelihood was used to estimate the cluster-level (volunteer) variance. The variance and covariance parameters were unstructured and so, distinctly estimated. To test whether the lower SNR in the b3000 experiments confounded the estimates of the multiple fibre orientations, the SNR was added to the mixed model as a interaction term with b-value (given that to two are co-linear and SNR) for a sensitivity analysis.

1.17.3 <u>Results</u>

In this chapter, data from 6 adults (4 females and 2 males of mean age 29 years [SD 6, range 19-36]) are presented. This includes two datasets from each experimental setting:

- Two adults scanned at b-max 2100 mm^2/s with N_D 150

- Two adults scanned at b-max 2100 mm^2/s with N_D 192

- Two adults scanned at b-max 3000 mm^2/s) with N_D 150

1.17.3.1 <u>Fibre populations within the spinal cord and brachial plexus</u>

Overall, 2 fibre orientation were detected in 37% (range 27-44%) of voxels representing the brachial plexus. Moreover, 29% (range 18-25%) of voxels contained >2 fibre orientations. The volume of the brachial plexus with multiple fibre orientations did not increase when the b-max was increased from 2100 to 3000 s/mm^2 (Figure 135) or with greater sample of q-space (N_D increased from 150 to 192, Figure 136).
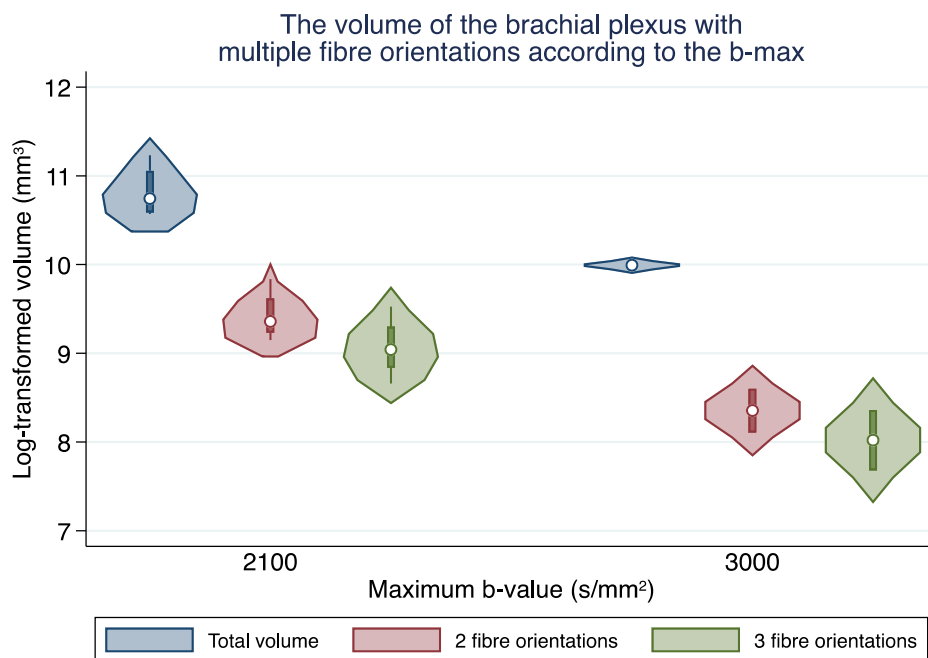
Figure 135. A violin plot showing that an increased b-max (2100 to 3000 s/mm^2) was not associated with higher estimates of multiple fibre orientations
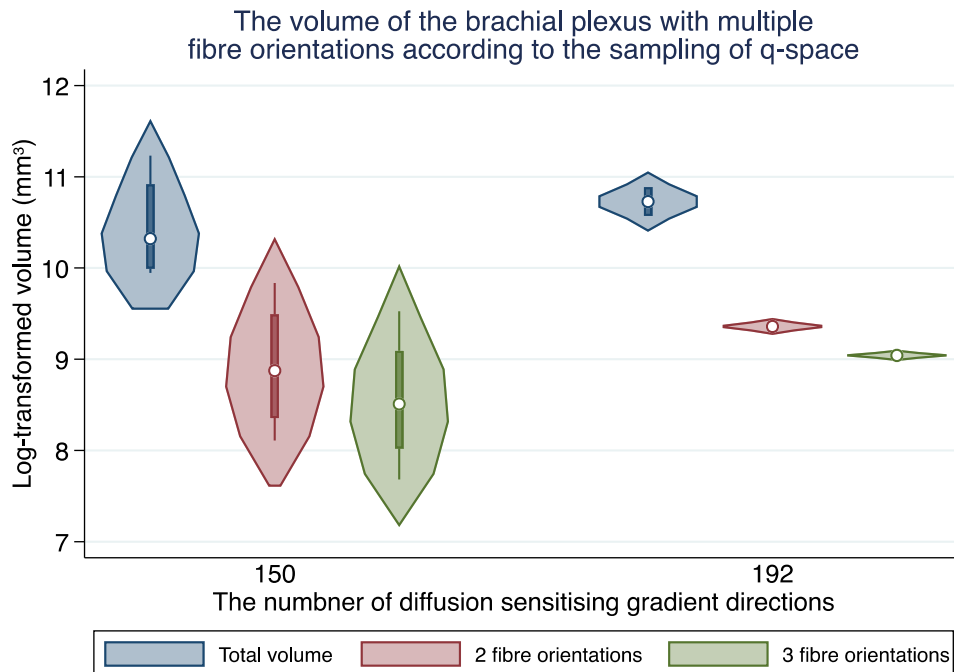
Figure 136. A violin plot showing that increased sampling of q-space (N_D 150 versus 192) was not associated with higher estimates of multiple fibre orientations

1.17.3.2 Intrathecal and intraformational regions

In all experimental settings (b-max 2100 mm^2/s with N_D 150, b-max 3000 mm^2/s with N_D 150, and b-max 2100 mm^2/s with N_D 192) multiple fibre orientations were consistently demonstrated by both GQI and bedpostx (Figure 138). These were typically seen within the intrathecal and intraforaminal regions where the numerous dorsal and ventral rootlets emerge from the spinal cord, cross the thecal space and merge to form the spinal nerve root (Figure 137), as demonstrated in the anatomical dissections presented in Chapter 13.
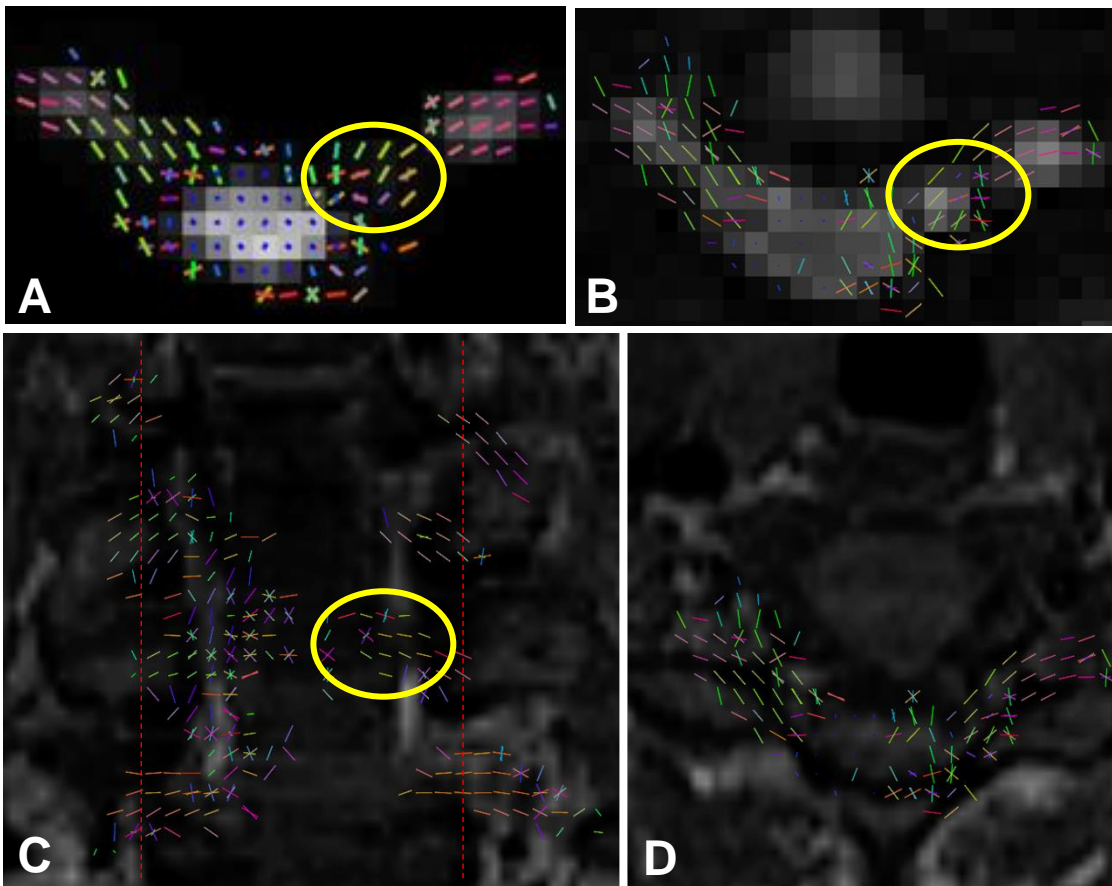
Figure 137. Axial sections through the spinal cord and bilateral C7 roots reconstructed with GQI (A). Panels B, C and D are data reconstructed using bedpost overlaid on the DWI (B) and T1-weighted image in coronal (C) and axial (D) planes. Both GQI and bedpostx detected multiple fibre orientations within the intrathecal and intraforaminal portions of the C7 roots (yellow circles). The red lines denote the lateral coronal limits of the vertebrae.
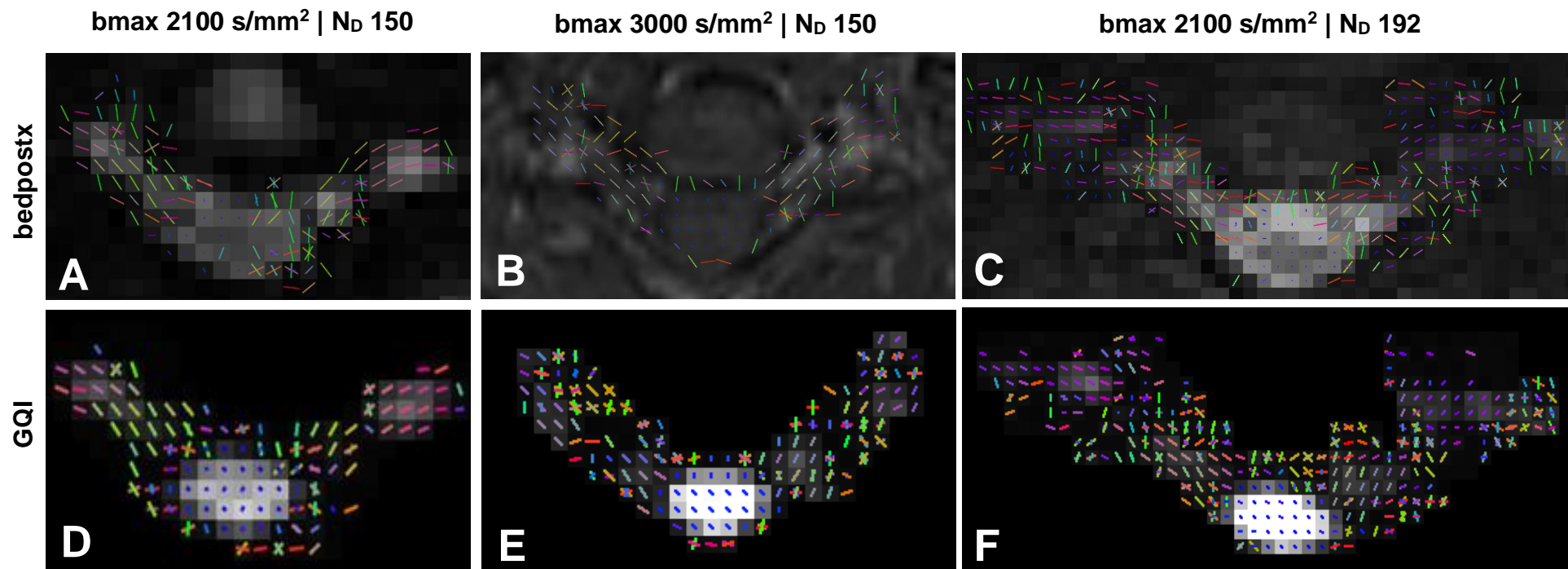
Figure 138. The 7th cervical root in three subjects, reconstructed using bedpostx (A, B and C) and GQI (D, E and F). Each subject was scanned with different combinations of b-values and directions. All datasets show crossing fibres within the proximal elements of the brachial plexus at the point that rootlets emerge and merge to form the spinal nerve roots.

The observation of multiple fibre orientations in the intrathecal and intraforaminal section regions may explain why the local and streamline FA was lower than expected (coloured red in Figure 139), and why relatively streamlines between the spinal cord and extraforaminal plexus, as shown low FA thresholds are required for the propagation of in Chapter 15.
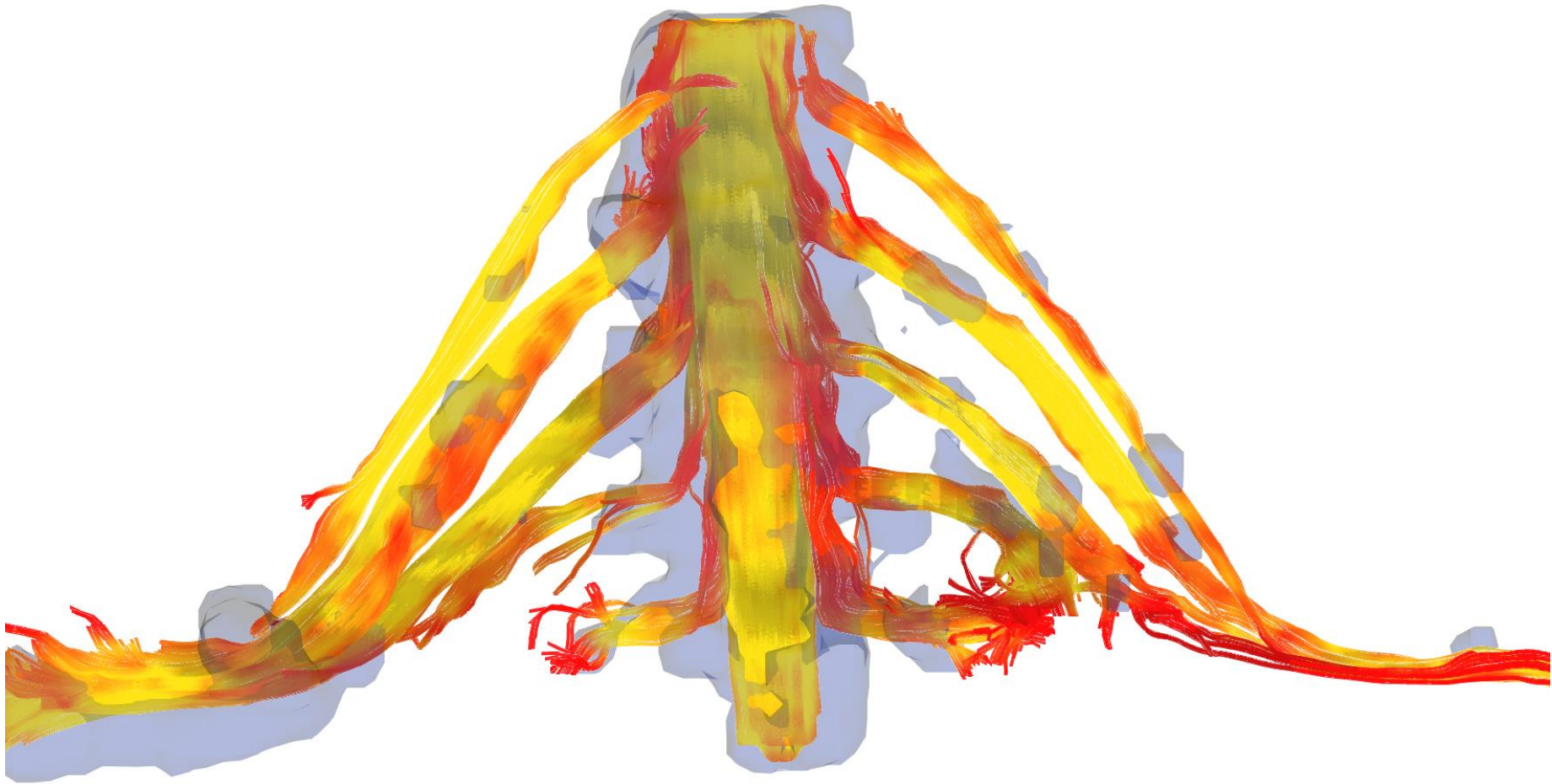
Figure 139. A deterministic tractograms of the brachial plexus coloured by the local FA (red=0, yellow=0.5). The areas of low FA (red) correspond to areas that bedpostx detected >2 fibre orientations (blue regions).

1.17.3.3 The extraforaminal spinal roots and trunks

Both GQI and bedpostx demonstrated that a single fibre population was predominate in the extraformanial brachial plexus (Figure 140).
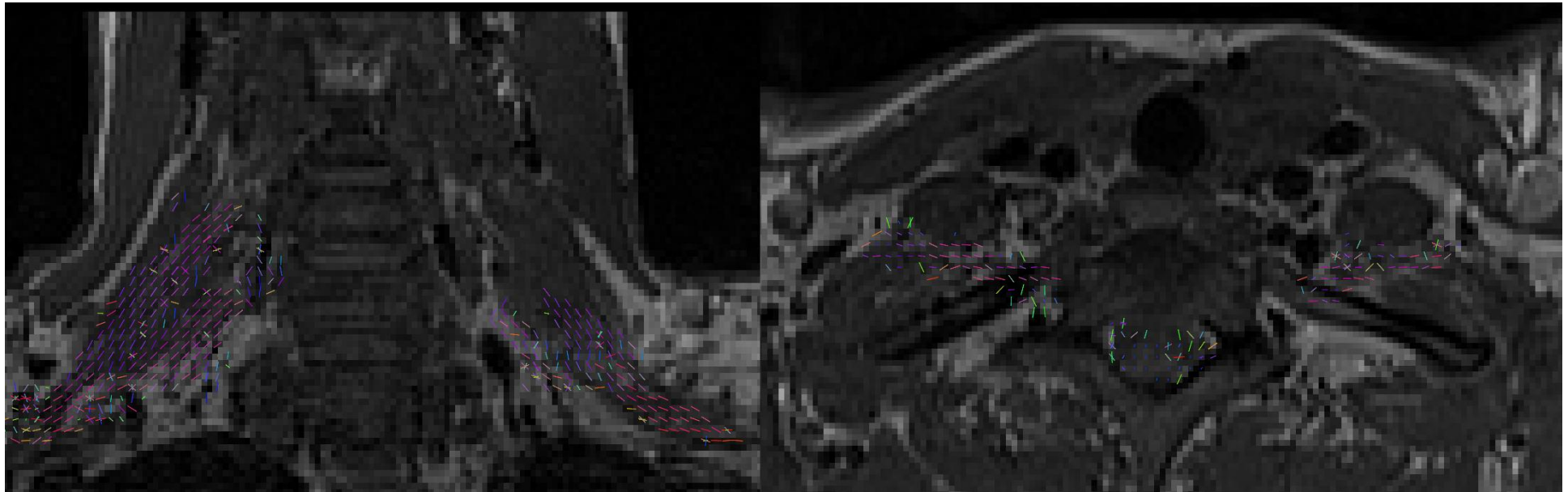
Figure 140. Sticks from bedpostx overlaid on coronal (left) and axial (right) T1-weighted images showing that lateral to the vertebral foramina, a single fibre orientation is sufficient to model diffusion within the brachial plexus

When comparing the dODF from GQI and fODF from bedpostx, at the same anatomical location, a single fibre orientation is depicted which also corresponds well to v1 of the diffusion tensor (Figure 141).
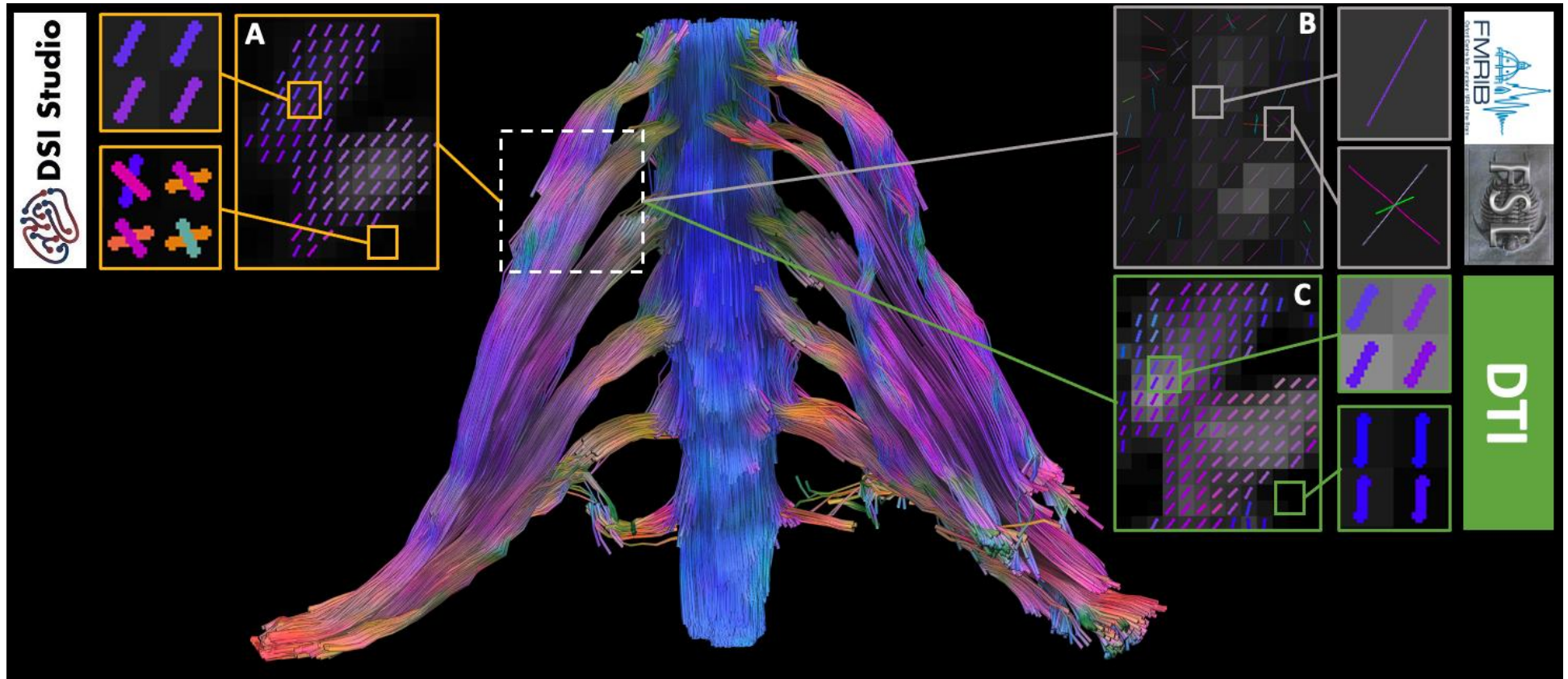
Figure 141. Deterministic streamlines from GQI. Closer examination of the right upper trunk modelled by GQI (A), bedpostx (B) and DTI (C) shows that a single fibre orientation is seen within the highly anisotropic voxels representing the upper trunk. NB, in panels A and C, a threshold is applied to the graphic to show voxels with a minimum QA.

1.17.3.4 Deterministic versus probabilistic tractography

Overall, the mean voxel-based Dice of deterministic versus probabilistic tractography was 0.70 (SD 0.13) (Figure 142). Mixed-effects modelling showed that neither a higher b-max (3000 s/mm^2) or more diffusion sensitising gradient directions (N$_D$ 192) affected the voxel-based Dice coefficient (adjusted ß 1.54 x10^{-5} [95% CI -0.88x10^{-5}, 1.19x10^{-4}] and adjusted ß 6.58 x10^{-5} [95% CI -0.14, 0.80]) of deterministic versus probabilistic tractography. With the addition of SNR as an interaction term with the b-value, the experimental conditions were still not associated with the voxel-based Dice of deterministic versus probabilistic tractography.
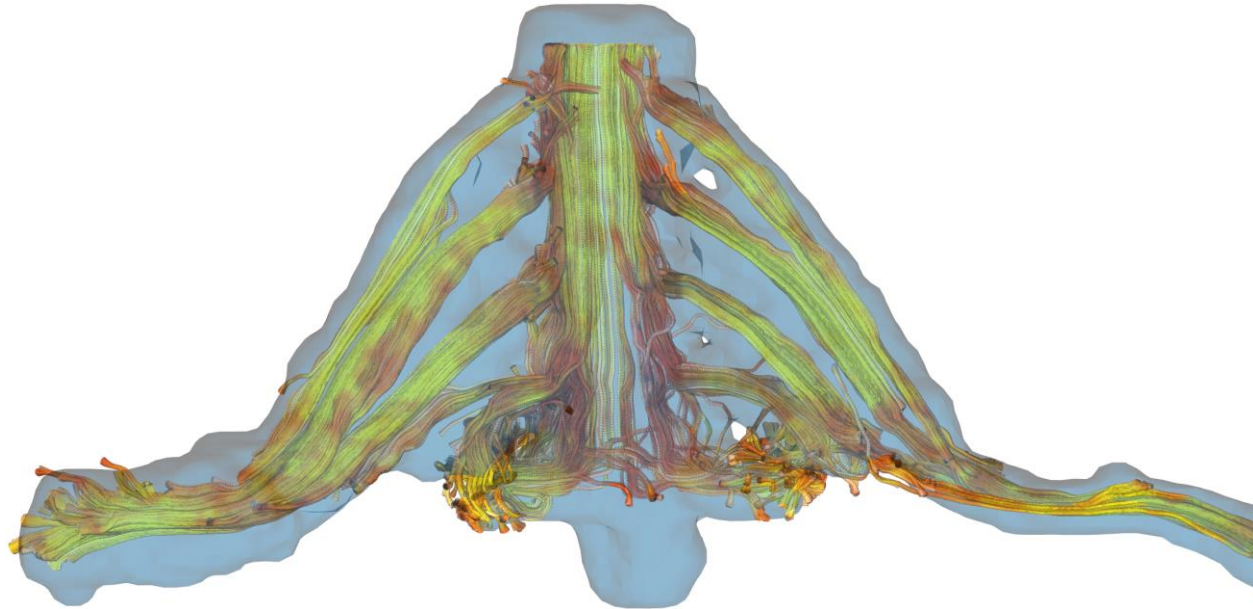
Figure 142. Deterministic streamlines from GQI (colours determined by the local FA; 0=red, 0.4=yellow) with the paths from proabtrackx overlaid in blue.

However, when examined on a root-by-root basis, the mean voxel-based DIce for deterministic versus probabilistic tractography was considerably lower at 0.36 (SD 0.12, Figure 143), with no significant difference between roots (p=0.325).
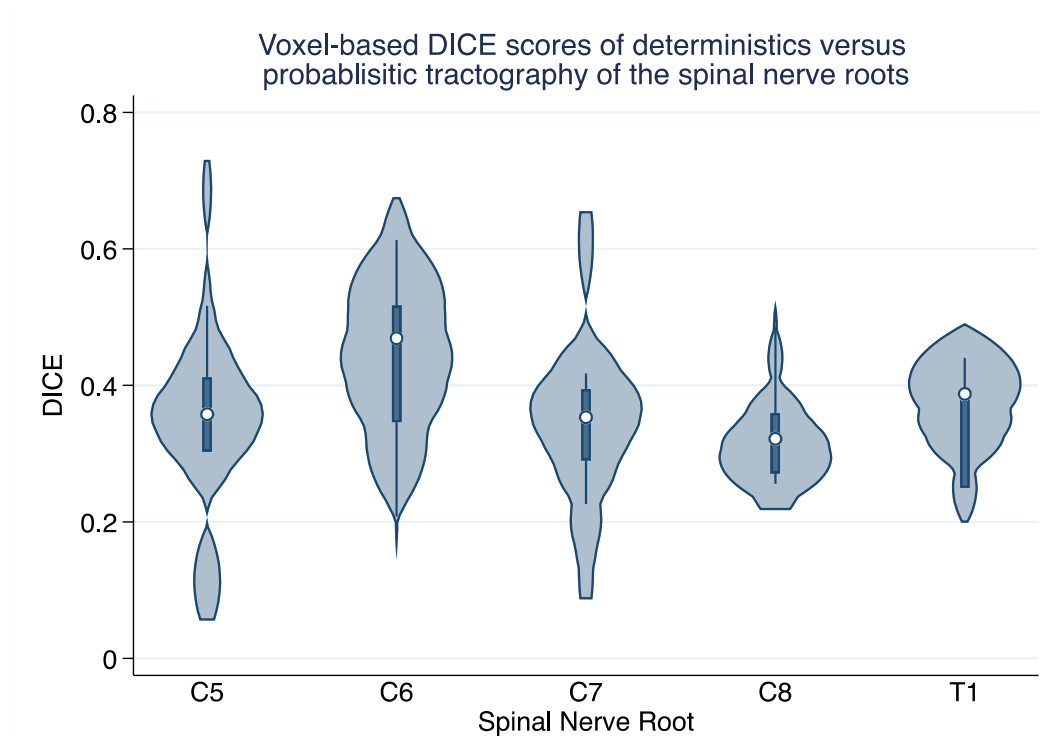
Figure 143. The voxel-based Dice similarity coefficients of deterministic (GQI) versus probabilistic (probtrackx) tractography of the roots of the brachial plexus

This appeared to be because paths generated in probtrackx were a mean 73% larger (7592mm^3 versus 12,460 mm^3, mean difference 4867mm^3 [95% CI 6278, 8907]). Also, probabilistic paths from probtrackx typically encompassed other ipsilateral (and occasionally contralateral) cervical roots whereas deterministic streamlines from GQI did not (Figure 144).
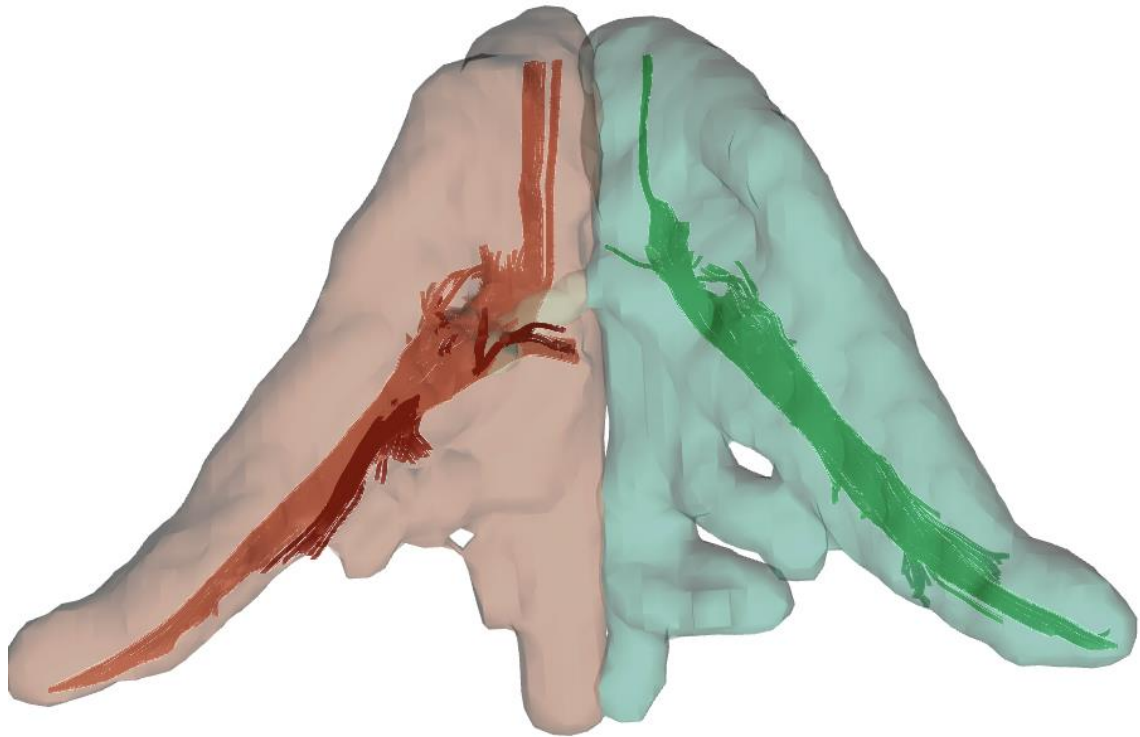
Figure 144. Paths and streamlines of the 7th cervical spinal nerve roots (right=red, left=green). The streamlines from GQI deterministic tractography (GQI) and appear to be constrained to the expected anatomical regions. In comparison, the coloured regions are probablistic paths generated from probtrackx using the same waypoint – they show paths which cover a larger area, encroaching on several other spinal root levels.

1.17.4 Discussion

This study demonstrates that both model-free and model-based methods detected multiple fibre orientations (crossing fibres) in 18-44% of the brachial plexus. These crossing fibres are located in the spinal nerve roots which are the structures most commonly injured[41]. Therefore, we suggest that our findings may have important ramifications for both the acquisition of dMRI data from the brachial plexus and its processing, within both the research and clinical setting

Our estimates of the prevalence of crossing fibres in the brachial plexus are lower than estimates within the brain (which are between 30-90%[307]) but of similar clinical and academic importance. Our observations are especially important in

light of recent work[308] which showed that peripheral nerves exhibit non-Gaussian diffusion at b-values lower than 1000 s/mm^2 (Figure 145).
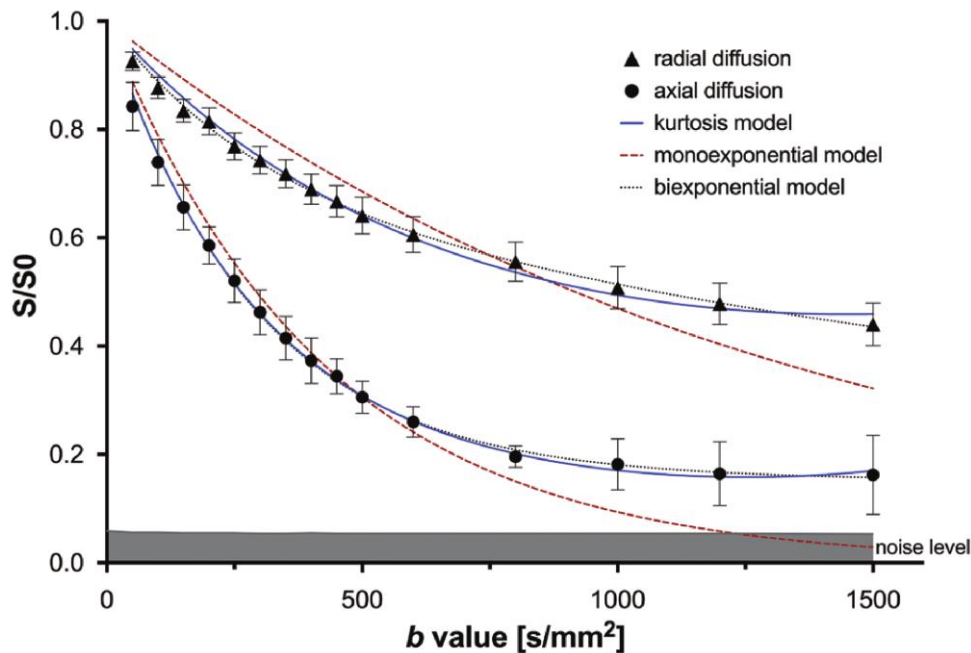
Figure 145. Curves fitting the dMRI signal as a function of the b-value. Error bars are 95% CIs. The standard monoexponential model was the worst fitting. Reproduced from Foesleitner et al (2022)[308].

To-date, all dMRI studies of the brachial plexus[309] have used b-values between 700 and 1000 s/mm^2 and reconstructed the data by means of a 2nd order tensors. Whilst this is the logical first step in an emerging field, there is now compelling evidence that future studies of the brachial plexus should incorporate higher b-values (up to approximately 2100 s/mm^2) with sufficient sampling of q-space (N_D ~150) and use postprocessing methods which take account of both non-Gaussian diffusion[308] and crossing fibres. We suggest that these values for b and N_D may be sufficient (until proven otherwise) because if there were truly more fibre orientations or fibres crossing at a small angle (Figure 132), then increasing the b-value from 2100 to 3000 s/mm^2 should yielded more voxels with multiple fibre orientations, but this was not observed.

We observed that the probability paths from probtrackx were substantially larger in volume than the deterministic streamlines from GQI. There are several possible

explanations for this discrepancy. For probtrackx, the default turning angle was 80° which is higher than the step angle prescribed within DSI Studio (45° for C5-7, 60° for C8 and 70° for T1[275]). Although a large burn-in sample helps to mitigate this problem (we used 1000, as advocated by the developers), we suspect that the larger turning in probtrackx was responsible for larger volume paths. Of note, in our testing phase we experimented with the use of identical step angles in probtrackx (45° for C5-7, 60° for C8 and 70° for T1[275]) but paths were invariable not propagated in the more cranial roots (C5-7) and so we regressed to using the developer recommended angle. Equally, the way in which the turning angles is used by the modified Euler algorithm within probtrackx is different to the RK4 algorithm in DSI Studio, so direct comparison of this angle may be inappropriate or misleading.

Currently, paths from probtrackx and streamlines from DSI Studio are saved in different file formats (nifti and .trk/tt, respectively) and each software uses a different diffusion 'space' (world space versus scanner coordinates, respectively). Ideally, popular software would harmonise important aspects of the workflow e.g., compute data within the same space and outputs files in the same file format. By making aspects congruent, more sophisticated and direct comparisons would be possible e.g., comparing streamlines using the Sherbrooke Connectivity Imaging Lab (SCIL) toolbox[301]. As the Sörenson-Dice coefficients between probtrackx paths and GQI streamlines are likely to be downwardly biased by small paths or spurious streamlines, weighting the Dice by streamline density[302,303] would be advantageous and equally desirable but this cannot be done by the SCILPY tools unless outputs are in .trk format. These differences between FSL and DSI Studio might be eliminated in future releases, but the current discrepancies mean that more informative quantitative comparisons are impossible.

1.17.4.1   Limitations

This is a single vendor, single site study with a small sample of young and middle-aged adults. It is possible that data acquired from other scanners, on a different sample of (children or adults), with a different pre-processing or reconstruction pipeline may reach different conclusions.

1.17.5 <u>Conclusions</u>

This study demonstrates that 18-44% of the brachial plexus contains multiple fibre orientations (crossing fibres), which are predominantly located within the structures most commonly injured, the spinal nerve roots. Our findings have important ramifications for both the acquisition of dMRI data from the brachial plexus and its processing, within the research and clinical setting

Chapter 18.   Outstanding Questions and Future Research

This work is the product of a 7-year journey, whereby at the outset there was little or no published work on dMRI in the extremity. We developed protocols used in the brain and other DW-MRI sequences from the extremity as a foundation to develop DTI and later, multishell high-b-value dMRI. At the outset, there were many failures both within the acquisition (e.g. Figure 146) and reconstruction domains. After a long period of development on a Siemens Verio, the research was migrated to a Siemens Prisma (which has better gradient performance). The several failed scans enabled us to learn what didn't work and ultimately, develop a clinically viable and potentially useful sequence.
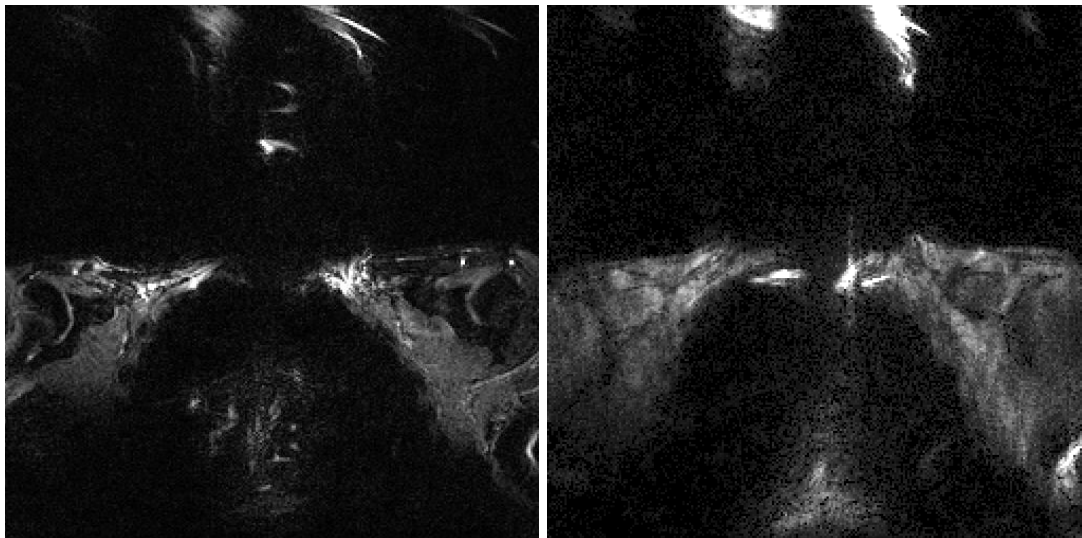
Figure 146. Two coronal b0s from two different volunteers during the early development phase. Both are examples of rsEPI of the brachial plexus. On the left, there was an absence of signal around the neck owing to poor shimming on a Siemens Verio 3T system. Ghosts of the head in the phase-encoding direction were assumed to by Nyquist ghosts. On the right, a different protocol again based on rsEPI was noisy, subject to ghosting and again lacked signal around the neck.

None-the-less, there are still many uncertainties in the field of dMRI of the brachial plexus. Based on the work presented in this thesis, some of the foremost issues which need to be investigated include:

1. The agreement between tractograms (deterministic and probabilistic) and macroscopic gross anatomy. It is unclear whether streamlines rendered adequately represent the gross anatomy, whether smaller important branches are missed (or pruned) and how to improve the image acquisition and processing to improve agreement. This would ideally done in fixed post-mortem specimens to allow high resolution data to be captured and the anatomy dissected.

2. The association between dMRI metrics (e.g., FA and MD) and the microscopic morphology of peripheral nerves in humans, both in health and states of disease. For obvious ethical reasons, there has been limited histopathological research on healthy human peripheral nerves. To-date, no studies have captured dMRI parameters from fresh healthy peripheral nerves and compared them to histological characteristics, such as axon counts, axon density, myelination, etc in cross-section. This information could be invaluable to clinicians as it may give insight into the regenerative potential of a nerve. Such research might be conducted in several ways, for example:
   a. Adults undergoing planned amputation could be scanned preoperatively and the peripheral nerves be excised at the time of surgery for histological analysis.
   b. Adults or children with suspected root avulsion could be scanned preoperatively and those who later undergo distal nerve transfers could have their (expendable) proximal neural tissue explanted for analysis.

3. Using the above data, further work must be done to understand the relationship between dMRI signals, the population of axons (i.e., their diameters) and equally, their myelination. Techniques exist which enable the generation of distributions of estimated diameters of axons from dMRI data, using regimes such as AxCaliber (Figure 147)[310], and novel diffusion encoding waveforms and gradients (e.g. oscillating gradients). These techniques have not been performed with human peripheral nerves but with access to tissue (as above) and now, expertise in the field of dMRI

we have a unique opportunity to develop tools to estimate axon density, diameter and myelination (taken either manually or perhaps using deep learning) from dMRI and compare these to digitalised whole slide histological images of nerves in cross-section.
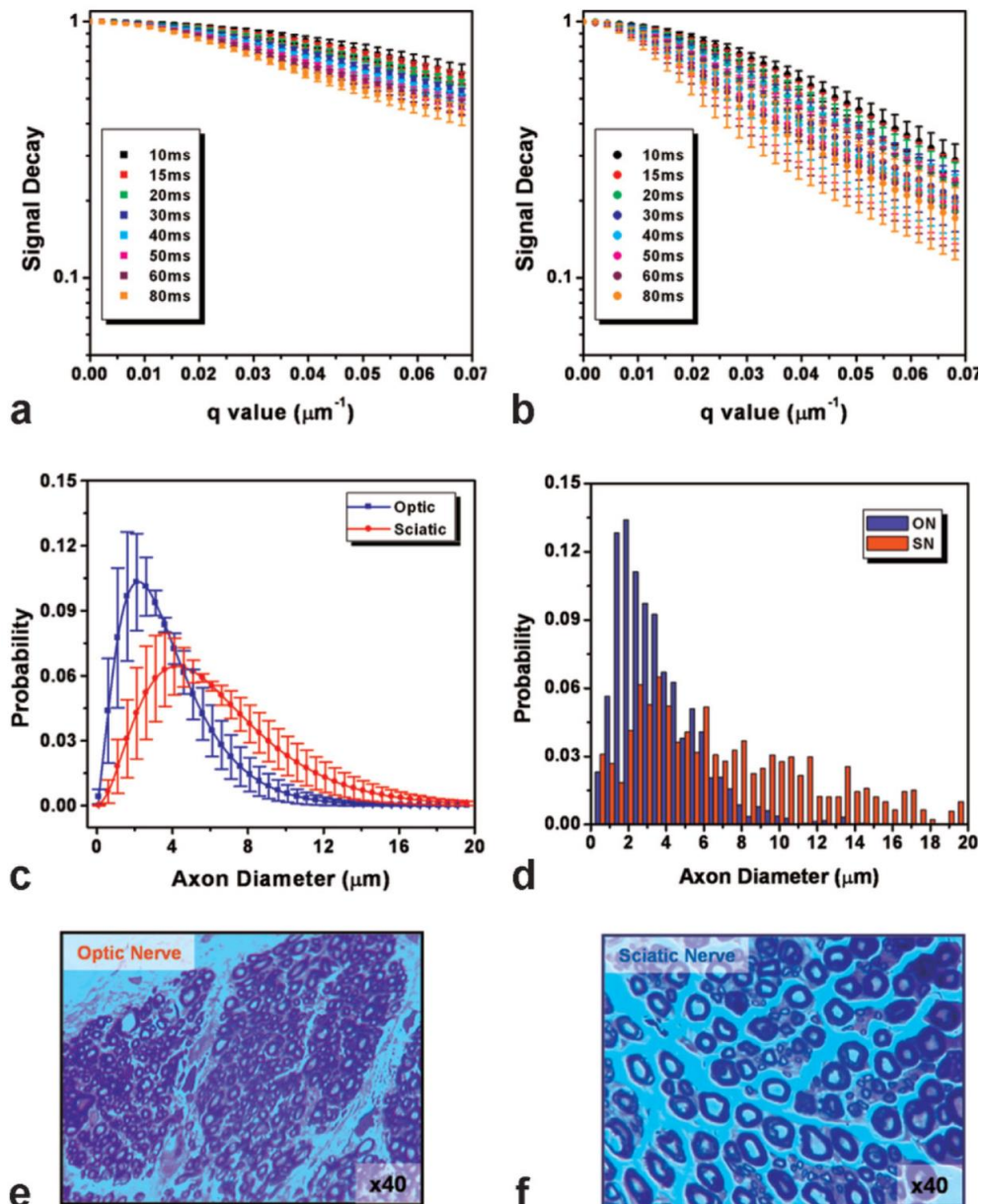
Figure 147. Results from AxCaliber using porcine nerves. The dMRI signal decay as a function of the q-value in the (a) optic nerve and (b) sciatic nerve. The predicted axon diameters as a function of signal decay (c). The actual axon diameters measured using electron microscopy (d). Examples of microscopy (e and f). Reproduced from Assaf et al (2008)[310].

4. Develop novel diffusion encoding waveforms: b-tensor encoding is of growing research interest. This approach generates data that is independent of the orientation dispersion of the underlying tissue (i.e., robust to the degeneracy between the width of the response function and that of the fODF) from which additional biomarkers (e.g., µFA) can be derived. We are in the process of developing a safe b-tensor encoding sequence for the brachial plexus.
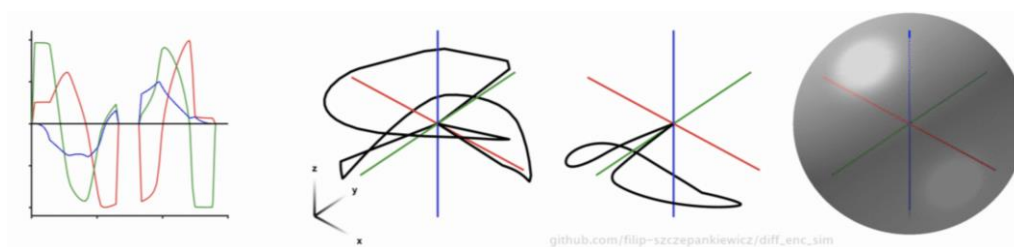
Figure 148. An example of the gradient waveform for spherical tensor encoding. Reproduced from https://github.com/filip-szczepankiewicz/diff_enc_sim/blob/master/animations/gwf_ste.gif

5. The ideal pre-processing pipeline for dMRI. Whilst this is still a matter of contention globally and under investigation via the ISMRM Diffusion Gropu, the agreement between corrected dMRI datasets using different pipelines to slice-matched structural scans (e.g., T1/2w) might provide some insight into which performs best for geometric correction of dMRI data in the upper limb. Equally, if the bias of each pipeline could be established, then corrections might be applied to harmonise dMRI between different vendors and pipelines.

Part 3. References

1. Helixitta. No Title. *Wikimedia Commons*. 2019. Available at: https://commons.wikimedia.org/wiki/File:Afferent_and_efferent_neurons_en.svg.

2. Anon. Medical gallery of Blausen Medical 2014. *WikiJournal Med.* 2014;1(2).

3. Min Y, Kristiansen K, Boggs JM, et al. Interaction forces and adhesion of supported myelin lipid bilayers modulated by myelin basic protein. *Proc. Natl. Acad. Sci.* 2009;106(9):3154–3159.

4. Erlanger J, Gasser HS. The action potential in fibers of slow conduction in spinal roots and somatic nerves. *Am. J. Physiol.-Leg. Content.* 1930;92(1):43–82.

5. Waxman SG. Determinants of conduction velocity in myelinated nerve fibers. *Muscle Nerve.* 1980;3(2):141–150.

6. Hall J, Guyon A. Guyton and Hall Textbook of Medical Physiology. In: ; 2010:563.

7. Anon. Experiments on the section of the glossopharyngeal and hypoglossal nerves of the frog, and observations of the alterations produced thereby in the structure of their primitive fibres. *Philos. Trans. R. Soc. Lond.* 1850;140:423–429.

8. Allodi I, Udina E, Navarro X. Specificity of peripheral nerve regeneration: Interactions at the axon level. *Prog. Neurobiol.* 2012;98(1):16–37.

9. Seddon HJ. Three types of nerve injury. *Brain.* 1943;66(4):237–288.

10. Sunderland S. A classification of peripheral nerve injuries producing loss of function. *Brain.* 1951;74(4):491–516.

11. Hems T. Nerve injury: Classification, clinical assessment, investigation, and management. *Living Textb. Hand Surg.* 2016:1–12.

12. Pellerin M, Kimball Z, Tubbs RS, et al. The prefixed and postfixed brachial plexus: A review with surgical implications. *Surg. Radiol. Anat.* 2010;32(3):251–260.

13. Sakellariou VI, Badilas NK, Mazis GA, et al. Brachial Plexus Injuries in Adults: Evaluation and Diagnostic Approach. *ISRN Orthop.* 2014;2014(January 2015):1–9.

14. Terzis JK. *Microreconstruction of Nerve Injuries*. Saunders; 1987.

15. Sinha S, Prasad GL, Lalwani S. A cadaveric microanatomical study of the fascicular topography of the brachial plexus. *J. Neurosurg.* 2016;125(2):355–362.

16. Gesslbauer B, Hruby LA, Roche AD, et al. Axonal components of nerves innervating the human arm. *Ann. Neurol.* 2017;82(3):396–408.

17. Midha R. Epidemiology of brachial plexus injuries in a multitrauma population. *Neurosurgery.* 1997;40(6):1182–8; discussion 1188-9.

18. Franzblau LE, Shauver MJ, Chung KC. Patient Satisfaction and Self-Reported Outcomes After Complete Brachial Plexus Avulsion Injury. *J. Hand Surg.* 2014;39(5):948-955.e4.

19. Kretschmer T, Ihle S, Antoniadis G, et al. Patient satisfaction and disability after brachial plexus surgery. *Neurosurgery.* 2009;65(suppl_4):A189–A196.

20. Dolan RT, Butler JS, Murphy SM, et al. Health-related quality of life and functional outcomes following nerve transfers for traumatic upper brachial plexus injuries. *J. Hand Surg. Eur. Vol.* 2012;37(7):642–51.

21. Maldonado AA, Kircher MF, Spinner RJ, et al. Free Functioning Gracilis Muscle Transfer versus Intercostal Nerve Transfer to Musculocutaneous Nerve for Restoration of Elbow Flexion after Traumatic Adult Brachial Pan-Plexus Injury. *Plast. Reconstr. Surg.* 2016;138(3):483e–488e.

22. Teixeira MJ, da Paz MG da S, Bina MT, et al. Neuropathic pain after brachial plexus avulsion - central and peripheral mechanisms. *BMC Neurol.* 2015;15(1):73.

23. Lee KJ, Joo WI, Chough CK, et al. Long term effect of thalamic deep brain stimulation for pain due to brachial plexus injury. *Stereotact Funct Neurosurg.* 2012;90(4 SUPPL. 1):161.

24. Brill S, Aryeh IG. Neuromodulation in the management of pain from brachial plexus injury. *Pain Physician.* 2008;11(1):81–5.

25. Teixeira MJ, da Paz MG da S, Bina MT, et al. Neuropathic pain after brachial plexus avulsion - central and peripheral mechanisms. *BMC Neurol.* 2015;15(1):73.

26. Franzblau L, Chung KC. Psychosocial outcomes and coping after complete avulsion traumatic brachial plexus injury. *Disabil Rehabil.* 2015;37(2):135–143.

27. Wilson TJ, Chang KWC, Yang LJ-S. Depression and Anxiety in Traumatic Brachial Plexus Injury Patients Are Associated With Reduced Motor Outcome After Surgical Intervention for Restoration of Elbow Flexion. *Neurosurgery.* 2016;78(6):844–850.

28. Mancuso CA, Lee SK, Dy CJ, et al. Expectations and limitations due to brachial plexus injury: a qualitative study. *Hand.* 2015;10(4):741–749.

29. Vargas MI, Viallon M, Nguyen D, et al. New approaches in imaging of the brachial plexus. *Eur. J. Radiol.* 2010;74(2):403–410.

30. Nardin R a, Patel MR, Gudas TF, et al. Electromyography and magnetic resonance imaging in the evaluation of radiculopathy. *Muscle Nerve.* 1999;22(2):151–155.

31. Zhu Y-S, Mu N-N, Zheng M-J, et al. High-Resolution Ultrasonography for the Diagnosis of Brachial Plexus Root Lesions. *Ultrasound Med. Biol.* 2014;40(7):1420–1426.

32. Mallouhi A, Meirer R, Bodner G. Sonographic features of brachial plexus traumatic rupture. *J. Neurosurg.* 2003;99(2):432–432.

33. Lapegue F, Faruch-Bilfeld M, Demondion X, et al. Ultrasonography of the brachial plexus, normal appearance and practical applications. *Diagn. Interv. Imaging.* 2014;95(3):259–275.

34. Chin B, Ramji M, Farrokhyar F, et al. Efficient Imaging: Examining the Value of Ultrasound in the Diagnosis of Traumatic Adult Brachial Plexus Injuries, A Systematic Review. *Neurosurgery.* 2017;0(0):1–10.

35. Sureka J, Cherian RA, Alexander M, et al. MRI of brachial plexopathies. *Clin. Radiol.* 2009;64(2):208–218.

36. Liu Y, Lao J, Gao K, et al. Functional outcome of nerve transfers for traumatic global brachial plexus avulsion. *Injury.* 2013;44(5):655–660.

37. Martin E, Senders JT, DiRisio AC, et al. Timing of surgery in traumatic brachial plexus injury: a systematic review. *J. Neurosurg.* 2019;130(4):1333–1345.

38. Jivan S, Kumar N, Wiberg M, et al. The influence of pre-surgical delay on functional outcome after reconstruction of brachial plexus injuries. *J. Plast. Reconstr. Aesthet. Surg.* 2009;62(4):472–479.

39. Makin TR, Scholz J, Filippini N, et al. Phantom pain is associated with preserved structure and function in the former hand area. *Nat. Commun.* 2013;4:1570.

40. Teixeira MJ, da Paz MG da S, Bina MT, et al. Neuropathic pain after brachial plexus avulsion - central and peripheral mechanisms. *BMC Neurol.* 2015;15(1):73.

41. Wade RG, Takwoingi Y, Wormald JCR, et al. MRI for Detecting Root Avulsions in Traumatic Adult Brachial Plexus Injuries: A Systematic Review and Meta-Analysis of Diagnostic Accuracy. *Radiology.* 2019;293(1):125–133.

42. Karalija A, Novikova LN, Orädd G, et al. Differentiation of Pre- and Postganglionic Nerve Injury Using MRI of the Spinal Cord. *Plos One.* 2016;11(12):e0168807.

43. Fournier HD, Mercier P, Menei P. Repair of avulsed ventral nerve roots by direct ventral intraspinal implantation after brachial plexus injury. *Hand Clin.* 2005;21(1):109–118.

44. Wali AR, Santiago-Dieppa DR, Brown JM, et al. Nerve transfer versus muscle transfer to restore elbow flexion after pan–brachial plexus injury: a cost-effectiveness analysis. *Neurosurg. Focus.* 2017;43(1):E4.

45. Yang LJ-S, Chang KW-C, Chung KC. A Systematic Review of Nerve Transfer and Nerve Repair for the Treatment of Adult Upper Brachial Plexus Injury. *Neurosurgery.* 2012;71(2):417–429.

46. de Mendonça Cardoso M, Gepp R, Correa JFG. Outcome following phrenic nerve transfer to musculocutaneous nerve in patients with traumatic brachial palsy: a qualitative systematic review. *Acta Neurochir. (Wien).* 2016;158(9):1793–1800.

47. Yang G, Chang KW-C, Chung KC. A Systematic Review of Outcomes of Contralateral C7 Transfer for the Treatment of Traumatic Brachial Plexus Injury. *Plast. Reconstr. Surg.* 2015;136(4):480e–489e.

48. Hems T. Nerve Transfers for Traumatic Brachial Plexus Injury: Advantages and Problems. *J. Hand Microsurg.* 2016;03(01):6–10.

49. Wali AR, Park CC, Brown JM, et al. Analyzing cost-effectiveness of ulnar and median nerve transfers to regain forearm flexion. *Neurosurg. Focus.* 2017;42(3):E11.

50. Tournier J-D, Calamante F, Connelly A. Robust determination of the fibre orientation distribution in diffusion MRI: Non-negativity constrained super-resolved spherical deconvolution. *NeuroImage.* 2007;35(4):1459–1472.

51. Rabi II, Zacharias JR, Millman S, et al. A New Method of Measuring Nuclear Magnetic Moment. *Phys. Rev.* 1938;53(4):318–318.

52. Bloch F, Hansen WW, Packard M. The Nuclear Induction Experiment. *Phys. Rev.* 1946;70(7–8):474–485.

53. Purcell EM, Torrey HC, Pound R V. Resonance Absorption by Nuclear Magnetic Moments in a Solid. *Phys. Rev.* 1946;69(1–2):37–38.

54. Lauterbur PC. Image formation by induced local interactions. Examples employing nuclear magnetic resonance. 1973. *Clin. Orthop.* 1989;(244):3–6.

55. Mansfield P, Grannell PK. NMR "diffraction" in solids? *J. Phys. C Solid State Phys.* 1973;6(22):L422–L426.

56. Zeeman P. The Effect of Magnetisation on the Nature of Light Emitted by a Substance. *Nature.* 1897;55(1424):347–347.

57. Ridgway JP. Cardiovascular magnetic resonance physics for clinicians: part I. *J. Cardiovasc. Magn. Reson.* 2010;12(1):71.

58. Stanisz GJ, Odrobina EE, Pun J, et al. T1, T2 relaxation and magnetization transfer in tissue at 3T. *Magn. Reson. Med.* 2005;54(3):507–512.

59. Universiteit T, Doi E, Version D. *Diffusion tensor imaging of mouse skeletal muscle.*; 2019.

60. Beaulieu C. The basis of anisotropic water diffusion in the nervous system - a technical review. *NMR Biomed.* 2002;15(7–8):435–455.

61. Heckel A, Weiler M, Xia A, et al. Peripheral Nerve Diffusion Tensor Imaging: Assessment of Axon and Myelin Sheath Integrity. *Plos One.* 2015;10(6):e0130833.

62. Andersson G, Orädd G, Sultan F, et al. In vivo Diffusion Tensor Imaging, Diffusion Kurtosis Imaging, and Tractography of a Sciatic Nerve Injury Model in Rat at 9.4T. *Sci. Rep.* 2018;8(1):12911.

63. Friedrich P, Fraenz C, Schlüter C, et al. The Relationship between Axon Density, Myelination, and Fractional Anisotropy in the Human Corpus Callosum. *Cereb. Cortex.* 2020;30(4):2042–2056.

64. Beaulieu C, Allen PS. Water diffusion in the giant axon of the squid: Implications for diffusion-weighted MRI of the nervous system. *Magn. Reson. Med.* 1994;32(5):579–583.

65. Beaulieu Peter S. CA. Determinants of anisotropic water diffusion in nerves. 1994;31(4):394–400.

66. Gulani V, Webb AG, Duncan ID, et al. Apparent diffusion tensor measurements in myelin-deficient rat spinal cords. *Magn. Reson. Med.* 2001;45(2):191–195.

67. Shemesh N. Axon diameters and myelin content modulate microscopic fractional anisotropy at short diffusion times in fixed rat spinal cord. *Front. Phys.* 2018;6(JUN):1–15.

68. Kristensson K, Olsson Y. Uptake and retrograde axonal transport of peroxidase in hypoglossal neurones. *Acta Neuropathol. (Berl.)*. 1971;19(1):1–9.

69. Olsson Y, Kristensson K. The perineurium as a diffusion barrier to protein tracers following trauma to nerves. *Acta Neuropathol. (Berl.)*. 1973;23(2):105–111.

70. Soderfeldt B, Olsson Y, Kristensson K. The perineurium as a diffusion barrier to protein tracers in human peripheral nerve. *Acta Neuropathol. (Berl.)*. 1973;25(2):120–126.

71. Reina MA, López A, Villanueva MC, et al. [The blood-nerve barrier in peripheral nerves]. *Rev. Esp. Anestesiol. Reanim.* 2003;50(2):80–6.

72. Tuch DS, Salat DH, Wisco JJ, et al. Choice reaction time performance correlates with diffusion anisotropy in white matter pathways supporting visuospatial attention. *Proc. Natl. Acad. Sci.* 2005;102(34):12212–12217.

73. Lebel C, Gee M, Camicioli R, et al. Diffusion tensor imaging of white matter tract evolution over the lifespan. *NeuroImage*. 2012;60(1):340–352.

74. Kronlage M, Schwehr V, Schwarz D, et al. Peripheral nerve diffusion tensor imaging (DTI): normal values and demographic determinants in a cohort of 60 healthy individuals. *Eur. Radiol.* 2018;28(5):1801–1808.

75. Griffiths TT, Flather R, Teh I, et al. Diffusion tensor imaging in cubital tunnel syndrome. *Sci. Rep.* 2021;11(1):1–8.

76. Mori Jiangyang SZ. Principles of Diffusion Tensor Imaging and Its Applications to Basic Neuroscience Research. 2006;51(5):527–539.

77. Le Bihan D. What can we see with IVIM MRI? *NeuroImage*. 2019;187:56–67.

78. Farrell JAD, Landman BA, Jones CK, et al. Effects of signal-to-noise ratio on the accuracy and reproducibility of diffusion tensor imaging-derived fractional anisotropy, mean diffusivity, and principal eigenvector measurements at 1.5T. *J. Magn. Reson. Imaging*. 2007;26(3):756–767.

79. Jones DK, Basser PJ. "Squashing peanuts and smashing pumpkins": How noise distorts diffusion-weighted MR data. *Magn. Reson. Med.* 2004;52(5):979–993.

80. Descoteaux M, Deriche R, Knösche TR, et al. Deterministic and probabilistic tractography based on complex fibre orientation distributions. *IEEE Trans. Med. Imaging*. 2009;28(2):269–286.

81. Jones DK, Knösche TR, Turner R. White matter integrity, fiber count, and other fallacies: The do's and don'ts of diffusion MRI. *NeuroImage*. 2013;73:239–254.

82. Tax CMW, Bastiani M, Veraart J, et al. What's new and what's next in diffusion MRI preprocessing. *NeuroImage*. 2022;249:118830.

83. Maffei C. New insights from the IronTract challenge: Simple post-processing enhances the accuracy of diffusion tractography. *Abstr. 2021 ISMRM SMRT Annu. Meet. Exhib.*

84. Jenkinson M, Beckmann CF, Behrens TEJ, et al. FSL. *NeuroImage*. 2012;62(2):782–790.

85. Veraart J, Fieremans E, Novikov DS. Diffusion MRI noise mapping using random matrix theory. *Magn. Reson. Med.* 2016;76(5):1582–1593.

86. Smith SM, Brady JM. SUSAN - A New Approach to Low Level Image Processing. *Int. J. Comput. Vis.* 1997;23(1):45–78.

87. Pierpaoli C. TORTOISE: an integrated software package for processing of diffusion MRI data. *SMRM 18th Annu. Meet. Stockh. Swed. Abstr. 1597*. 2009.

88. Andersson Stefan; Ashburner, John JLR; S. How to correct susceptibility distortions in spin-echo echo-planar images: application to diffusion tensor imaging. 2003;20(2):870–888.

89. Andersson Stamatios N. JLR; S. An integrated approach to correction for off-resonance effects and subject movement in diffusion MR imaging. 2015;125(NA):1063–1078.

90. Irfanoglu MO, Modi P, Nayak A, et al. DR-BUDDI (Diffeomorphic Registration for Blip-Up blip-Down Diffusion Imaging) method for correcting echo planar imaging distortions. *NeuroImage.* 2015;106:284–299.

91. Andersson JLR, Graham MS, Zsoldos E, et al. Incorporating outlier detection and replacement into a non-parametric framework for movement and distortion correction of diffusion MR images. *NeuroImage.* 2016;141:556–572.

92. Andersson JLR, Graham MS, Drobnjak I, et al. Towards a comprehensive framework for movement and distortion correction of diffusion MR images: Within volume movement. *NeuroImage.* 2017;152(February):450–466.

93. Andersson JLR, Graham MS, Drobnjak I, et al. Susceptibility-induced distortion that varies due to motion: Correction in diffusion MR without acquiring additional data. *NeuroImage.* 2018;171(July 2017):277–295.

94. Kellner E, Dhital B, Kiselev VG, et al. Gibbs-ringing artifact removal based on local subvoxel-shifts. *Magn. Reson. Med.* 2016;76(5):1574–1581.

95. Logan JK, Rais-Bahrami S, Turkbey B, et al. Current status of magnetic resonance imaging (MRI) and ultrasonography fusion software platforms for guidance of prostate biopsies. *BJU Int.* 2014;114(5):641–652.

96. Basser PJ, Mattiello J, LeBihan D. MR diffusion tensor spectroscopy and imaging. *Biophys. J.* 1994;66(1):259–267.

97. Alexander AL, Hasan K, Kindlmann G, et al. A geometric analysis of diffusion tensor measurements of the human brain. *Magn. Reson. Med.* 2000;44(2):283–291.

98. Wheeler-Kingshott Mara CAM; C. About \"axial\" and \"radial\" diffusivities. 2009;61(5):1255–1260.

99. Dell'Acqua F, Tournier J -Donald. Modelling white matter with spherical deconvolution: How and why? *NMR Biomed.* 2019;32(4):1–18.

100. Descoteaux M. High Angular Resolution Diffusion Imaging (HARDI). In: *Wiley Encyclopedia of Electrical and Electronics Engineering*. Hoboken, NJ, USA: John Wiley & Sons, Inc.; 2015:1–25.

101. Tuch DS, Reese TG, Wiegell MR, et al. High angular resolution diffusion imaging reveals intravoxel white matter fiber heterogeneity. *Magn. Reson. Med.* 2002;48(4):577–582.

102. Jansons KM, Alexander DC. Persistent angular structure: New insights from diffusion magnetic resonance imaging data. *Inverse Probl.* 2003;19(5):1031–1046.

103. Tuch DS. Q-ball imaging. *Magn. Reson. Med.* 2004;52(6):1358–1372.

104. Anderson AW. Measurement of fiber orientation distributions using high angular resolution diffusion imaging. *Magn. Reson. Med.* 2005;54(5):1194–1206.

105. Tournier JD, Calamante F, Gadian DG, et al. Direct estimation of the fiber orientation density function from diffusion-weighted MRI data using spherical deconvolution. *NeuroImage.* 2004;23(3):1176–1185.

106. Tournier JD, Calamante F, Connelly A. Robust determination of the fibre orientation distribution in diffusion MRI: Non-negativity constrained super-resolved spherical deconvolution. *NeuroImage.* 2007;35(4):1459–1472.

107. Behrens TEJ, Berg HJ, Jbabdi S, et al. Probabilistic diffusion tractography with multiple fibre orientations: What can we gain? *NeuroImage.* 2007;34(1):144–155.

108. Zhang H, Schneider T, Wheeler-Kingshott CA, et al. NODDI: Practical in vivo neurite orientation dispersion and density imaging of the human brain. *NeuroImage.* 2012;61(4):1000–1016.

109. Fang-Cheng Yeh, Wedeen VJ, Tseng W-YI. Generalized q-Sampling Imaging. *IEEE Trans. Med. Imaging.* 2010;29(9):1626–1635.

110. Callaghan PT, Eccles CD, Xia Y. NMR microscopy of dynamic displacements: K-space and q-space imaging. *J. Phys. [E].* 1988;21(8):820–822.

111. Wedeen VJ, Hagmann P, Tseng WYI, et al. Mapping complex tissue architecture with diffusion spectrum magnetic resonance imaging. *Magn. Reson. Med.* 2005;54(6):1377–1386.

112. Descoteaux M, Angelino E, Fitzgibbons S, et al. Regularized, fast, and robust analytical Q-ball imaging. *Magn. Reson. Med.* 2007;58(3):497–510.

113. Hess CP, Mukherjee P, Han ET, et al. Q-ball reconstruction of multimodal fiber orientations using the spherical harmonic basis. *Magn. Reson. Med.* 2006;56(1):104–117.

114. Nath V, Schilling KG, Parvathaneni P, et al. Tractography reproducibility challenge with empirical data (TraCED): The 2017 ISMRM diffusion study group challenge. *J. Magn. Reson. Imaging.* 2020;51(1):234–249.

115. Mori Barbara J.; Chacko, V. P.; van Zijl, Peter C.M. SC. Three-dimensional tracking of axonal projections in the brain by magnetic resonance imaging. 1999;45(2):265–269.

116. Basser Sinisa; Pierpaoli, Carlo; Duda, Jeffrey T.; Aldroubi, Akram PJ; P. In vivo fiber tractography using DT-MRI data. 2000;44(4):625–632.

117. Aganj I, Lenglet C, Jahanshad N, et al. A Hough transform global probabilistic approach to multiple-subject diffusion MRI tractography. *Med. Image Anal.* 2011;15(4):414–425.

118. JONES D. Studying connections in the living human brain with diffusion MRI. *Cortex.* 2008;44(8):936–952.

119. Jones DK. Challenges and limitations of quantifying brain connectivity in vivo with diffusion MRI. *Imaging Med.* 2010;2(3):341–355.

120. Jones DK. Tractography Gone Wild: Probabilistic Fibre Tracking Using the Wild Bootstrap With Diffusion Tensor MRI. *IEEE Trans. Med. Imaging.* 2008;27(9):1268–1274.

121. Behrens Mark W.; Jenkinson, Mark; Johansen-Berg, Heidi; Nunes, Rita G.; Clare, Stuart; Matthews, Paul M.; Brady, J.M.; Smith, Stephen M. TEJ; W. Characterization and propagation of uncertainty in diffusion-weighted MR imaging. 2003;50(5):1077–1088.

122. Farinas AF, Manzanera Esteve I V., Pollins AC, et al. Diffusion Magnetic Resonance Imaging Predicts Peripheral Nerve Recovery in a Rat Sciatic Nerve Injury Model. *Plast. Reconstr. Surg.* 2020;145(4):949–956.

123. Andersson G, Orädd G, Sultan F, et al. In vivo Diffusion Tensor Imaging, Diffusion Kurtosis Imaging, and Tractography of a Sciatic Nerve Injury Model in Rat at 9.4T. *Sci. Rep.* 8(1):12911.

124. Manzanera Esteve I V., Farinas AF, Pollins AC, et al. Noninvasive diffusion MRI to determine the severity of peripheral nerve injury. *Magn. Reson. Imaging.* 2021;83(July):96–106.

125. Farinas AF, Manzanera Esteve I V., Pollins AC, et al. Diffusion Tensor Tractography Visualizes Partial Nerve Laceration Severity as Early as 1 Week after Surgical Repair in a Rat Model Ex Vivo. *Mil. Med.* 2020;185:35–41.

126. Manzanera Esteve I V., Farinas AF, Pollins AC, et al. Probabilistic Assessment of Nerve Regeneration with Diffusion MRI in Rat Models of Peripheral Nerve Trauma. *Sci. Rep.* 2019;9(1):19686.

127. Afshari A, Nguyen L, Kelm ND, et al. Assessment of the Effect of Autograft Orientation on Peripheral Nerve Regeneration Using Diffusion Tensor Imaging. *Ann. Plast. Surg.* 2018;80(4):384–390.

128. Wu Yanfeng; Kong, Xiangquan; Liu, Dingxi; Long, Xi; Shu, Shenglei; Su, Xiaoyun; Wang, Bing; Liu, Xiaoming; Ma, Yamei; Wang, Lixia WN. Application of diffusion tensor imaging in quantitatively monitoring chronic constriction injury of rabbit sciatic nerves: correlation with histological and functional changes. 2017;91(1083):20170414-NA.

129. Wan Q, Yu Y, Bao Y, et al. Evaluation of peripheral nerve acute crush injury in rabbits: comparison among diffusion kurtosis imaging, diffusion tensor imaging and electromyography. *Magn. Reson. Mater. Phys. Biol. Med.* 2021;(0123456789).

130. Farinas AF, Pollins AC, Stephanides M, et al. Diffusion tensor tractography to visualize axonal outgrowth and regeneration in a 4-cm reverse autograft sciatic nerve rabbit injury model. *Neurol. Res.* 2019;41(3):257–264.

131. Breckwoldt MO, Stock C, Xia A, et al. Diffusion Tensor Imaging Adds Diagnostic Accuracy in Magnetic Resonance Neurography. *Invest. Radiol.* 2015;50(8):7.

132. Rojoa D, Raheman F, Rassam J, et al. Diffusion Tensor Imaging of the Median Nerve: A Systematic Review and Meta-Analysis of Normal Values in Asymptomatic Adults and How They Change in Carpal Tunnel Syndrome. *SSRN Electron. J.* 2021:1–11.

133. Griffiths T, et al. Diffusion MRI for diagnosing cubital tunnel syndrome: A proof of concept study. *J. Peripher. Nerv. Syst.* 2020;25(4):448–449.

134. Breitenseher Gottfried; Hold, Alina; Berzaczy, Dominik; Nemec, Stefan F.; Sycha, Thomas; Weber, Michael; Prayer, Daniela; Kasprian, Gregor JK. MR neurography of ulnar nerve entrapment at the cubital tunnel: a diffusion tensor imaging study. 2015;25(7):1911–1918.

135. Ho M, Becker A, Ulbrich E, et al. Comparison of simultaneous multi-slice readout-segmented EPI and conventional single-shot EPI for diffusion tensor imaging of the ulnar nerve. *Heliyon.* 2018;4(10):e00853.

136. Park S, et al. Determination of optimum pixel size and slice thickness for tractography and ulnar nerve diffusion tensor imaging at the cubital tunnel using 3T MRI. *Acta Radiol.* 2020.

137. Altun Y, Aygun MS, Cevik MU, et al. Relation between electrophysiological findings and diffusion weighted magnetic resonance imaging in ulnar neuropathy at the elbow. *J. Neuroradiol.* 2013;40(4):260–266.

138. Iba K. et al. Diffusion-weighted magnetic resonance imaging of the ulnar nerve in cubital tunnel syndrome. *Hand Surg.* 2010;15(1):11–15.

139. Liang W, Han B, Hai Y, et al. Diffusion tensor imaging with fiber tracking provides a valuable quantitative and clinical evaluation for compressed lumbosacral nerve roots: a systematic review and meta-analysis. *Eur. Spine J.* 2021;30(4):818–828.

140. Sun X, Liu X, Zhao Q, et al. Proximal nerve MR neurography with diffusion tensor imaging in differentiating subtypes of Charcot-Marie-Tooth disease. *Eur. Radiol.* 2022.

141. Cheah PL, Krisnan T, Wong JHD, et al. Microstructural Integrity of Peripheral Nerves in Charcot–Marie–Tooth Disease: An MRI Evaluation Study. *J. Magn. Reson. Imaging.* 2021;53(2):437–444.

142. Kim HS, Yoon YC, Choi BO, et al. Diffusion tensor imaging of the sciatic nerve in Charcot–Marie–Tooth disease type I patients: a prospective case–control study. *Eur. Radiol.* 2019;29(6):3241–3252.

143. Pridmore MD, et al. Initial findings in traumatic peripheral nerve injury and repair with diffusion tensor imaging. *Ann. Clin. Transl. Neurol.* 2021;8(2):332–347.

144. Farinas AF, Manzanera Esteve I V, Pollins AC, et al. Diffusion Tensor Tractography Visualizes Partial Nerve Laceration Severity as Early as 1 Week After Surgical Repair in a Rat Model Ex Vivo. *Mil. Med.* 2020;185(Supplement_1):35–41.

145. Bruno Francesco; Mariani, Silvia; Patriarca, Lucia; Palumbo, Pierpaolo; Natella, Raffaele; Ma, Liheng; Guglielmi, Giuseppe; Galzio, Renato; Splendiani,

Alessandra; Di Cesare, Ernesto; Masciocchi, Carlo; Barile, Antonio FA. Application of diffusion tensor imaging (DTI) and MR-tractography in the evaluation of peripheral nerve tumours: state of the art and review of the literature. 2019;90(5-S):68–76.

146. Oudeman J, Verhamme C, Engbersen MP, et al. Diffusion tensor MRI of the healthy brachial plexus. Gelderblom M, ed. *PLOS ONE*. 2018;13(5):e0196975.

147. Ho MJ, Manoliu A, Kuhn FP, et al. Evaluation of Reproducibility of Diffusion Tensor Imaging in the Brachial Plexus at 3.0 T. *Invest. Radiol.* 2017;52(8):482–487.

148. Vargas MI, Viallon M, Nguyen D, et al. Diffusion tensor imaging (DTI) and tractography of the brachial plexus: feasibility and initial experience in neoplastic conditions. *Neuroradiology*. 2010;52(3):237–245.

149. Tagliafico A, Calabrese M, Puntoni M, et al. Brachial plexus MR imaging: accuracy and reproducibility of DTI-derived measurements and fibre tractography at 3.0-T. *Eur. Radiol.* 2011;21(8):1764–1771.

150. Gasparotti R, Lodoli G, Meoded A, et al. Feasibility of diffusion tensor tractography of brachial plexus injuries at 1.5 T. *Invest. Radiol.* 2013;48(2):104–112.

151. Simon J, Lutsky K, Maltenfort M, et al. The Accuracy of the Scratch Collapse Test Performed by Blinded Examiners on Patients With Suspected Carpal Tunnel Syndrome Assessed by Electrodiagnostic Studies. *J. Hand Surg.* 2017:1–5.

152. D'Arcy CA. Does This Patient Have Carpal Tunnel Syndrome? *JAMA*. 2000;283(23):3110.

153. Sanders RJ, Hammond SL, Rao NM. Diagnosis of thoracic outlet syndrome. *J. Vasc. Surg.* 2007;46(3):601–604.

154. Lu Y-T, Deol AK, Sears ED. The Association Between Electrodiagnostic Severity and Treatment Recommendations for Carpal Tunnel Syndrome. *J. Hand Surg.* 2021;46(2):92–98.

155. Roll SC, Case-Smith J, Evans KD. Diagnostic Accuracy of Ultrasonography VS. Electromyography in Carpal Tunnel Syndrome: A Systematic Review of Literature. *Ultrasound Med. Biol.* 2011;37(10):1539–1553.

156. Graham B, Peljovich AE, Afra R, et al. The American Academy of Orthopaedic Surgeons Evidence-Based Clinical Practice Guideline on. *J. Bone Jt. Surg.* 2016;98(20):1750–1754.

157. Smith BW, Chang KWC, Yang LJS, et al. Comparative accuracies of electrodiagnostic and imaging studies in neonatal brachial plexus palsy. *J. Neurosurg. Pediatr.* 2019;23(1):119–124.

158. Mackenzie SP, Stone OD, Jenkins PJ, et al. Carpal tunnel decompression in patients with normal nerve conduction studies. *J. Hand Surg. Eur. Vol.* 2020;45(3):260–264.

159. Erickson M, Lawrence M, Lucado A. The role of diagnostic ultrasound in the examination of carpal tunnel syndrome: an update and systematic review. *J. Hand Ther.* 2021:S0894113021000612.

160. Fisse AL, Katsanos AH, Gold R, et al. Cross-sectional area reference values for peripheral nerve ultrasound in adults: a systematic review and meta-analysis—Part I: Upper extremity nerves. *Eur. J. Neurol.* 2021;28(5):1684–1691.

161. Torres-Costoso A, Martínez-Vizcaíno V, Álvarez-Bueno C, et al. Accuracy of Ultrasonography for the Diagnosis of Carpal Tunnel Syndrome: A Systematic Review and Meta-Analysis. *Arch. Phys. Med. Rehabil.* 2018;99(4):758-765.e10.

162. Anon. NIHR 2020 Investigation and Intervention Tariff 1.2.pdf.

163. Perumal AR, Anyamele UA, Bhogal RK, et al. Incidental findings associated with magnetic resonance imaging of the brachial plexus. *Br. J. Radiol.* 2021;94(1117):20200921.

164. Brogan DM, et al. Prevalence of rotator cuff tears in adults with traumatic brachial plexus injuries. *J. Bone Joint Surg. Am.* 2014;96(16):e139.

165. Nordmark PF, Pruszynski JA, Johansson RS. BOLD Responses to Tactile Stimuli in Visual and Auditory Cortex Depend on the Frequency Content of Stimulation. *J. Cogn. Neurosci.* 2012;24(10):2120–2134.

166. Makin TR, Scholz J, Henderson Slater D, et al. Reassessing cortical reorganization in the primary sensorimotor cortex following arm amputation. *Brain.* 2015;138(8):2140–2146.

167. Yu XJ, He HJ, Zhang QW, et al. Somatotopic reorganization of hand representation in bilateral arm amputees with or without special foot movement skill. *Brain Res.* 2014;1546:9–17.

168. Bruurmijn MLCM, Pereboom IPL, Vansteensel MJ, et al. Preservation of hand movement representation in the sensorimotor areas of amputees. *Brain.* 2017;140(12):3166–3178.

169. Serino A, Akselrod M, Salomon R, et al. Upper limb cortical maps in amputees with targeted muscle and sensory reinnervation. *Brain.* 2017;140(11):2993–3011.

170. Rae CD. A guide to the metabolic pathways and function of metabolites observed in human brain 1H magnetic resonance spectra. *Neurochem. Res.* 2014;39(1):1–36.

171. Stagg CJ. Magnetic Resonance Spectroscopy as a tool to study the role of GABA in motor-cortical plasticity. *NeuroImage.* 2014;86:19–27.

172. Kim HS, Yoon YC, Choi BO, et al. Muscle fat quantification using magnetic resonance imaging: case–control study of Charcot–Marie–Tooth disease patients and volunteers. *J. Cachexia Sarcopenia Muscle.* 2019;10(3):574–585.

173. Huang AE, Noland SS, Spinner RJ, et al. Outcomes of Reconstructive Surgery in Traumatic Brachial Plexus Injury with Concomitant Vascular Injury. *World Neurosurg.* 2020;135:e350–e357.

174. Wade RG, Itte V, Rankine JJ, et al. The diagnostic accuracy of 1.5T magnetic resonance imaging for detecting root avulsions in traumatic adult brachial plexus injuries. *J. Hand Surg. Eur. Vol.* 2018;43(3):250–258.

175. Stepansky F, Hecht EM, Rivera R, et al. Dynamic MR Angiography of Upper Extremity Vascular Disease: Pictorial Review. *RadioGraphics*. 2008;28(1):e28–e28.

176. Wade RG, Takwoingi Y, Wormald JCR, et al. Magnetic resonance imaging for detecting root avulsions in traumatic adult brachial plexus injuries: protocol for a systematic review of diagnostic accuracy. *Syst. Rev.* 2018;7(1):76.

177. McInnes MDF, Moher D, Thombs BD, et al. Preferred Reporting Items for a Systematic Review and Meta-analysis of Diagnostic Test Accuracy Studies. *JAMA*. 2018;319(4):388.

178. Sambasivan A, Pandit S. Bilateral Brachial Plexus Injury after a Hanging Suicide Attempt: A Case Report. *PM&R*. 2013;5(9):S187.

179. Anwar F, McLaughlin D. Bilateral brachial plexus injury. *J. Coll. Physicians Surg. Pak.* 2012;22(3):176–178.

180. Dubuisson AS, Kline DG. Brachial plexus injury: A survey of 100 consecutive cases from a single service. *Neurosurgery*. 2002;51(3):673–683.

181. Hems TEJ, Birch R, Carlstedt T. The Role of Magnetic Resonance Imaging in the Management of Traction Injuries to the Adult Brachial Plexus. *J. Hand Surg.* 1999;24(5):550–555.

182. Whiting P, Rutjes AWS, Reitsma JB, et al. The development of QUADAS: a tool for the quality assessment of studies of diagnostic accuracy included in systematic reviews. *BMC Med. Res. Methodol.* 2003;3:25.

183. Chu H, Cole SR. Bivariate meta-analysis of sensitivity and specificity with sparse data: a generalized linear mixed model approach. *J. Clin. Epidemiol.* 2006;59(12):1331–1332.

184. Reitsma JB, Glas AS, Rutjes AWS, et al. Bivariate analysis of sensitivity and specificity produces informative summary measures in diagnostic reviews. *J. Clin. Epidemiol.* 2005;58(10):982–990.

185. Collaboration TC. The Cochrane Handbook for Diagnostic Test Accuracy Reviews. 2016. Available at: http://methods.cochrane.org/sdt/handbook-dta-reviews.

186. Deeks JJ, Macaskill P, Irwig L. The performance of tests of publication bias and other sample size effects in systematic reviews of diagnostic test accuracy was assessed. *J. Clin. Epidemiol.* 2005;58(9):882–893.

187. Upadhyaya V, Upadhyaya DN, Kumar A, et al. MR neurography in traumatic brachial plexopathy. *Eur. J. Radiol.* 2015;84(5):927–932.

188. Ning D, Sun M, Sun B, et al. Magnetic resonance imaging with three-dimensional fast imaging employing steady-state acquisition with phase-cycled and short T1 inversion recovery pulse sequence for evaluating brachial plexus injury. *Neural Regen. Res.* 2011;6(14):1097–1102.

189. Penkert G, Carvalho G, Nikkhah G, et al. Diagnosis and Surgery of Brachial Plexus Injuries. *J. Reconstr. Microsurg.* 1999;15(01):3–8.

190. Gerevini S, Mandelli C, Cadioli M, et al. Diagnostic value and surgical implications of the magnetic resonance imaging in the management of adult patients with brachial plexus pathologies. *Surg. Radiol. Anat.* 2008;30(2):91–101.

191. Carvalho GA, Nikkhah G, Matthies C, et al. Diagnosis of root avulsions in traumatic brachial plexus injuries: value of computerized tomography myelography and magnetic resonance imaging. *J. Neurosurg.* 1997;86(1):69–76.

192. Schmidt T, Kretschmer T, Heinen C, et al. Clinical Application of Diffusion Tensor Tractography (DTT) of Traumatic Brachial Plexus Injuries: Oral Presentations, 2011 AANS Meeting, Denver, Colorado, April 9-13, 2011. *J. Neurosurg.* 2011;115(2):A402–A452.

193. Disawal A, Taori K, Rathod J. Role of newer MR imaging techniques in traumatic brachial plexopathies - Our experience. *J. Med. Imaging Radiat. Oncol.* 2012;56:40.

194. Caporrino FA, Moreira L, Moraes VY, et al. Brachial Plexus Injuries: Diagnosis Performance and Reliability of Everday Tools. *Hand Surg.* 2014;19(01):7–11.

195. Veronesi BA, Rodrigues MB, Sambuy MTC De, et al. Use of magnetic resonance imaging to diagnose brachial plexus injuries. *Acta Ortopédica Bras.* 2018;26(2):131–134.

196. Abul-Kasim K, Backman C, Björkman A, et al. Advanced radiological work-up as an adjunct to decision in early reconstructive surgery in brachial plexus injuries. *J. Brachial Plex. Peripher. Nerve Inj.* 2014;05(01):e75–e81.

197. Chanlalit C, Vipulakorn K, Jiraruttanapochai K, et al. Value of clinical findings, electrodiagnosis and magnetic resonance imaging in the diagnosis of root lesions in traumatic brachial plexus injuries. *J. Med. Assoc. Thai.* 2005;88(1):66–70.

198. Doi K, Otsuka K, Okamoto Y, et al. Cervical nerve root avulsion in brachial plexus injuries: magnetic resonance imaging classification and comparison with myelography and computerized tomography myelography. *J. Neurosurg. Spine*. 2002;96(3):277–284.

199. Hayashi N, Yamamoto S, Okubo T, et al. Avulsion injury of cervical nerve roots: enhanced intradural nerve roots at MR imaging. *Radiology*. 1998;206(3):817–822.

200. Qin B-G, Yang J-T, Yang Y, et al. Diagnostic Value and Surgical Implications of the 3D DW-SSFP MRI On the Management of Patients with Brachial Plexus Injuries. *Sci. Rep.* 2016;6(1):35999.

201. Gasparotti R, Ferraresi S, Pinelli L, et al. Three-dimensional MR myelography of traumatic injuries of the brachial plexus. *AJNR Am. J. Neuroradiol.* 1997;18(9):1733–42.

202. Nakamura T, Yabe Y, Horiuchi Y, et al. Magnetic Resonance Myelography in Brachial Plexus Injury. *J. Bone Jt. Surg.* 1997;79(5):764–769.

203. Yang J, Qin B, Fu G, et al. Modified Pathological Classification of Brachial Plexus Root Injury and Its MR Imaging Characteristics. *J. Reconstr. Microsurg.* 2013;30(03):171–178.

204. Rutjes AWS. Evidence of bias and variation in diagnostic accuracy studies. *Can. Med. Assoc. J.* 2006;174(4):469–476.

205. Whiting PF, Rutjes AWS, Westwood ME, et al. A systematic review classifies sources of bias and variation in diagnostic test accuracy studies. *J. Clin. Epidemiol.* 2013;66(10):1093–1104.

206. Di Girolamo N, Winter A, Meursinge Reynders R. High and unclear risk of bias assessments are predominant in diagnostic accuracy studies included in Cochrane reviews. *J. Clin. Epidemiol.* 2018;101:73–78.

207. Leeflang MMG, Rutjes AWS, Reitsma JB, et al. Variation of a test's sensitivity and specificity with disease prevalence. *Can. Med. Assoc. J.* 2013;185(11):E537–E544.

208. Jivan S, Novikova LN, Wiberg M, et al. The effects of delayed nerve repair on neuronal survival and axonal regeneration after seventh cervical spinal nerve axotomy in adult rats. *Exp. Brain Res.* 2006;170(2):245–254.

209. Wade RG, Bland JM, Wormald JCR, et al. The importance of the unit of analysis. *J. Plast. Reconstr. Aesthet. Surg.* 2016;69(9):1299–1300.

210. Sauerland S, Lefering R, Bayer-Sandow T, et al. Fingers, Hands or Patients? the Concept of Independent Observations. *J. Hand Surg.* 2003;28(2):102–105.

211. Naaktgeboren CA, Bertens LCM, van Smeden M, et al. Value of composite reference standards in diagnostic research. *BMJ.* 2013;347:f5605.

212. Fuzari HKB, Dornelas de Andrade A, Vilar CF, et al. Diagnostic accuracy of magnetic resonance imaging in post-traumatic brachial plexus injuries: A systematic review. *Clin. Neurol. Neurosurg.* 2018;164(November 2017):5–10.

213. Ochodo EA, Hooft L, Bossuyt PM, et al. Misreporting of Diagnostic Accuracy Studies : Evidence. *Radiology.* 2013;267(2):581–588.

214. Vavasour IM, Meyers SM, Mädler B, et al. Multicenter Measurements of T 1 Relaxation and Diffusion Tensor Imaging: Intra and Intersite Reproducibility. *J. Neuroimaging.* 2019;29(1):42–51.

215. Prohl AK, Scherrer B, Tomas-Fernandez X, et al. Reproducibility of Structural and Diffusion Tensor Imaging in the TACERN Multi-Center Study. *Front. Integr. Neurosci.* 2019;13(July):1–15.

216. Kimura M, Yabuuchi H, Matsumoto R, et al. The reproducibility of measurements using a standardization phantom for the evaluation of fractional anisotropy (FA) derived from diffusion tensor imaging (DTI). *Magn. Reson. Mater. Phys. Biol. Med.* 2019:15–19.

217. Cai LY, Yang Q, Kanakaraj P, et al. MASiVar: Multisite, multiscanner, and multisubject acquisitions for studying variability in diffusion weighted MRI. *Magn. Reson. Med.* 2021;86(6):3304–3320.

218. Bossuyt PM, Reitsma JB, Bruns DE, et al. STARD 2015: an updated list of essential items for reporting diagnostic accuracy studies. *BMJ.* 2015;277(3):h5527.

219. McGrath TA, Alabousi M, Skidmore B, et al. Recommendations for reporting of systematic reviews and meta-analyses of diagnostic test accuracy: a systematic review. *Syst. Rev.* 2017;6(1):194.

220. Chung AW, Thomas DL, Ordidge RJ, et al. Diffusion tensor parameters and principal eigenvector coherence: Relation to b-value intervals and field strength. *Magn. Reson. Imaging.* 2013;31(5):742–747.

221. Oudeman J, Verhamme C, MP E, et al. Diffusion tensor MRI of the healthy brachial plexus. *PloS One.* 2018;13(5):e0196975.

222. Tagliafico A. Brachial plexus assessment with three- dimensional isotropic resolution fast spin echo MRI : Comparison with conventional MRI at 3 . 0 Brachial plexus assessment with three-dimensional isotropic resolution fast spin echo MRI : comparison with conventional. 2011;(November 2015):0–7.

223. MJ H, Manoliu A, FP K, et al. Evaluation of Reproducibility of Diffusion Tensor Imaging in the Brachial Plexus at 3.0 T. *Invest. Radiol.* 2017;52(8):482–487.

224. Zhang J, Jones M, DeBoy CA, et al. Diffusion tensor magnetic resonance imaging of Wallerian degeneration in rat spinal cord after dorsal root axotomy. *J. Neurosci. Off. J. Soc. Neurosci.* 2009;29(10):3160–71.

225. Cohen-Adad J, Leblond H, Delivet-Mongrain H, et al. Wallerian degeneration after spinal cord lesions in cats detected with diffusion tensor imaging. *NeuroImage.* 2011;57(3):1068–1076.

226. Zhao C, Rao J-S, Pei X-J, et al. Diffusion tensor imaging of spinal cord parenchyma lesion in rat with chronic spinal cord injury. *Magn. Reson. Imaging.* 2018;47(August 2017):25–32.

227. Brennan FH, Cowin GJ, Kurniawan ND, et al. Longitudinal assessment of white matter pathology in the injured mouse spinal cord through ultra-high field (16.4T) in vivo diffusion tensor imaging. *NeuroImage.* 2013;82:574–585.

228. Yu C, Zhu C, Zhang Y, et al. A longitudinal diffusion tensor imaging study on Wallerian degeneration of corticospinal tract after motor pathway stroke. *NeuroImage.* 2009;47(2):451–458.

229. Puig J, Pedraza S, Blasco G, et al. Wallerian Degeneration in the Corticospinal Tract Evaluated by Diffusion Tensor Imaging Correlates with Motor Deficit 30 Days after Middle Cerebral Artery Ischemic Stroke. *Am. J. Neuroradiol.* 2010;31(7):1324–1330.

230. Ma C, Liu A, Li Z, et al. Longitudinal study of diffusion tensor imaging properties of affected cortical spinal tracts in acute and chronic hemorrhagic stroke. *J. Clin. Neurosci.* 2014;21(8):1388–1392.

231. Kim H-J, Moon W-J. Prolonged Wallerian degeneration in the corticospinal tract following external capsular hemorrhage. *J. Neurol. Sci.* 2016;365:154–155.

232. Zeestraten EA, Benjamin P, Lambert C, et al. Application of Diffusion Tensor Imaging Parameters to Detect Change in Longitudinal Studies in Cerebral Small Vessel Disease. Boltze J, ed. *PLOS ONE.* 2016;11(1):e0147836.

233. Schilling KG, Rheault F, Petit L, et al. Tractography dissection variability: What happens when 42 groups dissect 14 white matter bundles on the same dataset? *NeuroImage*. 2021;243(November 2020):118502.

234. Schilling KG, Daducci A, Maier-Hein K, et al. Challenges in diffusion MRI tractography – Lessons learned from international benchmark competitions. *Magn. Reson. Imaging*. 2019;57(October 2018):194–209.

235. Schilling KG, Nath V, Hansen C, et al. Limits to anatomical accuracy of diffusion tractography using modern approaches. *NeuroImage*. 2019;185(August 2018):1–11.

236. Parizel PM, Van Rompaey V, Van Loock R, et al. Influence of user-defined parameters on diffusion tensor tractography of the corticospinal tract. *Neuroradiol. J.* 2007;20(2):139–147.

237. Xiang J-P, Liu X-L, Xu Y-B, et al. Microsurgical anatomy of dorsal root entry zone of brachial plexus. *Microsurgery*. 2008;28(1):17–20.

238. Zhong L yuan, Wang A ping, Hong L, et al. Microanatomy of the brachial plexus roots and its clinical significance. *Surg. Radiol. Anat.* 2017;39(6):601–610.

239. Vargas MI, Viallon M, Nguyen D, et al. Diffusion tensor imaging (DTI) and tractography of the brachial plexus: feasibility and initial experience in neoplastic conditions. *Neuroradiology*. 2010;52(3):237–245.

240. Tagliafico Massimo; Puntoni, Matteo; Pace, Daniele; Baio, Gabriella; Neumaier, Carlo Emanuele; Martinoli, Carlo AC. Brachial plexus MR imaging: accuracy and reproducibility of DTI-derived measurements and fibre tractography at 3.0-T. 2011;21(8):1764–1771.

241. Gasparotti Giovanni; Meoded, Avner; Carletti, Francesco; Garozzo, Debora; Ferraresi, Stefano RL. Feasibility of diffusion tensor tractography of brachial plexus injuries at 1.5 T. 2013;48(2):104–112.

242. Oudeman J, Verhamme C, Engbersen MP, et al. Diffusion tensor MRI of the healthy brachial plexus. Gelderblom M, ed. *PLOS ONE*. 2018;13(5):e0196975.

243. Wade RG, Tanner SF, Teh I, et al. Diffusion Tensor Imaging for Diagnosing Root Avulsions in Traumatic Adult Brachial Plexus Injuries: A Proof-of-Concept Study. *Front. Surg.* 2020;7:Article 19.

244. Yeh F-C, Panesar S, Barrios J, et al. Automatic Removal of False Connections in Diffusion MRI Tractography Using Topology-Informed Pruning (TIP). *Neurotherapeutics*. 2019;16(1):52–58.

245. X. S, X. K, D. L, et al. Multimodal magnetic resonance imaging of peripheral nerves: Establishment and validation of brachial and lumbosacral plexi measurements in 163 healthy subjects. *Eur. J. Radiol.* 2019;117:41–48.

246. Haakma W, Pedersen M, Froeling M, et al. Diffusion tensor imaging of peripheral nerves in non-fixed post-mortem subjects. *Forensic Sci. Int.* 2016;263:139–146.

247. Higgins JPT, Green S (editors). Cochrane Handbook for Systematic Reviews of Interventions Version 5.1.0 [updated March 2011]. *Cochrane Collab.* 2011.

248. Moher D, Liberati A, Tetzlaff J, et al. Systematic Reviews and Meta-Analyses: The PRISMA Statement. *Annu. Intern. Med.* 2009;151(4):264–269.

249. Sterne JA, Hernán MA, Reeves BC, et al. ROBINS-I: a tool for assessing risk of bias in non-randomised studies of interventions. *BMJ.* 2016;355:i4919.

250. McGuinness LA, Higgins JPT. Risk-of-bias VISualization (robvis): An R package and Shiny web app for visualizing risk-of-bias assessments. *Res. Synth. Methods.* 2020;(February):jrsm.1411.

251. Ho MJ, Ciritsis A, Manoliu A, et al. Diffusion Tensor Imaging of the Brachial Plexus: A Comparison between Readout-segmented and Conventional Single-shot Echo-planar Imaging. *Magn. Reson. Med. Sci.* 2019;18(2):150–157.

252. Ho MJ, Manoliu A, Kuhn FP, et al. Evaluation of Reproducibility of Diffusion Tensor Imaging in the Brachial Plexus at 3.0 T. *Invest. Radiol.* 2017;52(8):482–487.

253. Chen M, Li X, Chen J, et al. Quantitative analysis of the normal brachial plexus with diffusion tensor imaging. *Chin. J. Med. Imaging Technol.* 2012;28(1):77–81.

254. Su X, Kong X, Liu D, et al. Multimodal magnetic resonance imaging of peripheral nerves: Establishment and validation of brachial and lumbosacral plexi measurements in 163 healthy subjects. *Eur. J. Radiol.* 2019;117(February):41–48.

255. Wade RG, Teh I, Andersson G, et al. Diffusion Tensor Imaging of the Brachial Plexus: Defining the Fractional Anisotropy Threshold for Deterministic Tractography of the Roots. *FigShare Prepr.* 2020.

256. Samardzic M, Rasulic L, Grujicic D, et al. Nerve transfers using collateral branches of the brachial plexus as donors in patients with upper palsy-thirty years' experience. *Acta Neurochir. (Wien).* 2011;153(10):2009–2019.

257. Tagliafico A, Calabrese M, Puntoni M, et al. Brachial plexus MR imaging: accuracy and reproducibility of DTI-derived measurements and fibre tractography at 3.0-T. *Eur. Radiol.* 2011;21(8):1764–1771.

258. Yap QJ, Teh I, Fusar-Poli P, et al. Tracking cerebral white matter changes across the lifespan: insights from diffusion tensor imaging studies. *J. Neural Transm.* 2013;120(9):1369–1395.

259. Aboitiz F, Scheibel AB, Fisher RS, et al. Fiber composition of the human corpus callosum. *Brain Res.* 1992;598:143–153.

260. Yokoyama I. [Study on the intraneural topography of the brachial plexus]. *Nihon Seikeigeka Gakkai Zasshi*. 1989;63(9):1085–1102.

261. Helmer KG, Chou M-C, Preciado RI, et al. Multi-site study of diffusion metric variability: effects of site, vendor, field strength, and echo time on regions-of-interest and histogram-bin analyses. In: Gimi B, Krol A, eds. *Physiology & Behavior*.Vol 176.; 2016:97882U.

262. Schilling KG, Nath V, Blaber J, et al. Effects of b-value and number of gradient directions on diffusion MRI measures obtained with Q-ball imaging. Styner MA, Angelini ED, eds. *Proc SPIE Int Soc Opt Eng.* 2017:101330N.

263. Qin W, Shui Yu C, Zhang F, et al. Effects of echo time on diffusion quantification of brain white matter at 1.5T and 3.0T. *Magn. Reson. Med.* 2009;61(4):755–760.

264. Giannelli M, Cosottini M, Michelassi MC, et al. Dependence of brain DTI maps of fractional anisotropy and mean diffusivity on the number of diffusion weighting directions. *J. Appl. Clin. Med. Phys.* 2010;11(1):176–190.

265. Taylor PA, Alhamud A, van der Kouwe A, et al. Assessing the performance of different DTI motion correction strategies in the presence of EPI distortion correction. *Hum. Brain Mapp.* 2016;37(12):4405–4424.

266. Haddad SMH, Scott CJM, Ozzoude M, et al. Comparison of quality control methods for automated diffusion tensor imaging analysis pipelines. Yap P-T, ed. *PLOS ONE.* 2019;14(12):e0226715.

267. Vos SB, Jones DK, Viergever MA, et al. Partial volume effect as a hidden covariate in DTI analyses. *NeuroImage.* 2011;55(4):1566–1576.

268. Le Bihan D, Mangin J-F, Poupon C, et al. Diffusion tensor imaging: Concepts and applications. *J. Magn. Reson. Imaging.* 2001;13(4):534–546.

269. Watanabe M, Sakai O, Ozonoff A, et al. Age-related Apparent Diffusion Coefficient Changes in the Normal Brain. *Radiology.* 2013;266(2):575–582.

270. Kronlage M, Schwehr V, Schwarz D, et al. Peripheral nerve diffusion tensor imaging (DTI): normal values and demographic determinants in a cohort of 60 healthy individuals. *Eur. Radiol.* 2018;28(5):1801–1808.

271. Tagliafico A, Calabrese M, Puntoni M, et al. Brachial plexus MR imaging: accuracy and reproducibility of DTI-derived measurements and fibre tractography at 3.0-T. *Eur. Radiol.* 2011;21(8):1764–1771.

272. Ho MJ, Ciritsis A, Manoliu A, et al. Diffusion Tensor Imaging of the Brachial Plexus: A Comparison between Readout-segmented and Conventional Single-shot Echo-planar Imaging. *Magn. Reson. Med. Sci.* 2019;18(2):150–157.

273. Maier-Hein KH, Neher PF, Houde J-C, et al. The challenge of mapping the human connectome based on diffusion tractography. *Nat. Commun.* 2017;8(1):1349.

274. Yeh F-C, Verstynen TD, Wang Y, et al. Deterministic Diffusion Fiber Tracking Improved by Quantitative Anisotropy. Zhan W, ed. *PLoS ONE.* 2013;8(11):e80713.

275. Wade RG, Bligh ER, Nar K, et al. The Geometry of the roots of the Brachial Plexus. *J. Anat.* 2020:joa.13270.

276. Won SJ, Kim B-J, Park KS, et al. Measurement of cross-sectional area of cervical roots and brachial plexus trunks. *Muscle Nerve.* 2012;46(5):711–716.

277. Saliani A, Perraud B, Duval T, et al. Axon and Myelin Morphology in Animal and Human Spinal Cord. *Front. Neuroanat.* 2017;11:1–31.

278. Firmin L, Field P, Maier MA, et al. Axon diameters and conduction velocities in the macaque pyramidal tract. *J. Neurophysiol.* 2014;112(6):1229–1240.

279. Chen Z, Zhang J, Chen T, et al. Study of Sensory and Motor Fascicles in Brachial Plexus and Establishment of a Digital Three-Dimensional Graphic Model. *Ann. Plast. Surg.* 2011;67(6):615–619.

280. Seo Y. Effects of different field strengths, gradient directions, and acquisitions on fractional anisotropy in diffusion tensor imaging: A tract-based spatial statistics study. *Concepts Magn. Reson. Part B Magn. Reson. Eng.* 2013;43B(1):41–48.

281. Pujol S, Wells W, Pierpaoli C, et al. The DTI Challenge: Toward Standardized Evaluation of Diffusion Tensor Imaging Tractography for Neurosurgery. *J. Neuroimaging.* 2015;25(6):875–882.

282. Giraudo C, Motyka S, Weber M, et al. Diffusion Tensor Imaging of Healthy Skeletal Muscles. *Invest. Radiol.* 2019;54(1):48–54.

283. Domin M, Langner S, Hosten N, et al. Comparison of Parameter Threshold Combinations for Diffusion Tensor Tractography in Chronic Stroke Patients and Healthy Subjects. Baron J-C, ed. *PLoS ONE.* 2014;9(5):e98211.

284. Taoka T, Morikawa M, Akashi T, et al. Fractional Anisotropy–Threshold Dependence in Tract-Based Diffusion Tensor Analysis: Evaluation of the Uncinate Fasciculus in Alzheimer Disease. *Am. J. Neuroradiol.* 2009;30(9):1700–1703.

285. Melhem ER, Mori S, Mukundan G, et al. Diffusion Tensor MR Imaging of the Brain and White Matter Tractography. *Am. J. Roentgenol.* 2002;178(1):3–16.

286. Esteban O, Daducci A, Caruyer E, et al. Simulation-based evaluation of susceptibility distortion correction methods in diffusion MRI for connectivity analysis. In: *2014 IEEE 11th International Symposium on Biomedical Imaging (ISBI).*Vol 582. IEEE; 2014:738–741.

287. Carp J. On the Plurality of (Methodological) Worlds: Estimating the Analytic Flexibility of fMRI Experiments. *Front. Neurosci.* 2012;6.

288. Graham MS, Drobnjak I, Jenkinson M, et al. Quantitative assessment of the susceptibility artefact and its interaction with motion in diffusion MRI. Yap P-T, ed. *PLOS ONE.* 2017;12(10):e0185647.

289. Esteban O, Daducci A, Caruyer E, et al. Simulation-based evaluation of susceptibility distortion correction methods in diffusion MRI for connectivity analysis. In: *2014 IEEE 11th International Symposium on Biomedical Imaging (ISBI).* IEEE; 2014:738–741.

290. Brun L, Pron A, Sein J, et al. Diffusion MRI: Assessment of the Impact of Acquisition and Preprocessing Methods Using the BrainVISA-Diffuse Toolbox. *Front. Neurosci.* 2019;13.

291. Schilling KG, Blaber J, Hansen C, et al. Distortion correction of diffusion weighted MRI without reverse phase-encoding scans or field-maps. Yap P-T, ed. *PLOS ONE.* 2020;15(7):e0236418.

292. Voss HU, Watts R, Uluğ AM, et al. Fiber tracking in the cervical spine and inferior brain regions with reversed gradient diffusion tensor imaging. *Magn. Reson. Imaging.* 2006;24(3):231–239.

293. Hedouin R, Commowick O, Bannier E, et al. Block-Matching Distortion Correction of Echo-Planar Images With Opposite Phase Encoding Directions. *IEEE Trans. Med. Imaging.* 2017;36(5):1106–1115.

294. Irfanoglu MO, Sarlls J, Nayak A, et al. Evaluating corrections for Eddy-currents and other EPI distortions in diffusion MRI: methodology and a dataset for benchmarking. *Magn. Reson. Med.* 2018;(March):1–14.

295. Yeh F. DSI Studio is an integrated tractography software tool that maps brain connections and correlates findings with brain disorders. It is a collective implementation of several diffusion MRI methods and deterministic fiber tracking. 2021.

296. Holland D, Kuperman JM, Dale AM. Efficient correction of inhomogeneous static magnetic field-induced distortion in Echo Planar Imaging. *NeuroImage.* 2010;50(1):175–183.

297. Ruthotto L, Mohammadi S, Heck C, et al. Hyperelastic Susceptibility Artifact Correction of DTI in SPM. In: ; 2013:344–349.

298. Li X, Morgan PS, Ashburner J, et al. The first step for neuroimaging data analysis: DICOM to NIfTI conversion. *J. Neurosci. Methods.* 2016;264:47–56.

299. NEMA. NEMA Standards Publication MS 1-2001: Determination of Signal-to-Noise Ratio (SNR) in Diagnostic Magnetic Resonance Imaging. *Natl. Electr. Manuf. Assoc.* 2014;2008:21.

300. Yeh F-C. Shape analysis of the human association pathways. *NeuroImage.* 2020;223:117329.

301. Anon. Sherbrooke Connectivity Imaging Lab (SCIL) toolbox. 2021. Available at: https://github.com/scilus/scilpy.

302. Cousineau M, Jodoin P-M, Garyfallidis E, et al. A test-retest study on Parkinson's PPMI dataset yields statistically significant white matter fascicles. *NeuroImage Clin.* 2017;16:222–233.

303. Rheault F, Bayrak RG, Wang X, et al. TractEM: Evaluation of protocols for deterministic tractography white matter atlas. *Magn. Reson. Imaging.* 2022;85(April 2021):44–56.

304. Chan RW, von Deuster C, Giese D, et al. Characterization and correction of eddy-current artifacts in unipolar and bipolar diffusion sequences using magnetic field monitoring. *J. Magn. Reson.* 2014;244:74–84.

305. Caruyer E, Lenglet C, Sapiro G, et al. Design of multishell sampling schemes with uniform coverage in diffusion MRI. *Magn. Reson. Med.* 2013;69(6):1534–1540.

306. Yeh F-C, Liu L, Hitchens TK, et al. Mapping immune cell infiltration using restricted diffusion MRI. *Magn. Reson. Med.* 2017;77(2):603–612.

307. Jeurissen B, Leemans A, Tournier JD, et al. Investigating the prevalence of complex fiber configurations in white matter tissue with diffusion magnetic resonance imaging. *Hum. Brain Mapp.* 2013;34(11):2747–2766.

308. Foesleitner O, Sulaj A, Sturm V, et al. Diffusion MRI in Peripheral Nerves: Optimized b Values and the Role of Non-Gaussian Diffusion. *Radiology*. 2022;302(1):153–161.

309. Wade RG, Whittam A, Teh I, et al. Diffusion tensor imaging of the roots of the brachial plexus : a systematic review and meta - analysis of normative values. *Clin. Transl. Imaging*. 2020;(0123456789).

310. Assaf Y, Blumenfeld-Katzir T, Yovel Y, et al. Axcaliber: A method for measuring axon diameter distribution from diffusion MRI. *Magn. Reson. Med.* 2008;59(6):1347–1354.

Part 4. Appendices

Systematic Reviews

Open Access

Magnetic resonance imaging for detecting root avulsions in traumatic adult brachial plexus injuries: protocol for a systematic review of diagnostic accuracy

CrossMark

Ryckie G. Wade[1,2*], Yemisi Takwoingi[3], Justin C. R. Wormald[4,5], John P. Ridgway[7], Steven Tanner[7], James J. Rankine[6,7] and Grainne Bourke[1,2]

Abstract

Background: Adult brachial plexus injuries (BPI) are becoming more common. The reconstruction and prognosis of pre-ganglionic injuries (root avulsions) are different to other types of BPI injury. Preoperative magnetic resonance imaging (MRI) is being used to identify root avulsions, but the evidence from studies of its diagnostic accuracy are conflicting. Therefore, a systematic review is needed to address uncertainty about the accuracy of MRI and to guide future research.

Methods: We will conduct a systematic search of electronic databases alongside reference tracking. We will include studies of adults with traumatic BPI which report the accuracy of preoperative MRI (index test) against surgical exploration of the roots of the brachial plexus (reference standard) for detecting either of the two target conditions (any root avulsion or any pseudomeningocoele as a surrogate marker of root avulsion). We will exclude case reports, articles considering bilateral injuries and studies where the number of true positives, false positives, false negatives and true negatives cannot be derived. The methodological quality of the included studies will be assessed using a tailored version of the QUADAS-2 tool. Where possible, a bivariate model will be used for meta-analysis to obtain summary sensitivities and specificities for both target conditions. We will investigate heterogeneity in the performance of MRI according to field strength and the risk of bias if data permits.

Discussion: This review will summarise the current diagnostic accuracy of MRI for adult BPI, identify shortcomings and gaps in the literature and so help to guide future research.

Systematic review registration: PROSPERO CRD42016049702.

Keywords: Review, Diagnostic test accuracy, Root avulsion, Pre-ganglionic, Brachial plexus, Magnetic resonance imaging, Sensitivity, Specificity

Background

Traumatic brachial plexus injuries (BPI) in adults are common following road traffic collisions. In England, there are 48,000 cases of major trauma per annum [1] and 1% have a brachial plexus injury [2]. Such injuries can result in permanent disability [3–7], pain [8, 9],

psychological morbidity [10, 11] and reduced quality of life [3, 5, 12]. With optimal reconstructive surgery, patients can recover useful function [3, 4, 12, 13] which is associated with improved quality of life [5].

To date, magnetic resonance imaging (MRI) is the best indicator of various pathologies affecting the brachial plexus [14], and in the context of trauma it is superior to pre-operative nerve conduction studies [15], high-resolution ultrasonography [16–18] and intraoperative somatosensory-evoked potentials [19]. However, MRI is still unable to differentiate nerve injuries which need

* Correspondence: ryckiewade@gmail.com
[1]Department of Plastic and Reconstructive Surgery, Leeds Teaching Hospitals Trust, Leeds, UK
[2]Faculty of Medicine and Health Sciences, University of Leeds, Leeds, UK
Full list of author information is available at the end of the article

Radiology

MRI for Detecting Root Avulsions in Traumatic Adult Brachial Plexus Injuries: A Systematic Review and Meta-Analysis of Diagnostic Accuracy

Ryckie G. Wade, MBBS, MSc, MClinEd, MRCS, FHEA • *Yemisi Takwoingi, DVM, MSc, PhD* •
Justin C. R. Wormald, MBBS, MRes, MRCS • *John P. Ridgway, BSc, MSc, PhD* • *Steven Tanner, BSc, MSc, PhD* •
James J. Rankine, MBChB, MRCP, MRad, FRCR, MD • *Grainne Bourke, MB, BCh, BAO, FRCSI, FRCS(Plast)*

From the Department of Plastic and Reconstructive Surgery, Academic Plastic Surgery Office (R.G.W., G.B.), Department of Medical Physics and Engineering (J.P.R., S.T.), and Department of Musculoskeletal Radiology (J.J.R.), Leeds Teaching Hospitals Trust, Leeds General Infirmary, Leeds LS1 3EX, England; Faculty of Medicine and Health Sciences, University of Leeds, Leeds, England (R.G.W., G.B.); Institute of Applied Health Research, University of Birmingham, Birmingham, England (Y.T.); Nuffield Department of Orthopaedics, Rheumatology and Musculoskeletal Sciences, University of Oxford, Oxford, England (J.C.R.W.); Department of Plastic and Reconstructive Surgery, Stoke Mandeville Hospital, Buckinghamshire Healthcare NHS Trust, Aylesbury, England (J.C.R.W.); and National Institute for Health Research Leeds Biomedical Research Centre, Leeds, England (J.P.R., S.T., J.J.R.). Received January 30, 2019; revision requested April 15; final revision received May 24; accepted June 17. **Address correspondence to** R.G.W. (e-mail: *ryckiewade@gmail.com*).

R.G.W. is supported by the National Institute for Health Research (NIHR) through a doctoral research fellowship award (DRF-2018-11-ST1-159) in Leeds. Y.T. is supported by the NIHR through a postdoctoral fellowship award (PDF-2017-10-059) and the NIHR Birmingham Biomedical Research Centre. The views expressed in this publication are those of the author(s) and not necessarily those of the National Health Service, the NIHR, or the Department of Health and Social Care.

Conflicts of interest are listed at the end of this article.

Background: Traumatic brachial plexus injuries affect 1% of patients involved in major trauma. MRI is the best test for traumatic brachial plexus injuries, although its ability to differentiate root avulsions (which require urgent reconstructive surgery) from other types of nerve injury remains unknown.

Purpose: To evaluate the accuracy of MRI for diagnosing root avulsions in adults with traumatic brachial plexus injuries.

Materials and Methods: For this systematic review, MEDLINE and Embase were searched from inception to August 20, 2018. Studies of adults with traumatic nonpenetrating unilateral brachial plexus injuries were included. The target condition was root avulsion. The index test was preoperative MRI, and the reference standard was surgical exploration. A bivariate meta-analysis was used to estimate summary sensitivities and specificities of MRI for avulsion.

Results: Eleven studies of 275 adults (mean age, 27 years; 229 men) performed between 1992 and 2016 were included. Most participants had been injured in motorcycle collisions (84%). All studies were at risk of bias, and there were high applicability concerns for the index test (ie, MRI) in four studies given the lack of diagnostic criteria, inadequate descriptions of pulse sequences, and multiplicity of reporting radiologists. Overall, 72% of patients with brachial plexus injuries had at least one root avulsion (interquartile range [IQR]: 53%–86%); meta-analysis of patient-level data was not performed because of sparse and heterogeneous data. With the nerve root as the unit of analysis, 583 of 918 roots were avulsed (median, 55%; IQR: 38%–71%); the mean sensitivity of MRI for root avulsion was 93% (95% confidence interval [CI]: 77%, 98%) with a mean specificity of 72% (95% CI: 42%, 90%).

Conclusion: On the basis of limited data, MRI offers modest diagnostic accuracy for traumatic brachial plexus root avulsion(s), and early surgical exploration should remain as the preferred method of diagnosis.

Published under a CC BY 4.0 license.

Online supplemental material is available for this article.

Traumatic brachial plexus injuries affect 1% of patients involved in major trauma (1). Brachial plexus injuries may cause permanent disability (2–6), pain (6–8), psychologic morbidity (9,10), and reduced quality of life (2,4,11). Early reconstructive nerve surgery is associated with better functional recovery in the upper limb (2,3,11,12), which improves quality of life (4).

Nerve reconstruction for patients with root avulsion(s) is a clinical priority for several reasons. After root avulsion, the cell bodies of motor neurons in the spinal cord recede (4,5,12,13), so the limb never reanimates spontaneously. Because reimplantation of avulsed roots yields no meaningful recovery (14–16), nerve transfers are performed, which significantly improves function (11,17–20). Nerve transfers are relatively minor and cost-effective procedures (21,22) with low morbidity (20,23–25). Furthermore, 95% of patients with traumatic brachial plexus injuries have neuropathic pain (6), and the evolving evidence suggests that early reconstructive nerve surgery reduces cortical reorganization and thus neuropathic or phantom limb pain (26–28). Therefore, correctly identifying patients with root avulsions is of paramount importance.

MRI is the best noninvasive test for brachial plexus injuries (29). MRI is superior to nerve and muscle electrophysiology studies (30), US (31–34), and intraoperative somatosensory-evoked potentials (35). Currently, MRI

Appendix 3. Title page for https://doi.org/10.3389/fsurg.2020.00019

Diffusion Tensor Imaging for Diagnosing Root Avulsions in Traumatic Adult Brachial Plexus Injuries: A Proof-of-Concept Study

Ryckie G. Wade [1,2*], Steven F. Tanner [3,4], Irvin Teh [5], John P. Ridgway [3,4], David Shelley [6], Brian Chaka [3], James J. Rankine [7], Gustav Andersson [8,9,10], Mikael Wiberg [8,9] and Grainne Bourke [1,2,8,9]

[1] Department of Plastic and Reconstructive Surgery, Leeds Teaching Hospitals Trust, Leeds, United Kingdom, [2] Faculty of Medicine and Health Sciences, University of Leeds, Leeds, United Kingdom, [3] National Institute for Health Research (NIHR), Leeds Biomedical Research Centre, Leeds, United Kingdom, [4] Department of Medical Physics and Engineering, Leeds Teaching Hospitals Trust, Leeds, United Kingdom, [5] Leeds Institute for Cardiovascular and Metabolic Medicine, University of Leeds, Leeds, United Kingdom, [6] The Advanced Imaging Centre, Leeds Teaching Hospitals Trust, Leeds, United Kingdom, [7] Department of Radiology, Leeds Teaching Hospitals Trust, Leeds, United Kingdom, [8] Department of Integrative Medical Biology (Anatomy), Faculty of Medicine, Umeå University, Umeå, Sweden, [9] Department of Surgical and Perioperative Science (Hand and Plastic Surgery), Faculty of Medicine, Umeå University, Umeå, Sweden, [10] Wallenberg Centre for Molecular Medicine, Umeå University, Umeå, Sweden

Cross-sectional MRI has modest diagnostic accuracy for diagnosing traumatic brachial plexus root avulsions. Consequently, patients either undergo major exploratory surgery or months of surveillance to determine if and what nerve reconstruction is needed. This study aimed to develop a diffusion tensor imaging (DTI) protocol at 3 Tesla to visualize normal roots and identify traumatic root avulsions of the brachial plexus. Seven healthy adults and 12 adults with known (operatively explored) unilateral traumatic brachial plexus root avulsions were scanned. DTI was acquired using a single-shot echo-planar imaging sequence at 3 Tesla. The brachial plexus was visualized by deterministic tractography. Fractional anisotropy (FA) and mean diffusivity (MD) were calculated for injured and avulsed roots in the lateral recesses of the vertebral foramen. Compared to healthy nerves roots, the FA of avulsed nerve roots was lower (mean difference 0.1 [95% CI 0.07, 0.13]; $p < 0.001$) and the MD was greater (mean difference 0.32×10^{-3} mm^2/s [95% CI 0.11, 0.53]; $p < 0.001$). Deterministic tractography reconstructed both normal roots and root avulsions of the brachial plexus; the negative-predictive value for at least one root avulsion was 100% (95% CI 78, 100). Therefore, DTI might help visualize both normal and injured roots of the brachial plexus aided by tractography. The precision of this technique and how it relates to neural microstructure will be further investigated in a prospective diagnostic accuracy study of patients with acute brachial plexus injuries.

Keywords: brachial plexus (D001917), diffusion tensor imaging (D056324), spinal nerve roots (D013126), peripheral nerve injuries (D059348), neurosurgery (D009493), tractography

IV

ORIGINAL PAPER

ANATOMICAL SOCIETY | Journal of Anatomy | WILEY

The Geometry of the roots of the Brachial Plexus

Ryckie G. Wade[1,2] | Emily R. Bligh[3,4] | Kieran Nar[5] | Rebecca S. Stone[6] | David J Roberts[3] | Irvin Teh[7] | Grainne Bourke[1,2]

[1]Leeds Institute for Medical Research, University of Leeds, Leeds, UK

[2]Department of Plastic and Reconstructive Surgery, Leeds Teaching Hospitals Trust, Leeds

[3]Division of Anatomy, Leeds Institute of Medical Education, University of Leeds, Leeds, UK

[4]Faculty of Medicine, Dentistry & Health, University of Sheffield Medical School, Sheffield, UK

[5]Faculty of Engineering, University of Sheffield, Sheffield, UK

[6]School of Computing, University of Leeds, Leeds, UK

[7]Leeds Institute of Cardiovascular and Metabolic Medicine, University of Leeds, Leeds, UK

Correspondence
Ryckie G. Wade, Academic Plastic Surgery Office, Department of Plastic and Reconstructive Surgery, Leeds General Infirmary, Leeds LS1 3EX, UK.
Email: ryckiewade@gmail.com

Abstract

Diffusion tensor magnetic resonance imaging (DTI) can be used to reconstruct the brachial plexus in 3D via tracts connecting contiguous diffusion tensors with similar primary eigenvector orientations. When creating DTI tractograms, the turning angle of connecting lines (step angle) must be prescribed by the user; however, the literature is lacking detailed geometry of brachial plexus to inform such decisions. Therefore, the spinal cord and brachial plexus of 10 embalmed adult cadavers were exposed bilaterally by posterior dissection. Photographs were taken under standardised conditions and spatially calibrated in MATLAB. The roots of the brachial plexus were traced from the dorsal root entry zone for 5 cm laterally using a 2.5-mm^2 Cartesian grid overlay. The trace was composed of points connected by lines, and the turning angle between line segments (the step angle) was resolved. Our data show that the geometry of the roots increased in tortuosity from C5 to T1, with no significant differences between sides. The 1st thoracic root had the most tortuous course, turning through a maximum angle of 56° per 2.5 mm (99% CI 44° to 70°). Significantly higher step angles and greater variability were observed in the medial 2 cm of the roots of the brachial plexus, where the dorsal and ventral rootlets coalesce to form the spinal root. Throughout the brachial plexus, the majority of step angles (>50%) were smaller than 20° and <1% of step angles exceeded 70°. The geometry of the brachial plexus increases in tortuosity from C5 to T1. To reconstruct 99% of tracts representing the roots of the brachial plexus by DTI tractography, users can either customise the step angle per root based on our findings or select a universal threshold of 70°.

KEYWORDS

anatomy, angle, Brachial plexus, diffusion tensor imaging, geometry, magnetic resonance imaging, microanatomy, pre-ganglionic, root

V

META-ANALYSIS

Diffusion tensor imaging of the roots of the brachial plexus: a systematic review and meta-analysis of normative values

Ryckie G. Wade[1,2] · Alexander Whittam[3] · Irvin Teh[4] · Gustav Andersson[5,6,8] · Fang-Cheng Yeh[7] · Mikael Wiberg[5,6] · Grainne Bourke[1,2,5,6]

Abstract

Purpose Diffusion tensor magnetic resonance imaging (DTI) characterises tissue microstructure and provides proxy measures of myelination, axon diameter, fibre density and organisation. This may be valuable in the assessment of the roots of the brachial plexus in health and disease. Therefore, there is a need to define the normal DTI values.

Methods The literature was systematically searched for studies of asymptomatic adults who underwent DTI of the brachial plexus. Participant characteristics, scanning protocols, and measurements of the fractional anisotropy (FA) and mean diffusivity (MD) of each spinal root were extracted by two independent review authors. Generalised linear modelling was used to estimate the effect of experimental conditions on the FA and MD. Meta-analysis of root-level estimates was performed using Cohen's method with random effects.

Results Nine articles, describing 316 adults (1:1 male:female) of mean age 35 years (SD 6) were included. Increments of ten diffusion sensitising gradient directions reduced the mean FA by 0.01 (95% CI 0.01, 0.03). Each year of life reduced the mean MD by 0.03×10^{-3} mm^2/s (95% CI 0.01, 0.04). At 3-T, the pooled mean FA of the roots was 0.36 (95% CI 0.34, 0.38; I^2 98%). The pooled mean MD of the roots was 1.51×10^{-3} mm^2/s (95% CI 1.45, 1.56; I^2 99%).

Conclusions The FA and MD of the roots of the brachial plexus vary according to experimental conditions and participant factors. We provide summary estimates of the normative values in different conditions which may be valuable to researchers and clinicians alike.

Keywords Diffusion tensor · Brachial plexus · Normal · Normative · Healthy · Peripheral nerve

Introduction

The brachial plexus is a network of nerves which supply the upper limb with movement and feeling (Fig. 1 and Supplementary Fig. 1). Magnetic resonance imaging (MRI) is generally considered the best non-invasive imaging modality for

✉ Ryckie G. Wade
  ryckiewade@gmail.com

1 Department of Plastic and Reconstructive Surgery, Leeds Teaching Hospitals Trust, Leeds LS1 3EX, UK

2 Leeds Institute for Medical Research, University of Leeds, Leeds, UK

3 Sheffield Teaching Hospitals NHS Foundation Trust, Sheffield, UK

4 Leeds Institute for Cardiovascular and Metabolic Medicine, University of Leeds, Leeds, UK

5 Department of Integrative Medical Biology, Faculty of Medicine, Umeå University, Umeå, Sweden

6 Department of Surgical and Perioperative Science, Section for Hand and Plastic Surgery, Umeå University, Umeå, Sweden

7 Department of Neurological Surgery, University of Pittsburgh, Pittsburgh, USA

8 Wallenberg Centre for Molecular Medicine, Umeå University, Umeå, Sweden

🙋 Springer

scientific reports

OPEN

Fractional anisotropy thresholding for deterministic tractography of the roots of the brachial plexus

Ryckie G. Wade[1,2✉], Irvin Teh[3], Gustav Andersson[4,5,6], Fang-Cheng Yeh[7], Mikael Wiberg[4,5,6] & Grainne Bourke[1,2,4,5]

Diffusion tensor imaging (DTI) metrics, such as the fractional anisotropy (FA) and estimates of diffusivity are sensitive to the microstructure of peripheral nerves and may be displayed as tractograms. However, the ideal conditions for tractography of the roots of the brachial plexus are unclear, which represents the rationale for this study. Ten healthy adults were scanned using a Siemens Prisma (3T) and single-shot echo-planar imaging (b-value 0/1000 s/mm^2, 64 directions, 2.5 mm^3 with 4 averages; repeated in opposing phase encoding directions). Susceptibility correction and tractography were performed in DSI Studio by two independent raters. The effect of FA thresholding at increments of 0.01 (from 0.04 to 0.10) were tested. The mean FA varied between subjects by 2% (95% CI 1%, 3%). FA thresholds of 0.04, 0.05 and 0.06 all propagated 96% of tracts representing the roots; thresholding at 0.07 yielded 4% fewer tracts ($p = 0.2$), 0.08 yielded 11% fewer tracts ($p = 0.008$), 0.09 yielded 15% fewer tracts ($p = 0.001$) and 0.1 yielded 20% fewer tracts ($p < 0.001$). There was < 0.1% inter-rater variability in the measured FA and 99% agreement for tractography ($\kappa = 0.92$, $p < 0.001$). The fractional anisotropy thresholds required to generate tractograms of the roots of the brachial plexus appears to be lower than those used in the brain. We provide estimates of the probability of generating true tracts for each spinal nerve root of the brachial plexus, at different fractional anisotropy thresholds.

The structures most commonly affected in adults with a brachial plexus injury (BPI) are the spinal nerve roots[1]. Dedicated magnetic resonance imaging (MRI, including imaging in multiple planes with different sequences) is the best non-invasive test for diagnosing root injury although it misclassifies up to 25% of in-continuity nerve roots as avulsed[1], meaning that many surgeons still undertake exploratory surgery. This shortfall in conventional imaging might be improved by diffusion tensor imaging (DTI), which is sensitive to changes in the microstructure of peripheral nerves (e.g. myelination, axon population, fibre organisation, etc.)[2] through metrics such as the fractional anisotropy (FA), mean diffusivity (MD), axial diffusivity (AD) and radial diffusivity (RD). Further, DTI tractography may help clinicians to evaluate changes in the diffusivity and anisotropy throughout the length of the roots, which we speculate might help to identify areas of pathology or targets for surgery.

Previous studies have shown the feasibility of DTI tractography of the brachial plexus in adults[3–8] and others have shown the reproducibility of DTI metrics without tractography[9,10]. Tagliafico[4] and Vargas[3] used different FA thresholds for tractography across patients, citing thresholds of 0.15 +/− 0.05 but it is unclear how and from where these values were measured, and what the +/− 0.05 represents. Tagliafico[4] does not report the frequency of propagated tracts whilst Vargas[3] propagated C5-T1 tracts in all healthy volunteers. Conversely, work from our group[8] and Oudeman[5] used fixed FA thresholds of 0.06 and 0.1, respectively. Oudeman[5] reconstructed fibres representing the C5–C8 root in all cases, but in 52% of datasets, the 1st thoracic root was not reconstructed. Similarly, we propagated tracts of the C5–C8 roots in 96% of cases, although the T1 root was only visualised in 54% of datasets. Neither Gasparotti[6] or Su[7] described the FA thresholds they used for tractography, with the former reconstructing all roots in all subjects and the latter only reporting on the C5-8 roots.

[1]Academic Plastic Surgery Office, Department of Plastic and Reconstructive Surgery, Leeds General Infirmary, Leeds Teaching Hospitals Trust, Leeds LS1 3EX, UK. [2]Faculty of Medicine and Health Sciences, University of Leeds, Leeds, UK. [3]Leeds Institute for Cardiovascular and Metabolic Medicine, University of Leeds, Leeds, UK. [4]Department of Integrative Medical Biology, Faculty of Medicine, Umeå University, Umeå, Sweden. [5]Department of Surgical and Perioperative Science, Faculty of Medicine, Umeå University, Umeå, Sweden. [6]Wallenberg Centre for Molecular Medicine, Umeå University, Umeå, Sweden. [7]Department of Neurological Surgery, University of Pittsburgh, Pittsburgh, USA. ✉email: medrgwa@leeds.ac.uk

Appendix 7. Search Strategy for Brachial Plexus Injury MRI DTA review

Medline (1946 onwards)

1. exp brachial plexus (tree A08.800.800.720.050)
2. (brachial AND plexus).ti,ab
3. (root AND avulsion).ti,ab
4. (pre?ganglion*).ti,ab
5. ((brachial AND plexus) AND pseudomeningocoele).ti,ab
6. exp magnetic resonance imaging (tree E01.370.350.825.500)
7. (MR?).ti,ab
8. (magnetic AND resonance).ti,ab
9. (NMR).ti,ab
10. (neurogra*).ti,ab
11. (DTI).ti,ab
12. ((diffusion AND tensor) AND imaging).ti,ab
13. (1 OR 2 OR 3 OR 4)
14. (5 OR 6 OR 7 OR 8 OR 9 OR 10 OR 11 OR 12)
15. (13 AND 14)

EMBASE (1947 onwards)

1. exp brachial plexus
2. (brachial AND plexus).ti,ab
3. (root AND avulsion).ti,ab
4. (pre?ganglion*).ti,ab
5. ((brachial AND plexus) AND pseudomeningocoele).ti,ab
6. exp magnetic resonance imaging
7. (MR?).ti,ab
8. (magnetic AND resonance).ti,ab
9. (NMR).ti,ab
10. (neurogra*).ti,ab
11. (DTI).ti,ab
12. ((diffusion AND tensor) AND imaging).ti,ab
13. (1 OR 2 OR 3 OR 4)
14. (5 OR 6 OR 7 OR 8 OR 9 OR 10 OR 11 OR 12)
15. (13 AND 14)

Cochrane Library

"brachial plexus" with no limitations

Study ID:

Patients (setting, intended use of index test, presentation, prior testing):

Index test(s):

Reference standard and target condition:

---

1 – Patient Selection

1A. Risk of Bias

Describe methods of patient selection:

Was a consecutive or random sample of patients enrolled?   Yes / No / Unclear

Was a case-control design avoided?   Yes / No /
Unclear

Did the study avoid inappropriate exclusions (eg. unclear   Yes / No / Unclear

       avulsion status at surgery, older patients, etc)?

Could the selection of patients have introduced bias?   LOW   /   HIGH   /

UNCLEAR

Code low risk if the answers to all signalling questions were yes.

Code as high risk if any answer to the signalling questions was no.

Otherwise, code as unclear.

1B. Concerns regarding applicability

Describe included patients (prior testing, presentation, intended use of index test and setting)

Is there concern that the included patients do not match the review question? **LOW / HIGH / UNCLEAR**

Code as unclear concern if any of the following were not described: prior tests, mechanisms of injuries, the role and of the MRI and conditions (pulse sequence, interpretation, etc) or surgical method of exploration.

Code as low concern if any above factors were described and appropriate.

Code as high concern if: there were inappropriate exclusions of eligible cases or the series was non-consecutive.

2: Index test

2A. Risk of Bias

Describe the index test and how it was conducted and interpreted

Were the MRI results interpreted without knowledge of the exploration? Yes / No / Unclear

If a threshold for either test was used, was it pre-specified Yes / No / Unclear

Code as low risk if both the diagnosis of avulsion was defined for the MRI and exploratory surgery

Code as high risk the diagnosis of avulsion was not described for the MRI or reference standard

Otherwise, code as unclear.

Could the conduct or interpretation of the index

test have introduced bias? **LOW / HIGH /**

UNCLEAR

Code as low risk if all the signalling questions were answered yes.

Code as high risk if any signalling question were answered no.

Otherwise, code as unclear.

2B. Concerns regarding applicability

Is there concern that the index test, its conduct, or

interpretation differ from the review question? **LOW / HIGH /**

UNCLEAR

Code as high concern if no threshold was defined.

Code as low concern if the MRI was performed by an appropriate person with described

thresholds.

Code as unclear if images were interpreted by multiple radiologists as this does not

reflect practice or the methods of reporting were not described.

3: Reference Standard

3A. Risk of Bias

Describe the reference standard and how it was conducted and interpreted

Is the reference standard likely to correctly classify the target condition?

Yes/No/Unclear

Were the reference standard results interpreted without knowledge of the

results of the index test?

Yes/No/Unclear

Could the reference standard, its conduct, or its

Interpretation have introduced bias?   **LOW / HIGH**

/ UNCLEAR

Code as low risk if both signalling questions answer yes.

Code as high risk if both signalling question answers no.

Otherwise code as unclear risk.

3B. Concerns regarding applicability

Is there concern that the target condition as defined by

the reference standard does not match the review question?   LOW   /   HIGH   /

UNCLEAR

Code as unclear concern if the criteria for diagnosis of root avulsion at surgery was

unclear or incompletely described in the methods and results are reported.

Code as low concern if the criteria for root avulsion at surgery was clearly defined and

results reported.

Code as high concern if there was no description of the methods for surgical exploration

and results alone are reported.

4 – Flow and Timing

4A. Risk of Bias

Describe any patients who did not receive a preoperative MRI and/or exploration or who

were excluded from the 2x2 table:

Describe the time interval and any interventions between index test(s) and reference

standard

Was the interval between MRI and exploration <12 months?   Yes / No /

Unclear

Did all cases receive the same brachial plexus exploration?   Yes / No /

Unclear

Were all patients included in the analysis?   Yes / No / Unclear

Could the patient flow have introduced bias?   LOW / HIGH / UNCLEAR

Code as low risk if all signalling questions were answered yes

Code as high risk if any answer was no

Otherwise, code as unclear

Appendix 9. Studies excluded from https://doi.org/10.1038/s41598-020-79840-8

Evaluation of Brachial Plexus Using Combined Stereological Techniques of Diffusion Tensor Imaging and Fiber Tracking. 2019. Acer N and Turgut M. Journal of brachial plexus and peripheral nerve injury. e16-e23. 14. 10.1055/s-0039-1687913

Zobrazeni perifernich nervu pomoci difuzniho tenzoru a mr traktografieImaging of peripheral nerves using diffusion tensor imaging and MR tractography. 2018. Humhej I. et al. Ceska a Slovenska Neurologie a Neurochirurgie. 420-426. 81. 4. 10.14735/amcsnn2018csnn.eu3

Diffusion tensor imaging of the brachial plexus as an aid to the diagnosis of inflammatory neuropathies: Preliminary results. 2016. Oudeman J. et al. Journal of the Peripheral Nervous System. 198. 21. 3. 1529-8027. Blackwell Publishing Inc.

New technologies for the assessment of neuropathies.2017. Gasparotti R, et al. Nature Reviews Neurology. 203-216. 13. 4. 10.1038/nrneurol.2017.31

Diffusion tensor imaging of the brachial plexus and cervical spinal nerve roots: Case control study in CIDP patients and controls.2017. Chanson E, et al. Neurology. 88. 16. 1526-632X

Clinical application of diffusion tensor tractography (DTT) of traumatic brachial plexus injuries. 2011. Schmidt T, et al. Journal of Neurosurgery. 115. 2. 0022-3085. American Association of Neurological Surgeons

Mri of the brachial plexus and chronic inflammatory demyelinating polyradiculoneuropathy: assessment of dti-derived measurements at 3.0-t. 2017. Chanson E, et al. Journal of the Peripheral Nervous System. 226-414. 22. 3. 10.1111/jns.12225

Feasibility of diffusion tensor tractography of brachial plexus injuries at 1.5 T. 2013. Gasparotti R, et al. Investigative Radiology. 104-112. 48. 2. 10.1097/RLI.0b013e3182775267

Quantitative MR neurography of brachial plexus lesions based on diffusivity measurements
2018. Hend Galal Eldeen et al. The Egyptian Journal of Radiology and Nuclear Medicine. 1093-1102

49. 4. 10.1016/j.ejrnm.2018.05.005

Quantitative magnetic resonance (MR) neurography for evaluation of peripheral nerves and plexus injuries. 2017. Noguerol M, et al. Quantitative imaging in medicine and surgery. 398-421. 7. 4

3T MR tomography of the brachial plexus: Structural and microstructural evaluation. 2012. Mallouhi A, et al. European Journal of Radiology. 2231-2245. 81. 9. 10.1016/j.ejrad.2011.05.021

High-resolution and functional magnetic resonance imaging of the brachial plexus using an isotropic 3D T2 STIR (Short Term Inversion Recovery) SPACE sequence and diffusion tensor imaging
2008. Viallon M, et al. European Radiology. 1018-1023. 18. 5. 10.1007/s00330-007-0834-4

Nervenverletzungen und traumatische Läsionen des Plexus brachialis. 2017. 1. Schwarz D, et al. Der Radiologe. 184-194. 57. 3. 10.1007/s00117-017-0207-1

"Diffusion tensor imaging and tractography of traumatic brachial plexus palsies" presented at the 38th european society of neuroradiology Diagnostic and Interventional annual meeting. 2015. Gasparotti R, et al. Neuroradiology. 1-169. 57. S1. 10.1007/s00234-015-1557-x

"Diffusion tensor imaging and tractography of traumatic brachial plexus palsies. Preliminary experience". 2010. Gasparotti R, et al. Neuroradiology Journal. 361. 23. 1971-4009

DTI of brachial plexus. 2010. Pellicano G, et al.Neuroradiology Journal. 80. 23. 1971-4009

Cerebral plasticity in painful phantom limb: a study with transcranial magnetic stimulation and functional magnetic resonance imaging. 2009. de Oliveira, et al. European Journal of Pain. S70. 13. 10.1016/S1090-3801(09)60218-4

Visualizing nerve fibers surrounding a brachial plexus tumor using MR diffusion tensor imaging
no normal DTI data. Gallagher TA, et al. Neurology. 2016. 65. 582-583. 10.1212/WNL.00000000000023602016